Modeling of Dry and Saturated Soil-Foundation Interfaces

By

Sumeet Kumar Sinha
B.S. (Indian Institute of Technology Delhi) 2014

Thesis

Submitted in partial satisfaction of the requirements for the degree of

Master of Science

in

Civil And Environmental Engineering

in the

Office of Graduate Studies

of the

University of California

Davis

Approved:

Professor Boris Jeremić, Chair

Professor Bruce L Kutter

Professor Alejandro Martinez

Committee in Charge

2017

This thesis is dedicated to my parents ,. . .

uncle and the whole family back in India.

Contents

List of Figures

List of Tables

Abstract

Modeling of Dry and Saturated Soil-Foundation Interfaces

Modeling and simulation of earthquake soil-structure interaction (ESSI) requires a number of sophisticated modeling and simulation approaches to reduce modeling uncertainty and improve the accuracy of results. The superstructure can be supported by either shallow or deep foundation and in the dry, partially saturated, or fully saturated soil. An interface element is thus required to accurately model the interaction of dry as well as partially saturated soil with the foundation. The current modeling techniques mostly assume a hard normal contact behavior i.e. normal contact stiffness is constant with penetration. However, a more physical contact stress expected between the soil-foundation interface is non-linear. The normal contact stiffness increases with penetration until the soil surface becomes hard. At this state, any further penetration can be assumed to be of hard contact. In this thesis, a soft contact formulation is presented to model the non-linear stiffness at soil-foundation interface. The cyclic shear behavior of the soil-structure is highly non-linear and sophisticated. It includes hysteresis, hardening, softening (dilation) and particle breakage. Depending upon the normal stress or confinement, the shear behavior of the interface can have hardening until a peak shear strength is attained and then softening to the critical or residual shear strength. In this thesis, apart from the most popular Elastic Perfectly Plastic shear model, two additional shear models with nonlinear hardening and non-linear hardening/softening are proposed with minimum modeling parameters to model the monotonic as well as cyclic shear behavior at soil-foundation interface. In partially or fully saturated conditions, during dynamic events (seismic shaking) pore fluid pressures in soil adjacent to foundations will change dynamically. Moreover, for strong shaking, the structure might rock, and foundation-soil interface might develop gaps and create suction pressure pulling the water up in tension. A coupled element is developed to model the changes in dynamic pore-fluid pressures and effective stress at soil-foundation interface for submerged conditions. An extensive verification for all the components of the proposed elements is also performed.

Acknowledgments

I would like to express my deepest gratitude to my advisor Professor Boris Jeremić for his insight, guidance, and support which provided a steep learning experience and made me grow in ways I would have never imagined. I am completely grateful for his support and belief in my work. I am deeply thankful to the Department of Energy (DOE) for providing funding for this research work.

Much gratefulness is due to my thesis committee Professor Bruce L Kutter and Professor Alejandro Martinez. Thank you for reviewing and appreciating my work, as well as for your valuable feedback.

I would also like to express my gratitude and appreciation to the UC Davis Civil and Environmental Engineering Department and the excellent faculty it has. The coursework has been instrumental in the development of my technical and computational skills as a geotechnical engineer.

I would also like to thank the Computational Geomechanics Group (Yuan, Han, Maxime, Fatemah, and Hexiang) for the countless number of discussions and the fun we had while performing our research.

Lastly, I would like to thank my family back in India for their unconditional love, care and support at all times.

Chapter 1

Introduction

1.1 Soil-Foundation Interface

Soil-structure interaction (SSI) effects have been studied since 1960's Jardine et al. [1986]; Wolf and Hall [1989]; Tang et al. [1989]; Wolf [1989]; Stewart et al. [1999]; Breysse et al. [2005] and have continued to be a hot topic of research. It mainly involves prediction of stresses, deformation, frequency content of the induced structural motion by ground excitation and energy flow. SSI effects emerge primarily from an inelastic and heterogeneous soil, geology, uncertain ground motions, superstructure, and soil-foundation interface. One of the most important among them is the soil foundation interface. Sheng et al. [2007] notes the importance of application of frictional contact (interface) modeling in geotechnical engineering. At the interface, there can be two possible modes of response.

1. **Normal Contact:** The foundation and the soil interacts with only normal stress with no tangential loading. The interaction is purely compressive. However, during uplift, the interface can possess a gap opening leading to zero stiffness in contact normal direction.

2. **Slip (Sliding):** The foundation and soil develops frictional slip. The foundation can stick or slide depending upon the tangential loading and normal stress. For rigid type of contact, sticking and sliding states are governed by Newton's Friction law.

The soil being a multi-phase particulate material comprise of solid particles, pore fluids, and gases. It can behave as dry, partial-, fully- or unsaturated mixture. Being a particulate material, the mechanical properties of soil depends upon confinement and pore-fluid pressure and follows Bishop's generalized effective stress σ'_{ij} principle [Bishop, 1959; Bishop and Blight, 1963].

$$\sigma'_{ij} = \sigma_{ij} - \delta_{ij}[u_a - \chi(u_a - u_w)] \tag{1.1}$$

Where, χ[1] is the effective stress parameter and it is generally assumed to be equal to the degree of saturation, u_a, u_w are the pore pressures of air and fluid respectively, σ_{ij} is the total stress tensor and δ_{ij} is the Kronecker delta function.

1.1.1 Dry Soil

For dry soils, the effective stress σ'_{ij} becomes equal to the total stress σ_{ij} subtracted by the air pressure u_a. The effective stress principal changes to Equation 1.3. The effective stress parameter χ becomes equal to 0.

$$\sigma'_{ij} = \sigma_{ij} - \delta_{ij} u_a \tag{1.2}$$

$$p = u_a \tag{1.3}$$

Under this condition, the interface between soil and contact can be assumed to be dry and is modeled using Dry Contact (Section 1.2). There is no generation of pore-pressure under static or dynamic loadings. However cyclic shear can result in gradual compaction of soil.

1.1.2 Saturated Soil

For saturated soils, the effective stress parameter is $\chi = 1$. The effective stress σ'_{ij} becomes equal to the total stress σ_{ij} subtracted by the total pore-fluid pressure p.

$$\sigma'_{ij} = \sigma_{ij} - \delta_{ij} p \tag{1.4}$$

$$p = u_w \tag{1.5}$$

[1] In case of dry soil $\chi = 0$, and under fully saturation case $\chi = 1$

The development of instantaneous and steady state pore-fluid pressure subject to an externally applied loading depends upon porosity, permeability, density and bulk-modulus of the fluid and solid constituents of soil. The excess pore-pressure in sands is dissipated within few seconds to minutes as compared to clayey soils (very low permeability) where it can take weeks to months to years. For dynamic shaking events such as earthquakes or machine induced vibrations where loadings change in seconds, the steady state conditions do not prevail due to the generation of excess pore-pressure. Even for sands which have high permeability, this excess pore-pressure becomes an important factor in the determination of soils engineering properties. The cyclic shearing of loose or normally consolidated saturated soils in undrained conditions is accompanied by the reduction of effective stress, which in turns changes the shear stiffness and stress-strain response of soil. This can also lead to compaction under drained conditions.

At the soil-foundation interface, water cannot move upward (past the foundation) resulting in undrained conditions. As stated earlier, during uplift the foundation may have the potential to induce suction and pull water along with itself, thus creating a negative pore-pressures. All these effects must be taken into consideration while developing the contact element (Section 1.3).

1.2 Dry Contact Condition

The general contact [Wriggers, 2002] description for a frictionless problem of an elastic body (let's say soil) coming in contact with a firm (rigid) foundation or vice-versa as shown in Figure 1.1.

Due to the contact constraints, a variational inequality will appear instead of the standard variational equation known from classical mechanics. From elasticity, the equilibrium equation under static condition holds

$$\sigma_{ij,j} + b_i = 0 \tag{1.6}$$

where σ_{ij} is the stress tensor and b_i is the body force per unit volume. The small strain tensor $\epsilon_{ij}(u)$ is given as

$$\epsilon_{ij}(u) = \frac{1}{2}(u_{i,j} + u_{j,i}) \tag{1.7}$$

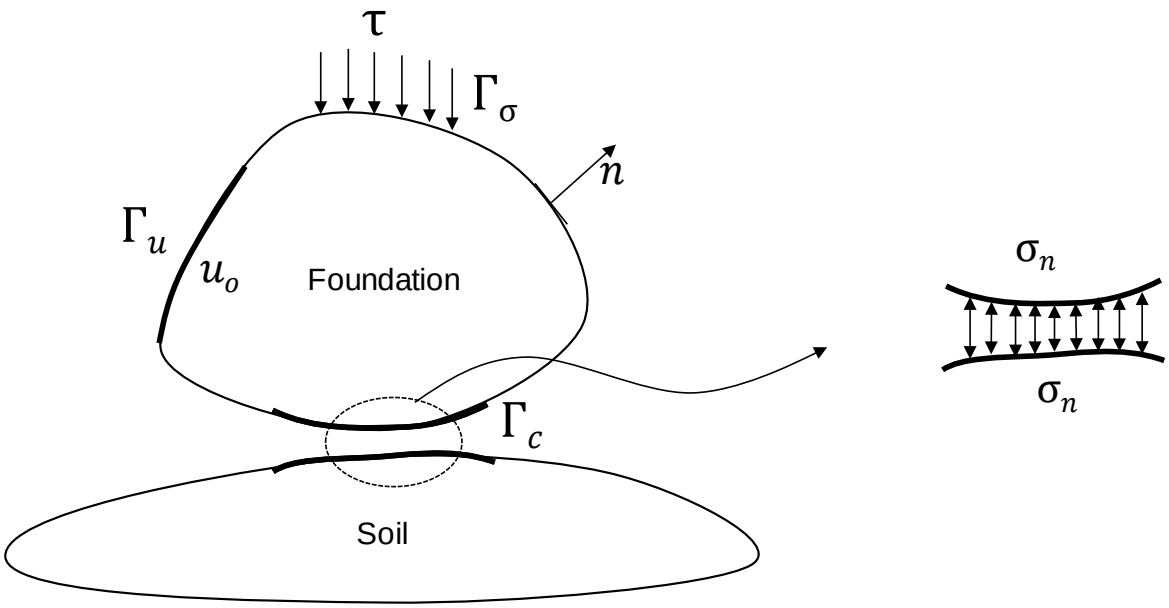

Figure 1.1: Contact between elastic body and rigid foundation.

and the stress-strain relationship is given by the constitutive law involving elasticity tensor C_{ijkl} as

$$\sigma_{ij}(u) = C_{ijkl}\epsilon_{kl}(u) \tag{1.8}$$

The boundary condition of the contact problem is shown in Figure 1.1. Ω is the domain in $\Re^3$ with boundary Γ. The boundary Γ is split into two three disjoint boundaries Γ_u, Γ_σ and Γ_c and are defined as

1. Dirichlet or Displacement boundary condition:

$$u_i = \bar{u_i} \quad on \quad \Gamma_u \tag{1.9}$$

2. Neuman or Traction boundary condition:

$$\sigma_{ij}(u)n_j = \tau_i \quad on \quad \Gamma_\sigma \tag{1.10}$$

where n is the normal vector on Γ_σ boundary surface and τ represents the given traction vector.

3. Contact Condition:

$$\begin{aligned} u_n^r - g_n &\leq 0 \\ p_n &\leq 0 \quad on \quad \Gamma_c \\ (u_n^r - g_n)p_n &= 0 \end{aligned} \tag{1.11}$$

where the u^r and g is the current and initial relative displacement between the two potential contact surfaces respectively . $u_n^r = u_i^r \cdot n_i$ and $g_n = x_i^r.n_i$ is the current and initial gap in contact normal direction respectively. $p_n = \tau_i \cdot n_i$ is the contact pressure developed at interface.

Thus the strong form of the equation is to *find the displacement field* $u \in \Omega$ *such that:*

$$\begin{aligned} \sigma_{ij,j} + b_i &= 0 \quad in \quad \Omega \\ u_i &= \bar{u_i} \quad on \quad \Gamma_u \\ \sigma_{ij}(u)n_i &= \tau t \quad on \quad \Gamma_\sigma \\ u_n^r - g_n &\leq 0 \\ p_n &\leq 0 \quad on \quad \Gamma_c \\ (u_n^r - g_n)p_n &= 0 \end{aligned} \tag{1.12}$$

1.2.1 Frictional Contact

When there is friction on the contact surface, along with the normal p_n, there will be tangential $q_{t_i} = \tau_i - p_n n_i$ components of traction. The maximum tangential traction q_t could be limited by the Coulomb's friction law $|q_t| \leq \mu p_n$ or by the equivalent interface material behavior. This induces additional constraint to the boundary value problem (BVP) shown in Equation 1.12

$$|q_t| - \mu|p_n| \leq 0 \quad \Gamma_c \tag{1.13}$$

$$v_{ti} = \delta u_i^r - u_n n_i \tag{1.14}$$

$$v_{ti} + \xi q_{ti} = 0 \tag{1.15}$$

$$\xi \geq 0 \tag{1.16}$$

$$(|q_t| - \mu|p_n|).\xi = 0 \tag{1.17}$$

Equation 1.13 states the Coulomb's friction condition. μ represents the evolving normalized shear stress q_n/p_n hardening softening variable. For elastic perfectly plastic interface, μ is constant and equal to the residual normalized shear stress $\mu_r = (q_t)/p_n$. u_t^r is the relative tangential slip displacement vector between the potential contact surfaces. Equation 1.14 represents the incremental slip v_t or is sometimes also referred as slip velocity. v_t can also be thought of the plastic flow direction similar to the elastic-plastic material model. Equation 1.15 and 1.16 constraints the tangential traction to work opposite to the direction of the slip. Finally, Equation 1.17 states another complementary condition that there is no slip if the tangential friction has not reached its local maximum and if there is a slip, then it reaches its maximum. The friction tractions are always complementary to the slip velocity.

Based on Equation 1.13, there can be two cases for frictional elastic perfectly plastic contact. One is the *sticking* case and the other is the sliding case based on whether $|q_t| - \mu|p_n|$ is ≤ 0 or > 0 respectively during the contact.

1. *Stick Condition*: $|q_t| - \mu|p_n| \leq 0$

$$v_{ti} = 0 \quad on \quad \Gamma_c \tag{1.18}$$

2. *Slip Condition*: $|q_t| - \mu|p_n| > 0$

$$\sigma_{ij}(u)t_j = q_{ti} \quad on \quad \Gamma_c \tag{1.19}$$

where v_t is relative incremental slip of potential surfaces in contact and $\sigma_{ij}(u).t_j$ is the tangential traction at interface on Γ_c boundary surface. More realistic soil-structure

interface, the response is highly non-linear with hardening and softening phase. In such case, the contact starts to slip as soon as some shear loading is applied.

1.3 Coupled Contact Condition

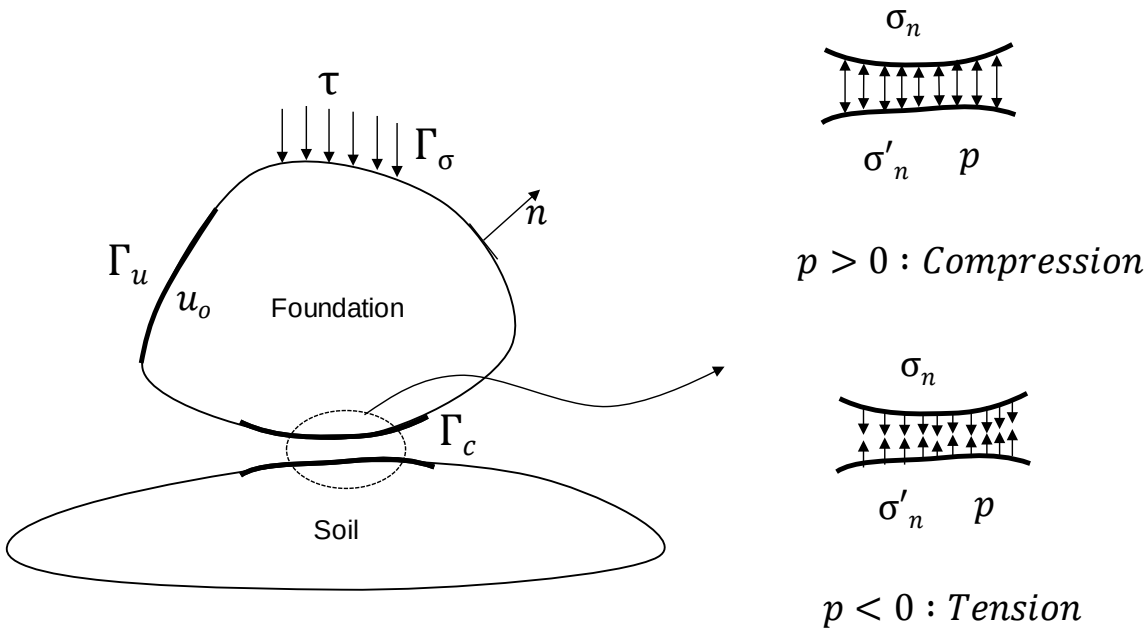

Figure 1.2: Coupled contact between foundation and soil

Figure 1.2 shows a general coupled problem between foundation and saturated soil. The contact problem follows the formulation presented in Section 1.2. In contact normal direction, positive pore-pressure gets developed during compression. The foundation prevents the fluid movement in the contact normal direction. However, uplift can result in suction effect at the soil-foundation interface resulting in pulling of water due to surface tension. Thus, both the effects during compression and uplift needs to be considered while modeling the coupled interface.

For partially saturated soils, unlike normal conditions, the interface is not dry but wet. At the interface, pore-fluid pressure (p) will develop and effective stress (σ'_{ij}) principle will govern engineering properties of soil whereas total stress (σ_{ij}) will govern the engineering properties of the foundation. In the derivations below, (u) and (U) represents the solid and fluid displacements of the soil mixture respectively. Since the foundation is in a dry

state, there is no fluid displacements (U). In the formulations, the pore-fluid pressure (p) is taken as positive during compression.

At the interface, during compression both foundation and soil would move together whereas during uplift the foundation can develop suction pulling water with itself and thus, creating negative pore pressure. Equations enforcing this frictionless contact conditions are

$$u_n^r - g_n \leq 0 \tag{1.20}$$

$$\sigma_n = \sigma^{'}{}_n + p \leq 0 \quad (Compression) \tag{1.21}$$

$$\sigma_n = -p \geq 0 \quad (Tension) \tag{1.22}$$

where, the normal component of displacement field u_n^r is $u^r \cdot n$ and $\sigma_n = n_i \cdot \sigma_{ij} \cdot n_j$ is the normal contact stress. g_n is the gap between the two-interface surface such that $g_n \geq 0$. In the presence of friction at the contact surface, along with normal, tangential contact stress σ_t gets also developed. The frictional part introduces additional constraints as follows.

$$|\sigma_t| - \mu|\sigma_n| \leq 0 \quad (Compression) \tag{1.23}$$

$$\sigma_t = 0 \quad (Tension) \tag{1.24}$$

where, μ is coefficient of friction based on Coulombs Frictional law. During uplift, no shear resistance is offered. Hence, tangential contact stress (σ_t) is zero.

The constraints for coupled contact follows the same steps for both frictionless and frictional surfaces as described in Section 1.2. However, in this case an additional level of constraint is introduced as shown in Equation 1.23, 1.24, 1.21 and 1.22. It comes as a result of undrained condition in contact normal direction which can be represented by the following equation

$$u_n^f = U_n^s \quad on \quad \Gamma_c \tag{1.25}$$

where, u_n^f and U_n^s represents the displacement of foundation and soil-fluid respectively in contact normal direction. In order to model the suction of water at interface, the above Equation 1.25 is assumed to hold always. This allows water to be sucked during uplift. It must be noted that a more general approach would to model suction only to a certain uplift distance, at which the liquid molecules break.

1.4 Contact Interface Behavior

Soil-structure interface is very important for dynamic soil structure interaction (SSI) effects. The cyclic behavior of the soil-structure is highly non-linear and sophisticated. It included hysteresis, hardening, softening (dilation) and particle breakage. The normal behavior of the interface is also highly non-linear. Depending upon the normal load or confinement σ_n, the shear behavior of the interface can have hardening until a peak strength τ_p is attained and then softening to the critical strength τ_c. On cyclic shearing, because of breakage of particles and hysteresis, the interface friction angle can degrades lower than the critical friction angle ϕ_c to residual friction angle ϕ_r. The following section presents a literature review of the development of soil-structure interface models.

1.4.1 Experimental Investigation

The response of the interface plays a very important role on the behavior of deep foundations, retaining walls, geo-membranes, submerged structures and soil-structure interaction. The load transfer mechanism from structure to the soil acts at the interface. The soil-structure interface comprise of a very thin small shearing band. The initial investigation by Yoshimi and Kishida [1981] indicated the thickness of the shear band as nine times the mean grain size diameter D_{50}. Tejchman and Wu [1995] conducted several tests on sand-steel interface and concluded that the thickness of the interface for rough interface is 30-40 D_{50} and for smooth interface is 6-10 D_{50}. Dejong et al. [2006]; DeJong and Westgate [2009] investigated the shear-zone thickness to be 5-10 times the mean particle diameter D_{50}. Martinez et al. [2015] conducted several axial and torsional shear experiments on sand-steel interface to understand the micro mechanics involved at interface. The micro-mechanical hypothesis proposed by Martinez et al. [2015] is shown in Figure 1.3. The

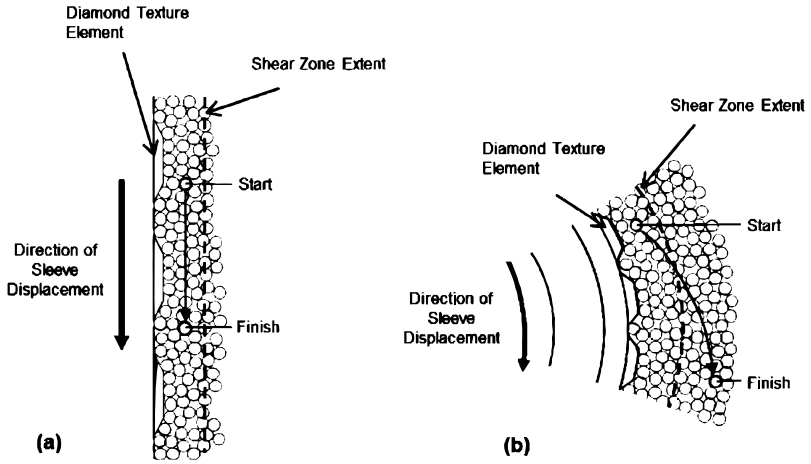

Figure 1.3: Hypothesis for a particle movement under (a) axial and (b) torsional loading (Martinez et al. [2015])

thickness of the interface zone formed by the particle in axial shearing migrates along the interface whereas for torsional shearing it migrates away from the interface.Similar mechanical hypothesis was observed by Dejong et al. [2006] It was also observed that for torsional shear the shear band zone was 2-3 times larger than the purely axial shearing. It also depends upon the characteristics of the soil beneath and the surface structural material and its roughness.

Since 1960's, researchers have been carrying out experiments to understand the interface behavior. The initial works have been contributed by Potyondy [1961]; Brumund and Leonards [1973]; Littleton [1976]. Potyondy [1961] studied the effect of soil-moisture content, structural surface roughness, soil-composition and normal load intensity on the skin-friction of the soil-structure interface. Brumund and Leonards [1973] investigated the static and dynamic friction angle between sand steel interface. Littleton [1976] performed drained and undrained tests on clay-steel interface and compared its behavior with clay-clay interface. At the clay-steel interface, a sudden failure at the interface was observed with further deformation leading to little change in shear stress. As a result, the initial shear stress strain response was observed to be comparatively stiffer with attainment of a peak shear stress and then softening than the usual clay-clay interface. Based on the normal confinement σ_n, an initial hardening was observed until the peak shear strength τ_p is

reached. After that softening to residual shear stress τ_r was observed. Later Desai [1981] emphasized on the importance of modeling of interface behavior for real soil-structure interactions. He also pointed out the lack of existing experimental data which could be used to develop constitutive models defining the interface behavior. Yoshimi and Kishida [1981] used a ring torsion apparatus to find the friction angle between dry sand and steel surface over a wide variation of surface roughness and sand density. Uesugi and Kishida

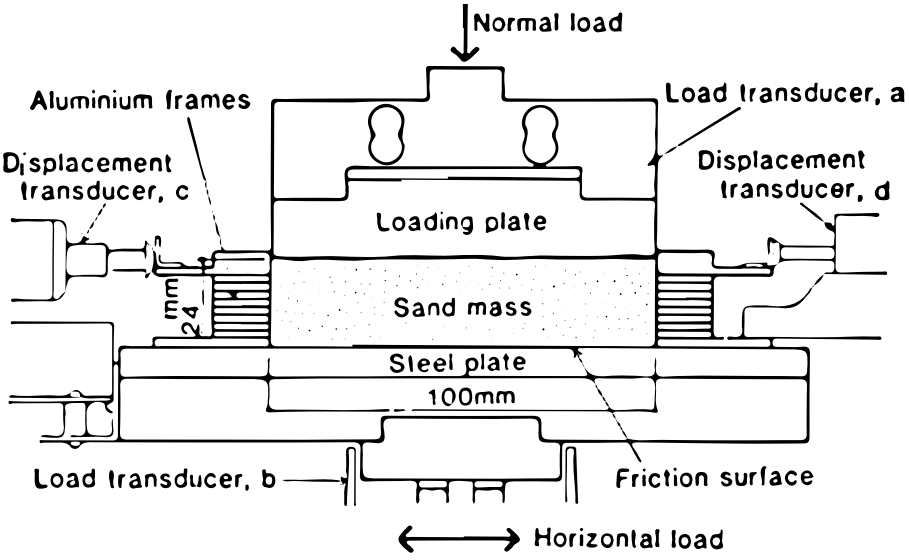

Figure 1.4: Section of friction test apparatus (Uesugi and Kishida [1986*a*])

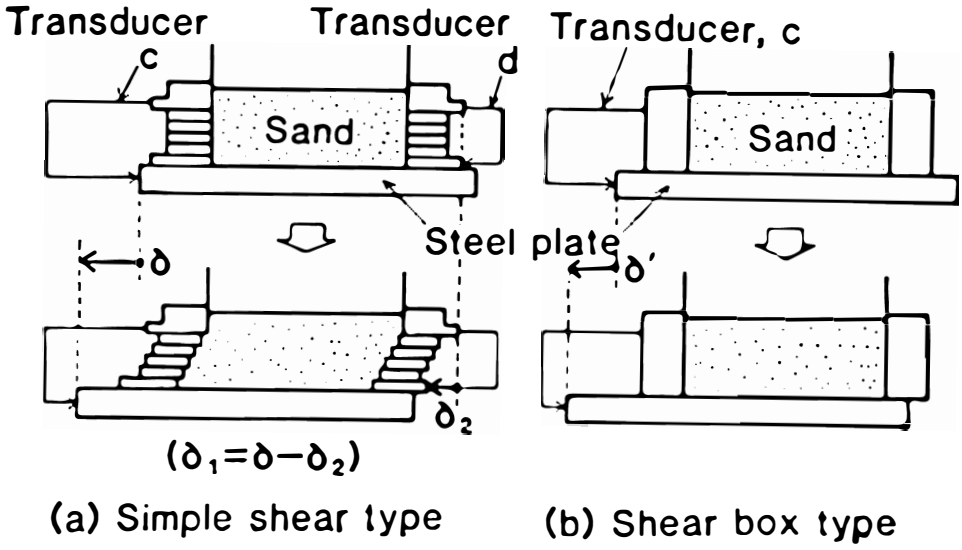

Figure 1.5: Measurement of tangential displacement (Uesugi and Kishida [1986*a*])

[1986*b*,*a*]; Kishida and Uesugi [1987] carried a series of laboratory experiments between steel and air-dried sands using simple shear apparatus shown in Figure 1.4 and Figure 1.5. It was found that the interface behavior is highly influenced by the sand type and surface roughness R_{max} while the effect of normal stress σ_n and mean grain size D_{50} are of poor significance. Thus, Kishida and Uesugi [1987] proposed a normalized roughness R_n to evaluate the relative coefficient of friction μ_y of sand-steel interface as shown in Figure 1.6.

$$R_{max}(L = D_{50})/D_{50} \tag{1.26}$$

where, $R_{max}(L = D_{50})$ is the R_{max} value of the steel surface with gauge length $L = D_{50}$.

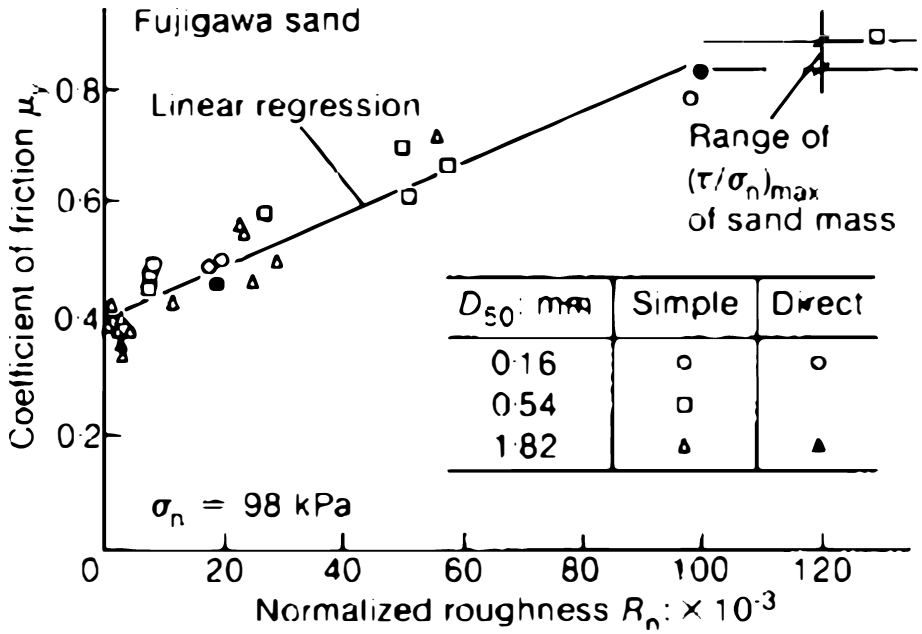

Figure 1.6: Coefficient of friction at yield μ_y and normalized roughness (after Kishida and Uesugi [1987])

Desai and Nagaraj [1988] performed a cyclic normal and shear tests on dry sand and concrete interface in translational shear box. Monotonic and cyclic normal loads along with cyclic shear loads were applied. The shear behavior was modeled with a modified form of Ramberg-Osgood (R-O) model. Although Desai and Nagaraj [1988] did not show any experimental results, he idealized the normal interface behavior to be composed of (1) Virgin loading; (2) unloading; (3) reloading; 4 tensile condition; (5) partial debonding;

and 6 rebonding as shown in Figure 1.7 assuming 1-D oedometric compression loading conditions. Uesugi et al. [1989, 1990] studied the frictional behavior of sand-steel interface

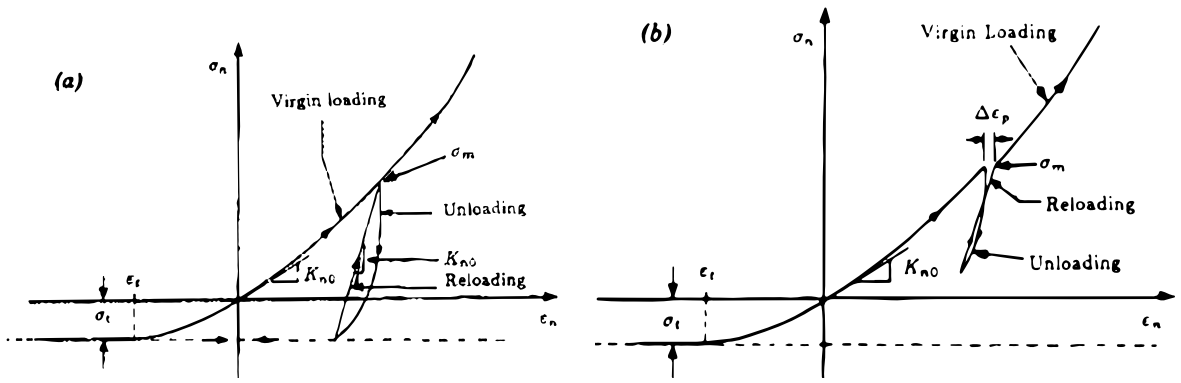

Figure 1.7: Schematic of stress-strain response for normal behavior (Desai and Nagaraj [1988]) : (a) Virgin loading and unloading with tensile stress condition; (b) Partial loading

subject to repeated shearing under one-way or two-way loadings. It was found that under repeated loading conditions the coefficient of friction μ converged close to the residual coefficient of friction μ_r as could be observed in Figure 1.8 Boulon [1989] performed

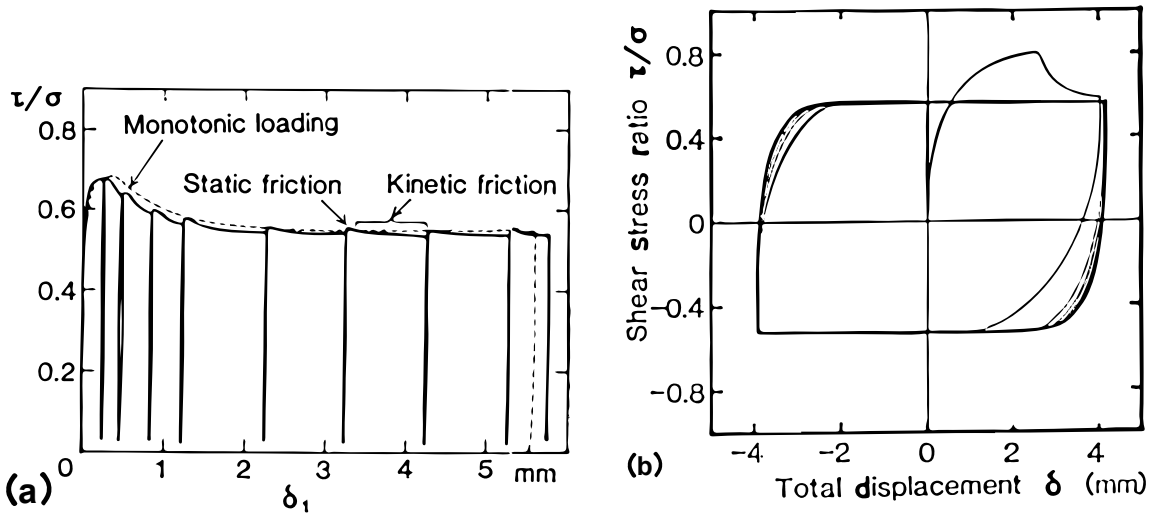

Figure 1.8: (a) Monotonic and (b) Cyclic response of Toyora sand with steel interface (Uesugi et al. [1989]) ($D_r = 90\%, \sigma_n = 98kPa, R_n = 150e^{-3}$)

a lot of experiments on piles in sand. Direct simple shear tests were carried out to investigate the shear behavior between the granular soil and rough construction material.

Based on the experimental results obtained later Boulon and Nova [1990] proposed a mathematical model and constitutive integration to model the interface behavior in finite element method (FEM). Aubry et al. [1990] proposed a dilatancy based cyclic elastic-plastic constitutive model for the interface. Cyclic loading functions with memory of last loading reversal was used to model subsequent loadings and unloading. The yield function was defined using simple Mohr Coulomb with additional parameter F as a function of normal stress σ_n and plastic compressibility β to account for curvature and dilation of the yield surface.

Fakharian and Evgin [1995] developed a 3-D apparatus capable of performing direct and simple shear type testing of interfaces between soil and structure. The developed apparatus was subsequently used to perform numerous experiments Fakharian and Evgin [1996]; Evgin and Fakharian [1997]; Fakharian and Evgin [1997]; Fakharian [1996]; Fakharian et al. [2002] over sand-steel interface for different stress paths for different relative densities D_r of sand. The 3-D apparatus made it possible to conduct 2-D shear test with constant normal stress σ_n. Monotonic and cyclic test results are shown in Figure 1.9 and Figure 1.10.

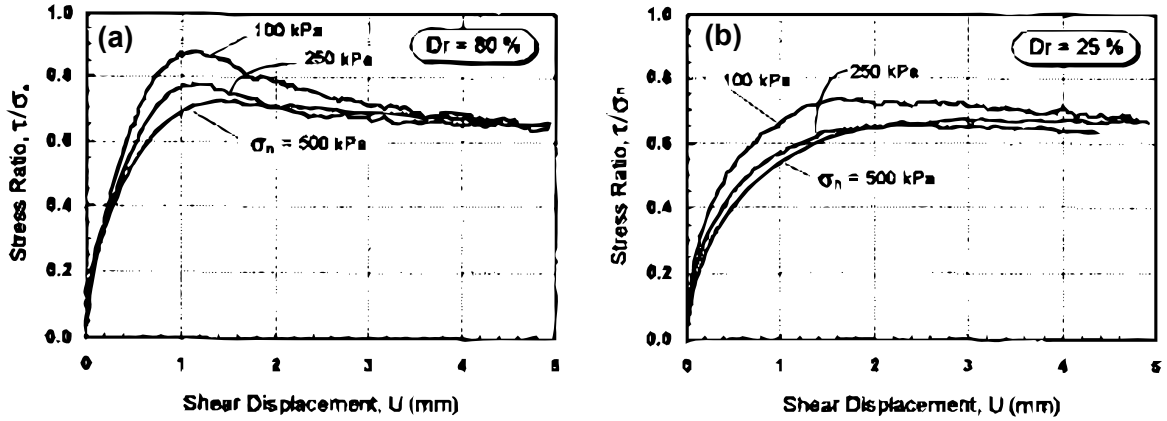

Figure 1.9: Stress ratio versus shear displacement for $\sigma_n = 100, 200, 500kPa$: (a) rough surface-dense sand ($D_r = 80\%$); (b) rough surface loose sand ($D_r = 25\%$) (Fakharian and Evgin [1996])

The experiment results in Figure 1.9 clearly shows a peak shear stress ratio $(\tau/\sigma_n)_p$ and a residual stress ratio $(\tau/\sigma_n)_r$. Initial hardening and then softening depends upon

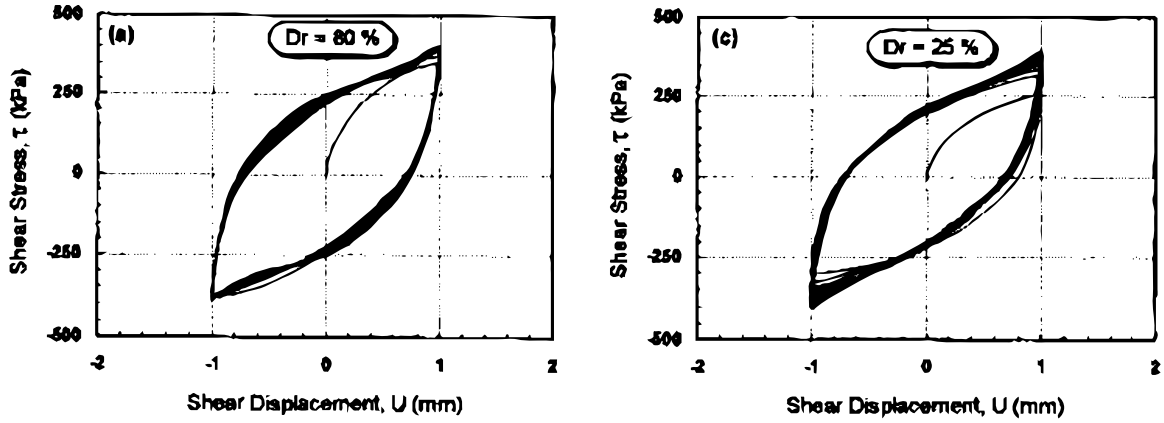

Figure 1.10: Cyclic test results, shear stress versus shear displacement for $\sigma_n = 500kPa$: (a) rough surface, dense sand ($D_r = 80\%$); (b) rough surface, loose sand ($D_r = 25\%$) (Fakharian and Evgin [1996])

the relative density D_r of the sand was observed. A higher relative density $D_r = 80\%$ sand shows dilation for lower confinement and thus a peak behavior whereas a low relative density $D_r = 25\%$ sand shows no dilation. For cyclic shear tests, the loose soil $D_r = 25\%$ shown in Figure 1.10(b) showed gain in strength due to densification resulting from particle breakage. While for soil with high relative density $D_r = 80\%$ almost no gain in shear strength was observed during cyclic shearing. The 3-D tests performed showed that the shear stress τ is almost isotropic for different shear stress paths.

Shahrour and Rezaie [1997] performed a series of monotonic and cyclic tests on Hostun Sand with rough and smooth surface with constant normal load condition. The results obtained were used to propose an elasto-plastic bounding surface based constitutive model for the interface behavior. The monotonic and cyclic test are shown in Figure 1.11 for rough and smooth interface surface. From Figure 1.11, it could be observed that for smooth interface, the shear stress τ increases only upto the critical shear stress τ_c. Whereas for rough soil, the shear stress τ hardens to a peak strength τ_p and then softens to the critical shear strength τ_c. The behavior observed for rough and smooth interface is similar to dense and loose soil as observed in tests by Fakharian and Evgin [1996]. The cyclic test shown in Figure 1.11(c) showed similar response as was observed by Fakharian

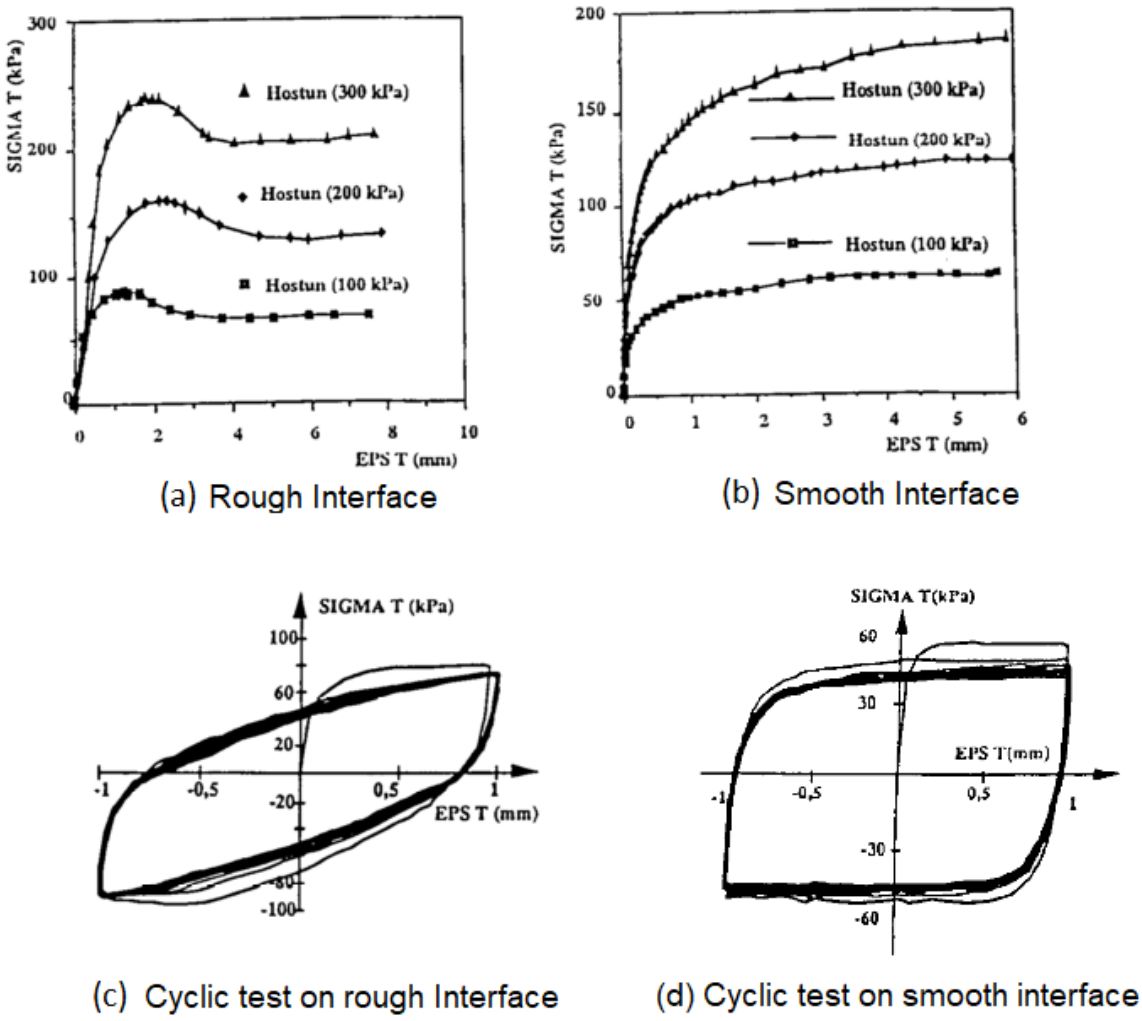

Figure 1.11: (a) and (b) Monotonic and (c) and (d) cyclic test on dense Hostun sand and steel interface(Shahrour and Rezaie [1997])

and Evgin [1996].

Dejong et al. [2006] performed laboratory soil-structure investigation under constant normal stiffness using particle image velocimetry (PIV)method. Cyclic shearing was carried out to simulate and understand the shear behavior at pile interface. Cyclic degradation exponential model was proposed of model the change in void ratio. Later Mortara et al. [2007] also performed cyclic shear tests on sand steel interfaces. DeJong and Westgate [2009] quantified the soil-structure interface behavior to the shearing on the factor like relative density D_r, particle angularity, particle hardness, surface roughness, normal stress and normal stiffness. Local as well as global load displacement response was recorded to understand the load-transfer mechanism.

1.4.2 Interface Constitutive Models

Section 1.4.1 talked about the experimental investigation of soil-structure interface behavior. Based on the the experimental results, Desai and Nagaraj [1988]; Boulon [1989]; Boulon and Nova [1990]; Aubry et al. [1990]; Shahrour and Rezaie [1997] have proposed a simple constitutive model for cyclic normal and shear behavior of interface. Overall, the whole research community have undertaken the constitutive modeling of interface behavior using elastic-plasticity (Section 1.4.2.1) and hypo-elasticity theory (Section 1.4.2.2).

In general, several classes of deformations exists in materials. It can be elastic, anelastic, viscoelastic, plastic and hyper-plastic. Elasto-plastic and Hypo-plastic material can be unified with the general constitutive law as presented in Equation 1.27.

$$\dot{\sigma_{ij}} = C_{ijkl}\dot{\epsilon_{kl}} \tag{1.27}$$

where, $\dot{\sigma_{ij}}$ is the stress rate or increment , $\dot{\epsilon_{kl}}$ is the strain rate or increment and C_{ijkl} is the tangent elastic-plastic stiffness tensor which can be function of stress (σ_{ij}), strain (ϵ_{ij}), back stress (α_{ij}), plastic strain rate ($|\dot{\epsilon^{pl}_{ij}}|$) and lot of other intrinsic variable that can be summarized as q^*.

1.4.2.1 Elasto-Plasticity Theory Models

In elasto-plasticity theory, the strain increment $\dot{\epsilon_{ij}}$ further decomposed into elastic $\dot{\epsilon_{ij}^{el}}$ and plastic strains $\dot{\epsilon_{ij}^{pl}}$.

$$\dot{\epsilon_{ij}} = \dot{\epsilon_{ij}}^{el} + \dot{\epsilon_{ij}}^{pl} \tag{1.28}$$

where, $\dot{\epsilon_{ij}^{el}}$ is the recoverable strain and $\dot{\epsilon_{ij}^{pl}}$ is the irrecoverable strain. The stress increment is also written in elastic strain increment $\dot{\epsilon_{ij}^{el}}$ form apart from the total strain increment $\dot{\epsilon_{ij}}$ as shown in Equation 1.27.

$$\dot{\sigma_{ij}} = C_{ijkl}^{el} \dot{\epsilon_{kl}^{el}} \tag{1.29}$$

where, C_{ijkl}^{el} is the elastic stiffness of the material.

The elasto-plasticity theory have been present since late 18th century Hill [1950]; Temam [1985]; Wu Tai [1966]; Lubliner [1990]; de Borst and Feenstra [1990]; de Borst [1987] and has received a lot of developments in terms of theory Kojić and Bathe [1987]; Klisinski et al. [1992]; Runesson and Sture [1989]; Dafalias [1986, 1985] as well as its application to computational mechanics Crisfield [1981]; Simo and Taylor [1986]; Dodds and Robert [1987]; Klisinski et al. [1992] and implementation Nguyen [1977]; Simo and Taylor [1985]; Runesson et al. [1986]; Ortiz and Simo [1986]; Simo et al. [1988]; Jetteur [1986] in finite element packages.

Having said that, a lot of models have been developed using elasto-plasticity theory to model response of interface behavior. Boulon and Nova [1990]; Aubry et al. [1990] proposed simplistic elasto-plastic models for the interface. Shahrour and Rezaie [1997] proposed a cyclic bounding surface model for constant normal load condition. Navayogarajah et al. [1992] proposed a hierarchical single surface (HISS) approach to model strain hardening and strain-softening of the interface behavior. Fakharian and Evgin [2000] generalized the interface model in 3-D space based on the experimental results by Fakharian and Evgin [1996]; Evgin and Fakharian [1997]; Fakharian and Evgin [1997]; Fakharian [1996]. Mortara et al. [2002] presented a 2-D constitutive for monotonic as well as cyclic loading conditions. De Gennaro and Frank [2002] used the Mohr-Coulomb failure criteria with deviatoric hardening/softening, phase transformation state and ultimate state. Hu and Pu [2004] performed tests and proposed a damage based material model to capture

the cyclic softening of interface behavior. Boulon et al. [2003] formulated a non-associated elasto-plastic model with two plastic surfaces : external surface for isotropic hardening and internal one subject to kinematic rotational hardening. Flow rules similar to the Cam Clay model were used.

Liu et al. [2006]; Liu and Ling [2008] proposed an 2-D elasto-plastic model based on critical state soil mechanics extended from Pastor et al. [1990] plasticity model for soils. Liu et al. [2014] extended the same model to 3-D space and considered the particle breakage based on work hardening rule to model the degradation of strength with cycles. DAguiar et al. [2011] modified the 3-D ECP multi-mechanism models Aubry et al. [1982] to 3-D interface plain-stress model.

Since, the interface behavior is similar to a thin layer of soil, all the above models mentioned the use of critical state parameters with non-associated hardening laws to calibrate the model with experimental results.

1.4.2.2 Hypo-Plasticity Theory Models

Truesdell [1955] was the first to put forward the hypo-elasticity model. In the original proposed hypo-elasticity by Truesdell [1963], stiffness tensor C_{ijkl} has both minor and major symmetry and is a function of stress. Whereas in elasticity C_{ijkl} depends also on strain ϵ_{kl} and rotation α_{ij} from the reference coordinate system. Later, Kolymbas [1977, 1985, 1991]; Kolymbas and Wu [1993] extended the theory to hypo-plasticity and applied it to model behaviors of sandy and clayey soils. The model received significant developments and contributions from Kolymbas et al. [1995]; von Wolffersdorff [1996]; Mašín [2005] and others.

In hypo-plasticity model, the stress increment $\dot{\sigma_{ij}}$ is defined in terms of total strain rate $\dot{\epsilon_{ij}^{pl}}$. Since the stress increment $\dot{\sigma_{ij}}$ depends upon the current stress σ_{ij}, the constitutive integration is challenging and should be applied to very small strains ϵ_{ij}. Tamagnini et al. [2000]; Batista et al. [2003] presented schemes that could provide accuracy and stability to constitutive integration.

Arnold and Herle [2006] developed a plane stress interface model derived from von Wolffersdorff [1996] hypo-plastic model. The mean stress and strain were assumed to have

isotropic behavior. Stutz et al. [2016, 2017] extended the interface model of Arnold and Herle [2006] to 3-D continuum space. The reduced stress and stretching tensor was relaxed in this approach which automatically satisfied the load angle assumption of $cos3\theta = 0$.

More details about the hypo-plastic interface model can be found in Stutz [2016].

1.4.3 Numerical Challenges

The recently developed constitutive models discussed in Section 1.4.2 tries to closely predict the behavior of the soil-structure interface and thus often have more than 10 parameters to calibrate. However, their implementation to the finite element code is often ignored during the their development, thus making the analyst helpless. Some of the challenges with these models are summarized below.

- Integrating the constitutive equations for a given strain increment $\dot{\epsilon_{ij}}$ is often difficult. The constitutive models are usually developed and verified at the Gauss level with very small strain increments $\dot{\epsilon_{ij}}$. In Finite Element Method (FEM), the strain increments $\dot{\epsilon_{ij}}$ are often large resulting in predicted stress ${\sigma_{ij}}^p$ state often outside the yield surface. Under this case, a robust return mapping algorithm needs to be defined.

- The interface models Aubry et al. [1990]; Shahrour and Rezaie [1997]; Navayogarajah et al. [1992]; Fakharian and Evgin [2000]; Mortara et al. [2002] are verified and validated only at Gauss level with very small strain increments. Their performance have never been tested for realistic soil-structure interaction problems.

- Many of the advance models proposed by Liu et al. [2006]; Liu and Ling [2008]; Liu et al. [2014] are based on Pastor et al. [1990] which does not have a predefined yield surface. Pastor et al. [1990] started with generalized elasto-plasticity and later switched to non-realistic hardening/softening laws without any reference to consistency condition. Absence of yield surface will only add error at each loading step. Larger strain increments $\dot{\epsilon_{ij}}$ will leads to completely absurd response.

- The hypo-plasticity models Arnold and Herle [2006]; Stutz et al. [2017] are very sensitive to the strain increment $\dot{\epsilon_{ij}}$ and does not posses an yield function. Stutz et al.

[2017] implemented the model in ABAQUS with a simple Euler forward integration. In FEM, where strains are large, such methods would lead to erroneous results.

Chapter 2

Contact Interface Models

2.1 Introduction

Chapter 1 introduced the soil-foundation interface problem and the normal and shear behavior that is to be modeled for both dry and saturated soils. This chapter proposes contact interface models for modeling of normal and shear interface behavior. Penalty method is used to model the normal behavior of hard and soft contact types. For shear behavior, three models with increasing level of sophistication are proposed. Hardening and Softening incremental evolution laws are also discussed for the interface models. Simplicity as well as ability to capture realistic behavior with less number of parameters was considered while developing the models.

2.2 Interface Shear Zone

At the soil-structure interface, there exists a very thin small shearing zone of 5-10 times the D_{50} Yoshimi and Kishida [1981]; Martinez et al. [2015]; Dejong et al. [2006]; DeJong and Westgate [2009] as shown in Figure 2.1. Since the interface constitutive models are defined in stress-strain space, the applied displacements must be converted to strains. Based on the shear zone thickness SZ_h, the total shear strain γ and incremental shear strain $\Delta\gamma$ can be calculated as

$$\begin{aligned} \gamma &= \Delta_t / SZ_h \\ \Delta\gamma &= \delta\Delta_t / SZ_h \end{aligned} \tag{2.1}$$

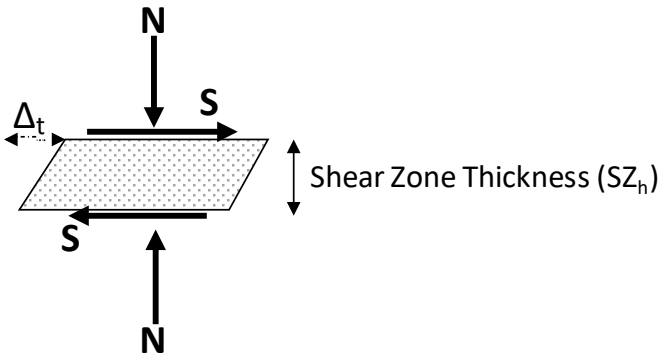

Figure 2.1: Thin shear zone at soil-structure interface

where Δ_t and $\delta\Delta_t$ are the total and incremental shear displacement at the interface between the two soil-structure contact surface.

Similarly, the normal strain ϵ and incremental normal strain $\Delta\epsilon$ can be calculated as

$$\begin{aligned} \epsilon &= \Delta_n / SZ_h \\ \Delta\epsilon &= \delta\Delta_n / SZ_h \end{aligned} \tag{2.2}$$

where Δ_n and $\delta\Delta_n$ are the total and incremental penetration in contact normal direction. In the interface constitutive models, the normal strain ϵ is generally also referred as volumetric strain ϵ_v Stutz [2016]. The normal stress is assumed to offer confinement to the interface shear band. It must be noted that although a shear band of thickness SZ_h is assumed, the interface element itself has zero thickness. The shear zone thickness SZ_h is a material parameter for the interface models. The shear zone thickness can vary based on the roughness of the soil-structure interface but for sands could be generally assumed to be around 5-10 mean particle size diameter D_{50}. For clays however, it can be more like 100 to 500 times D_{50}.

2.3 Normal Interface Models

The contact behavior in the normal direction is modeled as penalty stiffness function as described in the Section 2.3.1. The penalty function can be chosen as linear with fixed stiffness also known as Hard Contact (Section 2.3.2). Or can be assumed to be a non-linear function with stiffness increasing exponentially with penetration. This type of normal behavior is called as Soft Contact (Section 2.3.3). Soft Contact represents

more realistic soil-structure interface behavior. The soil becomes stiff as the penetration increases and gets relaxed upon unloading.

2.3.1 Penalty Method

At the interface of the soil-foundation system, an impenetrability constraint exists as shown in Equation 1.11 to 1.25. The contacting bodies cannot penetrate into each other. The impenetrability leads to an inequality constraint, which requires special methods such as penalty method, Lagrange, barrier, augmented Lagrangian, etc. as described in [Wriggers, 2002]. Penalty method is a common approach used for solving constrained minimization (or maximization) problems involving inequalities as described in section 1.2 and Section 1.3. In this approach, a large penalty term is added to the minimizing functional to prevent the solution from escaping the constrained space.

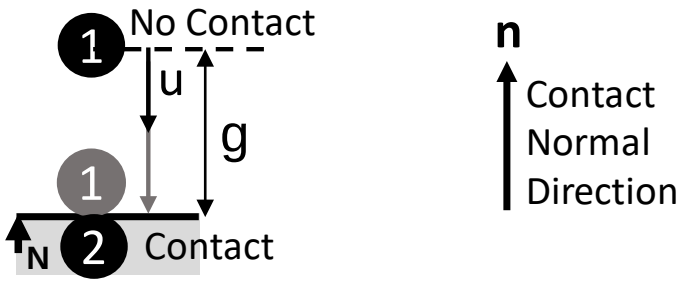

Figure 2.2: Contact Node Pairs

Figure 2.2 shows a two contact node pairs initially separated by a small distance of g in the contact normal direction. During pure contact, the two node penetrates against each other by Δ_n. The instantaneous relative distance between the two contact surfaces is u. Thus, if $u < g$ there is no contact and normal force $N = 0$ otherwise there is contact and a normal force N will act.

In the penalty stiffness formulation, a small penetration Δ_n is allowed between the mass and the floor having stiffness k_n such that during contact the normal force N is defined as

$$N = k_n \Delta_n \;\; if \;\; \Delta_n \geq 0 \tag{2.3}$$

where k_n can be thought of the normal contact stiffness and Δ_n is the relative displacement between the two contact surfaces with respect to the initial gap g in contact normal direction. It is defined as the following

$$\Delta_n = u_n^r - g_n = u - g \tag{2.4}$$

where u_n^r is the relative displacement in the contact normal direction and g_n is the initial gap in contact normal direction. Theoretically, for rigid contact case, the penalty stiffness k_n is assumed to infinite resulting in $\Delta_n = 0$. However, for numerical reasons, infinity is not possible, and thus $\Delta_n = 0$ is never enforced. This results in small penetration at contact surfaces resulting in $\Delta_n < 0$ during contact. For penalty method, the term penetration is thus normally referred to Δ_n defining the two possible states as:

- *No Contact* (Penetration $\Delta_n > 0$)
- *Contact State* (Penetration $\Delta_n \leq 0$)

In equation 2.3, if the penalty stiffness parameter k_n is assumed to be constant and independent of penetration (Δ_n), it is referred as a hard contact. This type of contact is more physical for interactions between two rigid surfaces or bodies. However, to model interaction between soft-soil and rigid foundation, a soft contact with penalty stiffness increasing with penetration is preferred. The following Section 2.3.2 and 2.3.3 describes hard and soft contact respectively.

For coupled contact problems described in Section 1.3, in order to enforce the no-drainage condition in contact normal direction between *upU* (soil) and u (foundation) degrees of freedom, an additional penalty stiffness parameter k_p is required. Section 3.5 describes how penalty stiffness k_p is used to enforce the undrained condition.

It must be noted that in the penalty or any other method (Lagrange, barrier .. etc.) as described in [Wriggers, 2002], to get to the solution it has to take into account of whether the contact is active or not. Thus, the inequality constraint has to be changed to the active (closed gap) or inactive (open gap) based on the state of contact. As a result, the topology of the structure changes due to contact. This points out one of the difficulties

while solving the contact problem i.e. the stiffness matrix changes with active or inactive constraint equations.

As compared to one of the popular Lagrange method, the penalty method leads to non-physical penetration but does not create any additional variables. However, the non-physical penetration could be utilized to model more complicated normal contact force function as such for soft contact shown in Figure 2.4a and non-linear shear interface models as described in section 2.4.

2.3.2 Hard Contact

In hard contact, the normal penalty stiffness k_n is assumed to be constant with penetration Δ_n. As a result, the normal contact force F_n or stress σ_n varies linearly with penetration.

$$\begin{aligned} F_n &= k_n \Delta_n \\ \sigma_n &= k_n \epsilon \end{aligned} \tag{2.5}$$

where k_n represents the normal stiffness between soil-structure interface and Δ_n is the penetration in contact normal direction.

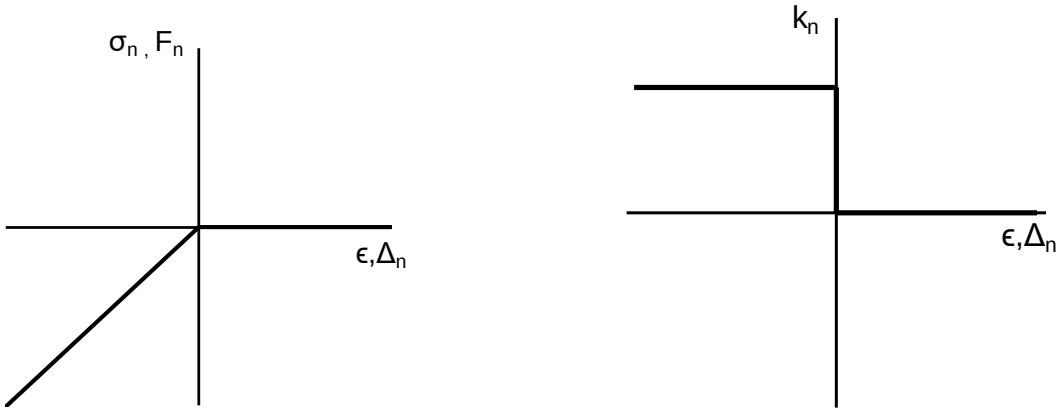

(a) Normal Contact Force (b) Normal Contact Stiffness

Figure 2.3: Hard contact normal (a) force and (b) stiffness function with penetration Δ_n

Figure 2.3 shows the normal force F_n or stress σ_n and stiffness k_n as a function of penetration Δ_n or normal strain ϵ respectively. The normal stiffness k_n is assumed to be

constant and thus has an abrupt jump or discontinuity at $\Delta_n = 0$ leading to C^0 continuity. The abrupt change of stiffness could often lead to numerical convergence problems.

2.3.3 Soft Contact

For rocks, [Gens et al., 1990] presented a nonlinear (hyperbolic) function of elastic normal stress with penetration. The function had different stiffness for loading and unloading up-to a permanent deformation u_{mc}. The hyperbolic function $u/(u - u_{mc})$ has a singularity at $u = u_{mc}$. It does not increase monotonically and does not poses continuous derivatives for $u \geq 0$. In FEM since, the stiffness cannot be infinite at $u = u_{mc}$ and the displacement u can be greater than $u \geq u_{mc}$, which can lead to numerical instability and convergence problems. As per authors knowledge, there has not been enough experimental investigation to understand the normal contact behavior of the soil-structure interface. Desai and Nagaraj [1988] claim to have performed cyclic normal tests on a concrete-soil interface on a shear box but did not show any experimental results. Desai and Nagaraj [1988] idealized the normal behavior based on the critical state soil mechanics as shown in Figure 1.7. Bandis et al. [1983] investigated the response of fresh and weathered rock. It could be observed that after $(2-4)$ cycles, the loading and unloading curve fairly overlaps and could be approximated by the same function.

Since there is an absence of experimental data for normal contact behavior at soil-structure interface, it is inherently assumed that the response would behave similar to the weathered rock Bandis et al. [1983]. The normal behavior at the interface being modeled here using penalty stiffness approach, thus assumes a non-linear exponential elastic function for soft contact. The parameters include an initial stiffness k_i and a stiffening rate S_r to control the normal stress σ_n function with penetration Δ_n. In comparison to hard contact, soft contact thus has a smooth exponential, normal contact force function with penetration as shown in Figure 2.4a. The exponential variation is expected to match the realistic increasing contact force with penetration as shown in Figure 1.7. As stated earlier, it must be noted that in this model the response is assumed to be fully non-linear elastic with no tensile region. As a result, the loading and unloading stiffness and response is the same.

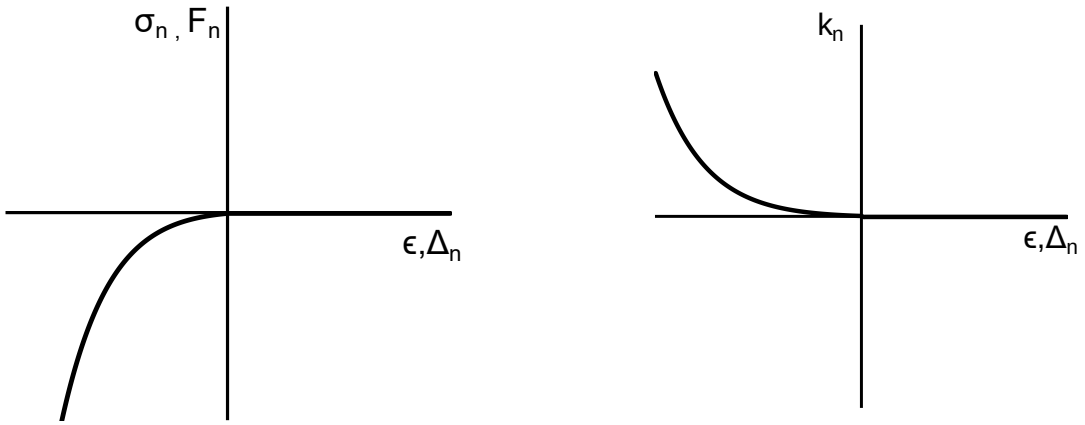

(a) Normal Contact Force (b) Normal Contact Stiffness

Figure 2.4: Soft contact normal (a) force and (b) stiffness function with penetration Δ_n

The non-linear normal force F_n or stress σ_n is defined as:

$$\begin{aligned} F_n &= k_i exp(-S_r \Delta_n)\Delta_n \\ \sigma_n &= k_i exp(-S_r \epsilon)\epsilon \end{aligned} \tag{2.6}$$

where k_i represents the initial normal stiffness between soil-structure interface and S_r represents the stiffening (or hardening) rate with penetration Δ_n or normal strain ϵ. It must be noted that for force based contact the units of S_r would be in $/m$ whereas for stress based contact it is unit-less. Equation 2.6 represents the normal force F_n and stress σ_n for force based and stress based contact respectively. At soil-foundation interface, as the foundation penetrates more, the soil becomes harder resulting in an increase of interface normal stiffness k_n and normal stress σ_n. The stiffening rate leads to an exponential increment of contact stress per unit of penetration Δ_n. From the above formulation it must be noted that for the stress based contact, the penetration Δ_n is replaced with normal strain ϵ. Subsequently, the parameters initial normal stiffness k_i and stiffening rate S_r should also be calibrated accordingly. Similarly, the stiffness and other derivatives could be obtained by replacing penetration Δ_n with normal strain ϵ. The normal stiffness k_n has unit of n/m for the force based contact and Pa for the stress based contact.

Equation 2.6 could be differentiated to get the stiffness k_n as:

$$\begin{aligned} k_n &= k_i exp(-S_r \Delta_n)(1 - S_r \Delta_n) \\ k_n &= k_i exp(-S_r \epsilon)(1 - S_r \epsilon) \end{aligned} \tag{2.7}$$

It can be observed from equation 2.7 that putting $\Delta_n = 0$, the normal stiffness k_n becomes equal to initial normal stiffness k_i i.e. $k_n = k_i$. When $\Delta_n \geq 0$, the stiffness grows exponentially. Extending Equation 2.6 and 2.7 to uplift (no-contact) ($\Delta_n \geq 0$), with the assumption of small initial stiffness k_i, the force and stiffness function would lead to C^1 continuity. The C^1 continuity thus would lead to a smooth stiffness function even at the border of contact and non-contact region resulting in quadratic convergence at global FEM level for the Newton-Raphson method. However the non-linear behavior would lead to comparatively larger number f iteration than hard contact,

It is also interesting to note that by setting the stiffening rate $S_r = 0$, hard contact can be recovered i.e. $k_n = k_i$ and $\sigma_n = k_n \epsilon$. This demonstrates the generality of soft contact formulation.

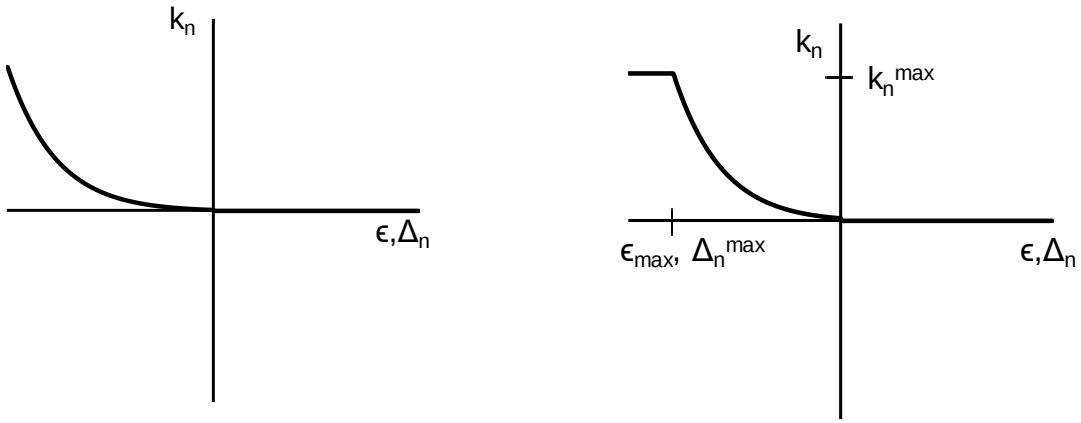

(a) Without Cap (b) With Cap

Figure 2.5: Soft Contact Stiffness function (a) without any limit and (b) with limit

The exponential growth of stiffness in finite element method (FEM) can lead to numerical instability for large values. To avoid this, a maximum normal stiffness k_n^{max} is applied to restrict its further growth. Figure 2.5 shows the stiffness k_n function with and

without a cap. The stiffness function thus can be written as:

$$\begin{aligned} k_n &= max(k_i exp(-S_r \Delta_n)(1 - S_r \Delta_n), k_n^{max}) \\ k_n^{max} &= k_i exp(-S_r \Delta_n^{max})(1 - S_r \Delta_n^{max}) \end{aligned} \tag{2.8}$$

For implementing the above Equation 2.8 in FEM, there would be a need to find Δ_n^{max} corresponding to maximum allowable normal stiffness k_n^{max} in order to integrate the stiffness function k_n. An efficient method to get Δ_n^{max} is described in Section 2.3.3.1 below.

2.3.3.1 Iterative Method To Find Δ_n^{max}

For soft contact implementation in FEM, it would be required to find out Δ_n^{max} for a given initial normal stiffness k_i, stiffening rate S_r and maximum normal stiffness k_n^{max}. Since Equation 2.8 is a nonlinear function, an iterative method is needed to get to the solution. One of the best solution search methods is the bisection method, which repeatedly bisects an assumed solution interval, choosing only one of the branches where the solution might exist. In this method, an initial guess of solution space is required.

Theoretically, a large solution space could be given but would not be computationally feasible and optimal. For the given problem, it is often desired to predict solution space to get in as fewer iterations as possible. To reach the solution optimally and efficiently, an initial guess of solution range for penetration Δ_n was found to be $[k_n^{max}/k_i, 0.5k_n^{max}/k_i]$.

2.4 Shear Interface Models

The models discussed in Section 1.4.2 being complicated and having integration issues at Gauss level are rarely used for practical realistic soil-structure interaction problems. Also, the number of parameters in these models is large which makes the calibration process difficult. Section 1.4.3 describes some of the challenges associated with those advanced models. As a result, Mohr Coulomb type model is readily used. Thus, there is a need to develop new models with a possible minimum number of parameters that could realistically model the shear interface behavior. Also, a yield function is necessarily required to return back the predicted stress σ_{ij}^p state back to the yield surface satisfying the consistency condition. This section describes three models to describe the non-linear

shear interface behavior which is intended to capture some of the actual soil-structure interface response.

Apart from the traditional Mohr-Coulomb i.e. Elastic-Perfectly Plastic Shear (EPPS) model, two additional non-linear models have been proposed. The Non-Linear Hardening Shear (NLHS) is a non-linear Armstrong-Frederick type hardening model where the normalized shear stress parameter $\mu = \tau/\sigma_n$ increases non-linearly from 0 to residual normalized shear stress $\mu_r = \tau_r/\sigma_n$. Non-Linear Hardening Softening Shear (NLHSS) adds one more level of sophistication. It can model the softening of normalized shear stress parameter μ. Once the peak normalized shear stress $\mu_p = \tau_p/\sigma_n$ is attained, it starts to decrease to the residual normalized shear stress μ_r. Figure 2.6 shows a typical monotonic response of the three models for a constant normal stress σ_n;

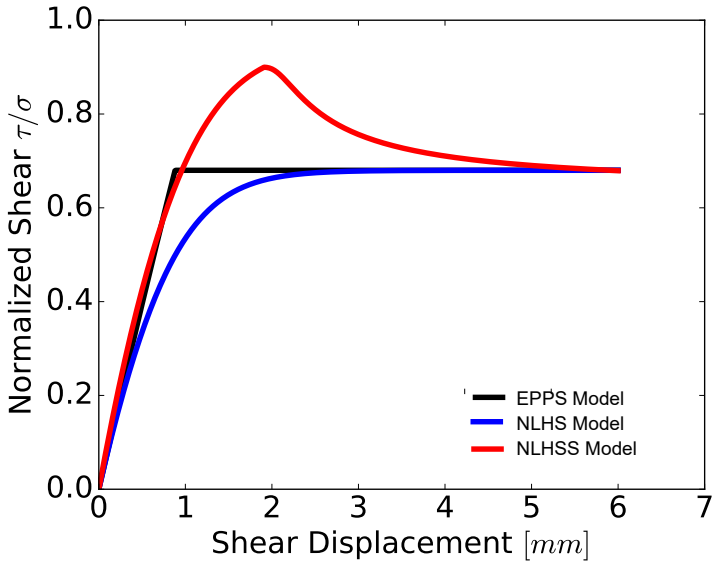

Figure 2.6: Comparison of the interface models with monotonic response

From Figure 2.6, it can be observed that the models behave quite differently. The EPPS model reaches the residual state at very small shear strain $\gamma = \Delta_u/SZ_h$ level whereas both non-linear NLHS and NLHSS models reach at comparatively larger shear strains γ. EPPS and NLHS do not show any peak behavior whereas NLHSS shows a peak followed by softening to residual strength. The models are explained in detail in the next section. NLHS and NLHSS model assume to have negligible to no elastic region and

follow the elasto-plasticity theory. And since, the linear Armstrong-Frederick hardening parameter H_a is assumed to be equal to the elastic stiffness k_t resulting in the overall elasto-plastic stiffness equal to $0.5k_t$. The thin shear zone at the soil-structure interface starts to develop plastic deformation as soon as a small shear stress τ is applied. It must also be noted in Figure 2.6 that the elastic shear stiffness k_t depends upon the normal stress σ_n. Thus, for a given normal stress σ_n, the shear stiffness k_t is defined as

$$k_t = k_t^{\sigma_n} = (k_t)^{\sigma_{p0}} \frac{\sigma_n}{\sigma_{p0}} \tag{2.9}$$

where σ_{p0} is the constant stress of $101.3kPa$ and $(k_t)^{\sigma_{p0}}$ is the shear stiffness for a normal stress of $\sigma_n = \sigma_{p0} = 100kPa$. The models are thus developed using kinematic hardening plasticity with initial kinematic hardening stiffness H_a equal to the elastic stiffness k_t. As stated above, this leads to initial elastic-plastic stiffness equal to $0.5k_t$ and also results in incremental elastic strain energy equal to the incremental plastic free energy as described in Section 3.3.

2.4.1 Elastic Perfectly Plastic Shear (EPPS) Model

The simplest shear interface model is the Mohr Coulomb interface model with an elastic stiffness under no slippage and zero stiffness when it slips. The material behavior is of type elastic-perfectly plastic type. The yield function (f) is thus given as

$$f := \tau - \mu\sigma_n \leq 0 \tag{2.10}$$

where μ is a constant coefficient of friction, τ is the shear stress and σ_n is the normal stress.

Figure 2.7 shows the performance of EPPS model for different loading conditions. Since it is a elastic perfectly-plastic model, the shear stiffness k_t is constant with shear strain γ or displacement Δ_t and becomes zero (perfectly-plastic state) when it reaches its residual friction coefficient μ_r. Figure 2.7(a) and 2.7(c) shows the monotonic and full cyclic response with elastic perfectly-plastic behavior respectively. Figure 2.7(b) and 2.7(d) shows the monotonic cyclic behavior before and after reaching the residual friction coefficient μ_r. This kind of interface behavior is mostly observed between rigid surfaces

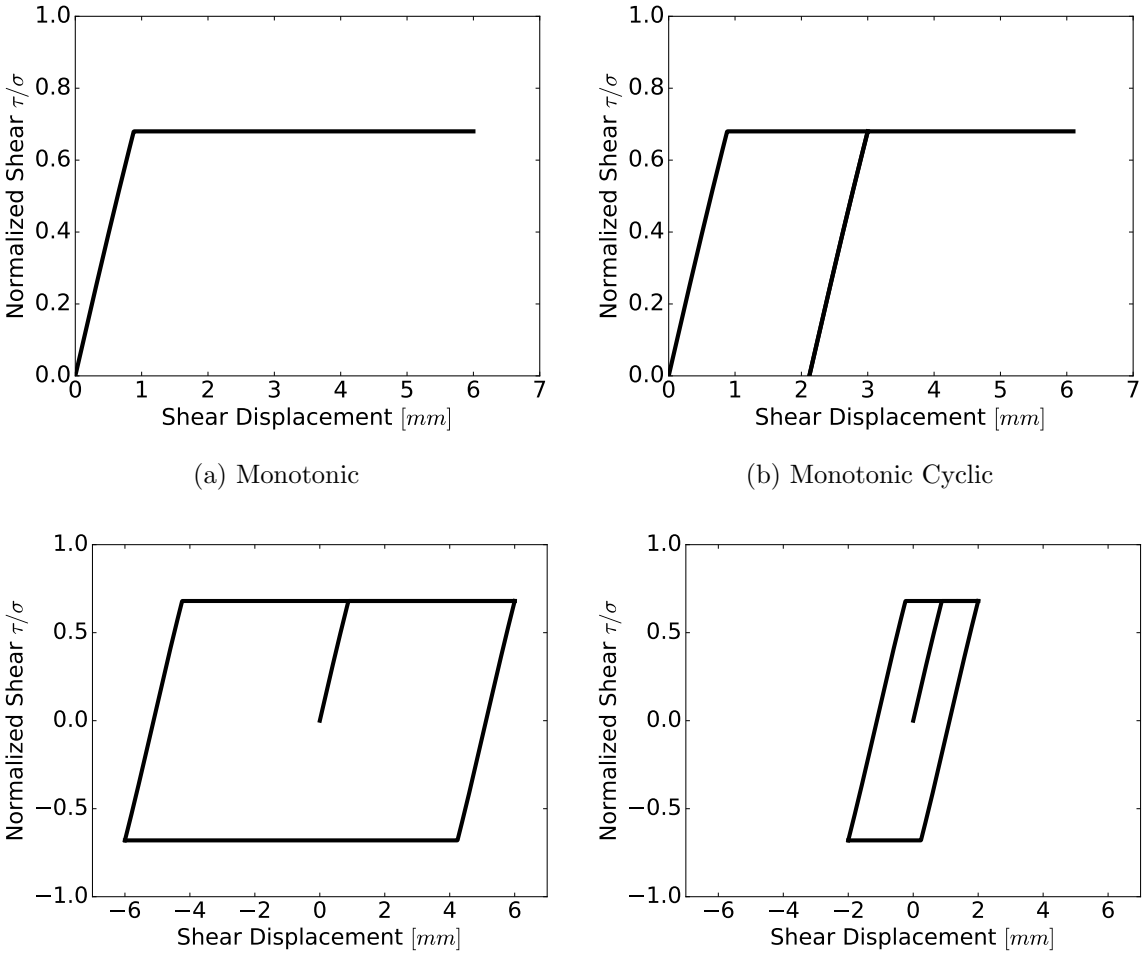

(a) Monotonic

(b) Monotonic Cyclic

(c) Full Cyclic

(d) Cyclic before achieving residual strength

Figure 2.7: Response of Linear Elastic Perfectly Plastic Shear (EPPS) Model with normal stress of $100kPa$, residual coefficient of friction $\mu_r = 0.68$, shear stiffness $k_t = 200kPa$ and shear zone length $SZ_h = 5mm$

in contact. For more realistic soil-structure interface non-linear yield function should be used as described in the coming sections.

2.4.2 Nonlinear Hardening Shear (NLHS) Model

In this model, the normalized shear stress hardening variable μ increases from 0 to critical or residual normalized shear stress μ_r using the non-linear Armstrong Frederick type hardening law. The evolution rule for frictional hardening variable μ is given as

$$\Delta\mu = k_t \Delta\gamma^p - \frac{k_t}{\mu_r}|\Delta\gamma^p|\mu \tag{2.11}$$

where k_t is the non-linear elastic hardening variable and $\Delta\gamma^p$ is the plastic part of the shear strain $\Delta\gamma$. The material behavior is thus of type non-linear hardening type.

The yield function (f) is still given as

$$f := \tau - \mu\sigma_n \leq 0 \tag{2.12}$$

where the normalized shear stress hardening variable μ evolves by Equation 2.11, τ is the shear stress and σ_n is the normal stress.

Figure 2.8 shows the performance of NLHS model for different loading conditions. It can be observed that the hardening variable μ increases non-linearly from 0 to residual normalized shear stress ratio μ_r at large shear displacements. As compared to the EPPS models, it is more realistic as the soil-structure interface develops the shear strength gradually with increments of shear strain $\Delta\gamma$ or shear displacements Δ_t.

For loose or low relative density D_r soil at soil-structure interface Fakharian and Evgin [1996]; Shahrour and Rezaie [1997] as shown in Figure 1.9(b) and 1.11(b), this model could be calibrated to model the non-linear hardening response. The monotonic and full cyclic response of this model shown in Figure 2.8(b) can be seen to match the interface behavior investigated by Uesugi et al. [1989] and is shown in Figure 1.8. Figure 2.8(d) shows the response of the model subject to cyclic shearing before reaching the residual strength. It could be observed that it is able to model the non-linear interface behavior as investigated by Fakharian and Evgin [1996]; Shahrour and Rezaie [1997] which is shown in Figure 1.10 and Figure 1.11(c) respectively.

For dense soil with higher relative density D_r, it is important to model the peak normalized shear stress μ_p, followed by the softening behavior until the residual shear stress μ_r is reached. The NLHSS model proposed in next section can be used to model both hardening and softening.

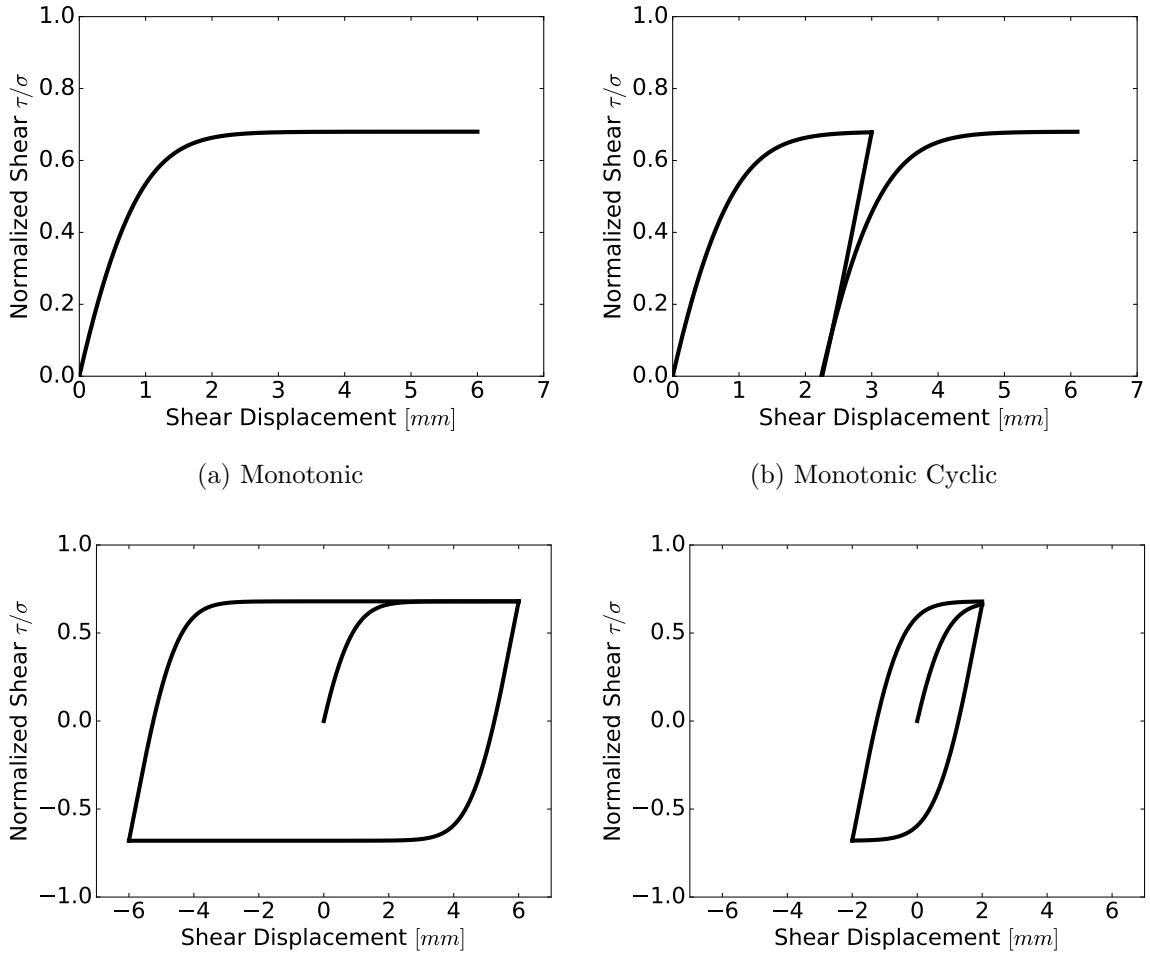

(a) Monotonic

(b) Monotonic Cyclic

(c) Full Cyclic

(d) Cyclic before achieving residual strength

Figure 2.8: Response of Non-Linear Hardening Plastic Contact (NLHS) model with normal stress of $100kPa$, residual normalized shear stress of $\mu_r = 0.68$, shear stiffness $k_t = 400kPa$ and shear zone length $SZ_h = 5mm$

2.4.3 Nonlinear Hardening Softening Shear (NLHSS) Model

In this model, the normalized shear stress hardening/softening variable μ increases from 0 to its peak limit μ_p and then with more shear displacement reaches to the residual normal-

ized shear stress of μ_r using a non-linear Armstrong Frederick type hardening/softening law. The evolution of the hardening/softening variable μ during hardening phase is given as

$$\Delta\mu = k_t \Delta\gamma^p - \frac{k_t}{\mu_p}|\Delta\gamma^p|\mu \tag{2.13}$$

where k_t is the non-linear hardening variable and $\Delta\gamma^p$ is the the plastic part of incremental shear strain $\Delta\gamma$. Once the peak normalized shear stress is attained, the material starts to soften. The softening behavior is modeled as reduction of normalized shear stress ratio μ as

$$\Delta\mu = -\frac{n * b(\mu_p - \mu_r)}{(\pi/2)^n \theta^{1/n-1}}\, cos^2\theta^{1/n}\Delta\gamma^p \tag{2.14}$$

$$\theta = \frac{\mu_p - \mu}{\mu_p - \mu_r}(\pi/2)^n \tag{2.15}$$

where b is the softening rate, $\Delta\gamma^p$ is the incremental plastic shear strain and n represents the size of the peak plateau as shown in Figure 2.9. This incremental form of softening phase is derived from the inverse tangent function raised to power n as

$$f = a * (arctan(b * \gamma^P))^n \tag{2.16}$$

where a is a constant parameter of the function and in Equation 2.15 is equal to $(\mu_p - \mu)/(\mu_p - \mu_r)$. The softening rate parameter b represents the rate at which the normalized shear stress μ_p decreases with further application of shear displacement Δ_t as shown in Figure 2.9. A larger value of b would result in faster decay. The size of peak plateau parameter n determines the size of the plateau formed at the peak as shown in Figure 2.9. A larger value of n would result in a larger plateau. It must be noted that the peak plateau size parameter n also influences the overall rate of softening as could be seen from the derived incremental Equation 2.15. The parameters n and b can be calibrated from monotonic shearing tests. Figure 2.10 shows the response of the model with the peak plateau size parameter $n = 4$ and softening rate parameter $b = 40$.

The yield function (f) is again given as

$$f := \tau - \mu\sigma_n \leq 0 \tag{2.17}$$

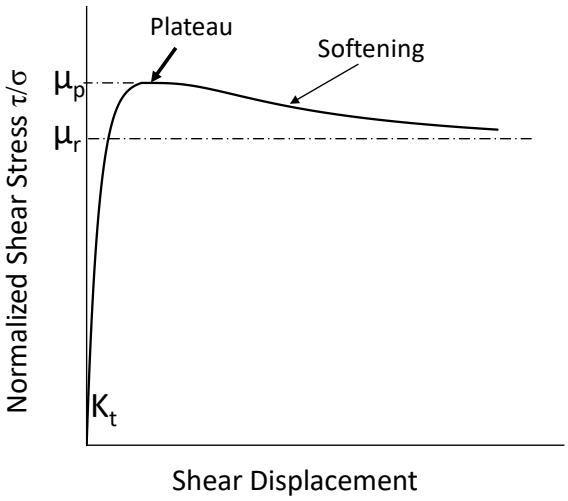

Figure 2.9: Non-Linear Hardening Softening Shear model parameters

where μ is a normalized shear stress hardening/softening variable evolved by Equation 2.13 and 2.15, τ is the shear stress and σ_n is the normal stress.

Since in the model, the hardening law is defined as Armstrong-Frederick type, the peak shear stress ratio μ_p is defined as only 95% of the asymptotic limit of the Equation 2.13. Thus, the asymptotic limit of Armstrong-Frederick type hardening is raised by a factor of 1/0.95 times the peak shear stress ratio μ_p.

In this model during cyclic shearing, it is assumed that once the peak strength is passed, the material would not be able to again attain the peak strength during cyclic loading. It is based on the assumption that as the material passes the peak strength, particle breakage and smoothening of the surface takes place which cannot be recovered back by any process. Thus as the material softens, the peak coefficient of friction μ_p is iteratively redefined to the coefficient of friction μ in the softening phase. This effect can also be observed from the tests performed by Uesugi et al. [1989] as shown in Figure 1.8(b). As soon as the peak shear stress ratio μ_p degrades to residual strength in the first cycle, other cycles follow the residual shear stress ratio μ_r.

Figure 2.10 shows the performance of NLHSS model for different loading conditions. The response of the model is very close to the realistic interface behavior observed by Uesugi et al. [1989] as shown in Figure 1.8(b). During cyclic shearing shown in Figure 2.8(c),

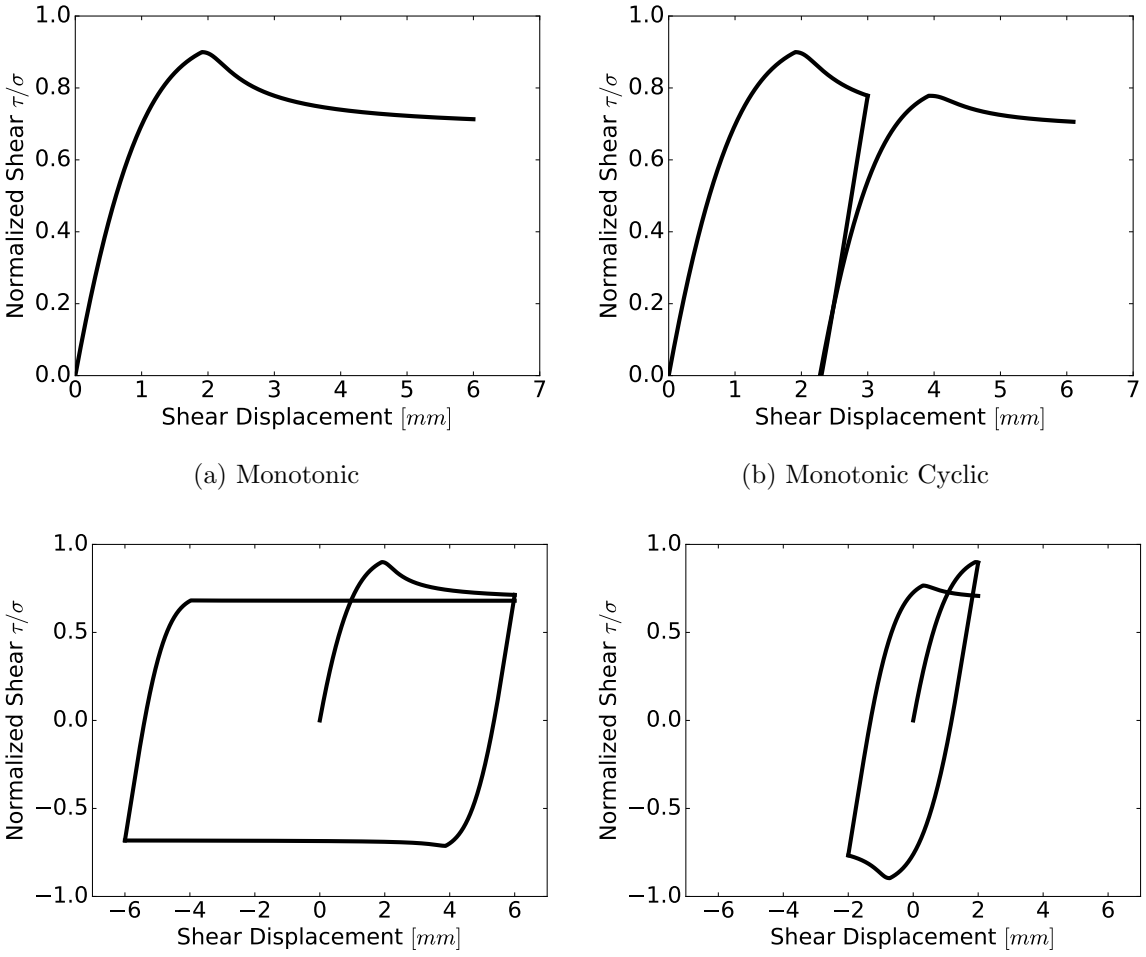

(a) Monotonic

(b) Monotonic Cyclic

(c) Full Cyclic

(d) Cyclic before achieving residual strength

Figure 2.10: Response of Non-Linear Hardening Softening Shear (NLHSS) model with normal stress of $100kPa$, residual normalized shear stress $\mu_r = 0.68$, peak normalized shear stress $\mu_p = 0.9$, shear stiffness $k_t = 800kPa$, peak-plateau parameter $n = 4$, softening rate parameter $b = 40$ and shear zone length $SZ_h = 5mm$

the model predicts the peak behavior only in the first cycle. After that, the response is governed by the residual normalized shear stress μ_r. Figure 2.8(d) shows the cyclic shearing behavior when the residual normalized shear stress μ_r is not attained in the first cycle. As a result during unloading and reloading, it again attains the last peak normalized shear stress μ_p that it had attained during the softening phase. It must be noted that the effect of unloading in softening phase has not been experimentally investigated as per authors knowledge to either verify or contradict the behavior of NLHSS model.

NLHSM can be extended further to model the variation of peak normalized shear stress μ_p for different normal stress σ_n conditions as observed in tests by Fakharian and Evgin [1996]; Shahrour and Rezaie [1997]; Evgin and Fakharian [1997]; Fakharian and Evgin [1997]; Fakharian [1996]; Fakharian et al. [2002]. For a given relative density D_r of soil in the sheared zone, the peak normalized shear stress μ_p can be generalized to be a logarithmic function of normal stress σ_n as

$$\mu_p = \mu_{p_0} - k * log(\sigma_n / P_0) \tag{2.18}$$

where μ_{p_0} is the peak normalized shear stress at normal stress of $\sigma_n = P_0$, k is the peak normalized shear stress rate of decrease and P_0 is the reference stress of $P_0 = 100kPa$. This is similar to the Bolton [1986] stress-dilatancy relationship observed in sands. In the above Equation 2.18, for the normal stress of $\sigma_n \leq P_0$, the peak normalized shear stress μ_p would become greater than μ_{p_0} as the term $log(\sigma_n/P_0)$ becomes negative. This would result in high peak normalized shear stress μ_p for low confining stress σ_n. As a result, the peak normalized shear stress μ_p needs to be restricted to a value. In this model, it is assumed that μ_{p_0} would also act as the maximum possible peak normalized shear stress μ_p for low normal stresses or confinement. Thus the above Equation 2.18 can be re-written with the limit on peak normalized shear stress μ_p as

$$\mu_p = max(\mu_{p_0}, \mu_{p_0} - k * log(\sigma_n / P_0)) \tag{2.19}$$

where μ_{p_0} also represents the maximum peak normalized shear stress μ_p^{max}, that the sheared zone soil could attain. Thus, with experiments conduction for different normal stress σ_n, the peak normalized shear stress μ_p can be calibrated as the function of normal

stress σ_n with peak normalized shear stress limit μ_{p0} and peak normalized shear stress rate of decrease k. Figure 4.95 shows the response of the model for different normal loads of $100kPa$, $250kPa$ and $500kPa$ and also validates the model with the experimental results from Fakharian and Evgin [1996] as shown in Figure 1.9.

2.5 Extending The Models to 3D

Section 2.4 described the model in 2-D in $\tau - \sigma_n$ space, to make the reader understand the basics of the model. The model can be easily extended to 3-D using the back stress variable α instead of the normalized shear stress μ for NLHS and NLHSS models. In 3-D, there would be normal stress component σ_n in contact normal direction n and two tangential stress components τ_1 and τ_2 in tangential contact plane in directions 1 and 2 respectively. Similarly, the shear strain γ has two components as γ_1 and γ_2 in the two tangential directions 1 and 2 respectively. As stated earlier, since normal interface behavior is assumed to be non-linear elastic, the plastic strains are only developed in shear. Thus the incremental plastic strain $\Delta\gamma^p$ and its magnitude $|\Delta\gamma^p|$ in these models is defined as

$$|\Delta\gamma^p| = \sqrt{\Delta\gamma_1^p \Delta\gamma_2^p} \tag{2.20}$$

$$\Delta\gamma^p = [\Delta\gamma_1^p, \Delta\gamma_2^p] \tag{2.21}$$

where $\Delta\gamma_1^p$ and $\Delta\gamma_2^p$ represents the incremental plastic shear strain components in contact tangential (shear) direction 1 and 2 respectively. The plastic flow direction m is defined as the direction of incremental plastic shear strain $\delta\gamma^p$ and thus is defined as $m = \delta\gamma^p/|\Delta\gamma^p|$

2.5.1 EPPS Model

EPPS Model described in Section 2.4.1, is the simplest Mohr Coulomb type elastic perfectly-plastic model. The yield function (f) is defined as

$$f := (\tau_1/\sigma_n - \mu_r)^2 + (\tau_2/\sigma_n - \mu_r)^2 = 0 \tag{2.22}$$

where σ_n is the normal stress, τ_1, τ_2 are the shear stress and μ_r is the residual friction coefficient. Being an elastic-perfectly plastic model with no internal variables, there is no hardening/softening evolution rule.

2.5.2 NLHS Model

The non-linear hardening shear model described in Section 2.4.2 is modeled in 3-D using the back stress internal variable α. The yield function (f), is defined as

$$f := (\tau_1/\sigma_n - \alpha_1)^2 + (\tau_2/\sigma_n - \alpha_2)^2 = 0 \tag{2.23}$$

where σ_n is the normal stress, τ_1, τ_2 are the shear stress and α_1, α_2 are the back stress components in contact tangential direction 1 and 2 respectively on the contact-interface plane. The hardening law would be then defined as

$$\Delta\alpha = k_t \Delta\gamma^p - \frac{k_t}{\mu_p}|\Delta\gamma^p|\alpha \tag{2.24}$$

$$\Delta\alpha = H_m|\Delta\gamma^p| \tag{2.25}$$

$$H_m = k_t m - \frac{k_t}{\mu_p}\alpha \tag{2.26}$$

where μ_p is the peak normalized shear stress, which depends upon the normal stress σ_n as stated in Equation 2.18 and k_t represents the initial elastic shear stiffness of soil-structure interface. H_m represents the non-linear Armstrong-Frederick type hardening modulus and m represents the plastic flow direction.

2.5.3 NLHSS Model

The non-linear hardening softening shear model described in Section 2.4.3 is also modeled in 3D using the back stress internal variable α. The yield function (f) is defined as Equation 2.23. The hardening evolution law for the back stress α is defined by Equation 2.26. The softening law is defined as Von-Mises type as

$$\Delta\alpha = -\frac{n * b(\mu_p - \mu_r)}{(\pi/2)^n \theta^{1/n-1}}\ cos^2(\theta^{1/n})\Delta\gamma^p \tag{2.27}$$

$$\theta = \frac{\mu_p - |\alpha|}{\mu_p - \mu_r}(\pi/2)^n \tag{2.28}$$

$$\Delta\alpha = S_m \Delta\gamma^p \tag{2.29}$$

$$S_m = \frac{-n * b(\mu_p - \mu_r)}{(\pi/2)^n \theta^{1/n-1}} cos^2(\theta^{1/n})$$

where μ_r is the residual normalized shear stress that is constant and depends upon the soil and structure material, μ_p is the peak normalized shear stress at the start of softening phase and S_m represents the softening modulus.

As stated in Section 2.4.3, for NLHSS model, the peak normalized shear stress μ_p of the material is iteratively defined to the back stress $\mu_p = |\alpha|$ in softening phase. It basically means that the dilatancy surface squeezes towards the critical surface as the sheared zone soil at interface continues to shear.

Using the incremental Equation 2.26 Equation 2.30 presented for both hardening and softening phase respectively, the 3-D model can be integrated. using the elastic-plastic theory Hill [1950]; Temam [1985]; Wu Tai [1966]; Lubliner [1990]; de Borst and Feenstra [1990]; de Borst [1987]. The elastic-plastic stiffness or consistent tangent stiffness Jeremić [1994]; Crisfield [1987] can then be computed easily at each loading increment or iteration. Section 3.2.3 presents the elastic-plastic integration for the interface models.

Chapter 3

Implementation in Real-ESSI Simulator System

At the interface of soil-foundation system, an impenetrability constraint exists. The contacting bodies cannot penetrate into each other. The impenetrability leads to an inequality constraint, which requires special interface elements. In general, the unknown contact surfaces and stresses coupled with inequality constraints makes the contact problem difficult. To model the interface problem, many methods have been proposed in the past. Francavilla and Zienkiewicz [1975]; Sachdeva and Ramakrishnan [1981] modeled the inequality at the interface using constrained equations. On the other hand, Herrmann [1978]; Frank et al. [1982] used discrete springs to connect continuum elements at the interface. Zienkiewicz [1970] treated the interface as quasi-continuum with very small thickness. Wang et al. [1998]; Nogami et al. [1992] and others have used non-linear P-Y springs to model soil-pile interaction. Goodman et al. [1968]; Ghaboussi et al. [1973] developed special 2-D rock-joint elements. Since then many contact Wriggers [2002]; Gajan and L.Kutter [2009]; Sheng et al. [2007] and thin layer interface (joint) elements Desai et al. [1984]; Day and Potts [1994]; Segura and Carol [2004, 2008] have been developed.

Among all these methods, Node-to-Node type formulation Zienkiewicz and Taylor [1991] presents the simplest contact element. They were initially developed for modeling of rock joints. Typically, a normal and tangential stiffness function is used to model the contact pressure and frictional force at the interface Wriggers [2002]; Haraldsson and

Wriggers [2000]; Desai and Siriwardane [1984]. As Sheng et al. [2007] notes, these elements are perfect for modeling small and continuous relative displacements at the interface. Konter [2005] presented several benchmarks in order to verify the results of the finite element analyses performed on 2D and 3D modelings. In all proposed benchmarks the results were approximated pretty well with a 2D or axisymmetric solutions. In addition, 3D analyses were performed and the results were compared with the 2D solutions. For large displacements at interface, more advanced contact detection algorithm with surface to surface contact as presented in Wriggers [2002] should be used.

In this thesis, the relative displacements at the soil-structure interface are assumed to be very small. As a result, node-to-node contact approach remains valid and is used.

3.1 Node to Node Contact

Node to node contact is one of the simplest contact formulation which establishes constraint equations and contact interface constitutive equations on a purely nodal basis. It must be noted that this contact approach can only be applied to geometrically linear problems i.e. for very small strains. It must be also noted that the node-to-node contact is only applicable for a conformal mesh. This methods assumes to have interaction between a fixed node pair with a predefined contact plane vector n in global coordinates direction as shown in Figure 3.4. The constraint equation for the contact thus can then be formulated directly from each nodal pair and contact plane vector n as shown in Figure 3.1

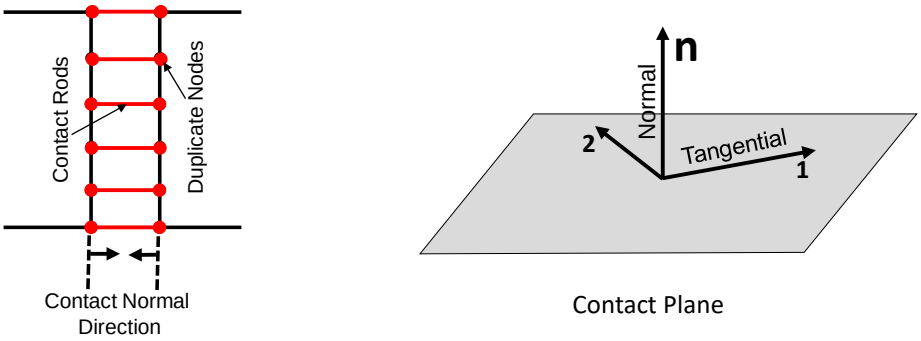

Figure 3.1: Description of node to node contact element

The geometrical contact constraint condition for the frictionless contact can be stated

for each node pair as:

$$u_n^r = (u_i^2 - u_i^1)n_i + g_n \geq 0 \tag{3.1}$$

where $u_i^\alpha, \alpha \in \mathbb{I}$ are the displacement vectors of the nodal pairs associated with dof indices i, n_i is the contact normal direction and g_n is the initial gap between the node pairs in contact normal direction.

Similarly, for the contact with friction, the shear displacement vector can be stated for contact node pair as

$$\begin{aligned} u_t^r &= (u_i^2 - u_i^1)t_i \geq 0 \\ v_t^r &= (\delta u_i^2 - \delta u_i^1)t_i \end{aligned} \tag{3.2}$$

where u_i^α is the displacement vector for the contact nodal pair (1,2) in tangential direction i, t_i is the tangential direction unit vector and v_t^r is the slip velocity.

It must be noted that for node-to-node contact (Section 3.2), the contact normal plane vector $\overrightarrow{n}$ in global coordinates system needs to be explicitly defined. The deformations are assumed to very small such that the interaction only acts between the predefined contact node pair with no contact normal plane vector n. This assumption can be used up to the point the analyst is aware of the limitations. For soil-structure interaction problems usually, the deformations are very small and this assumption would hold most of the time. However, in the case of large deformations, a more sophisticated incorporating dynamic update of contact node pairs and interface plane needs to be considered.

3.1.1 Surface Area Calculation

Since the contact interface behavior is stress-strain based, an important step is to find out the contact surface area for the given contact node pairs and contact normal n. Figure 3.2 shows the illustration of the algorithm to calculate the contact area for a given normal n at a contact node. The steps are described below.

- **Finding the Exposed Surfaces :** The first step is to find the exposed surface for the given contact node. An exposed surface is the one, whose nodes are not connected to any other common element apart from itself. Figure 3.2 shows the exposed surface (in green color) to the contact node (in red color)

- **Finding the Exposed Surface Normal :** The next step is to find the normal of the exposed surface at the contact node. Figure 3.2 shows normal n_1 and n_2 of the exposed surface S_1 and S_2 respectively.

- **Finding the Individual Shared Surface Area for Contact Node :** For each exposed surface the shared area for the contact node is found. Figure 3.2 shows are A_1 and A_2 (in Brown color) for the exposed surface S_1 and S_2 respectively for the given contact node.

- **Summation to get the total Surface Area :** The total surface area of the contact node is then evaluated as

$$A = \Sigma A_i(n.n_i) \quad \forall \quad (n.n_i \geq 0) \tag{3.3}$$

the summation of all the exposed surface area A_i shared by the contact node multiplied with the cosine of its normal n_i with the contact normal vector n for all the surfaces whose cosine is positive or greater than zero.

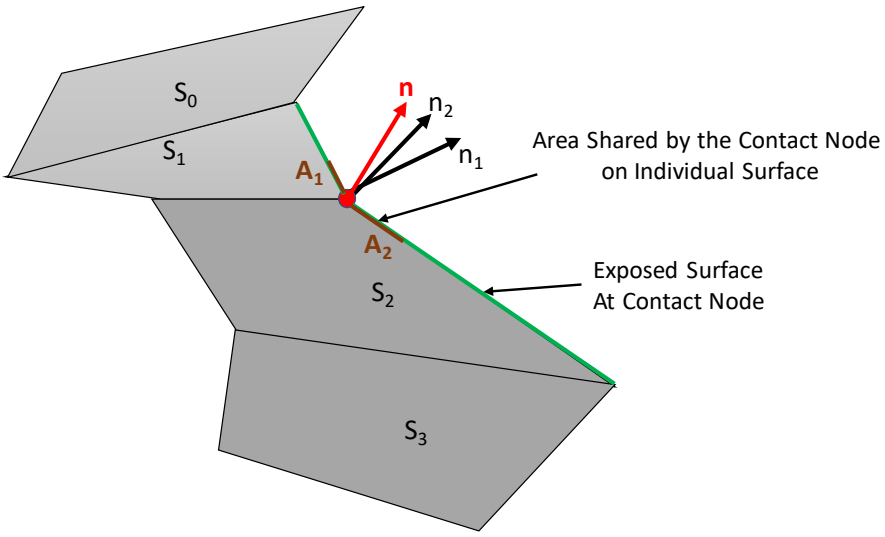

Figure 3.2: Contact Surface Area Calculation Algorithm Illustration

The above procedure can be used to calculate the contact surface area for a given contact

node pairs. For calculating contact surface area, there exist possibly three scenarios as state below

1. **Surface to Surface Contact :** In this case, the contact is applied to two conformal surface as a node-to-node contact type. As a result, for each of the contact node, an area can be evaluated for the given two surfaces. In this case the minimum of the area from each of the contact node pairs is taken.

2. **Node to Surface Contact :** In this case, the contact is applied between a node and surface as a node-to-node contact type. As a result, the contact area can only be evaluated at the node which is part of the surface. The other contact would evaluate to zero surface area. Thus, in this case, the contact area is taken as the area calculated from the surface node.

3. **Node to Node Contact :** In this case, the contact is applied between two nodes which are not part of any surface. As a result, the calculated area would be zero and a warning would be generated to the user. For such case, force based contact element should be used.

The implementation of both kinds of contact: Force Based and Stress Based follows the same steps. For stress based contact, the user would define the stiffness in units of pressure Pa. Whereas, for force type contact, the stiffness is defined in the units of N/m. For Finite Element (FE) method based on displacement, the stiffness are ultimately converted into units of N/m. Thus, for stress based contact, the global stiffness that is passed to the solver can be calculated as

$$K = E\frac{A}{SZ_h} \tag{3.4}$$

where E is the tangent stiffness in units of pressure Pa, A is the contact area, SZ_h is the shear zone thickness and K is global stiffness in units of N/m.

3.1.1.1 Verification Of Surface Area Calculation

Figure 3.3 shows possible three scenarios of surface edges possible for a given contact normal n. It is assumed that the contact normal is always provided correctly with its

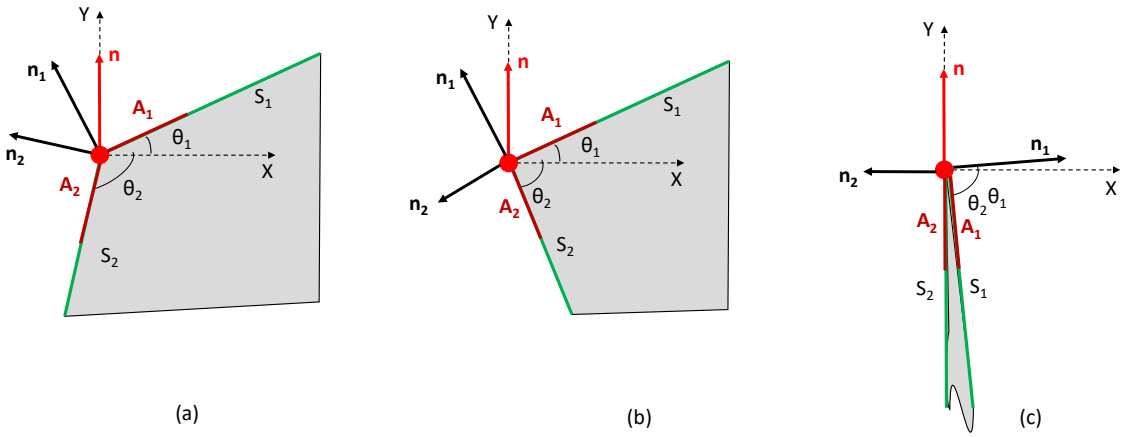

Figure 3.3: Verification of Contact Area Calculation Illustration

normal away from the surface. In the example presented in Figure 3.3, the contact normal is always defined in the y direction.

Three possible cases are considered with the exposed surface S_1 and S_2 with a shared area for the contact node as A_1 and A_2 respectively. Figure 3.3(a) represents a case when the contact normal n has acute angle with the surface normals n_1 and n_2 respectively. In this case, both the exposed surfaces take part in the total contact area calculation using the Equation 3.3. Figure 3.3(b) represents the case, in which the contact normal n makes acute angle with only one of the exposed surface S_1. Thus, in this case, since $n.n_2 < 0$, only surface S_1 takes part in the contact area calculation. Theoretically, looking at Figure 3.3(b), it could be observed that only surface S_2 should have been considered and the algorithm well captures that.

The third case is represented in Figure 3.3(c), where both the surface normals n_1 and n_2 makes almost 90^o degrees (no acute angle) with the contact normal n. This case is only possible if both the surfaces S_1 and S_2 merge to becomes a single surface, which theoretically cannot happen in any FEM mesh. For any angle θ between the two surfaces S_1 and S_2 greater than zero, there will be at least one surface normal which would make an acute angle with the contact normal n. Thus the third case (c) can never happen in a FEM mesh and even if it happens, the contact area calculated based on Equation 3.3 would be zero which again theoretically speaking would be correct.

The description of the above three cases (a), (b) and (c) possibly covers all the scenarios that could possibly happen for a corner contact node in 2-D mesh and theoretically verifies the working of contact surface area calculation algorithm presented in Section 3.1.1. The same explanation or the proof can be extended to 3-D mesh as well, verifying the correctness and robustness of contact area calculation algorithm.

3.2 Dry Contact Implementation

Node-to-node contact element can be thought of a 3D beam [Crisfield, 1997]. The formulation of node-to-node contact element starts with the 3D beam in reference configuration as shown in Figure 3.4.

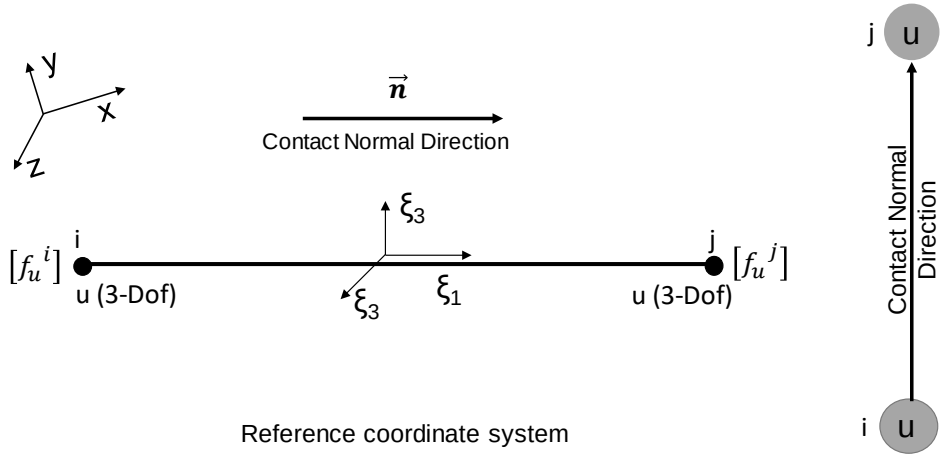

Figure 3.4: Node to Node interface element description for dry contact

In Figure 3.4, the local axes $[\xi_1, \xi_2, \xi_3]$ and the local normal and tangential force vectors $[f_n^i, f_{t1}^i, f_{t2}^i]$ and $[f_n^j, f_{t1}^j, f_{t2}^j]$ are shown. In this beam element implementation, the global normal contact vector $\overrightarrow{n}$ is defined with respect to node i. Locally ξ_1 direction corresponds to the contact normal direction $\overrightarrow{n}$ with initial normal gap $g \geq 0$. Although, the contact normal direction vector $\overrightarrow{n}$ is in the direction from node i to node j; it is not necessarily equal to the axial vector $x_i - x_j$ but can be chosen to any other direction as well. It must be noted that since most of the times, contact nodes i, j are initially at the same location, the axial vector $x_i - x_j$ is not necessarily defined.

The transformation matrix $[B]$ for the contact element from reference coordinate $[\xi_1, \xi_2, \xi_3]$ system (Figure 3.4) to the global coordinate system $[x, y, z]$ can be stated as

$$[B] = \begin{bmatrix} -x_{local} & x_{local} \\ -y_{local} & y_{local} \\ -z_{local} & z_{local} \end{bmatrix} \tag{3.5}$$

$$e_y = [0, 1, 0] \tag{3.6}$$

$$\tag{3.7}$$

$$\{x_{local}\} = \overrightarrow{n} \quad or \quad n \tag{3.8}$$

$$\{y_{local}\} = \frac{n \times e_y}{|n \times e_y|} \tag{3.9}$$

$$\{z_{local}\} = \frac{y_{local} \times n}{|y_{local} \times n|} \tag{3.10}$$

where n is the normal contact vector, which is assumed to be the axis of the contact element and web vector (e_y) is assumed as the global y-axis. In case, web vector e_y coincides n, it can be assumed to be as the global z-axis. Assuming k_n and k_t are the stiffness in contact normal and tangential direction, the local element stiffness matrix k^{dry} can be defined as

$$[k^{dry}] = \begin{bmatrix} k_n & 0 & 0 \\ 0 & k_t & 0 \\ 0 & 0 & k_t \end{bmatrix} \tag{3.11}$$

The global stiffness $[K^{dry}]$ can be then written as

$$[K^{dry}] = [B]^T [k^{dry}][B] \tag{3.12}$$

The global stiffness matrix is then assembled to the linear system of equations. It must be noted that the stiffness k_n and k_t have a *non-zero* value only when there is contact. The contact stiffness matrix shown in Equation 3.11 is symmetric for stick condition and becomes asymmetric for slip states.

3.2.1 Contact Element Updated Variables

In finite element method (FEM), any element has two basic tasks to perform. *First*, is to update the global tangent stiffness and *Second* is to calculate the resisting force. Here, six essential variables are described that needs to defined for implementation of the contact element.

- **Prev-Gap** g_{prev}: gap between the contact nodes in previous trial step
- **Current-Gap** g_{curr}: current gap between the contact node pairs

$$g_{curr} = (\delta u_j - \delta u_i) + g_{prev} \tag{3.13}$$

  where δu_2 and δu_1 is the displacement of the nodes i and node j in the current time step.

- **Whether-Prev-In-Contact** $is\_in\_contact\_prev$: stores whether the contact pairs were contact in previous trial iteration step
- **Whether-In-Contact** $is\_in\_contact$: stores the contact status of current trial iteration step
- **Trial-Resting-Force** R_{trial}: trial resisting force in the previous iteration step
- **Commit-Resting-Force** R_{commit}: resisting force in the previous converged step

The above variables can be used to check whether there is an active contact or not. Also, in case of contact, the condition for stick or slip should also be checked. The following section describes how to used these variables to decide the next step stiffness, resisting forces and gap function.

3.2.1.1 Normal Contact Condition

In the penalty method, there will be contact only when the penetration Δ_n is negative i.e $\Delta_n \leq 0$, else there will be no contact.

$$\begin{aligned} \Delta_n = g_{curr}.n \leq 0 \quad - \quad Contact \\ \Delta_n > 0 \quad - \quad No \quad Contact \end{aligned} \tag{3.14}$$

In the case of no-contact, the stiffness k_n and k_t are zero. The decision that must be taken for different situations encountered by contact element is summarized below.

1. **Prev-Not-In-Contact to Contact**: In the previous trial step there was no contact, but the element experiences contact in the current trial step

   - *Resisting-Force*: $R_{trial} = [k^{dry}][g_{curr}] \quad k_n, k_t \neq 0$
   - *Prev-Gap*: $g_{prev} = g_{curr}$
   - *Whether-Prev-In-Contact*: true
   - *Next-Stiffness*: $k_n, k_t \neq 0$

2. **Prev-In-Contact to Contact**: In the previous step there was contact and in the current step also there is contact

   - *Resisting-Force*: $R_{trial} = R_{commit} + [k^{dry}][g_{curr} - g_{prev}] \quad k_n, k_t \neq 0$
   - *Prev-Gap*: $g_{prev} = g_{curr}$
   - *Whether-Prev-In-Contact*: true
   - *Next-Stiffness*: $k_n, k_t \neq 0$

3. **Prev-In-Contact to No-Contact**: In the previous step there was contact but in the current step there is no contact

   - *Resisting-Force*: $R_{trial} = 0 \quad k_n, k_t = 0$
   - *Prev-Gap*: $g_{prev} = g_{curr}$
   - *Whether-Prev-In-Contact*: false
   - *Next-Stiffness*: $k_n, k_t = 0$

4. **Prev-In-No-Contact to No-Contact**: Previous time step as well as the current time-step is not in contact

   - *Resisting-Force*: $R_{trial} = 0 \quad k_n, k_t = 0$
   - *Prev-Gap*: $g_{prev} = g_{curr}$

- *Whether-Prev-In-Contact*: false
- *Next-Stiffness*: $k_n, k_t = 0$

In the above cases the stiffness $[k^{dry}]$ is defines as

$$[k^{dry}] = \begin{bmatrix} k_n & 0 & 0 \\ 0 & k_t & 0 \\ 0 & 0 & k_t \end{bmatrix} \tag{3.15}$$

For the case 1 and 2, there is contact whereas for other cases there is no contact. In the active contact condition, there can be two frictional states possible, one is stick case and other is the slip case which is discussed in the following Section 3.2.2. It must be noted that for soft contact (see Section 2.3.3), the stiffness matrix $[k^{dry}]$ should be updated with current normal stiffness k_n as it change in penetration Δ_n.

3.2.2 Tangential Contact Condition

The shear displacement Δ_t is defined as

$$\Delta_t = g_{curr}.t \tag{3.16}$$

where t is the unit tangential direction vector on contact plane vector as shown in Figure 3.1. The shear strain γ is then defined as $\gamma = \Delta_t / SZ_h$. The shear stress τ is defined with two shear components τ_1 and τ_2 in tangential direction $1, 2$ respectively as shown in Figure 3.1.

$$\tau = [\tau_1 \;\; \tau_2] \tag{3.17}$$

The magnitude of shear stress is defined as $|\tau| = \sqrt{\tau_1^2 + \tau_2^2}$.

For the Mohr-Coulomb (EPPS) type frictional behavior, there is no slippage of bodies if normalized shear stress $|\tau|/\sigma_n$ is less than the residual normalized shear strength μ_r. This state is known as the *stick* state and results in symmetric stiffness matrix $[C]$. However, when $|\tau|/\sigma_n \geq \mu_r$, the body slips and is said to be in a *slip* state, and consequently the stiffness matrix $[k^{dry}]$ becomes asymmetric. The two cases are described below.

1. **Stick State** $|\tau|/\sigma_n < \mu_r$: The resting force and stiffness matrix remains the same as described in 3.2.1.1.

2. **Slip State** $|\tau|/\sigma_n \geq \mu_r$: The contact element slips/slides resulting in an asymmetric stiffness matrix. At this state, the contact reaches to its yield stress as in case of the perfectly plastic material. The next step is thus to find out the plastic flow direction m, resisting force $R_{trial}$and the new tangent stiffness $[k^{dry}]$, which collectively is described as elastic-plastic integration in classical plasticity theory. Section 3.2.3 describes the process of constructing elastic-plastic and consistent tangent stiffness.

For Nonlinear Hardening Shear (NLHS) Model (Section 2.4.2) and Nonlinear Hardening Softening Shear (NLHSS) Model (Section 2.4.3), the material is assumed to start yielding (slipping) with even a very small shear loading. The interface model NLHS and NLHSS are modeled as a non-linear kinematic hardening with back stress variable α. Section 2.4.3 and 2.5 describes the incremental evolution law for the hardening and softening behavior.

3.2.3 Elastic-Plastic Integration

In the case of slip for frictional contact, an elastic-plastic integration needs to be performed to calculate the updated stiffness and resisting force. Just to be consistent with elastic-plastic theory, let us assume $\sigma_o = R_{commit}$ as the last converged stress state, $\sigma_p = R_{pred}$ as the predicted stress for the trial step, $\sigma_t^i = R_{trial}^i$ is the converged stress state for the i^{th} trial iteration step for the next state. Similarly, the incremental trial strain is taken as $\Delta\epsilon_t^i = \delta\Delta_t^i$. It must be noted that for the contact models considered in this thesis, only the shear models are assumed to be elastic-plastic while the normal models are assumed to be non-linear elastic. Thus, the elastic-plastic integration only needs to be evaluated for the shear stress τ. As noted in [Crisfield, 1991], the integration should always be performed on iterative rather than incremental strains.

Figure 3.5 shows the update strategy under these two schemes. σ_o is the initial converged state and σ_t^1 and σ_t^2 are the converged stress for iterative trial steps 1 and 2 respectively. Similarly, ϵ_o is the initial converged strain state and ϵ_1 and ϵ_2 are the strains for iterative trial steps 1 and 2 respectively. It can be observed for the strain $\epsilon_t^2 > \epsilon_o$, the iterative approach (Figure 3.5a) leads to a false unloading. Whereas, in incremental approach (Figure 3.5b), the integration is always performed from the last converged state,

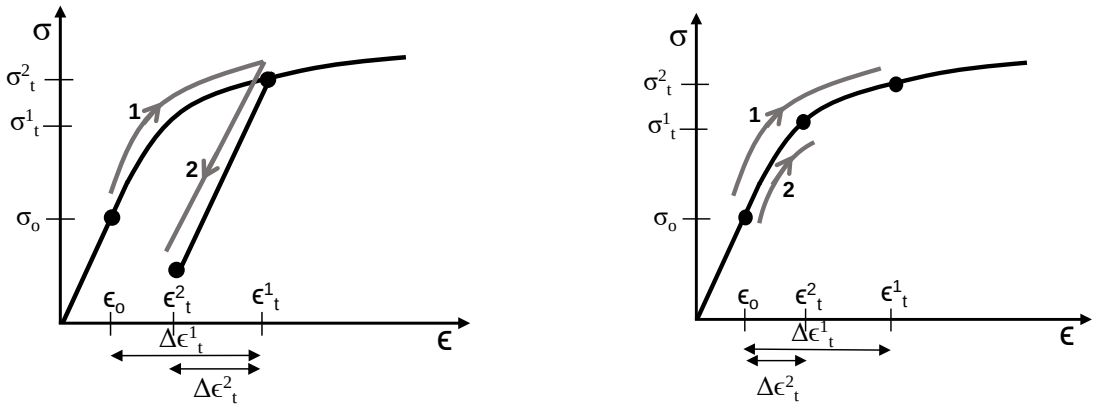

(a) Iterative Strategy

(b) Incremental Strategy

Figure 3.5: Iterative vs Incremental strategy of elastic-plastic integration

resulting in the correct prediction of stresses for the iterative strains. It must be noted that while the global Newton-Raphson convergence method is incremental, the local integration method has to be iterative. It must also be noted that the incremental and iterative approach both give the same stress state if the strains increase linearly or if the material is linear elastic. Keeping this in mind, the incremental approach should always be used in elastic-plastic integration to update stiffness and resisting force.

1. **Elasto-Plastic Stiffness**

   Figure 3.6 shows the yield and plastic flow potential surface for contact material. In classical elastic-plastic theory the predictor and the corrector is defined as shown below. It must be noted that ^{1} represented the iteration step number 1 or in more general i.

   For Elastic Plastic Shear (EPPS) model, the yield function is defined as

   $$f := \sqrt{(\tau_1^2 + \tau_2^2)} - \mu_r \sigma_n = 0 \tag{3.18}$$

   where τ_i is the shear components in contact tangential direction, σ_n is the normal stress and μ_r is the residual fiction coefficient.

   For Nonlinear Hardening Shear (NLHS) Model (Section 2.4.2) and Nonlinear Hardening Softening Shear (NLHSS) Model (Section 2.4.3) the yield function (f) is de-

fined as

$$f := (\tau_1/\sigma_n - \alpha_1)^2 + (\tau_2/\sigma_n - \alpha_2)^2 = 0 \tag{3.19}$$

where σ_n is the normal stress, τ_1, τ_2 are the shear stress and α_1, α_2 are the deviatoric back stress components in direction 1 and 2 direction respectively on the contact-interface plane (shown in Figure 3.1.

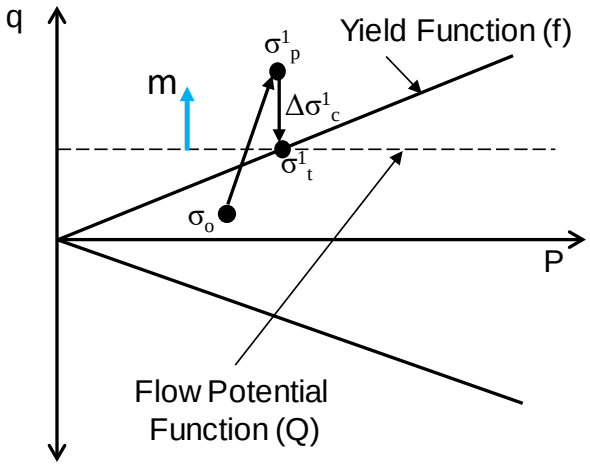

Figure 3.6: Elasto-Plastic integration for contact in slip state

$$\sigma_p^1 = \sigma_o + k_{el}^{dry} \Delta\epsilon_t^1 \tag{3.20}$$

$$\sigma_t^1 = \sigma_p^1 - \Delta\sigma_c^1 \tag{3.21}$$

$$\Delta\sigma_c^1 = \lambda k_{el}^{dry} m \tag{3.22}$$

$$\Delta\epsilon_{t,pl}^1 = \lambda m \tag{3.23}$$

where k_{el}^{dry} is the elastic stiffness k^{dry} as shown in Equation 3.11, $\Delta\sigma_c^1$ is the corrector stress, m is the unit vector in plastic-flow direction and λ is the magnitude of plastic strain or incremental slip. The plastic flow potential for frictional interface element

is non-associative and is defined in the deviatoric direction as

$$m = \frac{\tau}{|\tau|} \tag{3.24}$$

$$\tau = [\tau_1, \tau_2] \tag{3.25}$$

$$|\tau| = \sqrt{\tau_1^2 + \tau_2^2} \tag{3.26}$$

where τ_i is the shear stress component in directions 1 and 2 respectively, $|\tau|$ is represented as deviatoric stress component q and m is the plastic flow direction as shown in Figure 3.6.

When the yield function given in Equation 3.19 is $f < 0$, the contact is in stick state and elastic-plastic stiffness k_{el-pl}^{dry} would be equal to the elastic stiffness k_{el}^{dry}. If $f \geq 0$, the elasto-plastic stiffness k_{el-pl}^{dry} stiffness needs to be formulated. The above said is summarized below

- **Stick State :** $f < 0$
  - $k_{el-pl}^{dry} = k_{el}^{dry}$
  - $\sigma_t^1 = \sigma_p^1$
  - $\lambda = 0$
  - $\epsilon_{t,pl}^1 = 0$
- **Slip State :** $f \geq 0$

  Elastic-plastic integration is performed using Equation 3.20 to 3.26 to get correct stiffness and resisting force. The new resisting force is given as $R_{trial} = \sigma_t^1$. The elasto-plastic stiffness C_{el-pl}^{dry} is given as:

$$n = \frac{\partial f}{\partial \sigma} \tag{3.27}$$

$$k_{el-pl}^{dry} = k_{el}^{dry} - \frac{(n : k_{el}^{dry})(k_{el}^{dry} : m)}{n : k_{el}^{dry} : m - (Hm \ \ or \ \ Sm)} \tag{3.28}$$

  where n is a unit normal to the yield surface and Hm , Sm is the hardening or softening modulus defined in Equation 2.26 and 2.30. The NLHS and NLHSS model assume to have no elastic region resulting in slip $f > 0$ at all times.

The elasto-plastic stiffness matrix k_{el-pl}^{dry} is derived from pure mechanics and is incremental as opposed to iterative to Newton-Raphson method at global level. This leads to slow convergence at global level. In order to get the quadratic convergence, [Jeremić, 1994; Crisfield, 1987] suggest development of consistent stiffness matrix as described in Section 2

2. **Consistent Tangent Stiffness**

   The consistent stiffness is not a physical but a numerically derived stiffness matrix to get quadratic convergence at the global level. The derivation utilizes the incremental state parameter λ to get to the final consistent stiffness. [Jeremić, 1994] shows the complete derivation for a pressure dependent material. The final formulation of consistent tangent ${}^{cons}k_{el-pl}^{dry}$c an be worked out as shown below

$$ {}^{cons}k_{el-pl}^{dry} = R - \frac{(n:R)(R:m)}{n:R:m + (Hm \ \ or \ \ Sm)} \tag{3.29} $$

$$ R = T^{-1}k_{el}^{dry} \tag{3.30} $$

$$ T = I + \lambda k_{el}^{dry}\frac{\partial m}{\partial \sigma} \tag{3.31} $$

   where $Hm\,, Sm$ is the hardening or softening modulus defined in Equation 2.26 and 2.30 respectively.

It must be noted that the consistent stiffness becomes equal to the tangent stiffness i.e. ${}^{cons}k_{el-pl}^{dry} = k_{el-pl}^{dry}$ for $\lambda = 0$.

3.3 Energy Calculation

Dissipation of energy during seismic events is an important factor to consider in the design of superstructures for its safety and economy. Dissipating energy in structure can lead to material degradation and damage. It is desired to dissipate most of the energy in soil with an acceptable level of deformations in structure. Thus, it becomes important to calculate the energy dissipation at the contact interface. The energy gets dissipated when the contacting body slips/slides.

For elastic-perfectly plastic (EPPS) frictional materials, the amount of dissipation is equal to the product of shear stress τ with incremental slip Δ_t^{incr}. Thus the incremental energy dissipation E_{dis}^{incr} can be defined as

$$\Delta_t^{incr\_pl} = \lambda m \tag{3.32}$$

$$E_{dis}^{incr} = \tau \Delta_t^{incr\_pl} \tag{3.33}$$

It must be noted that $\Delta_t^{incr\_pl}$ is also known as slip velocity as refereed in Equation 1.14. Since slip happens only in tangential direction, energy gets only dissipated due to frictional slip. The normal behavior of the interface is assumed to be linear and non-linear elastic for hard and soft contact respectively. It must be noted that the incremental energy dissipation cannot be negative.

For the non-linear hardening and softening Armstrong-Frederick type material NLHS and NLHSS models, the incremental dissipation is calculated considering the plastic free energy Φ as described in Yang et al. [2017]. The incremental energy is given as

$$\Delta_t^{incr\_pl} = \lambda m \tag{3.34}$$

$$E_{dis}^{incr} = \tau \Delta_t^{incr\_pl} - \Delta\Phi \tag{3.35}$$

where incremental plastic work $W_{plastic}^{incr}$ is defined as $W_{plastic}^{incr} = \tau \Delta_t^{incr\_pl}$ and $\Delta\Phi$ represents the incremental plastic free energy of the material which is defined as

$$\Delta\Phi = \frac{\alpha : \Delta\alpha}{H_a} \tag{3.36}$$

where H_a is the linear Armstrong-Frederick hardening variable and α i the deviatoric back stress internal variable. For NLHS and NLHSS models, the linear hardening variable H_a is assumed to be equal to the elastic tangential stiffness k_t as described in the section 2.4.2 and 2.4.3. In order to get the total dissipation, Equation 3.33 is integrated integrated with time. It must be noted that the incremental dissipation E_{dis}^{incr} energy is always positive. Since both the NLHS and NLHSS models assume to have zero elastic region and same elastic stiffness k_t as the hardening parameter H_a, the incremental plastic free energy $\Delta\Phi$ and the incremental elastic strain energy $E_{strain}^{inc} = \tau \Delta_t^{incr\_el}$ would be equal.

The total incremental input energy W_{input} for the models is defined as

$$W_{input}^{incr} = \tau \Delta_t^{incr} \tag{3.37}$$

Thus, the total energy conservation in incremental form is defined as

$$W_{input}^{incr} = E_{strain}^{incr} + E_{dis}^{incr} + \Delta\Phi \tag{3.38}$$

3.4 Viscous Damping

At soil-foundation interface usually either there is fluid i.e. air or water (under submerged conditions). Continuous in and out movement of fluid at the interface because of opening and closing of gap causes energy dissipation at the interface. To model this behavior, a damper can be considered to act between the contact node pairs in both normal and tangential direction. The viscous-elastic stiffness of the damper is taken as c_n and c_t in contact normal and tangential direction.

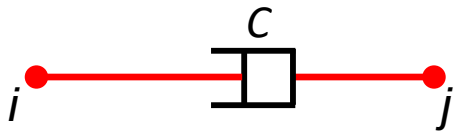

Figure 3.7: Modeling viscous damping in node to node contact element

Figure 3.7 shows a typical damper with visco-elastic stiffness c. Node i and j represents the contact node pairs as shown in Figure 3.4. For contact element, the damper would act on the relative velocity between the contact node pairs in local coordinate system i.e. $v_{local}^r = [B(:, 3:6)] \times (v_j - v_i)$. Similar, to Equation 3.11 and 3.12, the local $[c^{dry}]$ and global $[C^{dry}]$ stiffness matrix can be defined as

$$[c^{dry}] = \begin{bmatrix} c_n & 0 & 0 \\ 0 & c_t & 0 \\ 0 & 0 & c_t \end{bmatrix} \tag{3.39}$$

$$[C^{dry}] = [B]^T [c^{dry}][B] \tag{3.40}$$

The resisting damping force can then be given as

$$[R_{damp}] = [B]^T[v^r] \tag{3.41}$$

It must be noted that unlike normal stiffness k_n and shear stiffness k_t which acts only during contact and stick states, damping stiffness c_n and c_t would act always. In fact, the viscous force would increase with the opening as the relative velocity between contact nodes would increase. For closed gap state, the contact bodies move with the same velocity resulting in zero viscous force.

3.5 Coupled Contact Implementation

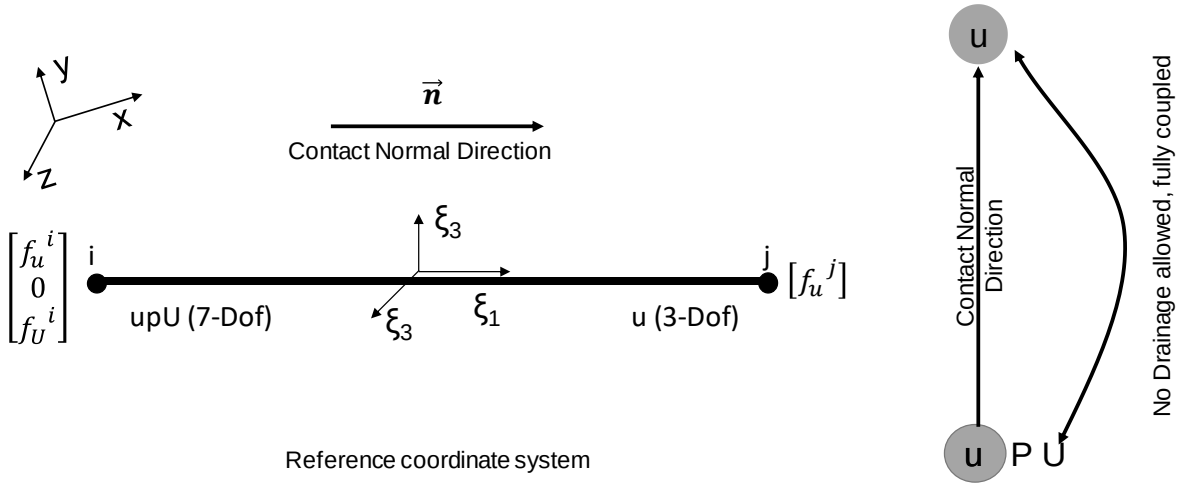

Figure 3.8: Node to Node interface element for coupled contact

Implementation of coupled contact in FEM follows the same steps as described in Section 3.2. Penalty stiffness is used for enforcing normal contact between $u-u$ degrees of freedom of foundation (solid) and soil. To enforce the effective stress principle and transfer pore-fluid pressure, again penalty stiffness method is enforced between translational (u) degree of freedom to fluid translational (U) degree of freedom in the normal contact direction as shown in Figure 3.8.

The enforcement of penalty between U-u ensures the transfer of stresses from soil (Eq 1.21) to the foundation and also models fluid-suction during uplift (Eq 1.22). It also

enforces the undrained condition as fluid cannot have displacement (U) during compression in the contact normal direction.

The full stiffness matrix $[K^{coupled}]$ for node-to-node coupled ($upU-u$) contact element can be derived from the regular stiffness matrix $[K^{dry}]$ of dry ($u-u$) contact element. Figure 3.8 shows the contact element as a 3-D beam element in the reference frame (ξ_1, ξ_2, ξ_3). The contact normal vector (n) is defined in terms of global coordinate system (x, y, z) from node 1(uPU) called as master node to node 2 (u) called as the slave node. Figure 3.8 also shows the force vector $[f]$ on the two nodes. Force vector $[f_u]$ can be further decomposed into normal force f_n and shear forces $[f_{t1} \quad f_{t2}]$ as in regular dry (u-u) contact as $f_u = [f_n \quad f_{t1} \quad f_{t2}]$. The transformation matrix $[B]$ from local to global coordinate system is defined by Equation 3.5 The local stiffness $[k^{dry}]$ for dry ($u-u$) contact element is written as

$$[k^{dry}] = \begin{bmatrix} k_n & 0 & 0 \\ 0 & k_t & 0 \\ 0 & 0 & k_t \end{bmatrix} \tag{3.42}$$

where k_n and k_t are the normal and shear stiffness. Under non-contact condition i.e. ($u_n^r - g_n > 0$), the normal stiffness k_n and the shear stiffness k_t would be zero. Under contact condition ($u_n^r - g_n \leq =0$), there could be further two conditions of stick and slip state as described in Section 3.2.2. The stiffness matrix $[K]$ for the stick state remains the same (Equation 3.42) whereas for the slip state an elastic-plastic stiffness is constructed as described in Section 3.2.3 Following Equation 3.5 and 3.42 the global stiffness matrix for the dry element is assembled as

$$\begin{aligned} [K^{dry}] &= [B][k^{dry}] \\ [K^{dry}] &= \begin{bmatrix} K^{dry}_{u_i-u_i} & K^{dry}_{u_i-u_j} \\ K^{dry}_{u_j-u_i} & K^{dry}_{u_j-u_j} \end{bmatrix} \end{aligned} \tag{3.43}$$

The enforcement of $U-u$ in contact vector direction can be ensured by adding penalty

stiffness (k_p) which creates a penalty-stiffness matrix $[k^{penalty}]$ as

$$[k^{penalty}] = \begin{bmatrix} k_p & 0 & 0 \\ 0 & 0 & 0 \\ 0 & 0 & 0 \end{bmatrix} \tag{3.44}$$

Similarly, the global penalty matrix for $U - u$ degree of freedom (DOF) interaction can be assembled as

$$\begin{aligned} [K^{penalty}] &= [B][k^{penalty}] \\ [K^{penalty}] &= \begin{bmatrix} K^{penalty}_{U_i - U_i} & K^{penalty}_{U_i - u_j} \\ K^{penalty}_{u_j - U_i} & K^{penalty}_{u_j - u_j} \end{bmatrix} \end{aligned} \tag{3.45}$$

The global stiffness matrix $[K^{coupled}]$ for coupled contact element, then can be assembled as

$$[K^{coupled}] = \begin{bmatrix} \overbrace{K^{dry}_{u_i - u_i}}^{u} & \overbrace{0}^{p} & \overbrace{0}^{U} & \overbrace{K^{dry}_{u_i - u_j}}^{u} \\ 0 & 0 & 0 & 0 \\ 0 & 0 & K^{penalty}_{U_i - U_i} & K^{penalty}_{U_i - u_j} \\ K^{dry}_{u_j - u_i} & 0 & K^{penalty}_{u_j - U_i} & K^{dry}_{u_j - u_j} + K^{penalty}_{u_j - u_j} \end{bmatrix} \tag{3.46}$$

The resisting force and the new stiffness is calculated in similar way as for the dry element as described in section 3.2. Appendix A lists down the domain specific language (DSL) for the contact elements implemented in Real ESSI Simulator System [Jeremić et al., 2017] of both soft and hard type with non-linear hardening/softening shear behavior.

3.6 Auto Surface to Surface Contact Detection

Section 3.1 described the node-to-node contact approach where the contact normal n was explicitly defined for each of the contact normal pairs in global coordinate system. The contact normal vector n being a geometrical mesh property of the problem, is difficult to be defined. For a curved mesh, where multiple surfaces with different normal vectors,

defining only one contact normal vector per node pairs would lead to serious errors. This is explained below using the example presented in Figure 3.9. The contact normal vectors and plane is defined as n_i and CP_i. The example demonstrates the effect of having only one contact normal to the case with as many contact normals for each of the surface connected.

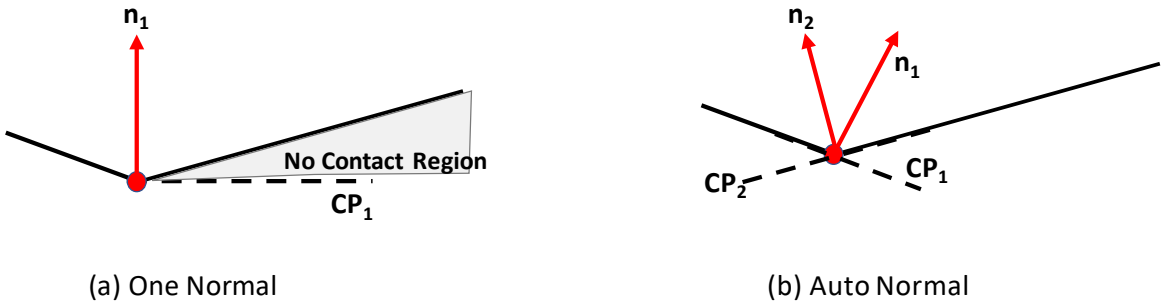

Figure 3.9: Illustration of no contact region for a single normal in comparison to multiple contact normals for a given contact node pair.

In Figure 3.9(a), only one contact normal n_1 is defined. As a result, the contact node (denoted in red) can move inside the no-contact region denoted by gray color. But, it can be seen that the contact node cannot move inside that region because it is physically constrained by the other surface. Thus, defining only one normal would lead to an erroneous result.

Figure 3.9(b) shows the same example but with two contact normals n_1 and n_2 defined for each of the surface connected. The contact normal planes are shown as CP_1 and CP_2 respectively. It can be observed that contact node cannot move inside the bottom surface as it is strictly enforced by the two contact planes. When the node tries to move in the gray region as shown in Figure 3.9(a), contact normal plane CP_1 detaches but contact normal plane CP_2 constrains it. Thus, the problem now gets properly constrained by defined two normal vectors.

For a contact node pair in 2-D there could be minimum 1 and maximum 2 contact normal vectors n possible for a given contact node as shown in Figure 3.10. But for 3-D, there could be many contact normal vectors n possible for a given node pair depending

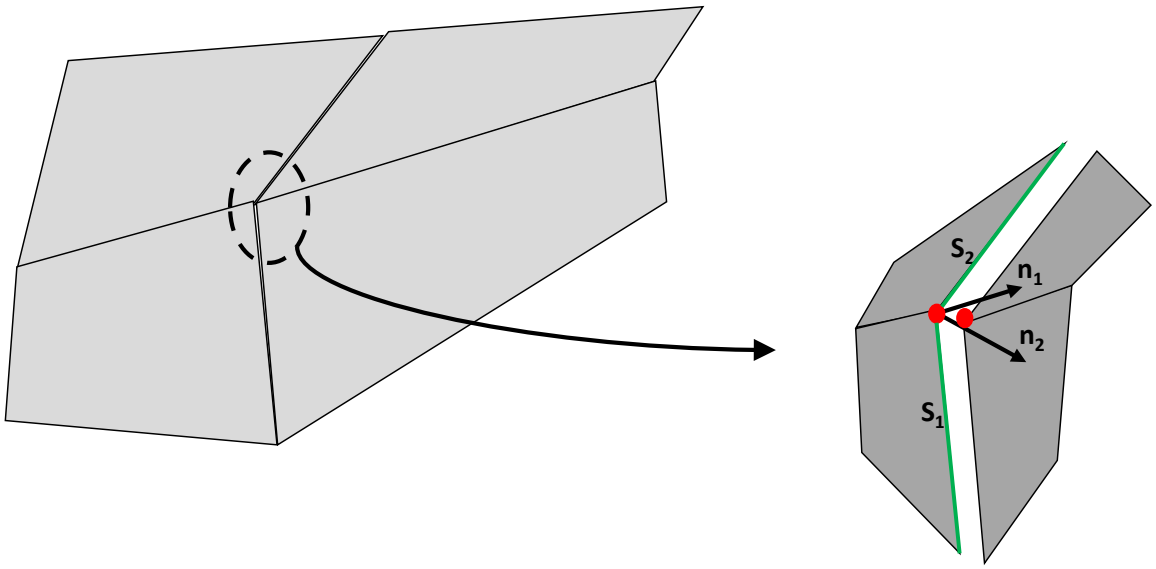

Figure 3.10: Auto detection of multiple surface normal directions n for a given contact node pair in 2-D.

upon the number of surfaces the nodes are connected or belong to. Figure 3.10 shows an example in which both the surface normal vectors n_1 and n_2 are possible for a given contact node pair. In order to correctly model the interface behavior, two contact elements need to be defined with the contact normals n_1 and n_2 respectively for the same pair of contact nodes. However, for the example presented in Figure 3.11, although two surface normals n_1 and n_2 exists the contact only exists in normal direction n_1. Thus there is need to automate the contact normal direction n detection and auto-creation of contact elements for a given conformal mesh and contact node pairs. The steps to auto-detect the contact normals for the given contact node pairs follow almost the similar steps as described in Section 3.1.1.

The steps summarized below are referred to a general case presented in Figure 3.11. The contact node pairs and their associated properties are referred as superscript i and j.

- **Finding the Exposed Surfaces :** For each of the node pairs i and j, the exposed surfaces are determined. In Figure 3.11, the exposed surfaces for node i are referred as S_1^i and S_2^i whereas for node j are referred as S_1^j and S_2^j.

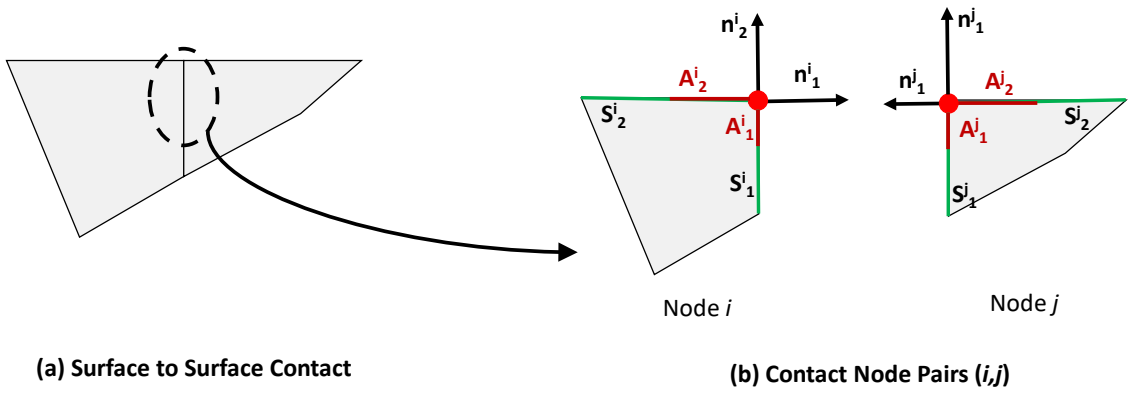

Figure 3.11: Auto detection of multiple surface normal directions n in an edge mesh for a given contact node pair in 2-D.

- **Determining Exposed Surface Area and Normal For the Contact Node :** For each of the exposed surface area found, the contact normal n_k^i and area A_k^i shared by each of the contact nodes are determined. In Figure 3.11, for node i the surface normal are defined as n_1^i and n_2^i and the surface area contribution to the node is defined as A_1^i and A_2^i respectively for the exposed surfaces S_1^i and S_2^i. Similarly, the surfaces normals n_1^j and n_2^j and their associated surface area A_1^j and A_2^j are defined for node j for the exposed surfaces S_1^j and S_2^j respectively.

- **Determining the Contact Normal Vectors :** The contact may not exist for all the exposed surfaces as is shown in Figure 3.11. Thus, there is a need to find the compatible exposed surfaces on which contact exists. The surface to surface contact of node-to-node type presented in this thesis is valid only for conformal mesh. Thus, for a contact to exists between two surfaces or the node pairs i, j, the exposed surfaces of the nodes i and j should have the same area A_k and equal and opposite surface normals n_k.

  One way to check whether there exists a contact normal n of equal and opposite normals for a given contact node pairs i and j is to find whether the dot product is equal to -1.

$$n_k^i . n_k^j = -1 \tag{3.47}$$

The above condition presented in Equation 3.47 is necessary but sufficient condition. Thus, the associated area should also be checked i.e. $A_k^i = A_k^j$. Thus the necessary and sufficient condition to know the contact normal directions n that could exists for a given conformal surface S, is to check whether

- **The normals from the contact node pairs i, j are equal and opposite :** $n_k^i . n_k^j = -1$
- **Both the surfaces share the same are at the corresponding nodes i, j :** $A_k^i = A_k^j$

From Figure 3.11, it could be seen that only surface normal n_1^i satisfies the above two conditions and thus the contact only exists in that direction. However, in Figure 3.10 both the normals n_1 and n_2 would satisfy the condition resulting in two contact normal directions. Since in finite precision machine (computers), the above equality conditions is never fully satisfied, a relative tolerance $|\delta x|/x$ check is applied.

- **Forming Contact Elements :** With the obtained possible contact normal directions n^i and surface area A^1, multiple individual contact elements are created between the same node pair. All the contact elements then collectively satisfy the impenetrability condition at that surface.

In this method, since the contact normal directions are automatically found, the user does not need to specify them. Appendix A.3 lists down all the domain-specific input language implemented in Real-ESSI Simulator.

Chapter 4

Verification and Validation

As [Oberkampf and Trucano, 2002] notes verification and validation (V&V) of computational simulations are the primary methods for building and quantifying this confidence. Verification is the assessment of the correctness of the model implementation, code debugging, mathematical errors and evaluating its limitation. The verification process can be subdivided into code verification and solution verification. While the code verification checks the correctness of code. Solution verification checks the correctness of solution obtained for the assumed mathematical model over a wide range of values for its parameters. This section performs verification of the contact elements implemented in Real ESSI (Realistic Earthquake Soil-Structure Interaction) Simulator System [Jeremić et al., 2017].

Validation on other hand is the process of evaluating the proposed mathematical model's accuracy to the actual physics observed by conducting experiments. It is an important means of identifying and minimizing model errors and uncertainties, and provides some assurance of the computational modeling capability. Section 4.11 discusses the validation of the proposed interface shear models. Later in Section 4.12, numerical issues with contact are discussed.

4.1 Interface Behavior

This section verifies the working of the interface element essentially by changing all the parameters over a wide range. Thus, it also demonstrates the sensitivity of parameters for the interface behavior.

4.1.1 Normal Contact Behavior

The normal interface behavior as discussed in Section 2.3 can be either a hard or soft contact. While both the contacts behavior use penalty stiffness method, hard contact as constant stiffness whereas soft contact has non-linear increasing stiffness with penetration.

4.1.1.1 Hard Contact

The hard contact described in Section 2.3.2 has a constant normal stiffness k_n and thus a linear normal-stress σ_n with penetration Δ_n. Thus, there is only one parameter defined for the normal contact which is the normal stiffness k_n.

Normal Stiffness k_n : The normal stiffness defines the stiffness in contact normal direction n. Figure 4.1 shows the response of interface element subject to a pure compressive load of $\sigma_n = 100kPa$ with shear zone thickness of $SZ_h = 5mm$. The normal stiffness k_n is changed over the range from $40kPa$ to $1GPa$. It can be observed in Figure 4.1 that as

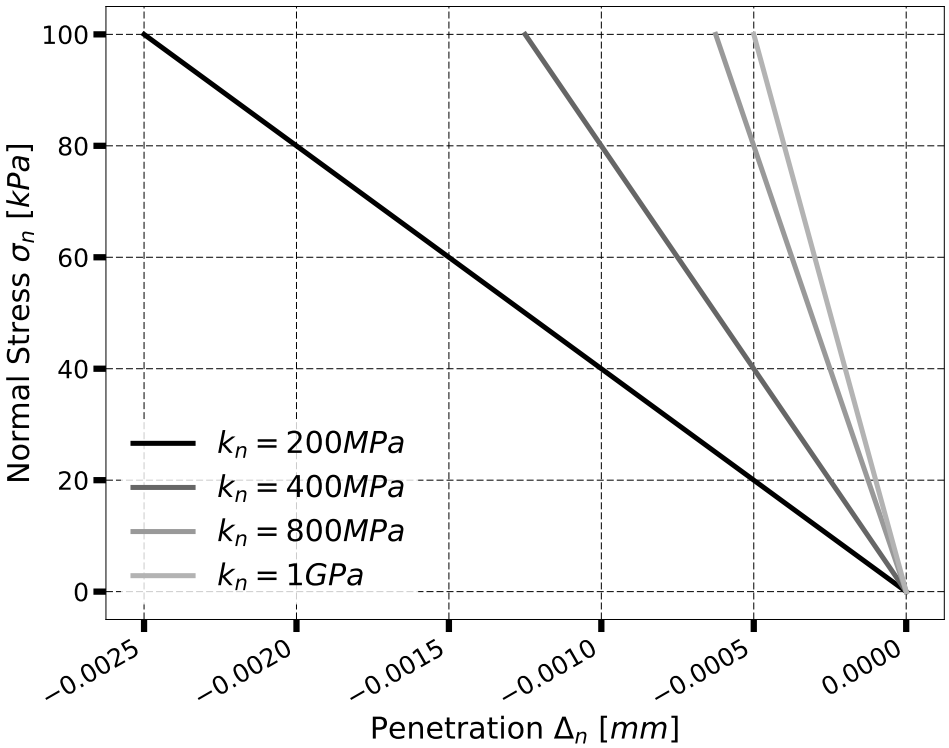

Figure 4.1: Response of Hard Contact for a pure compressive load of $\sigma_n = 100kPa$ with different normal stiffness k_n

the normal stiffness k_n is increased, the amount of penetration Δ_n for the load of $100kPa$

is decreased. The normal stress σ_n response is linear as the stiffness k_n is constant.

4.1.1.2 Soft Contact

The soft contact described in Section 2.3.2 has three modeling parameters: initial normal stiffness k_i, stiffening rate S_r and maximum normal stiffness k_n^{max}. The parameters define a non-linear normal response at the interface.

Initial Normal Stiffness k_i : It defines the initial stiffness between the contact node pairs when the penetration Δ_n is 0. As the penetration increases the stiffness increases exponentially by the Equation 2.7. Figure 4.2 shows the response of soft interface element subject to a pure compressive load of $\sigma_n = 500kPa$ with shear zone thickness of $SZ_h = 5mm$, stiffening rate of $S_r = 1000$ and maximum normal stiffness of $k_n^{max} = 10GPa$. The initial normal stiffness k_i is changed over the range from $40kPa$ to $1GPa$. It can be

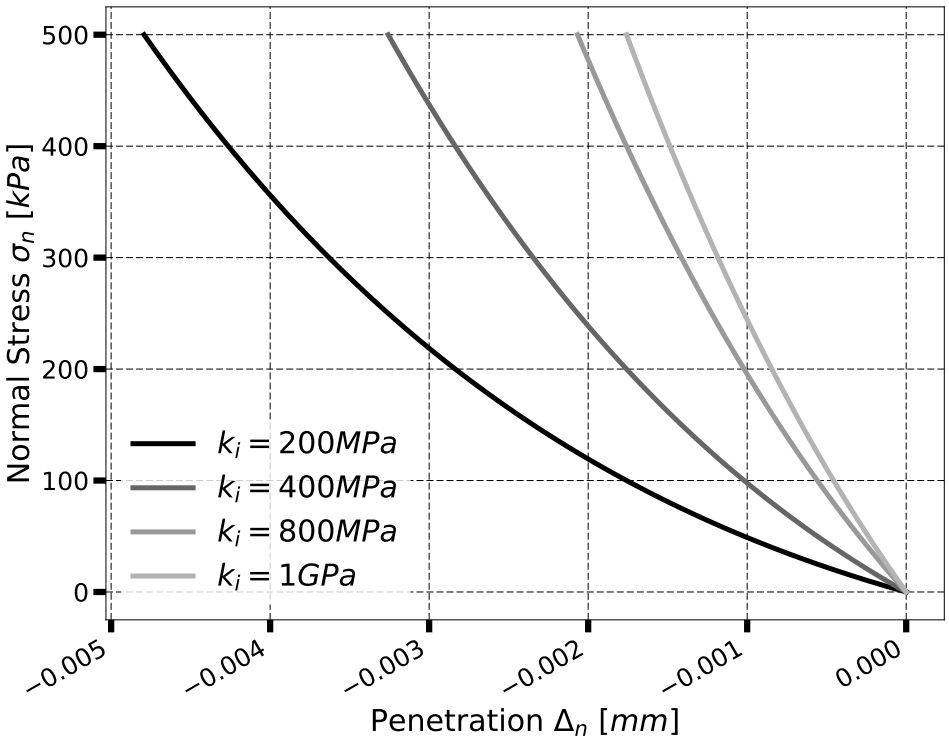

Figure 4.2: Response of Soft Contact for a pure compressive load of $\sigma_n = 500kPa$ with different initial normal stiffness k_i

observed from the Figure 4.2 that as the initial normal stiffness k_i is increased, the amount of penetration Δ_n for the normal load of $\sigma_n = 500kPa$ decreases. Figure 4.3 shows the

normal response to low initial normal stiffness $k_i \leq 1MPa$. It could be observed that the normal stiffness k_n is very small in the beginning but increases exponentially with penetration Δ_n.

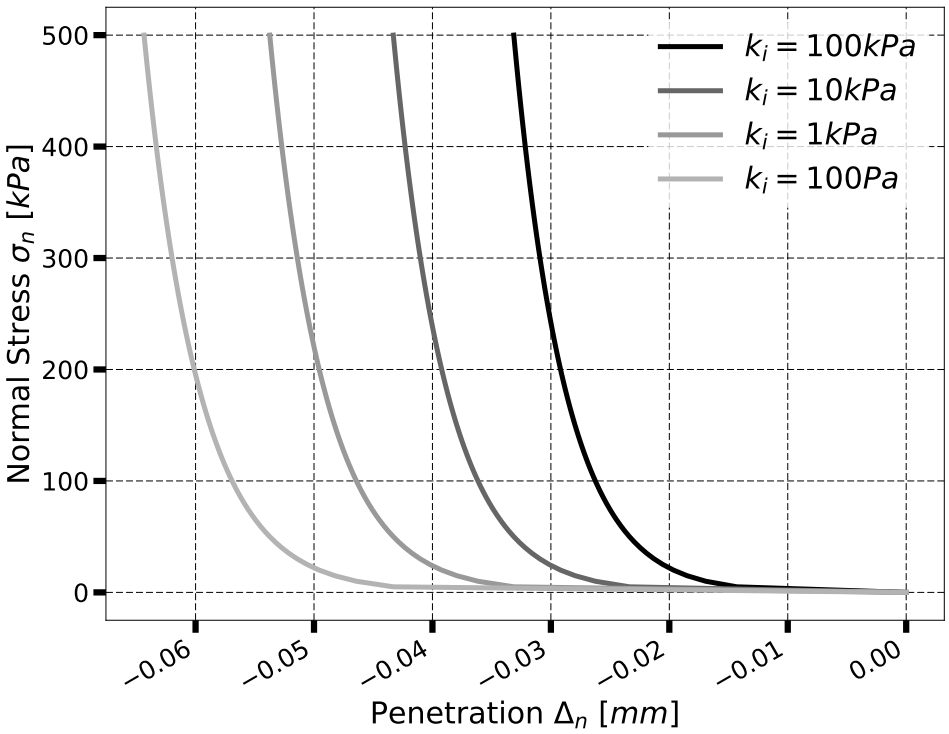

Figure 4.3: Response of Soft Contact for a pure compressive load of $\sigma_n = 500kPa$ with low initial normal stiffness $k_i \leq 1MPa$

Stiffening Rate S_r **:** It defines the rate at which the normal contact stress σ_n with penetration Δ_n increases as shown in Equation 2.6. As the penetration Δ_n increases the contact normal stress increases exponentially. Figure 4.4 shows the response of soft interface element subject to pure compressive load of $\sigma_n = 500kPa$ with shear zone thickness of $SZ_h = 5mm$, initial normal stiffness $k_i = 200MPa$ and maximum normal stiffness of $k_n^{max} = 10GPa$. The stiffening rate S_r is changed over the range of e^2 to e^5. It can be observed from the Figure 4.4 that as the stiffening rate S_r is increased, the amount of penetration Δ_n for the load of $\sigma_n = 500kPa$ decreases whereas the non-linearity increases exponentially.

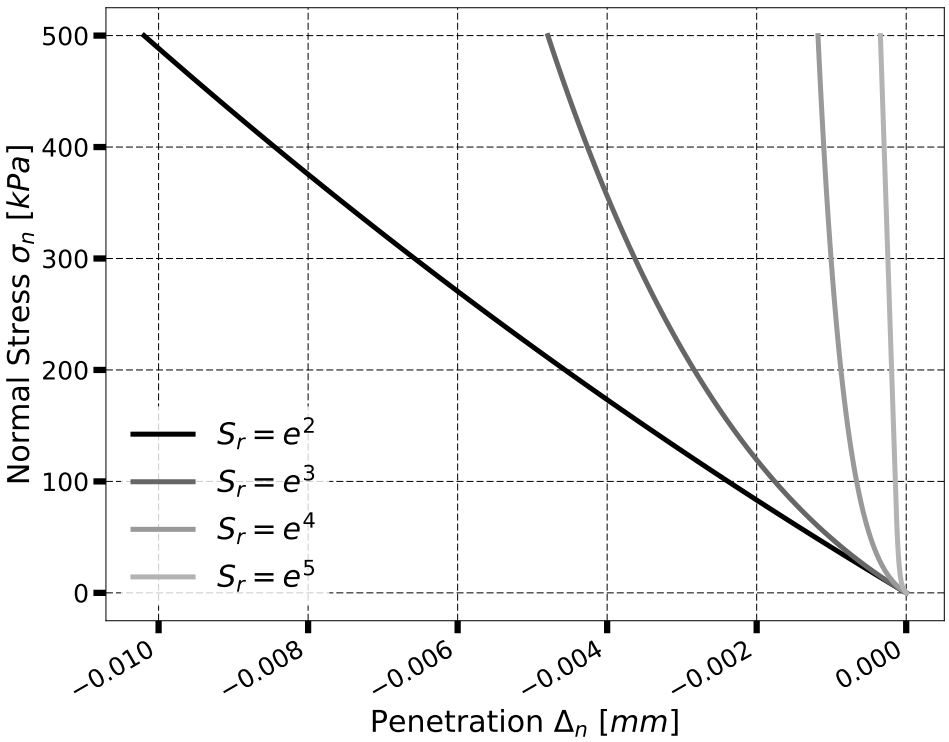

Figure 4.4: Response of Soft Contact for a pure compressive load of $\sigma_n = 500kPa$ with different stiffening rate S_r

Maximum Normal Stiffness k_n^{max} : It defines the limit to the normal contact stiffness k_n as shown in Equation 2.8. As the penetration increases the contact normal stress increases exponentially. Thus, the maximum normal stiffness k_n^{max} provides a limit to its value. Figure 4.5 shows the response of soft interface element subject to a compressive load of $500kPa$ with shear zone thickness of $SZ_h = 5mm$, initial normal stiffness $k_i = 200MPa$ and stiffening rate of $S_r = 1000$. The maximum normal stiffness k_n^{max} is changed over the range of $200MPa$ to $1GPa$. It can be observed from the Figure 4.5 that as the maximum normal stiffness k_n^{max} is increased, the amount of penetration Δ_n for the load of $500kPa$ decreases whereas the exponential non-linearity also increases. For maximum normal stiffness $k_n^{max} = 200MPa$ and $k_i = 200MPa$, the response is linear as there is no stiffening.

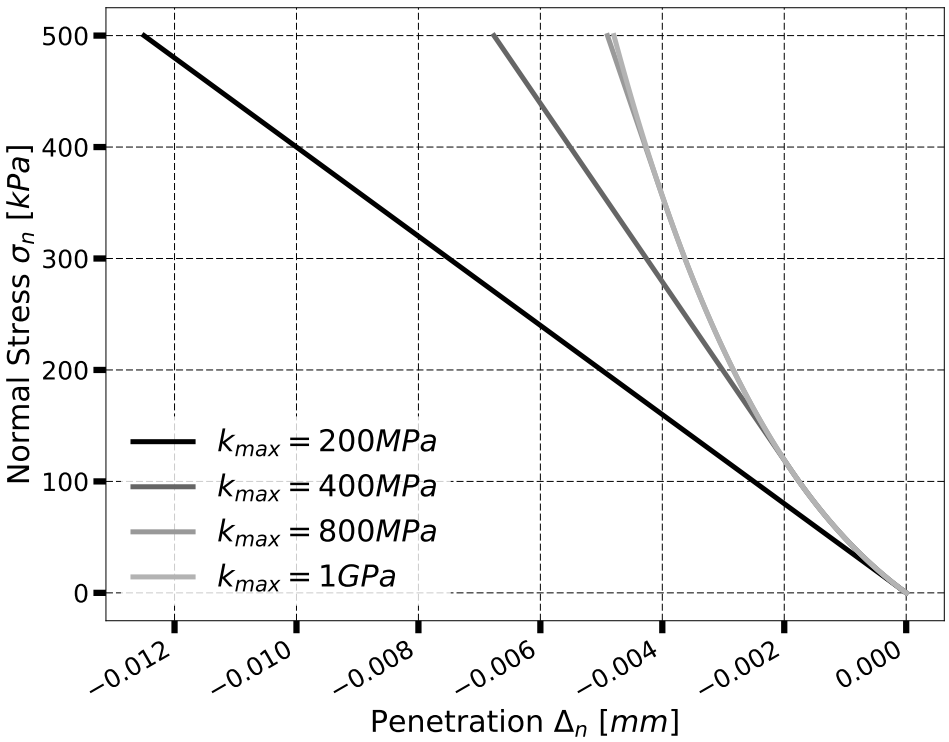

Figure 4.5: Response of Soft Contact for a compressive load of $\sigma_n = 500kPa$ with different maximum normal stiffness k_n^{max}

4.1.2 Interface Shear Behavior

The interface shear behavior as discussed in Section 2.4 are proposed of three types as EPPS, NLHS and NLHSS models. All these three models have an increasing level of sophistication and are able to model the behavior from pure elastic-perfectly plastic to non-linear hardening and softening.

4.1.2.1 Elastic Perfectly-Plastic Shear Model

The EPPS model described in Section 2.4.1 has two modeling parameters: the shear stiffness k_t and the residual friction coefficient μ_r.

Shear Stiffness k_t : It defines the elastic shear stiffness k_t of the interface. A low stiffness results in larger shear displacement before yielding or achieving the residual shear strength or the residual frictional coefficient μ_r. A higher shear stiffness would gain its full shear strength at small shear strain γ or displacement Δt. Figure 4.6 plots the response of interface element with a constant normal stress of $100kPa$ for a shear displacement of

$8mm$,shear zone thickness of $SZ_h = 5mm$, and residual frictional coefficient $\mu_r = 0.68$. The shear stiffness k_t is changed over the range of $40kPa$ to $1.2GPa$.

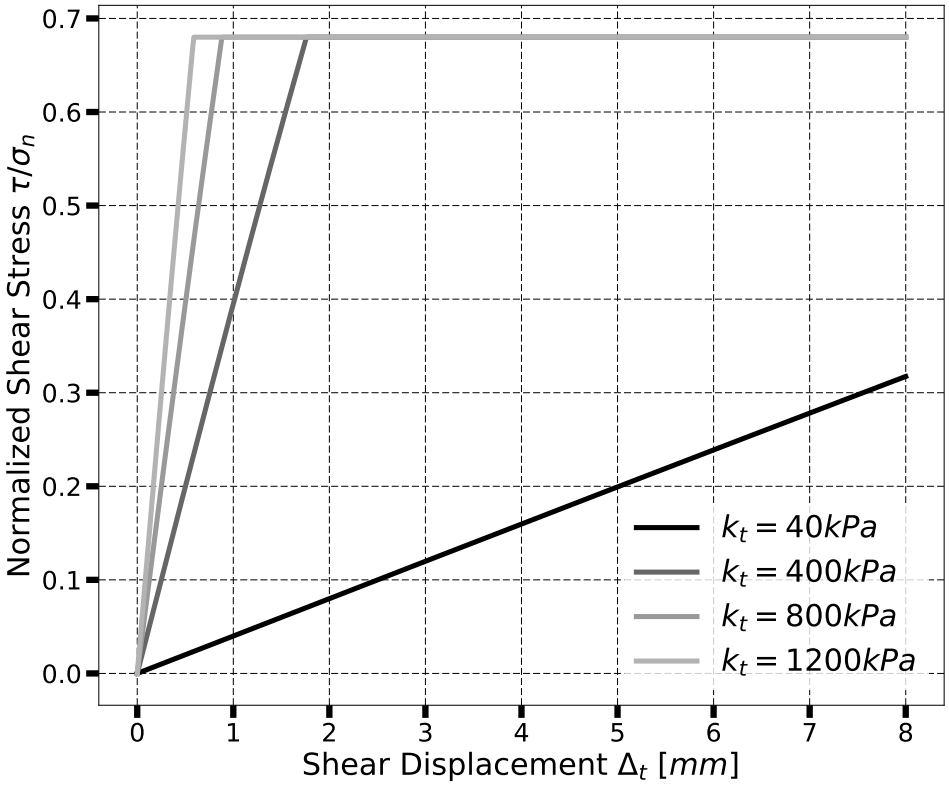

Figure 4.6: EPPS Model shear response for a constant normal stress of $\sigma_n = 100kPa$ with different shear stiffness k_t

It can be observed from the Figure 4.6 that for a given shear displacement Δt as the shear stiffness k_t is increased, the mobilized normalized shear stress also increases. Also, since the model is elastic-perfectly plastic, the response is linear until the full shear strength is achieved and after the interface cannot take anymore shear stress in the loading direction. For shear stiffness $k_t = 40kPa$, the full shear strength is still not mobilized even after the shear displacement of $\Delta t = 8mm$.

Residual Frictional Coefficient μ_r : It defines the residual normalized shear stress. Figure 4.7 shows the response of interface element subject to constant normal stress of $\sigma_n = 100kPa$ for a shear zone thickness of $SZ_h = 5mm$ and shear stiffness $k_t = 200MPa$ for a shear displacement of $\Delta t = 8mm$. The residual frictional coefficient μ_r is changed over the range of 0.01 to 1.

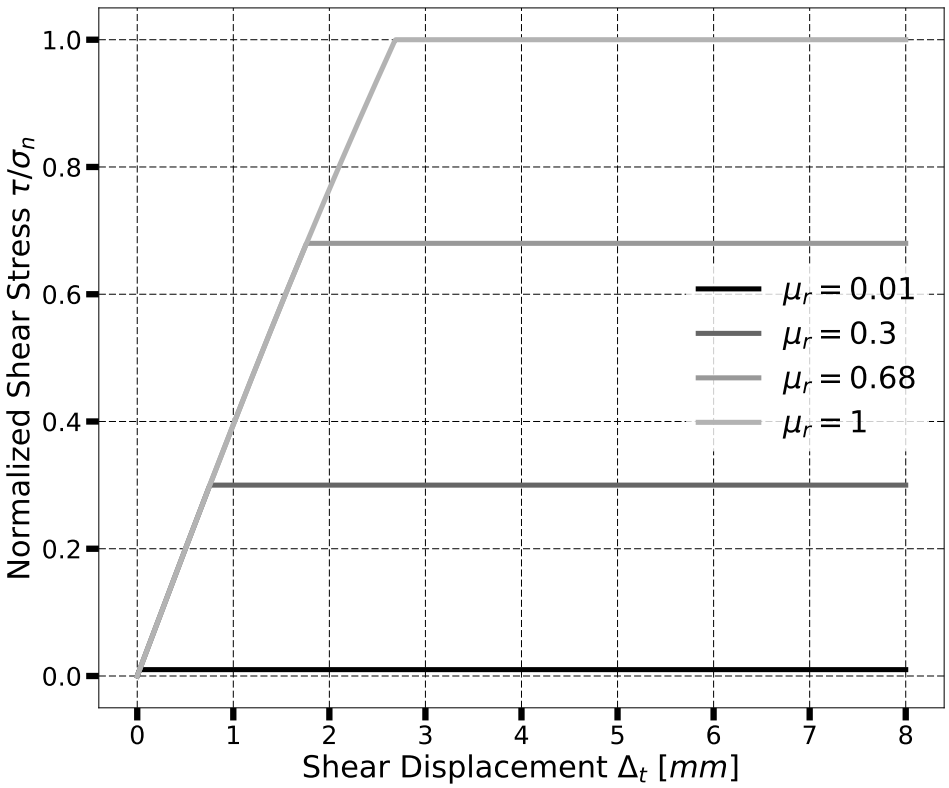

Figure 4.7: EPPS Model shear response for a constant normal stress of $\sigma_n = 100kPa$ with different residual friction coefficient μ_r

It can be observed from the Figure 4.7 that as the residual frictional coefficient μ_r is increased, the mobilized normalized shear stress τ/σ_n also increases. A residual frictional coefficient $\mu_r = 0.01$ results in low mobilization of normalized shear stress of $\tau/\sigma_n = 0.01$ whereas larger residual frictional coefficient mobilizes higher normalized shear stress τ/σ_n. The verification of shear zone thickness SZ_h is shown in Figure 4.55c.

4.1.2.2 Non-Linear Hardening Shear Model

The NLHS model described in Section 2.4.2 has also two modeling parameters: the elastic shear stiffness k_t and the residual shear stress ratio μ_r. It models a non-linear hardening shear stress function.

Shear Stiffness k_t : It defines the elastic shear stiffness k_t of the interface. A low stiffness results in larger shear displacement before achieving the ultimate residual shear strength μ_r. A higher shear stiffness would gain its full shear strength at small shear strain

or displacements. Figure 4.8 plots the response of interface element with a constant normal stress of $\sigma_n = 100kPa$ for a shear displacement of $\Delta t = 8mm$, shear zone thickness of $SZ_h = 5mm$, and residual frictional coefficient $\mu_r = 0.68$. The shear stiffness k_t is changed over the range of $40kPa$ to $1.2GPa$. It must be noted that k_t represents the elastic shear stiffness. Thus, since hardening parameter H_a in this model is assumed to be equal to elastic stiffness k_t with zero elastic range, the initial elasto- plastic shear stiffness would be equal to $0.5k_t$. This could be noticed as initial shear stiffness in the plots shown in Figure 4.10.

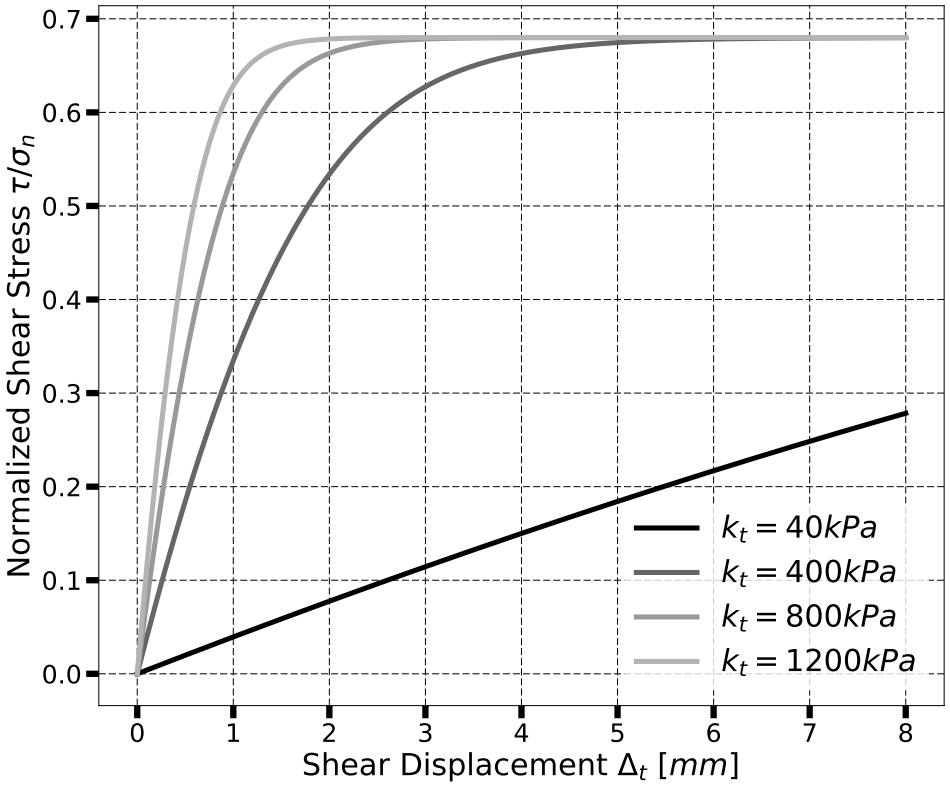

Figure 4.8: NLHS Model shear response for a constant normal stress of $\sigma_n = 100kPa$ with different shear stiffness k_t

It can be observed from the Figure 4.8 that for a given shear displacement Δt as the shear stiffness k_t is increased, the mobilized shear stress also increases. Also, since the model is a kinematic non-linear hardening type, the response is fully non-linear until the full shear strength is achieved. For shear stiffness $k_t = 40kPa$, the full shear strength is still not mobilized even after attaining shear displacement of $\Delta t = 8mm$. Although

the response is non-linear, it looks linear for shear stiffness $k_t = 40kPa$ due to its small curvature.

Residual Frictional Coefficient μ_r : It defines the residual normalized shear stress. Figure 4.9 shows the response of interface element subject to constant normal stress of $100kPa$ with shear zone thickness of $SZ_h = 5mm$ and shear stiffness $k_t = 200MPa$. The residual frictional coefficient μ_r is changed over the range from 0.01 to 1 for a shear displacement of $\Delta t = 8mm$.

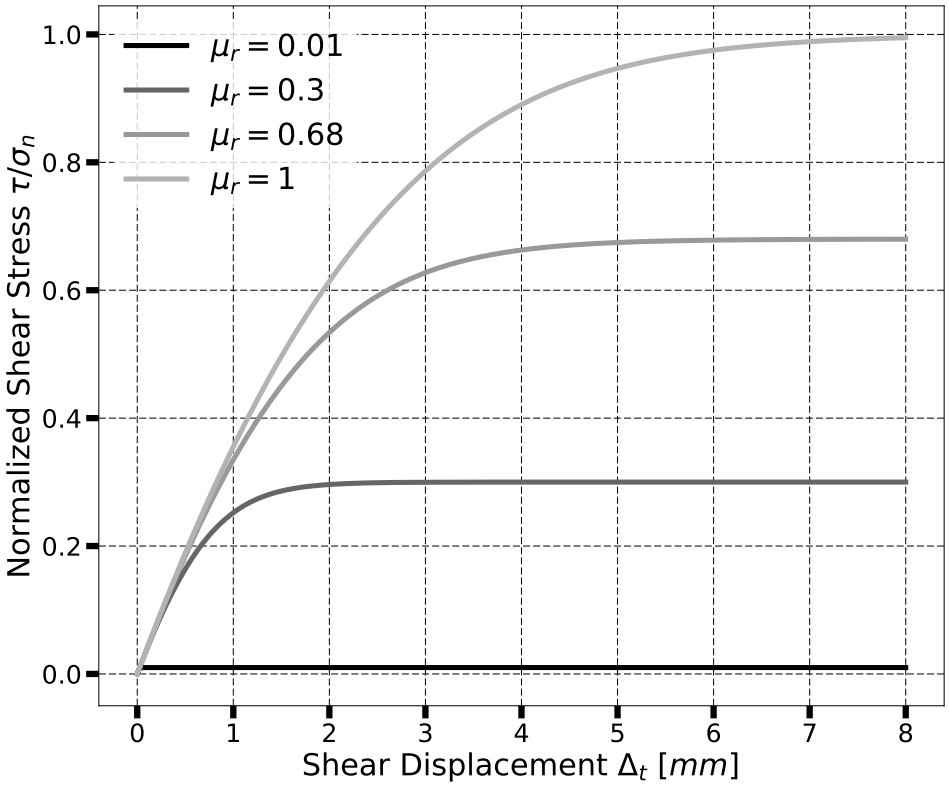

Figure 4.9: NLHS Model shear response for a constant normal stress of $\sigma_n = 100kPa$ with different residual normalized shear stress μ_r

It can be observed from the Figure 4.9 that as the residual normalized shear stress μ_r is increased, the mobilized normalized shear stress τ/σ_n also increases. Thus, a residual normalized shear stress $\mu_r = 0.01$ results in low mobilization shear stress τ whereas larger normalized shear stress leads to higher mobilization of shear stress τ. The verification of shear zone thickness SZ_h is shown in Figure 4.56c.

4.1.2.3 Non-Linear Hardening Softening Shear Model

The non-linear hardening/softening shear model described in Section 2.4.3 has four modeling parameters: the shear stiffness k_t, peak plateau size n, softening rate b and the peak normalized shear stress limit μ_{P0}, the rate of decrease of peak normalized shear stress k and the residual shear stress ratio μ_r. It models a non-linear hardening shear stress function.

Shear Stiffness k_t : It defines the elastic shear stiffness k_t of the interface. A low stiffness will result in larger shear displacement before achieving the peak shear strength μ_p. A higher shear stiffness leads to gaining of peak shear strength at small shear strain or displacement. Figure 4.10 plots the response of interface element with a constant normal stress of $\sigma_n = 100kPa$ for a shear displacement of $\Delta t = 8mm$, shear zone thickness of $SZ_h = 5mm$, plateau size parameter $n = 8$, softening rate $b = 40$, peak normalized shear stress limit $\mu_{p_0} = 0.76$, rate of decrease parameter $k = 0.1$ and residual normalized shear of $\mu_r = 0.68$. The elastic shear stiffness k_t is changed over the range of $k_t = 40kPa$ to $k_t = 2.2GPa$. It should be again be noted that k_t represents the elastic shear stiffness. Thus, in the model since hardening parameter H_a is assumed to be equal to elastic stiffness k_t with zero elastic range, the initial elasto- plastic shear stiffness would be equal to $0.5k_t$ as could be observed in the plots shown in Figure 4.10.

It can be observed from the Figure 4.10 that for a given shear displacement Δt as the shear stiffness k_t is increased, the mobilized normalized shear stress also increases. As a result, the peak normalized shear stress μ_p is attained significantly for large shear stiffness k_t. Once the peak is attained, the normalized shear stress decreases to its residual value. For low shear stiffness $k_t = 40kPa$, even after the shear displacement of $\Delta t = 8mm$ and the peak normalized shear stress has not been attained.

Peak Plateau Size n : It defines the size of the plateau of the softening branch once the peak normalized shear stress is obtained and is governed by Equation 2.15. Figure 4.11 plots the response of interface element with a constant normal stress of $\sigma_n = 100kPa$ for a shear displacement of $\Delta t = 8mm$, shear zone thickness of $SZ_h = 5mm$, shear stiffness $k_t = 1500kPa$, softening rate $b = 40$, peak normalized shear stress limit $\mu_{p_0} = 0.76$, rate

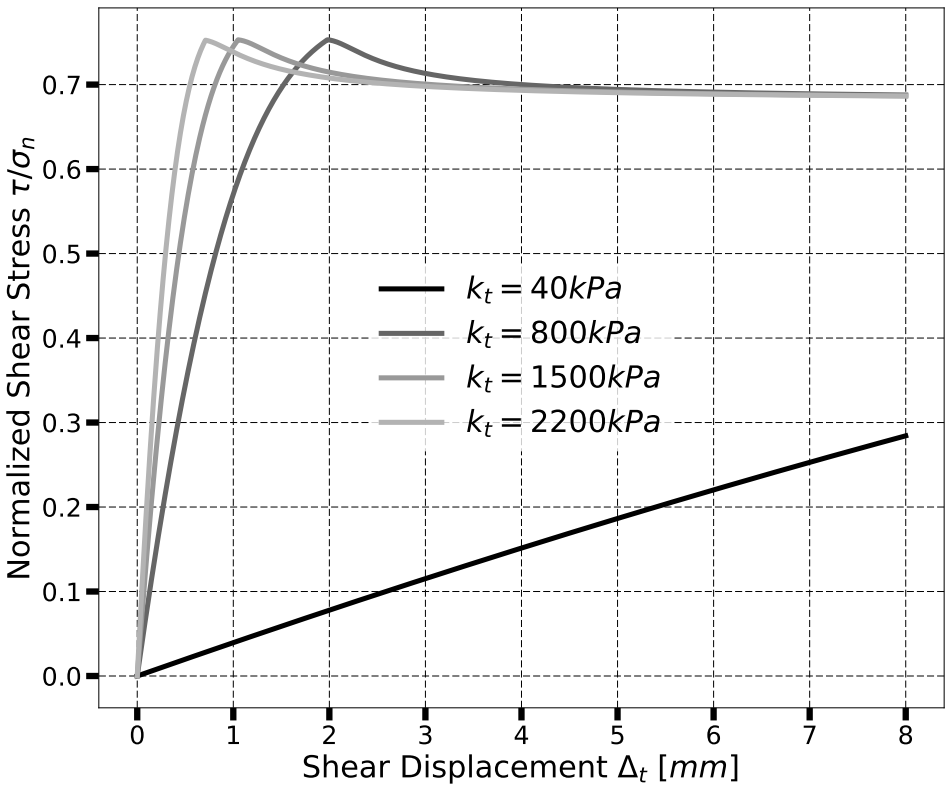

Figure 4.10: NLHSS Model shear response for a constant normal stress of $\sigma_n = 100kPa$ with different shear stiffness k_t

of decrease parameter $k = 0.1$ for peak normalized shear stress and residual frictional coefficient $\mu_r = 0.68$. The peak plateau size parameter n is changed over the range from 1 to 80.

It can be observed from the Figure 4.11 that as the peak plateau size parameter n is increased, the rate of softening decreases. However for large values of peak plateau size parameter $n = 80$, the rate of softening increases a lot such that the normalized shear stress drops down to residual strength much faster. As shown in Equation 2.15, the peak plateau size parameter n also dominates the rate of softening and is highly non-linear.

It must be noted that although the response seems to be unrealistic for large values of $n = 80$, Figure 4.11 shows the correctness of the mathematical model and its implementation for a wide range of peak plateau size parameter n.

Softening Rate b **:** It defines the rate of decrease in normalized shear stress in the softening phase once the peak strength is attained as per Equation 2.15. Figure 4.12

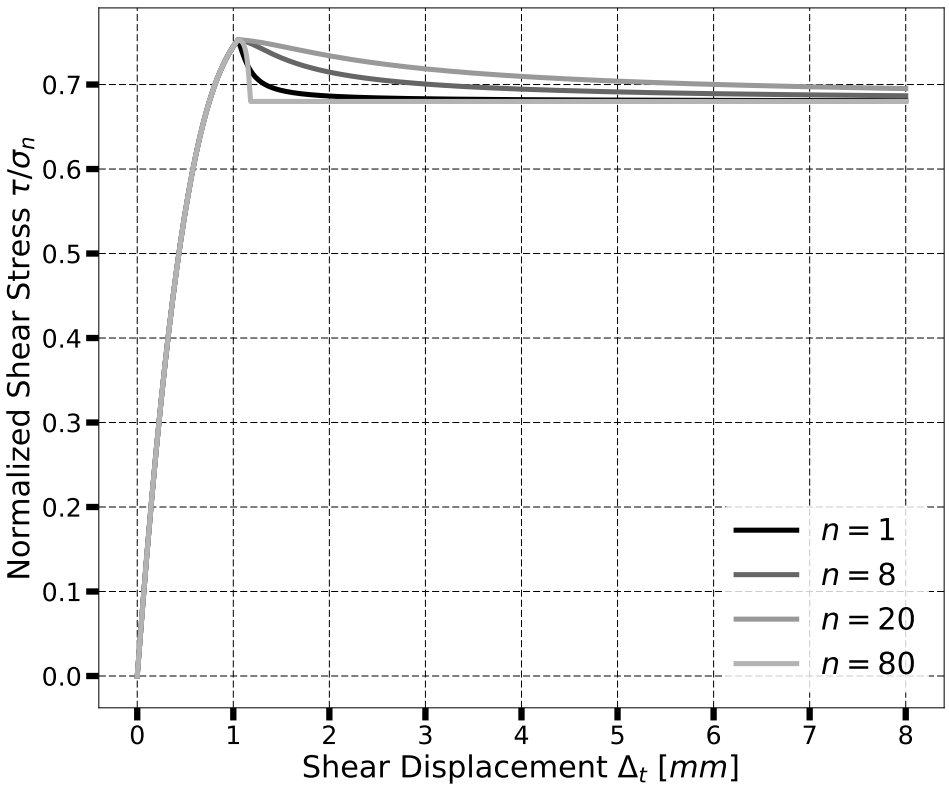

Figure 4.11: NLHSS Model shear response for a constant normal stress of $\sigma_n = 100kPa$ with different peak plateau size parameter n

shows the response of interface element with a constant normal stress of $\sigma_n = 100kPa$ for a shear displacement of $\Delta t = 8mm$, shear zone thickness of $SZ_h = 5mm$, shear stiffness $k_t = 1500kPa$, plateau size parameter $n = 8$, peak normalized shear stress limit $\mu_{p_0} = 0.76$, rate of decrease parameter $k = 0.1$ for peak normalized shear stress and residual frictional coefficient $\mu_r = 0.68$. The softening rate parameter b is changed over the range from 5 to 500.

It can be observed from the Figure 4.12 that as the softening rate parameter b is increased the rate of decrease of normalized shear stress τ/σ_n also increases. The same is also confirmed from the linear dependence of incremental normalized shear stress on softening parameter b as shown in Equation 2.15.

Residual Normalized Shear Stress μ_r : It defines the residual normalized shear stress. Figure 4.13 shows the response of interface element with a constant normal stress of $\sigma_n = 100kPa$ for a shear displacement of $\Delta t = 8mm$, shear zone thickness of $SZ_h = 5mm$,

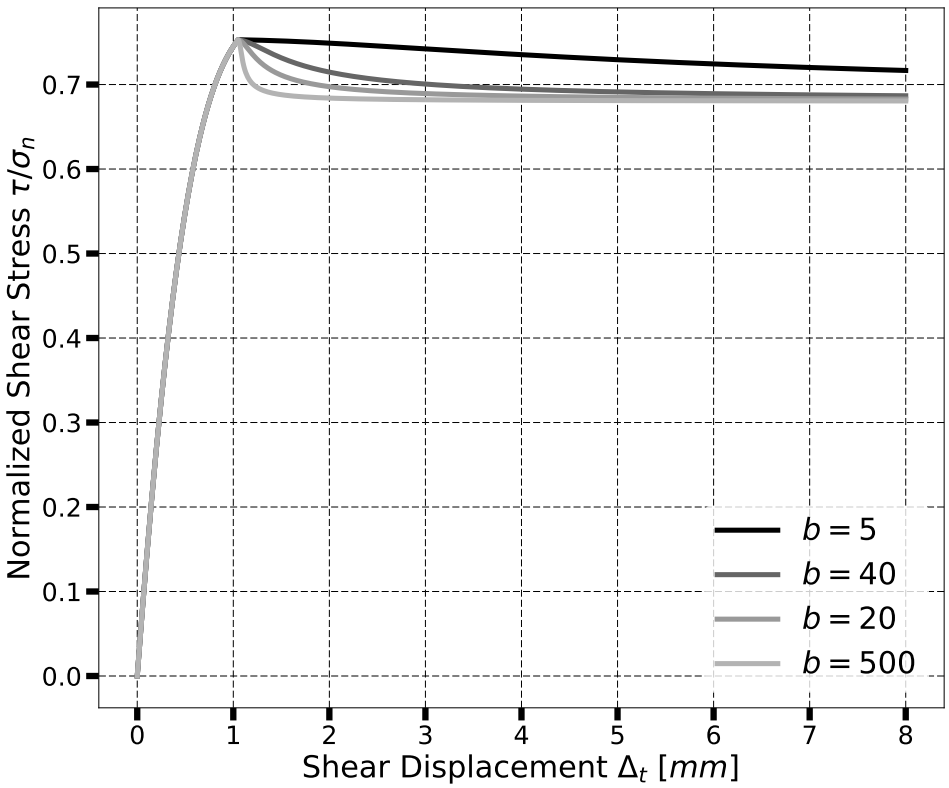

Figure 4.12: NLHSS Model shear response for a constant normal stress of $\sigma_n = 100kPa$ with different softening rate parameter b

shear stiffness $k_t = 1500kPa$, plateau size parameter $n = 8$, softening rate $b = 40$, peak normalized shear stress limit $\mu_{p_0} = 0.76$ and the rate of decrease parameter $k = 0.1$. The residual normalized shear stress μ_r is changed over the range of 0.01 to 0.76.

It can be observed from the Figure 4.13 that the residual normalized shear stress μ_r controls the shear stress limit during the softening phase. A lower value of residual normalized shear stress μ_r results in low ultimate shear strength or higher amount of softening from peak to residual shear stress.

Peak Normalized Shear Stress Limit μ_{p0} : It defines the function as well as the limit to the peak normalized shear stress μ_p with normal stress σ_n as shown in Equation 2.19.

Figure 4.14 shows the peak normalized shear stress response of interface element for normal stress of $\sigma_n = 1kPa$ to $\sigma_n = 1000kPa$. The peak normalized rate of decrease parameter k is taken as $k = 0.1$ and residual normalized shear stress as $\mu_r = 0.68$. The peak normalized shear stress limit μ_{p_0} is varied over the range from 0.01 to 0.76.

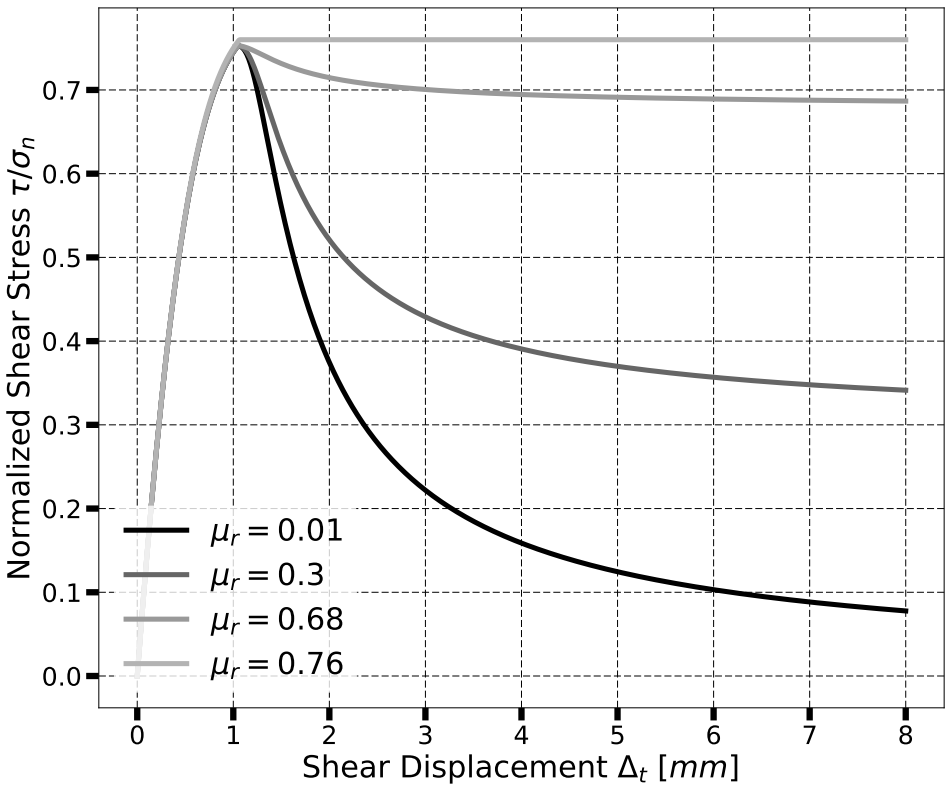

Figure 4.13: NLHSS Model shear response for a constant normal stress of $\sigma_n = 100kPa$ with different residual normalized shear stress $\mu_r = \tau/\sigma_n$

It can be observed from the Figure 4.14 that for a given normal stress σ_n, an increase in the peak normalized shear stress limit μ_{p0} would increase the peak normalized shear stress μ_p. It can also be observed from the Figure 4.14, that for value of Peak Normalized Shear Stress Limit μ_{p0}, the peak normalized shear stress μ_p reaches the residual normalized shear stress μ_r at comparatively lower normal stress σ_n. Since residual normalized shear stress μ_r is assumed to be the lowest shear strength that could be achieved, it also serves as the lower limit of peak normalized shear stress μ_p.

Peak Normalized Shear Stress Rate of Decrease k : It defines the rate of decrease of peak normalized shear stress μ_p with normal stress σ_n as shown in Equation 2.18. Figure 4.15 shows the peak normalized shear stress response of interface element for a normal stress $\sigma_n = 1kPa$ to $\sigma_n = 1000kPa$. The peak normalized shear stress limit μ_{p_0} is taken as $\mu_{p_0} = 0.9$ and residual normalized shear stress as $\mu_r = 0.68$. The peak normalized shear stress rate of decrease parameter k is varied over the range of 0.01 to 1.

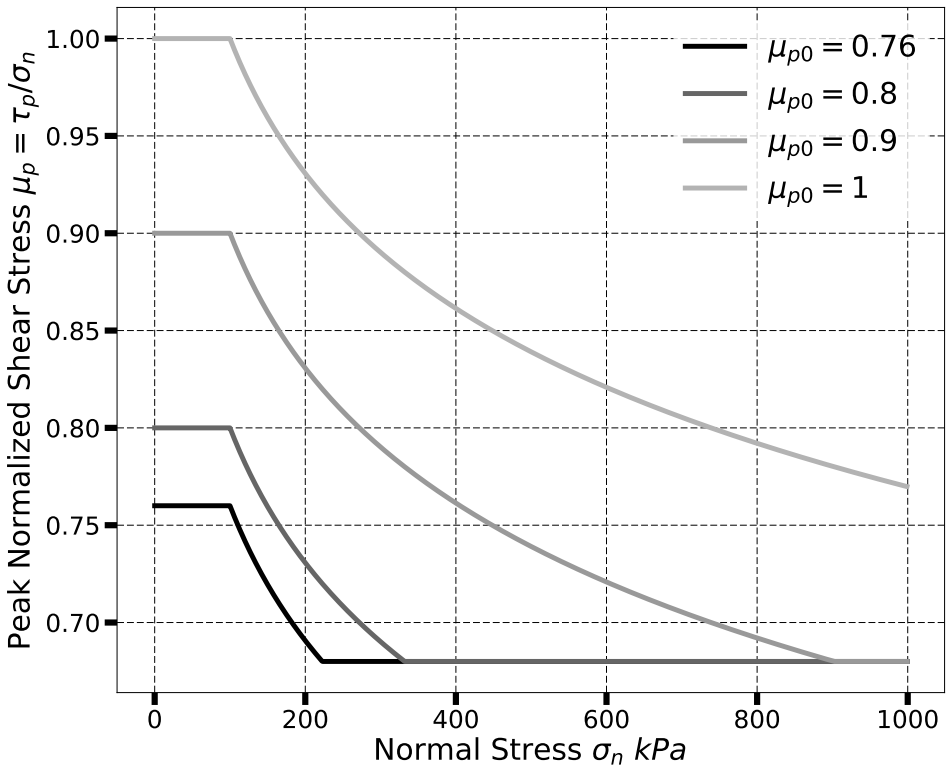

Figure 4.14: NLHSS Model peak normalized shear stress $\mu_p = \tau_p/sigma_n$ with different peak normalized shear stress limit μ_{p0}

It can be observed from the Figure 4.15 that as parameter k is increased, the peak normalized shear stress $\mu_p = \tau_p/\sigma_n$ decreases much faster with the increase of normal stress σ_n. A higher value of the rate of decrease parameter $k = 1$, results in peak normalized shear stress less than the residual value. Since residual normalized shear stress μ_r is assumed to be the lowest shear strength that could be achieved, it also serves as the lower limit of peak normalized shear stress μ_p. The verification of shear zone thickness SZ_h is shown in Figure 4.57c.

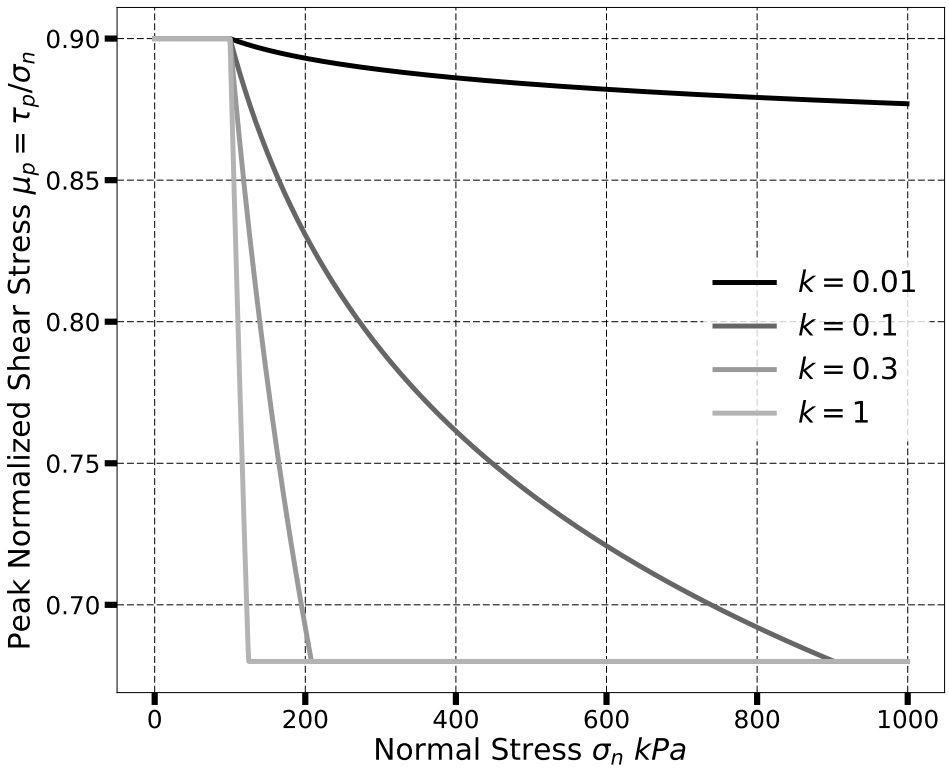

Figure 4.15: NLHSS Model peak normalized shear stress $\mu_p = \tau_p/sigma_n$ with different peak normalized shear stress rate of decrease parameter k

4.1.3 Energy Calculation

Energy dissipated at the soil-structure interface is an important attribute to be considered. For soil-structure interaction problems, it is preferred to dissipate energy anywhere except the structure itself. Idealistically for seismic loadings, one would like to dissipate a large part of the input energy at the interface with no loss of considerable shear strength. In other situations, the energy dissipated at contact interfaces could prove to be quite useful in damping out higher mode vibrations in structure. The energy calculation could also be used for defining the cyclic shear strength degradation at interface Liu and Ling [2008]. Section 3.3 describes the method to calculate different incremental energy forms for contact elements. The incremental dissipation energy can be integrated to evaluate total energy dissipation at the contact interface.

Since in this thesis it is assumed that the normal contact response at interface is non-linear elastic, there is no energy dissipation. However, the actual soil-structure nor-

mal interface response may be elastic-plastic resulting in some dissipation but there has been not any experimental evidence to either support or discard the fact presented here. Experiments must be carried out to investigate and understand the normal response of soil-structure interface for monotonic as well as cyclic loading conditions.

The interface shear models being hardening/softening elastic-plastic materials, energy calculation verification is an important aspect to be considered. Thus for the shear response, it must be verified that the total energy components should sum-up to the total input work W_{input} and the incremental energy dissipation E_{dis}^{incr} is always positive Yang et al. [2017].

$$W_{input} = E_{strain} + E_{dis} + \Phi \tag{4.1}$$

where W_{input} is the total input work, E_{strain} is the elastic strain energy and Φ is the plastic-free energy. Section 3.3 describes the equations of incremental plastic-free energy density $\Delta\Phi$ and incremental plastic dissipation E_{dis}^{incr}.

To verify the energy calculation of shear response at the interface, cyclic strain-strain response are considered with shear zone thickness of $SZ_h = 5mm$, residual normalized shear stress $\mu_r = 0.68$ and contact surface area of $1m^2$. Cyclic shear displacement of $\Delta t = 2mm$ was applied to the interface with the normal stress of $\sigma_n = 100kPa$. Figure 4.16 to 4.20 shows the different energy components of the shear behavior for EPPS, NLHS and NLHSS models. Number of cycles n in the plots define the total number of cyclic-shear loops. One cyclic-shear is defined as application of shear displacement from $\Delta t = 0mm$ to $\Delta t = \Delta t = \Delta t = +2mm$ to $\Delta t = \Delta t = -2mm$ to finally $\Delta t = 0mm$.

Figure 4.16 shows the shear stress-strain response and energy density for the elastic-perfectly plastic model with shear stiffness $k_t = 200kPa$. It can be observed that the plastic dissipation W_{dis} always increases as the number of cycles increase. Whereas, elastic strain energy density, plastic-free energy density, total input work density and plastic work oscillates (increase and decrease) during cyclic shearing. Also it must be noted that the different energy density components add up-to the input work W_{input}.

Figure 4.17 and Figure 4.18 plots the energy response for non-linear hardening shear (NLHS) model with shear stiffness $k_t = 400kPa$ and $k_t = 800kPa$ respectively. It can

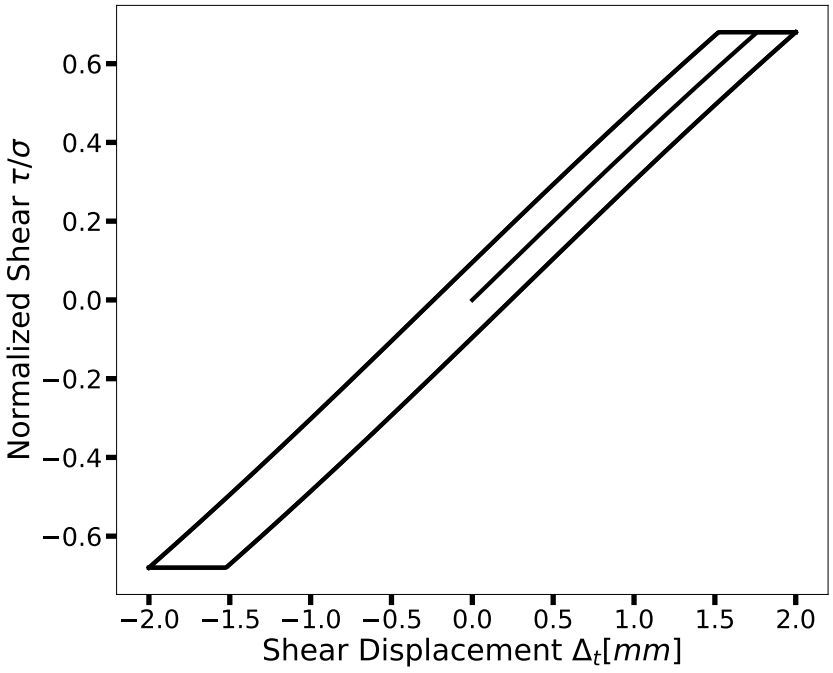

(a) Stress-Strain

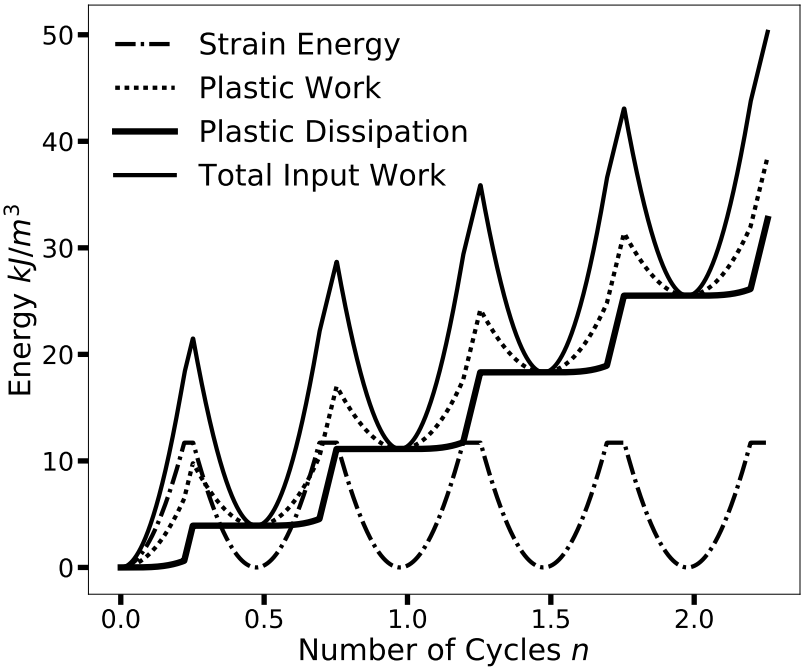

(b) Energy

Figure 4.16: Energy dissipation for EPPS model with shear stiffness $k_t = 400kPa$ and residual normalized shear stress $\mu_r = 0.68$.

be confirmed from the plots that the plastic dissipation energy density W_{dis} is always increasing while the strain and plastic work increases and decreases. It can be also noted that in this model the plastic-free energy Ψ comes in picture because of the non-linear hardening type. The plastic free energy Ψ also changes cyclically similarly to the elastic strain energy.

Figure 4.19 and Figure 4.20 plots the energy response for non-linear hardening-softening shear (NLHSS) model with shear stiffness $k_t = 800kPa$ and $k_t = 1500kPa$ respectively. The material parameters are : softening rate parameter $b = 40$, peak plateau size $n = 8$, peak normalized shear stress limit $\mu_{p0} = 0.9$, its rate of decrease parameter $k = 0.1$ and residual normalized shear stress $\mu_r = 0.68$. Figure 4.19 shows a cyclic hardening-softening interface response where the material softens in multiple cycles. Figure 4.20 presents cyclic shear response where the material reaches the residual shear strength in the first cycle. Energy plots of both the examples shows increasing dissipation and total energy balance.

The above plots shown in Figure 4.16 to 4.20 demonstrates the correctness of the energy calculation at the material level. All the models show positive incremental dissipation W_{dis}^{incr} resulting in always increasing total dissipation energy density. Also, all the energy components add up to the input work W_{input}.

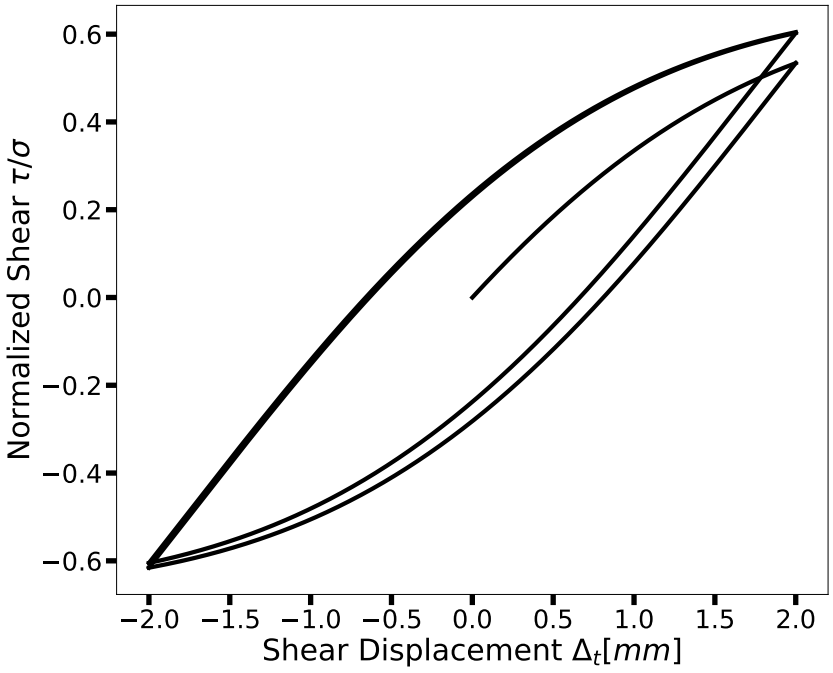

(a) Stress-Strain

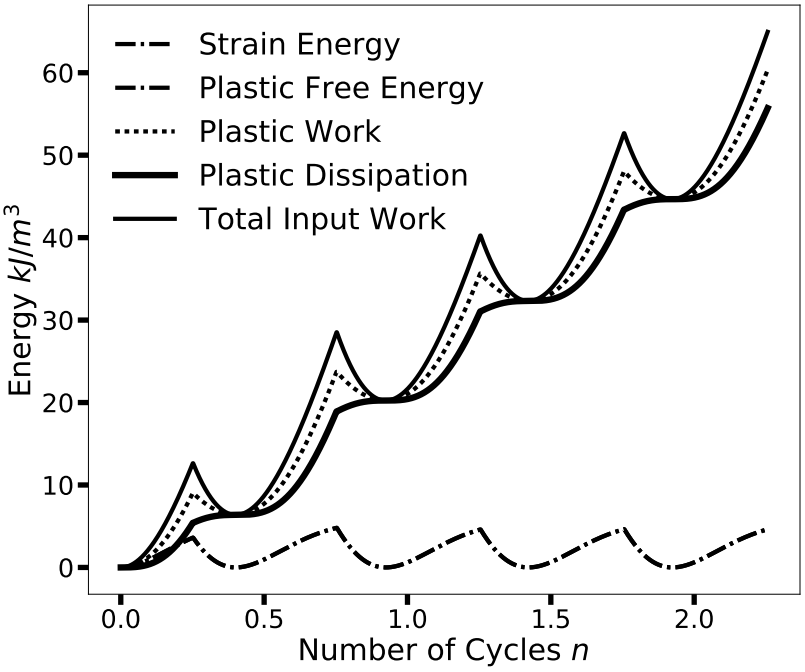

(b) Energy

Figure 4.17: Energy dissipation for NLHS model with shear stiffness $k_t = 400kPa$ and residual normalized shear stress $\mu_r = 0.68$.

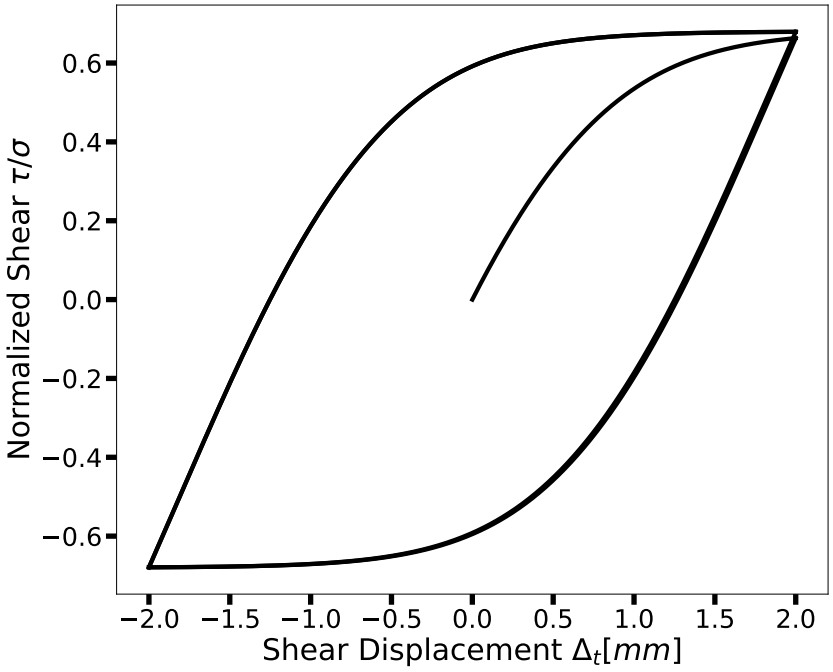

(a) Stress-Strain

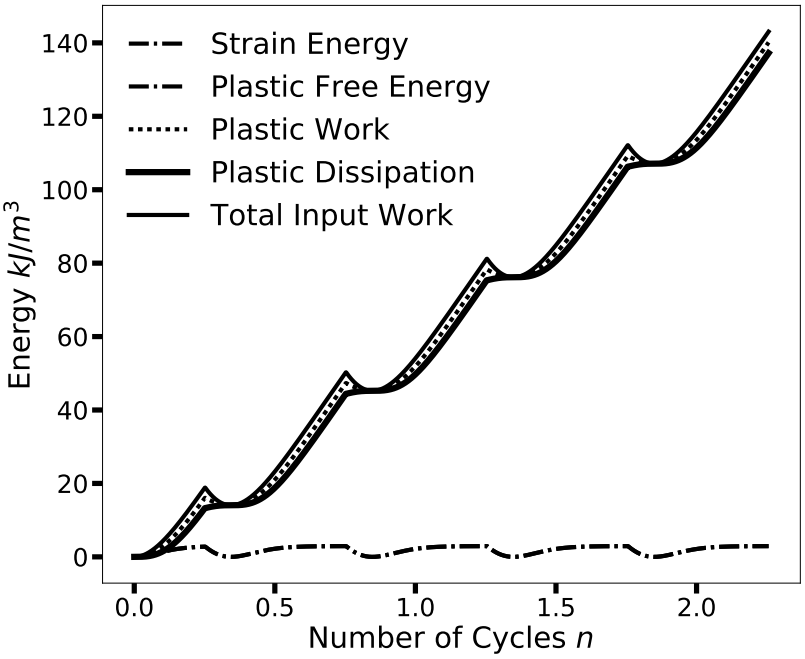

(b) Energy

Figure 4.18: Energy dissipation for NLHS model with shear stiffness $k_t = 800kPa$ and residual normalized shear stress $\mu_r = 0.68$.

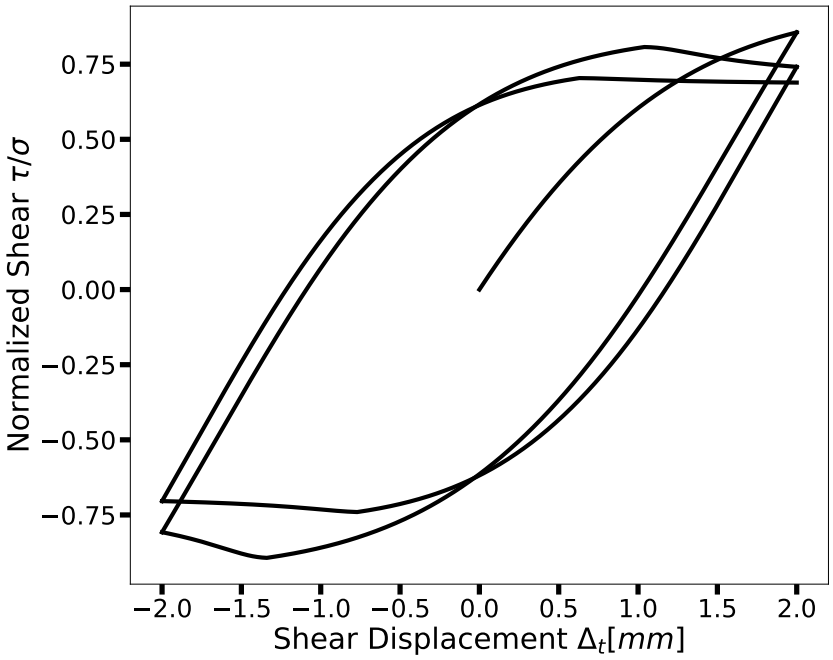

(a) Stress-Strain

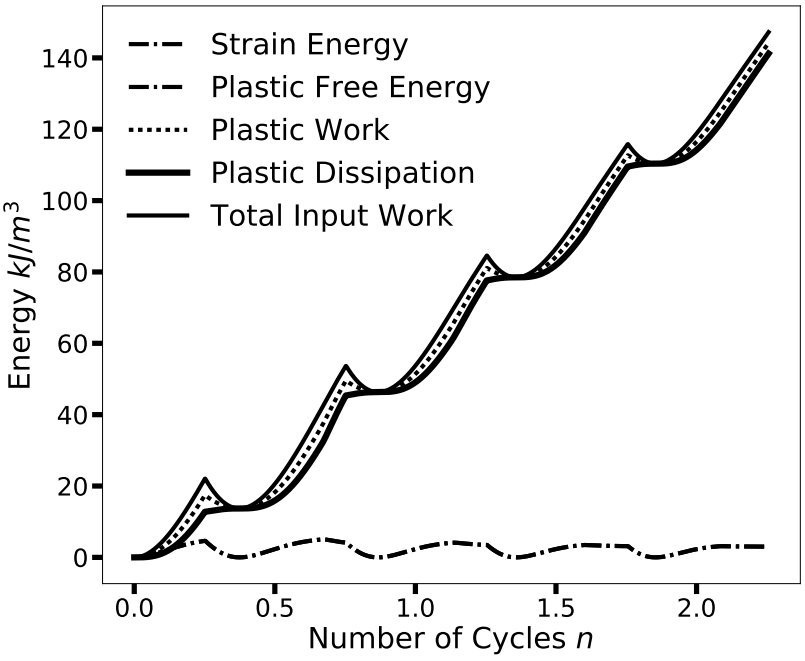

(b) Energy

Figure 4.19: Energy dissipation for NLHSS model with shear stiffness $k_t = 800$, residual normalized shear stress $\mu_r = 0.68$, softening parameter $b = 40$, peak plateau size parameter $n = 4$, peak normalized shear stress parameter $\mu_{p0} = 0.9$ and its rate of decrease parameter $k = 0.1$.

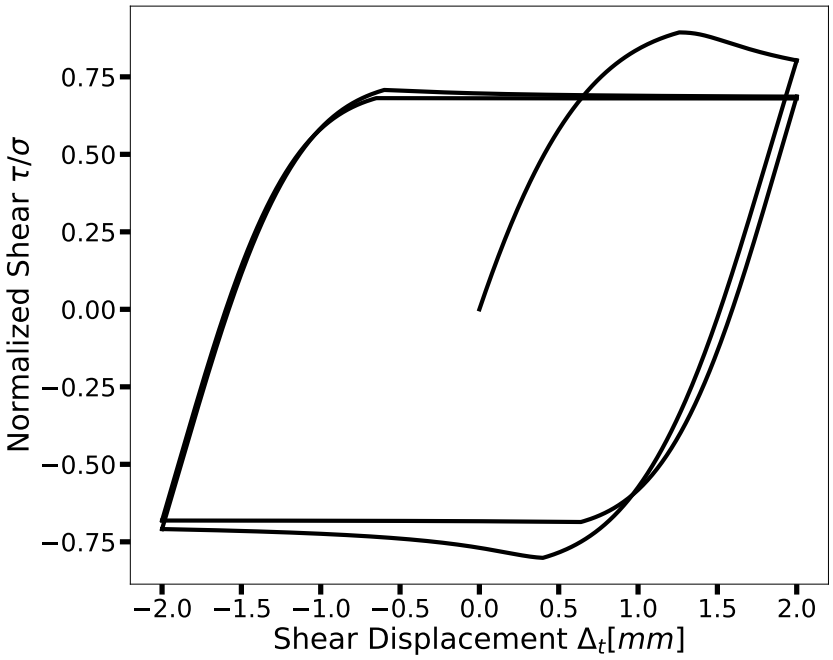

(a) Stress-Strain

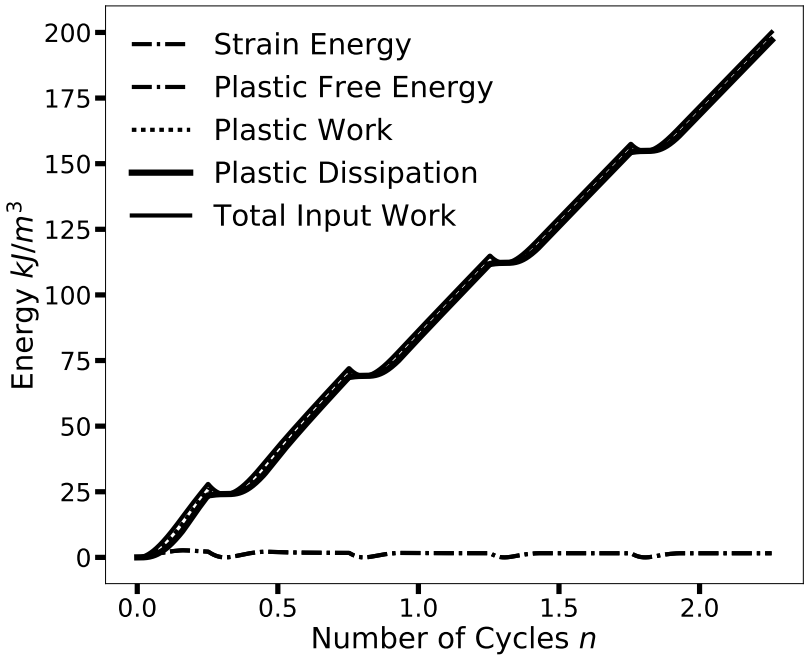

(b) Energy

Figure 4.20: Energy dissipation for NLHS model with shear stiffness $k_t = 1500kPa$, residual normalized shear stress $\mu_r = 0.68$, softening parameter $b = 40$, peak plateau size parameter $n = 4$, peak normalized shear stress parameter $\mu_{p0} = 0.9$ and rate of decrease of peak normalized shear stress $k = 0.1$.

4.2 Static Normal Contact Verification

A Two-bar truss example is considered here to verify the normal contact for different normal loading conditions and different normal stiffness k_n. This is an example of normal loading on a 1-D contact between two bars separated by an initial gap of $\delta_{in} = 0.1m$. An illustrative diagram of the problem statement is shown below.

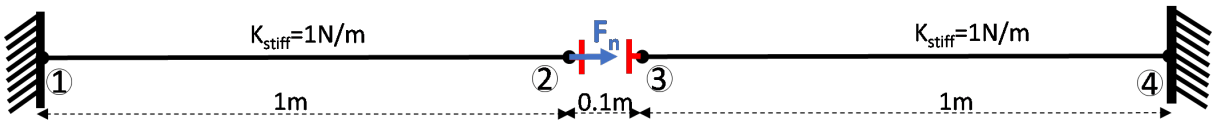

Figure 4.21: Illustration of Two Bar Normal Contact Problem under monotonic loading with initial gap

Case 1: Monotonic Loading with initial gap $\delta_{in} = 0.1m$ **-** In this case a normal force of $F_n = 0.3N$ is applied to Node 2. From Figure 4.22, it can be observed that the solution converges to the analytical result for $k_n = 100N/m$ i.e 100 times the stiffness of bar element. It also plots the solution for higher normal stiffness. Please note that, for very high normal stiffness $k_n > 10e^{15}$, the convergence fails (when the contact status of bars changes), as the global stiffness matrix becomes *ill-conditioned*. Thus, the normal penalty stiffness k_n cannot be too large.

With the application of external force F_n, the initial gap δ_{in} between the two bar reduces. With more application of force F_n, the two bars come in contact and the stiffness of the system increases. Both the bars then move together.

Case 2: Monotonic Loading with no initial gap $\delta_{in} = 0m$ **-** In this case a force of $F_n = 0.3N$ is applied to Node 2 but there is no initial gap between the two bars. The two bars are initially in contact and a normal force F_n is applied. From Figure 4.23, it can be observed that the solution again converges to the analytical result for $k_n = 100N/m$ i.e 100 times the stiffness of bar element.

With no initial gap $\delta_i n$, for application of force F_n, both the bars move together having the same displacement.

Case 3: Cyclic Loading with initial gap $\delta_{in} = 0.1m$ **-** A cyclic loading case is now considered with loading force F_n applied to node 2 as shown in Figure 4.24.

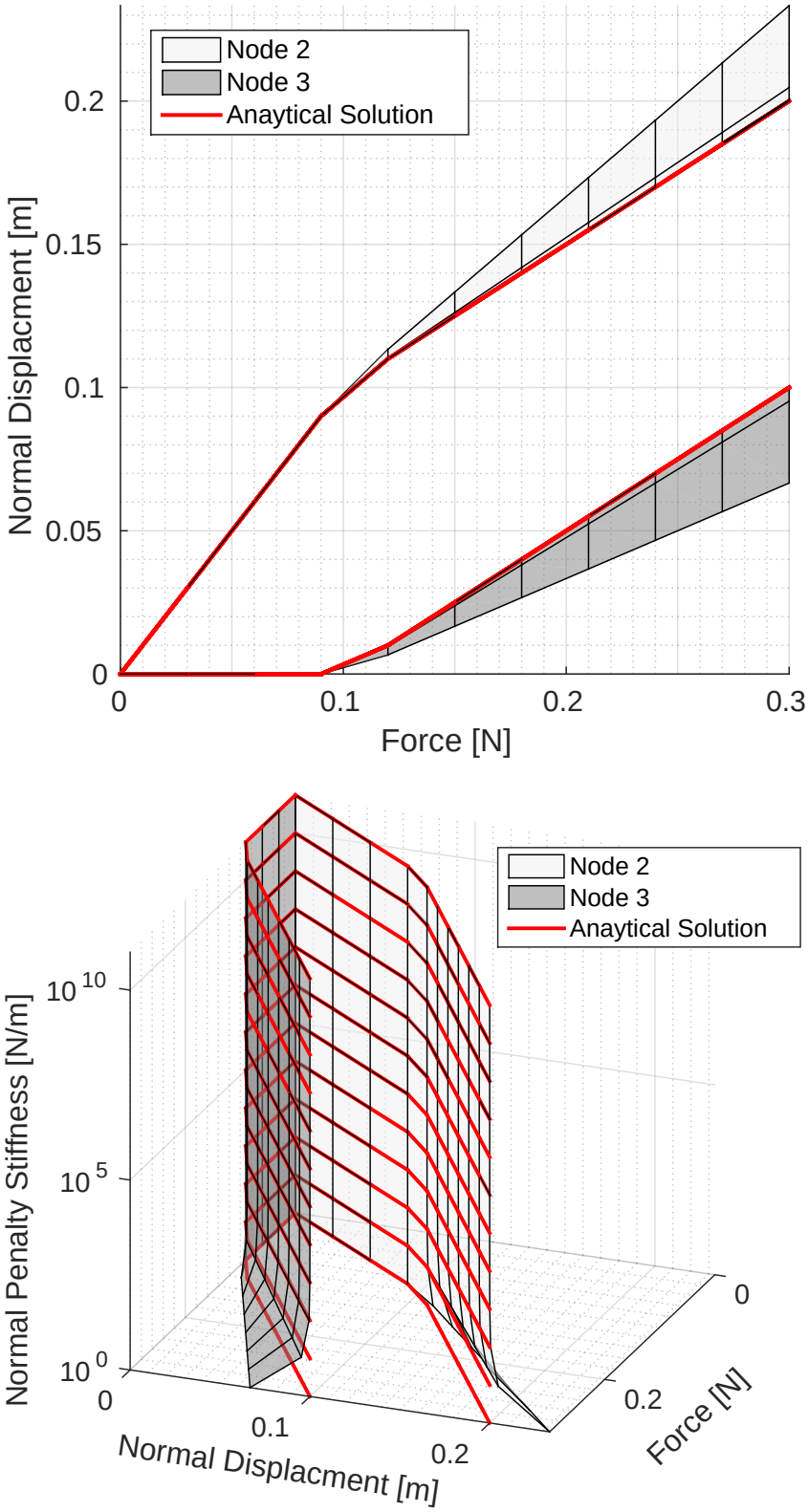

Figure 4.22: Displacements of Node 2 and Node 3 with change in normal stiffness k_n for $\delta_{in} = 0.1m$ subject to monotonic static loading.

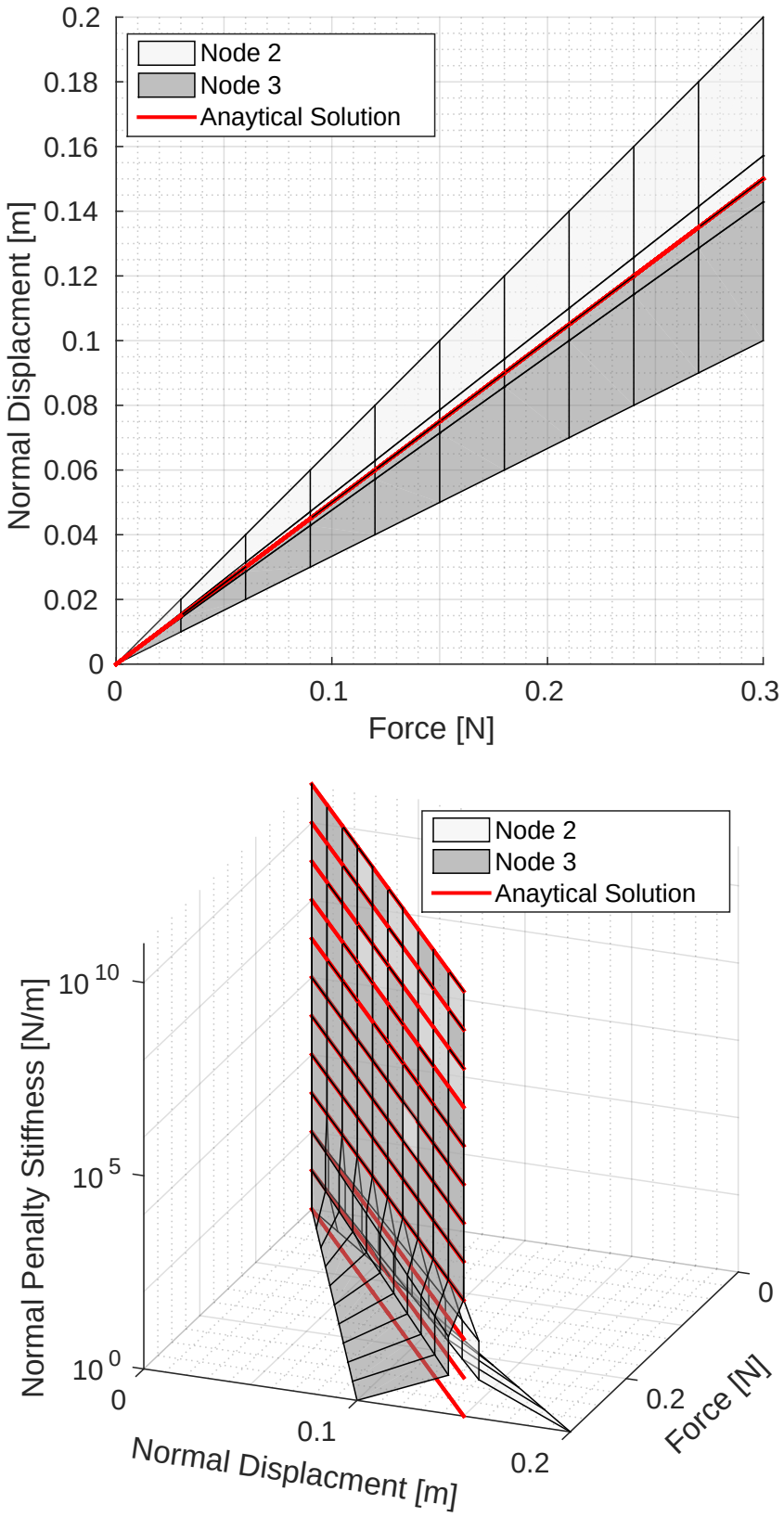

Figure 4.23: Displacements of Node 2 and Node 3 with change in normal penalty stiffness k_n for $\delta_{in} = 0m$ subject to monotonic static loading.

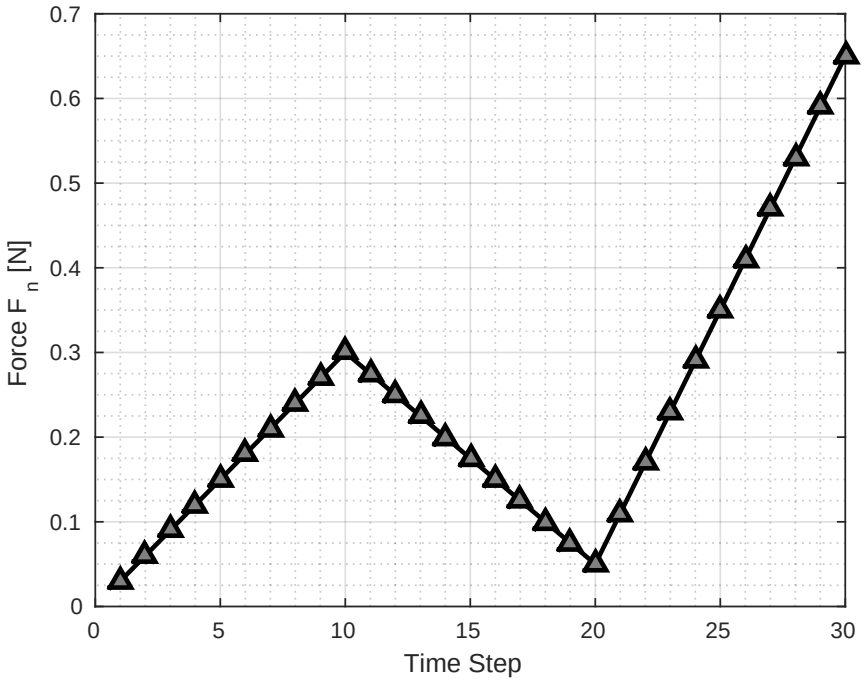

Figure 4.24: Cyclic normal load applied on Two bar Contact Problem

From Figure 4.25, it can be observed that the solution again converges to the analytical result for $k_n = 100N/m$ i.e 100 times the stiffness of bar element.

Case 4: Cyclic Loading with no initial gap $\delta_{in} = 0m$ - The same cyclic load shown in Figure 4.24 is applied again for the case with no gap. From Figure 4.26, it can be observed that the solution again converges to the analytical result for $k_n = 100N/m$ i.e 100 times the stiffness of bar element. It also converges for higher normal penalty stiffness as well.

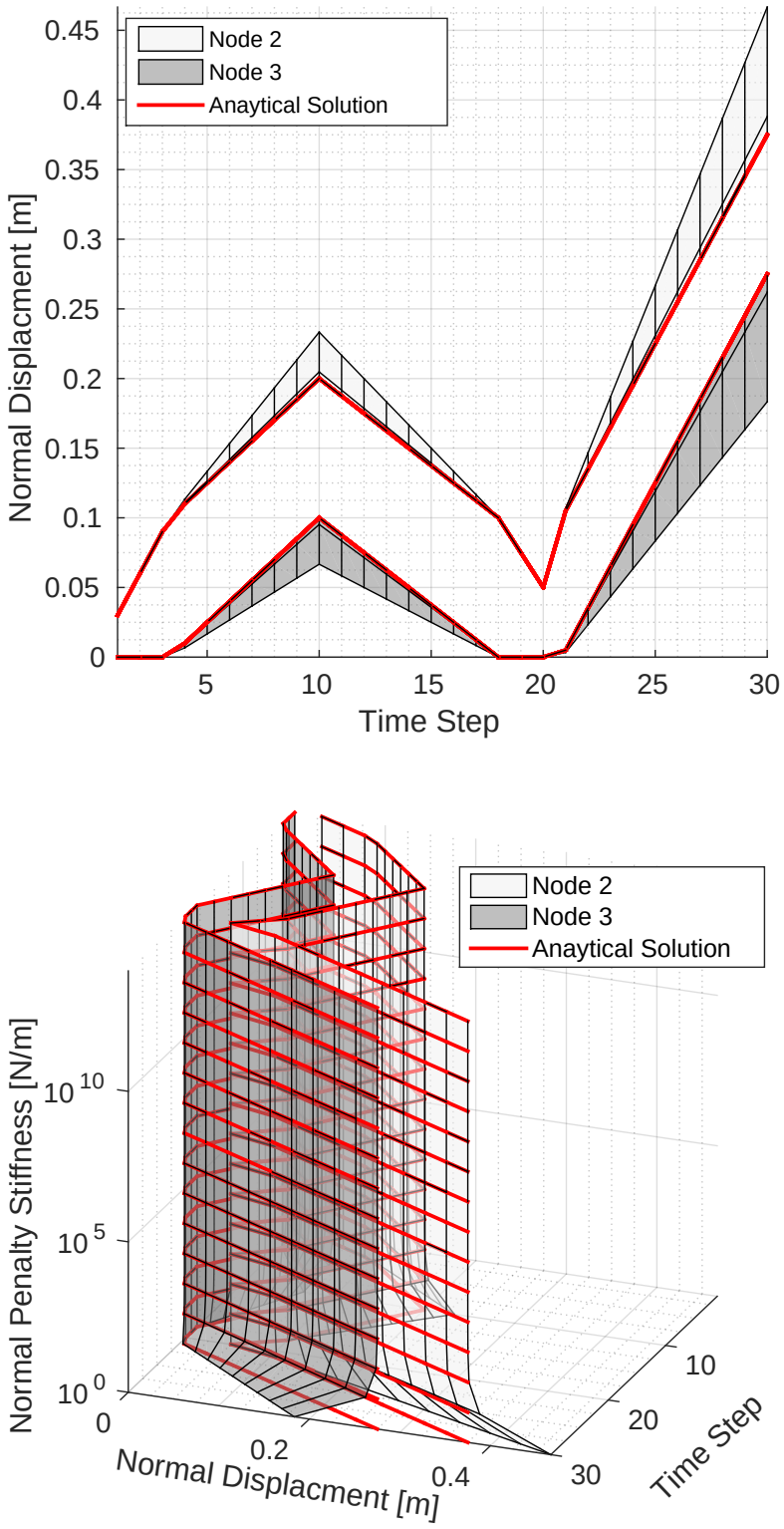

Figure 4.25: Displacements of Node 2 and Node 3 with change in normal penalty stiffness k_n for $\delta_{in} = 0.1m$ subject to cyclic monotonic loading.

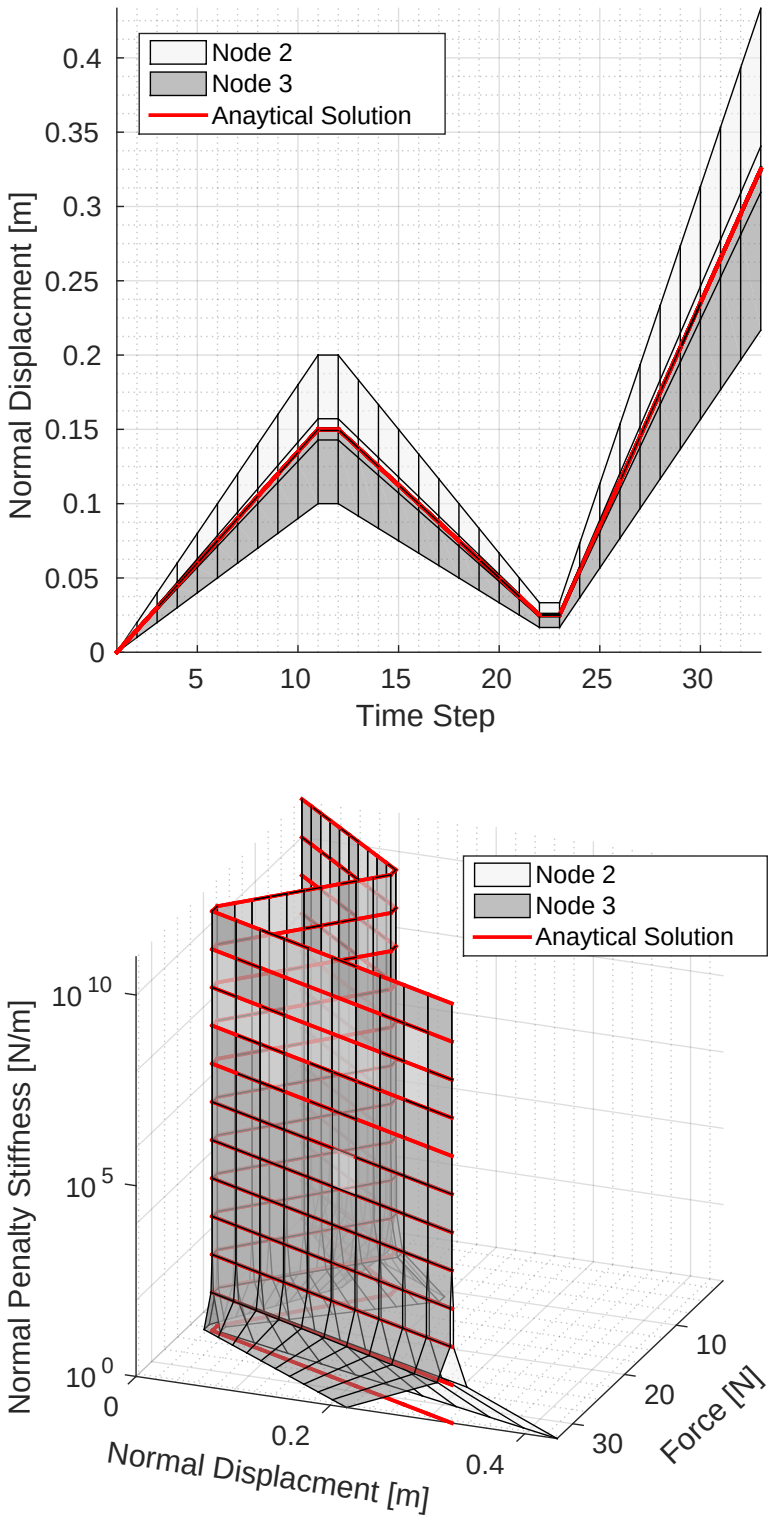

Figure 4.26: Displacements of Node 2 and Node 3 with change in normal penalty stiffness k_n for $\delta_{in} = 0m$ subject to monotonic cyclic loading.

4.3 Static Tangential Slip Verification

A simple 3-D truss example (Figure 4.27) with normal confinement of $F_n = 0.5N$ in z-direction , ultimate friction coefficient $\mu_r = 0.2$ and shear loading of magnitude $F_s = 0.5N$ is considered to verify the static tangential behavior of contact element. Figure 4.27 shows the illustration of the problem. It is used to verify the yield surface for simplified Mohr-Coulomb (EPPS) model for different loading angles with fixed normal confinement.

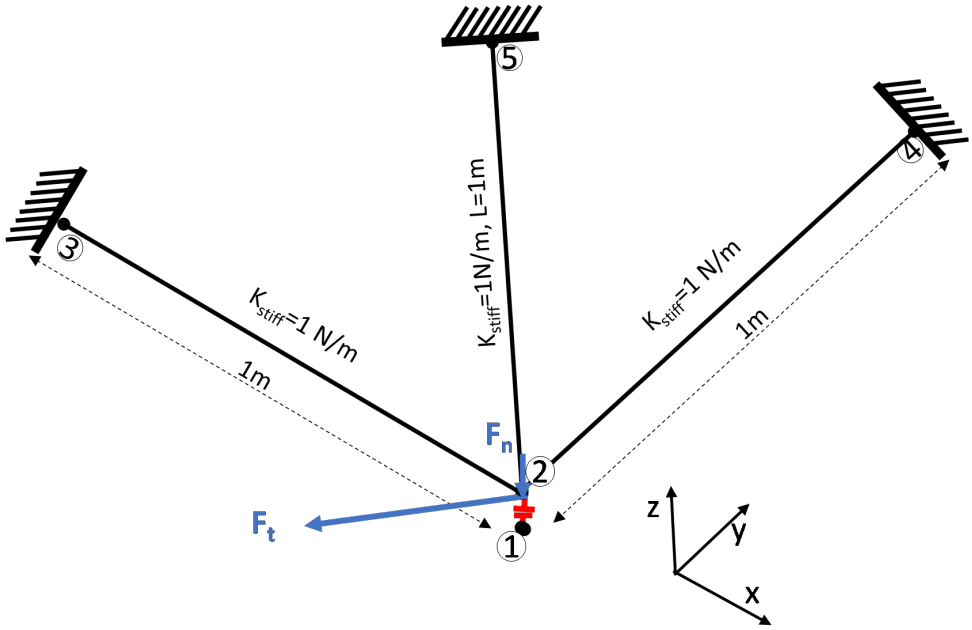

Figure 4.27: Illustration of 3-D Three Bar Contact Problem

A Shear force of magnitude of $F_t = 0.5N$ is applied in 20 steps in different loading directions on x-y plane as shown in Figure 4.27. The response of the contact element and the displacement of node 2 is shown in Figure 4.28 and Figure 4.29 respectively.

It can be observed that the contact element slips at magnitude of force $|F_t| = (F_n = 0.5) \times (\mu_r = 0.2) = 0.1N$ for all loading angles. In Figure 4.29, it can be observed that for the first 4 steps, there is no *(zero)* displacement for node 2 because of the stick case. When the load exceeds $F_t \geq 0.1N$, slip occurs and node 2 starts to undergo deformation. The conical and cylindrical surface of the frictional force respectively during the stick and slip case for all loading directions, verify the yield surface of the contact element during tangential loading.

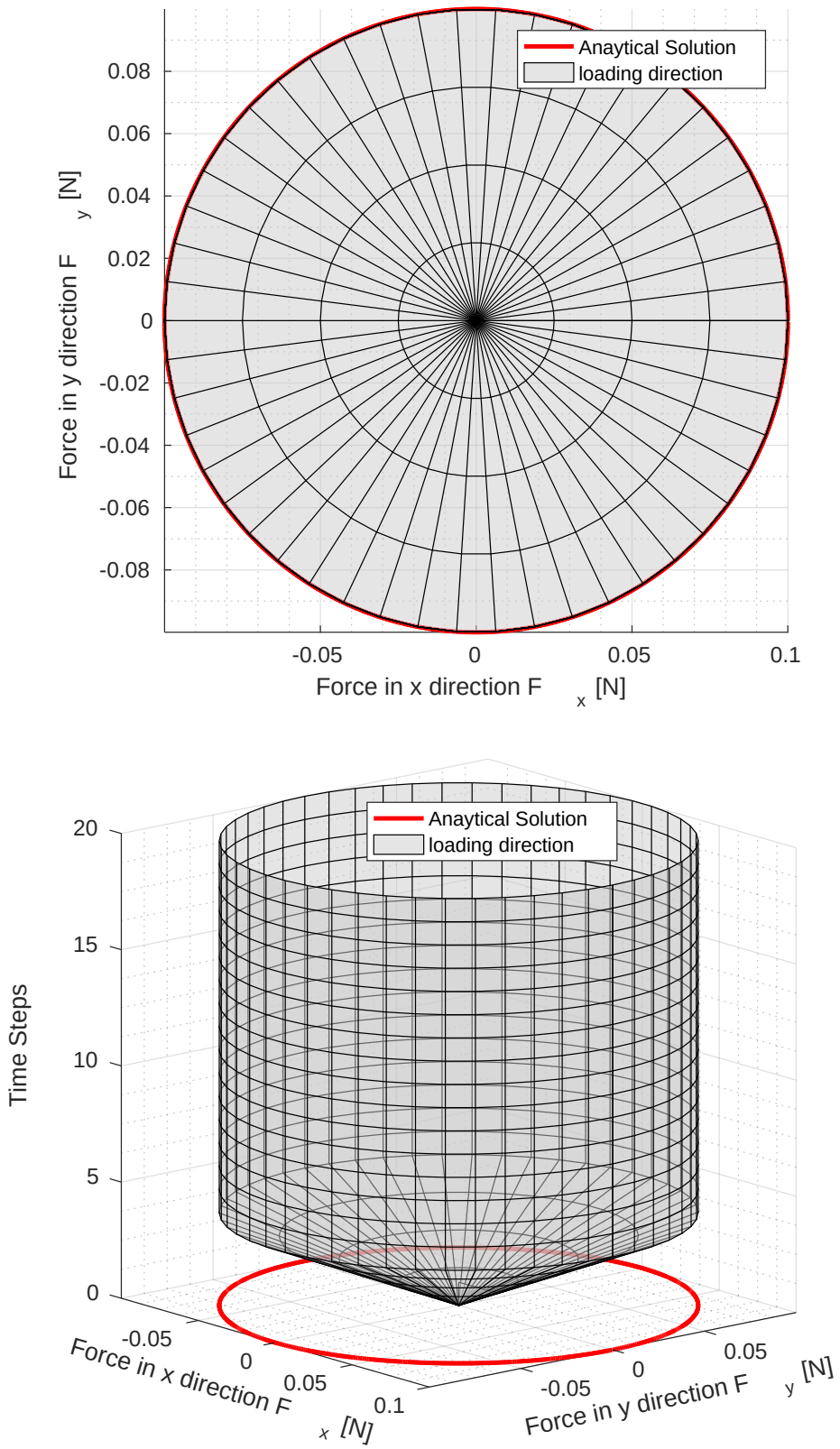

Figure 4.28: Response of the contact element for different loading angles for confinement of $F_n = 0.5N$ and coefficient of friction as $\mu = 0.2$

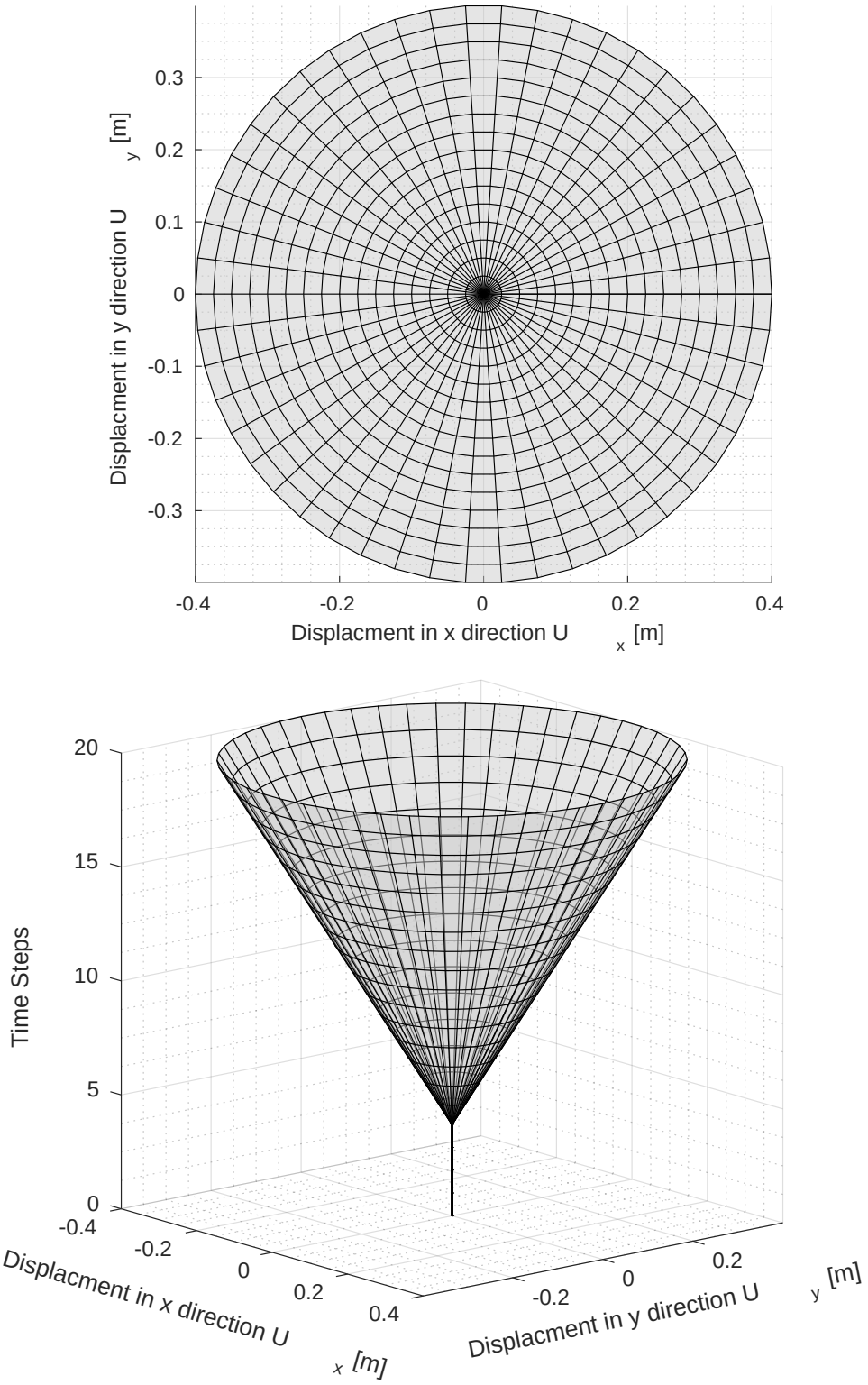

Figure 4.29: Displacement of Node 2 in x and y direction for different loading angles for confinement of $F_n = 0.5N$ and coefficient of friction as $\mu_r = 0.2$

Note : It must be noted that here only one contact pair was added in the model. In general, to model contact interface in all directions using node-to-node contact element, three contact elements needs to be defined with three independent contact normal directions.

4.4 Dynamic Normal Contact Verification

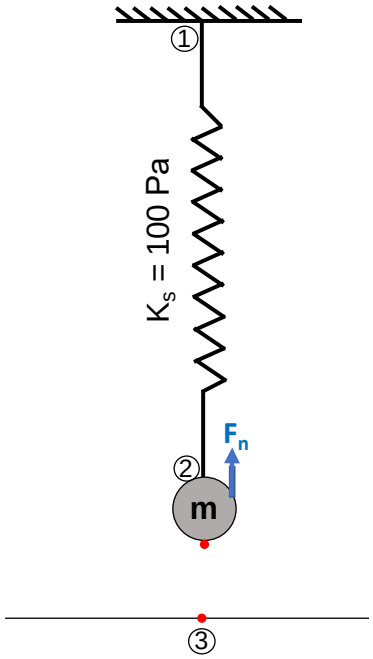

Figure 4.30: Illustration of one bar dynamics problem.

Figure 4.30 considers a dynamic response using normal contact. The problem is modeled under an impulse load of F_n without any gravity field g. Before the application of force F_n, there was no gap between node 2 and node 3 i.e. $g_n = 0$. A force $F_n = 1N$ is applied on node 2 and then removed in the next stage. The system is then left to respond to free vibration. The spring stiffness is taken as $K_s = 100Pa$ and the mass as $m = 1kg$ The cross-sectional area of the beam and contact area is taken as $1m^2$. The whole simulation was run for a total time of $t = 5s$. For all the simulations, relative convergence criteria of $1e^{-3}$ on the unbalanced forces were applied. No numerical damping was applied in simulations.

4.4.1 Dynamic Response With No Viscous Damping

In this case, no viscous damping was applied between the contact nodes. The response of node 2 with time for different contact normal stiffness k_n and different time steps Δt is shown in Figure 4.31 and Figure 4.32.

The natural frequency of the system is given by

$$\omega = \sqrt{K_s/m} \tag{4.2}$$

where $\omega = 10rad/s$ for stiffness $K_s = 100Pa$ and mass $m = 1kg$. For this case, the analytical response $u(t)$ is given as

$$u(t) = F_n/K_s|cos(\omega t)| \tag{4.3}$$

Figure 4.31 and 4.32 shows the response for smaller time steps Δt as well as for larger contact normal stiffness k_n. Since the spring stiffness is taken as $K_s = 100Pa$, the contact normal stiffness of $k_n = 1kPa$ and $k_n = 10kPa$ introduces some penetration which results in a pseudo response resulting in response with comparatively larger time period as compared to the analytical solution. It can also be seen from the plots, that as the contact normal stiffness k_n is increased, the penetration decreases and the solution gets closer to the analytical time period. However, for higher contact normal stiffness k_n, the response is not guaranteed to be close to analytical, even after achieving convergence. This can be observed for the case of normal stiffness $k_n = 100MPa$ and $\Delta t = 1e^{-3}s$. The period matches the analytical solution with very small penetrations but the displacement is completely way off. Whereas, for $\Delta t = 1e^{-5}s$, the response matches the analytical solution.

In dynamic analysis, since explicit integration is used, time step Δt becomes an important factor. A smaller time step Δt would give more accurate results. From Figure 4.32, it can be seen that for larger contact normal stiffness $k_n \geq 10kPa$, smaller time steps are required to get close to the analytical solution. For the normal stiffness $k_n = 100MPa$, a smaller time step of $\Delta t = 1e^{-5}s$ is required to get the response close to the analytical solution.

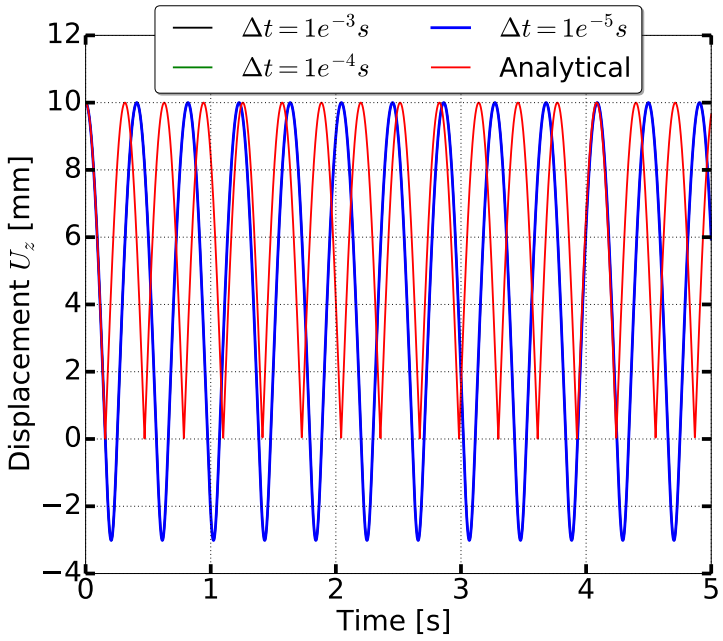

(a) $k_n = 1kPa$

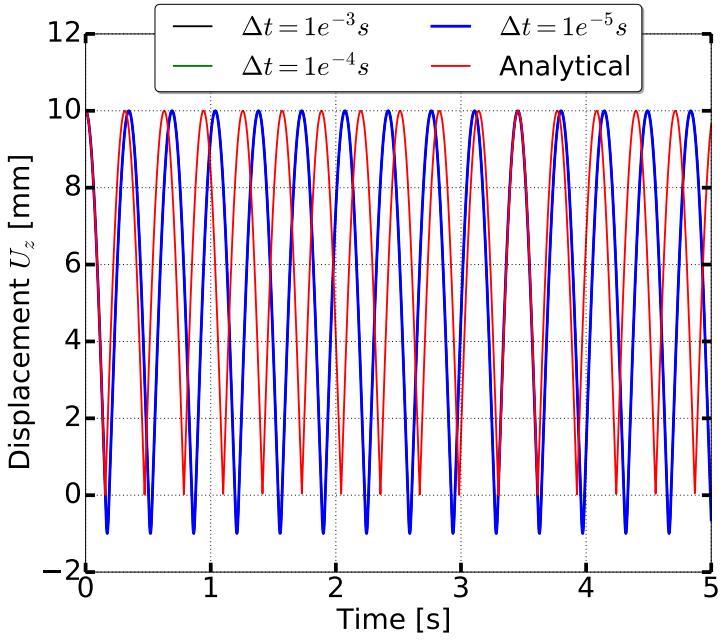

(b) $k_n = 10kPa$

Figure 4.31: Comparison of node 2 response with contact normal stiffness $k_n = 1Pa$ and $k_n = 10kPa$ for different time steps Δt to the analytical solution with no numerical and viscous damping.

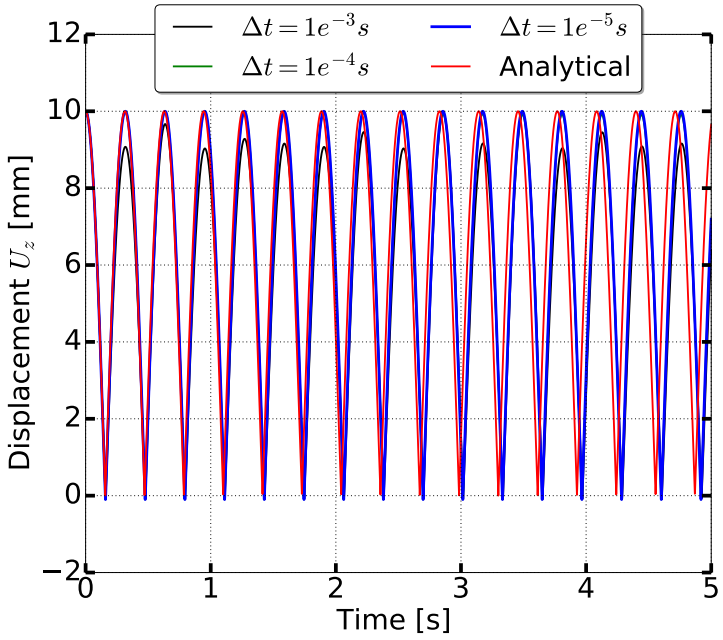

(a) $k_n = 1MPa$

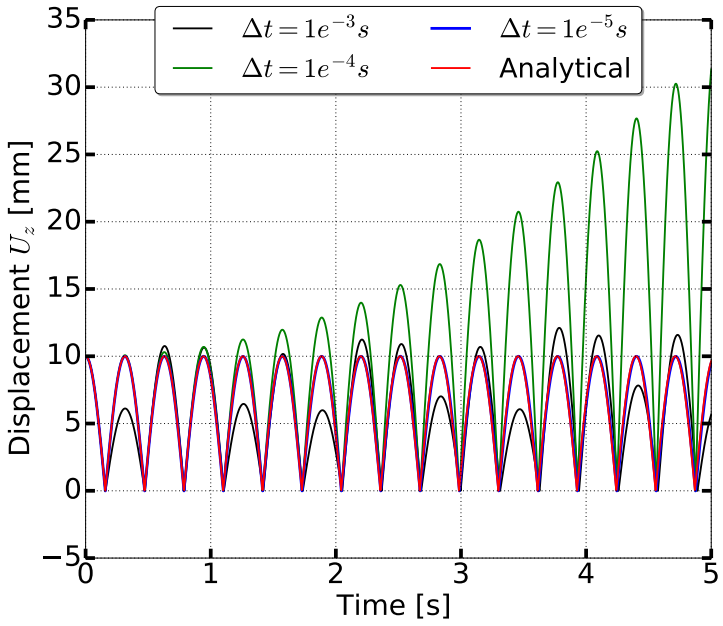

(b) $k_n = 100MPa$

Figure 4.32: Comparison of node 2 response with contact normal stiffness $k_n = 1MPa$ and $k_n = 100MPa$ for different time steps Δt to the analytical solution with no numerical and viscous damping.

In short, for having small penetration in dynamic analysis, the contact normal stiffness should be at least three orders larger than the stiffness of bodies in contact and simultaneously, the time steps Δt should also be small enough. The time step Δt should also follow the minimum requirement as noted by [Jeremić et al., 2009] for mesh size and shear wave velocity V_s.

The analytical response $u(t)$ for this problem in shown in Equation 4.3 Assuming a normal penalty stiffness as k_n and time step as Δt, the incremental displacement is given as

$$\Delta u(t)) = F_n/K_s|sin(\omega t)|\omega\Delta t \tag{4.4}$$

$$|\Delta u(t)|_{max} = F_n/K_s\omega\Delta t \tag{4.5}$$

Using Equation 4.5, the incremental maximum contact normal stiffness can be written as

$$\Delta F^{max}_{penalty} = (k_n/K_s)F_n\omega\Delta t \tag{4.6}$$

$$\Delta F^{max}_{penalty} = O(p)O(f)O(t)\omega \approx O(p)O(f)O(t)O(1) \tag{4.7}$$

$$\Delta F^{max}_{penalty} = O(p+f+t+1) \tag{4.8}$$

where $O(p)$ is the order of the ratio of contact normal stiffness to the minimum of the stiffness of bodies in contact, $O(f)$ is the order of external applied force and $O(t)$ is the order of the incremental time step Δt. In the above equation, the order of ω is assumed to be 1. In dynamic analysis, displacement, acceleration, and velocity for the next step are predicted using explicit integration rules (like Newmark, Central Difference .. etc.). Thus, to get the simulation response close to the analytical solution, the sum of the orders $p+f+t+1$ as shown in Equation 4.8 should be close to the order of applied force F_n. Although in finite element method, since iterations are performed to get to the converged solution, the sum of orders $p+f+t+1$ could be relaxed to be few orders q (2-3) higher than F_n. Thus, Equation 4.8 can be re-written to define the relationship between penalty stiffness k_n and time step Δt as

$$p+f+t+1 \leq f+q \tag{4.9}$$

$$p+t+1 \leq q \tag{4.10}$$

where q is the difference in order of magnitude of penalty force with the external force. As noted above, the unbalanced force is preferred to be of the same order $q = 0$ to the external force but can be taken as $q \leq 2$. Similarly, penalty stiffness k_n should be chosen depending upon the resolution and minimum penetration requirement of the solution.

For small allowable penetration of $1mm$ between the bodies in contact, the order of p can be taken as 3. Restricting the penetration to even very small values would increase the order of p. In the considered problem, it can be observed that the penalty stiffness $k_n = 1MPa$ of order $p = 4$ is apt to obtain response close to the analytical solution. Thus according to Equation 4.10, order of time step required for $p = 4$ would be $t \leq q-5$ i.e. for $q = 1or2$ the time step required would be $\Delta t \leq O(-3)$. Similarly, for $k_n = 100MPa$ the order p is $O(6)$. Thus, the time step required for simulation results close to the analytical solution would be $\Delta t \leq -5$ for $q = 2$. The above results demonstrate that for different penalty stiffness k_n, the time requirement Δt predicted for $q = 2$, gave close results to the analytical solution. Thus, the Equation 4.10 could be re-written as

$$p + t \leq 1 \tag{4.11}$$

$$\Delta t \leq O(1 - p) \quad for \quad q = 2 \tag{4.12}$$

The above Equation 4.12 can be used to decide time step of the simulation. If $q = 0$, then the time step Δt requirement decreases by order 2.

$$p + t \leq -1 \tag{4.13}$$

$$\Delta t \leq O(-1 - p) \quad for \quad q = 0 \tag{4.14}$$

Section 4.12.1 describes how to chose a correct normal penalty stiffness. The time step Δt evaluation for soft contact is described below.

The normal force function of hard contact can be thought as a linear elastic material whereas the soft contact as a non-linear elastic material. Which means that as the penetration Δ_n increases, for the soft contact the incremental resisting force increases

exponentially in comparison to be constant for the hard contact .

$$Hard \quad Contact :: \delta F_n = k_n \delta \Delta_n \tag{4.15}$$

$$Soft \quad Contact :: \delta F_n = k_i exp(-S_r \Delta_n)(1 - S_r \Delta_n)\delta \Delta_n \tag{4.16}$$

The above Equation 4.16 shows that with an increase in penetration, the incremental penalty normal force for soft contact is much higher than its previous step. Whereas it remains the same for hard contact. Thus, for the soft contact, the minimum time step Δt requirement established in Section 4.4, should be applied on maximum penalty stiffness k_n^{max}. Equation 4.16 also confirms that for same penetration $\delta \Delta_n$, the rebounding force in soft contact is higher.

It must be noted that the discussion made above depends upon the values chosen for k_i, k_n, S_r and k_n^{max}. For soft contact, it would be recommended to choose k_n^{max} same to the hard contact penalty stiffness k_n, in order to make the time requirement of simulation Δt same for both the contact elements. However, in this case, for the soft contact, the incremental penetration force δF_n as shown in Equation 4.16 would become comparatively much smaller than hard contact unless $k_n = k_n^{max}$, resulting in comparatively higher convergence rate with some small permissible penetration Δ_n. Later in this thesis, Section 4.12 talks about how to pick stiffness and tackle associated convergence problems.

The same problem as illustrated in Figure 4.30 is now modeled with soft contact. Here the effect of soft contact parameters k_i and S_r would be studied and verified. Maximum penalty stiffness k_n^{max} as shown earlier directly does not affect the response unless $k_n \geq k_n^{max}$. Thus, for all the simulations below, k_n^{max} is chosen sufficiently large as $k_n^{max} = 1GPa$. For reference, the parameters are taken as, the initial penalty stiffness $k_i = 100Pa$, stiffening parameter $S_r = 100$ and maximum penalty stiffness $k_n^{max} = 1GPa$. It has already been seen that as the time step Δt is made smaller, the solution obtained becomes closer to the analytical. Thus, for verification purpose two time steps of $\Delta t = 1e^{-3}s$ and $\Delta t = 1e^{-5}s$ is considered.

The response of node 2 with time for different initial normal penalty stiffness k_i, stiffening rate S_r and time steps Δt is shown in Figure 4.33 to 4.36.

From Figure 4.33 and 4.34, it can be observed that as the initial normal stiffness rate

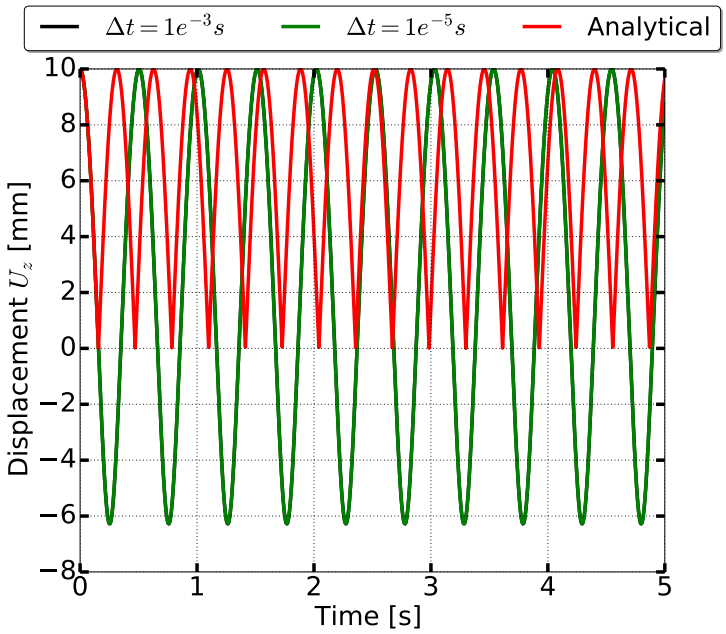

(a) $k_i = 100Pa$

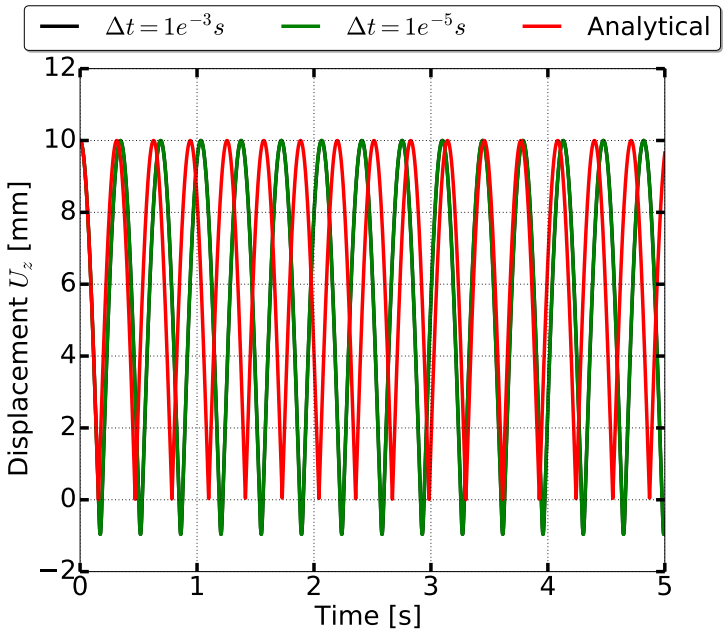

(b) $k_i = 10kPa$

Figure 4.33: Comparison of node 2 response with initial penalty stiffness $k_i = 100Pa$ and $k_i = 10kPa$, maximum normal stiffness of $k_n^{max} = 1GPa$ and stiffening rate of $S_r = 100$ for different time steps Δt to the analytical solution with no numerical and viscous damping

.

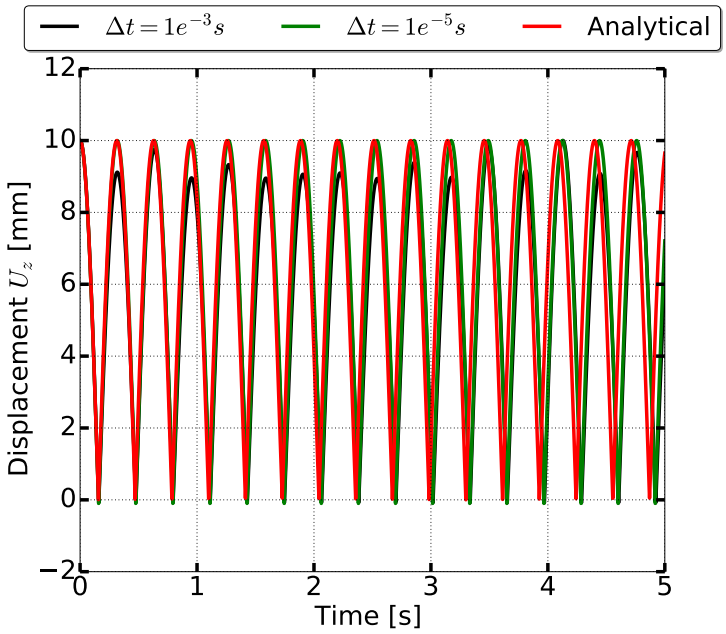

(a) $k_i = 1MPa$

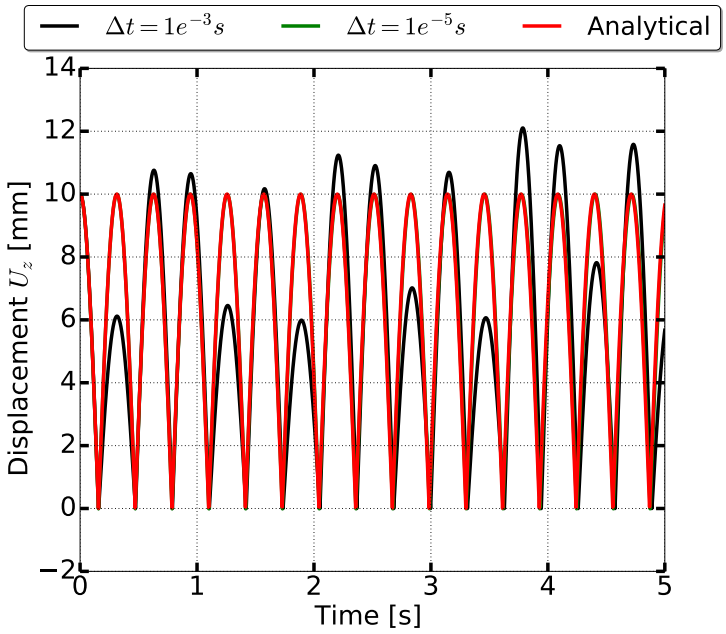

(b) $k_i = 100MPa$

Figure 4.34: Comparison of node 2 response with initial penalty stiffness $k_i = 1MPa$ and $k_i = 100MPa$, maximum normal stiffness of $k_n^{max} = 1GPa$ and stiffening rate of $S_r = 100$ for different time steps Δt to the analytical solution with no numerical and viscous damping

.

S_r is increased, the contact behaves as the hard contact. With higher initial stiffness k_i, smaller time step Δt is needed.

From Figure 4.35 and 4.36, it can be observed that as the stiffening rate S_r increases, the contact stiffness k_n becomes more of hard type with increase in penetration Δ_n. Smaller time steps are again needed to make the solution close to analytical solution for larger stiffening rate S_r.

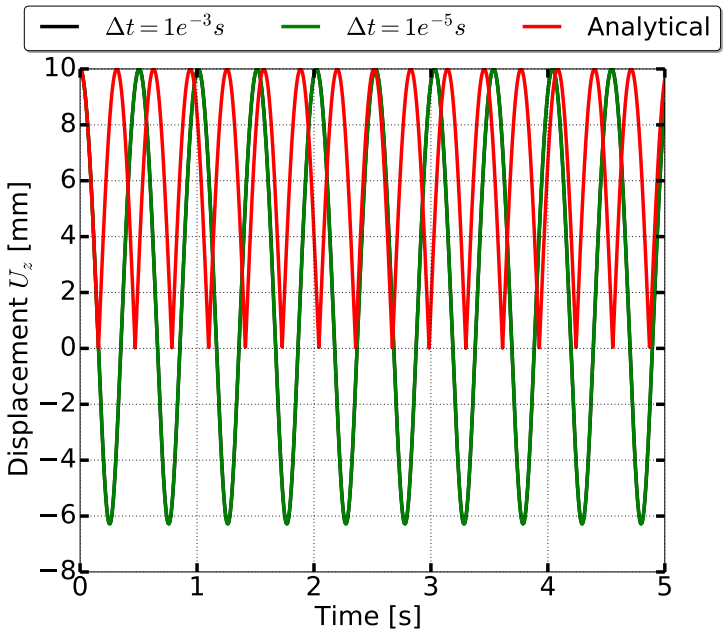

(a) $S_r = 1e^2$

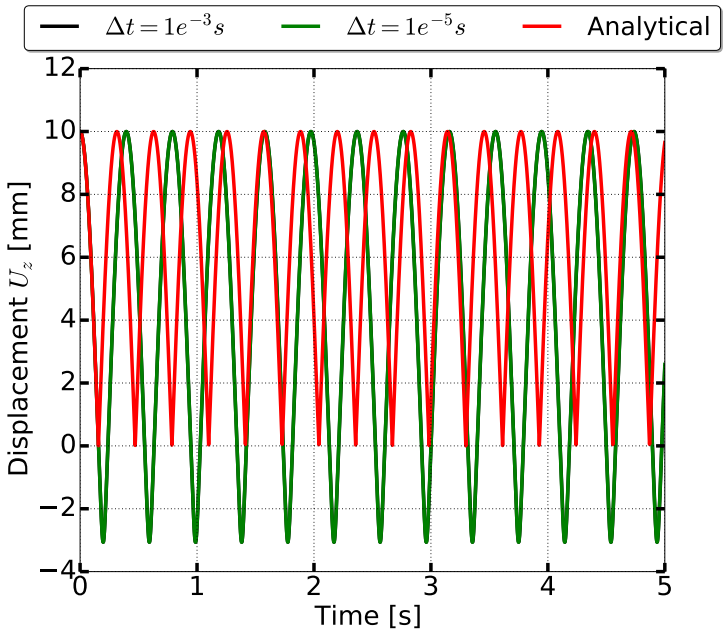

(b) $S_r = 1e^3$

Figure 4.35: Comparison of node 2 response with stiffening rate of $S_r = 1e^2$ and $S_r = 1e^3$, initial normal stiffness of $k_i = 100Pa$, maximum normal stiffness of $k_n^{max} = 1GPa$ for different time steps Δt with analytical solution with no numerical and viscous damping

.

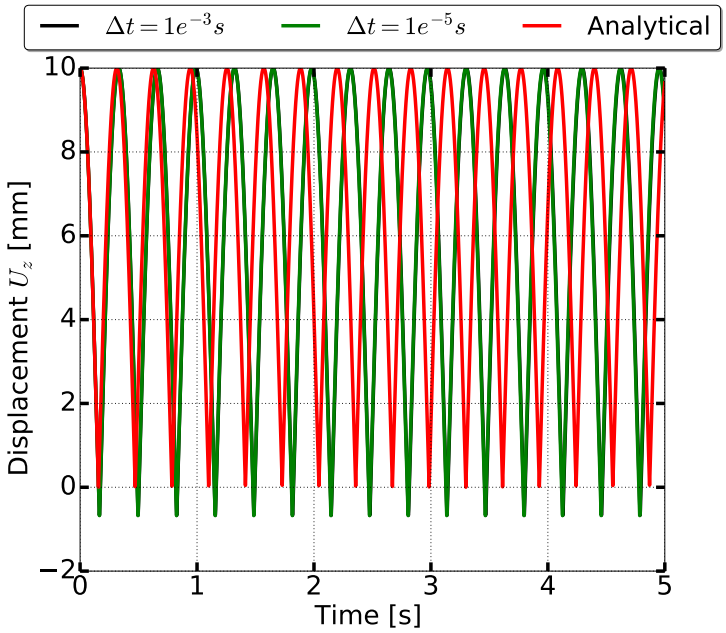

(a) $S_r = 1e^4$

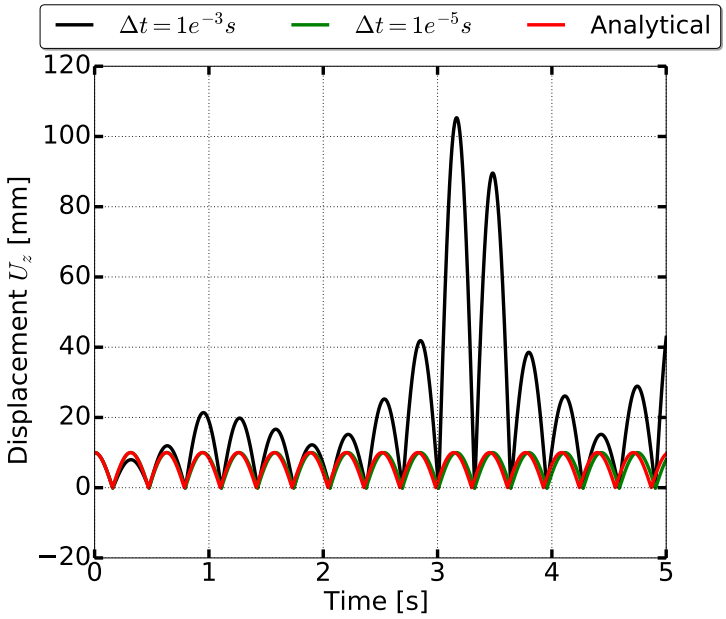

(b) $S_r = 1e^5$

Figure 4.36: Comparison of node 2 response with stiffening rate of $S_r = 1e^4$ and $S_r = 1e^5$, initial normal stiffness of $k_i = 100Pa$, maximum normal stiffness of $k_n^{max} = 1GPa$ for different time steps Δt to the analytical solution with no numerical and viscous damping

.

4.4.2 Response Under Viscous Damping

The same example shown in Figure 4.30 is now run with viscous damping c_n in contact normal direction between the contact node pairs. The analytical solution for damping c_n is given as

$$u(t)) = F_n/K_s|sin(\omega_d t)|e^{-\xi\omega t} \tag{4.17}$$

where $\xi = c_n/(2 * m * \omega)$ is the damping ratio and $\omega_d = \sqrt{1-\xi^2}\omega$ is the damped natural frequency of the system. Figure 4.37 shows the analytical response for different amount of normal damping c_n for force $F_n = 1N$, spring stiffness $K_s = 100Pa$ and mass $m = 1Kg$. As the normal damping c_n is increased, the amplitude of the response decreases with time exponentially. In Figures 4.38 to 4.43, the response shown in red color represents the analytical response. The analytical response matches for a very small time step of $\Delta t = 1e^{-5}s$.

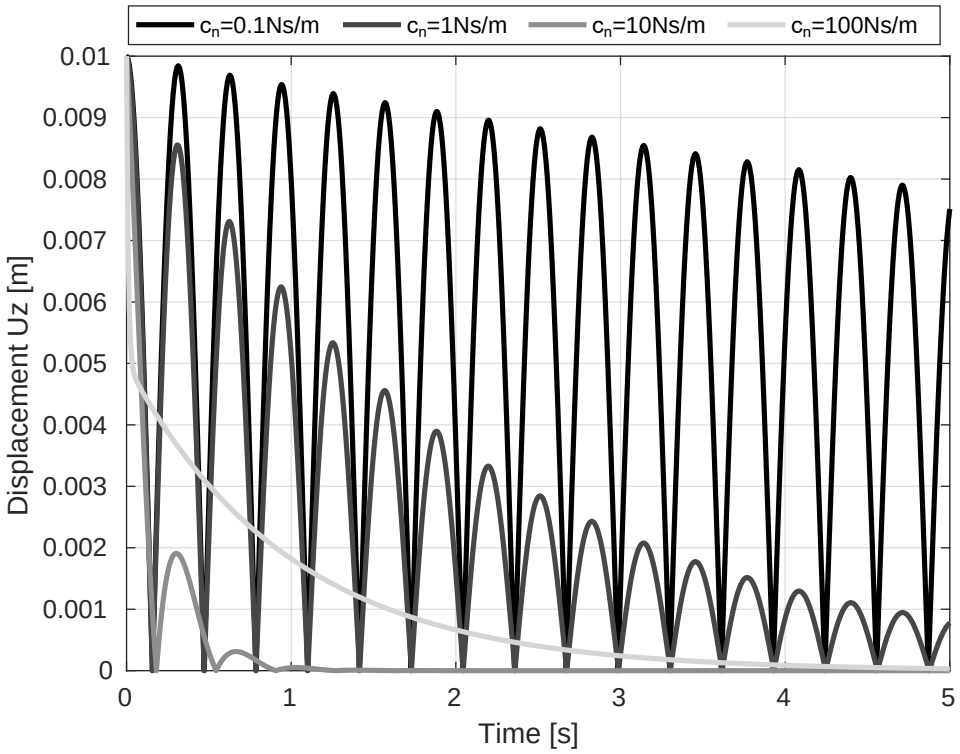

Figure 4.37: Analytical solution for damped response for different normal viscous damping $c_n = 0.1Ns/m$, $c_n = 1Ns/m$, $c_n = 10Ns/m$ and $c_n = 100Ns/m$.

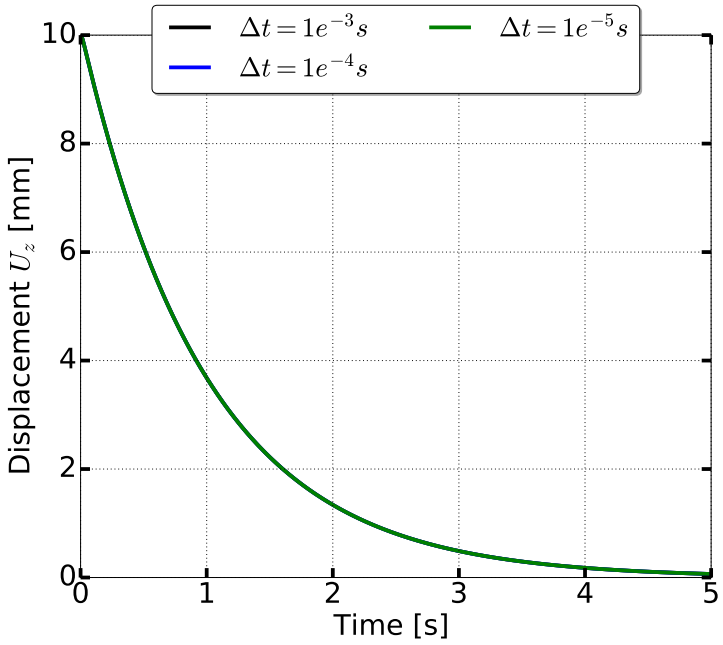

(a) $c_n = 100Ns/m$

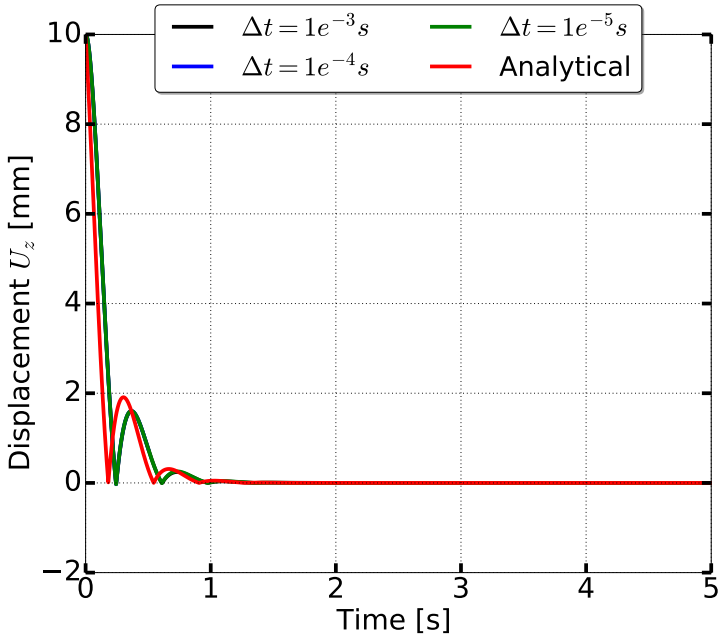

(b) $c_n = 10Ns/m$

Figure 4.38: Comparison of response of node 2 for penalty normal stiffness of $k_n = 1MPa$ for different time steps Δt and viscous damping of $c_n = 1e^2Ns/m$ and $c_n = 1e^1Ns/m$ with no numerical damping

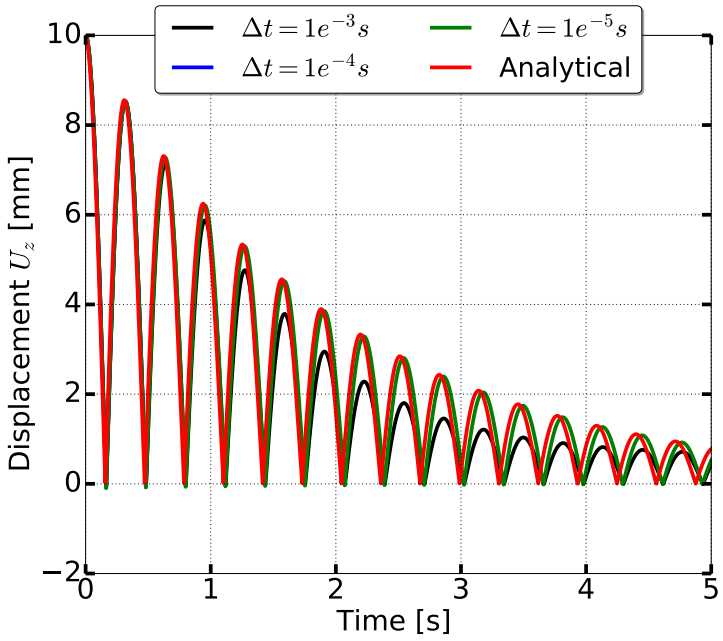

(a) $c_n = 1Ns/m$

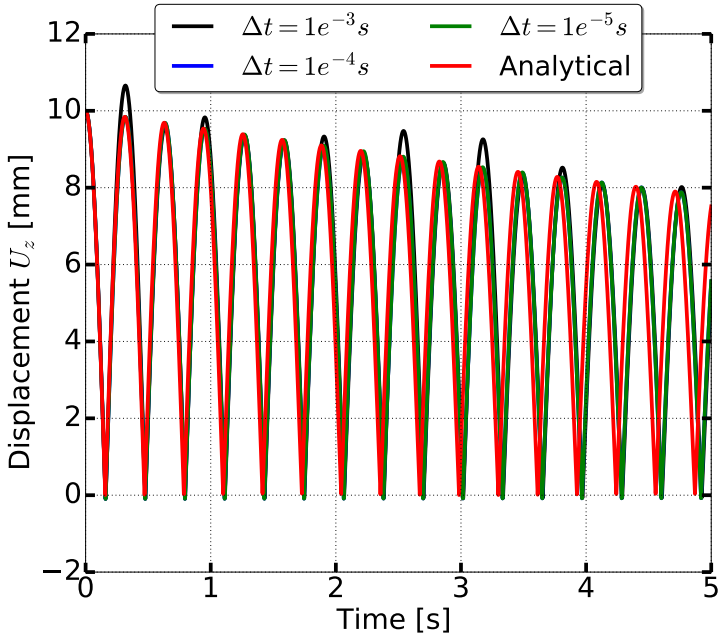

(b) $c_n = 0.1Ns/m$

Figure 4.39: Comparison of response of node 2 for penalty normal stiffness of $k_n = 1MPa$ for different time steps Δt and viscous damping of $c_n = 1Ns/m$ and $c_n = 1e^{-1}Ns/m$ with no numerical damping

Figure 4.38 and 4.40 shows the response for normal viscous damping of $c_n = 1e^{-1}Ns/m$, $c_n = 1e^{0}Ns/m$, $c_n = 1e^{1}Ns/m$ and $c_n = 1e^{2}Ns/m$ for time steps of $\Delta t = 1e^{-3}s$, $\Delta t = 1e^{-4}s$ and $\Delta t = 1e^{-5}s$. From these plots, it can be observed that viscous damped solutions comparatively does not require very small time steps Δt as compared to response with no viscous damping between contact nodes.

In Figure 4.40 for contact stiffness $k_n = 100MPa$, even time step $\Delta t = 1e^{-4}s$ also gives response close to the analytical solution. However, it could be seen that for $\Delta t = 1e^{-3}s$ the solution is way off. Thus, similar to the undamped case, the solution of dynamic simulations becomes close to the analytical solution as time steps Δt are made smaller.

The same example shown in Figure 4.30 is now run with viscous damping between the contact node pairs with soft contact. The initial normal penalty stiffness k_i and the stiffening rate S_r have been fixed to $k_i = 1kPa$ and $S_r = 1000$ respectively. Simulations are carried out for different damping stiffness c_n and time step Δt. From Figure 4.42 and 4.43 it can be observed that as the normal damping stiffness c_t increases, the response damps. For the given soft contact parameters $k_i = 10kPa$ and $S_r = 1000$, a small amount of penetration in contact could be observed. Choosing higher initial normal stiffness k_i and stiffening rate S_r would make the contact more hard, strictly enforcing the impenetrability condition ($\Delta_n = 0$). It can be also observed that because of the soft contact, the solution is comparatively stable and produces the same result for time step varying from $\Delta t = 1e^{-3}$ to $\Delta t = 1e^{-5}s$. Application of viscous damping leads to reduction of high frequency modes (response) generated due to the huge penalty rebounding forces (impenetrability constraint at interface). Thus, it is always important and practical to add a small amount of viscous damping to stabilize the numerical solution.

Note:- The response of the system for static simulations (see Figures 4.22 to 4.29), for increasing contact normal stiffness k_n always converged to the analytical solution. Whereas for dynamic simulations, the converged solution (see Figures 4.31 to 4.41), is not guaranteed to match the analytical results. This is because of the explicit integration that is assumed to integrate acceleration and velocity to displacements. What is guaranteed is that for smaller time steps Δt, the converged solution would be close to the analytical

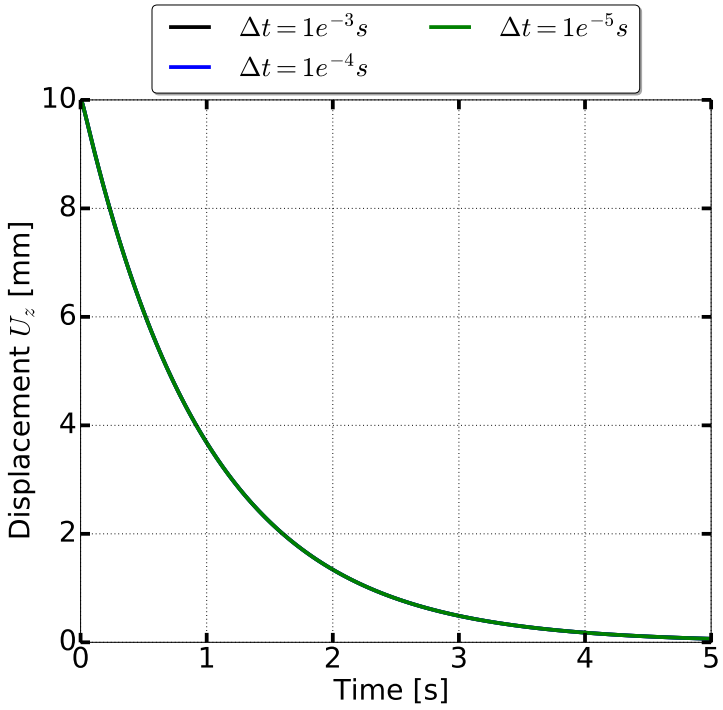

(a) $c_n = 100Ns/m$

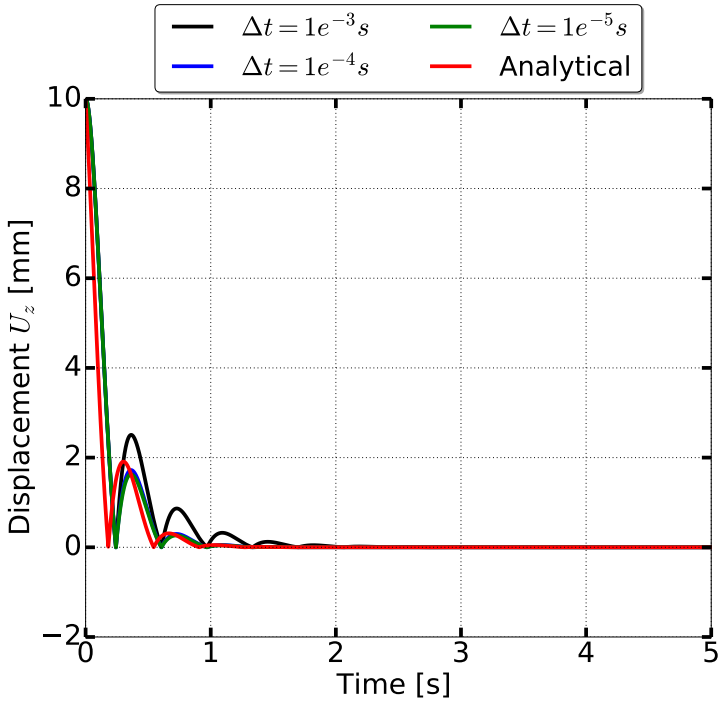

(b) $c_n = 10Ns/m$

Figure 4.40: Comparison of response of node 2 for contact normal stiffness of $k_n = 100MPa$ for different time steps Δt for different viscous damping of $c_n = 100Ns/m$ and $c_n = 10Ns/m$ with no numerical damping.

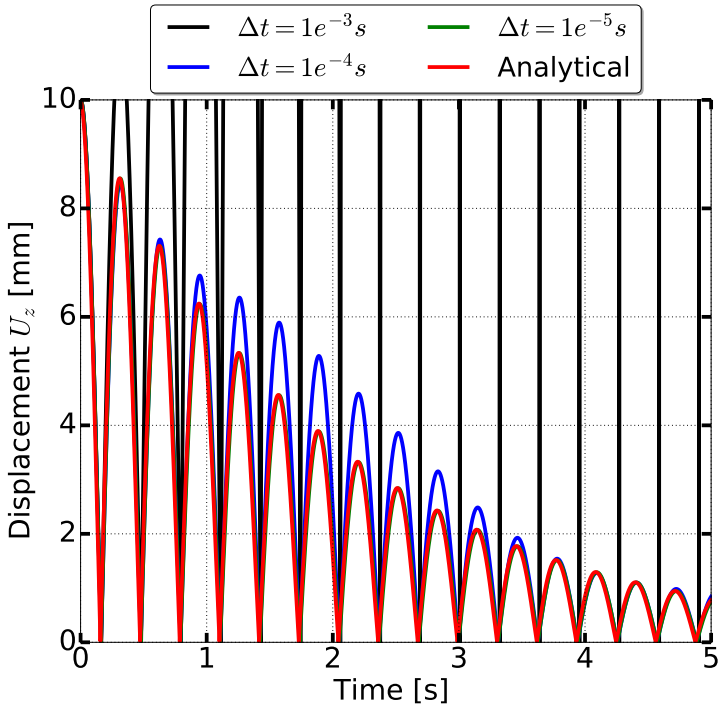

(a) $c_n = 1Ns/m$

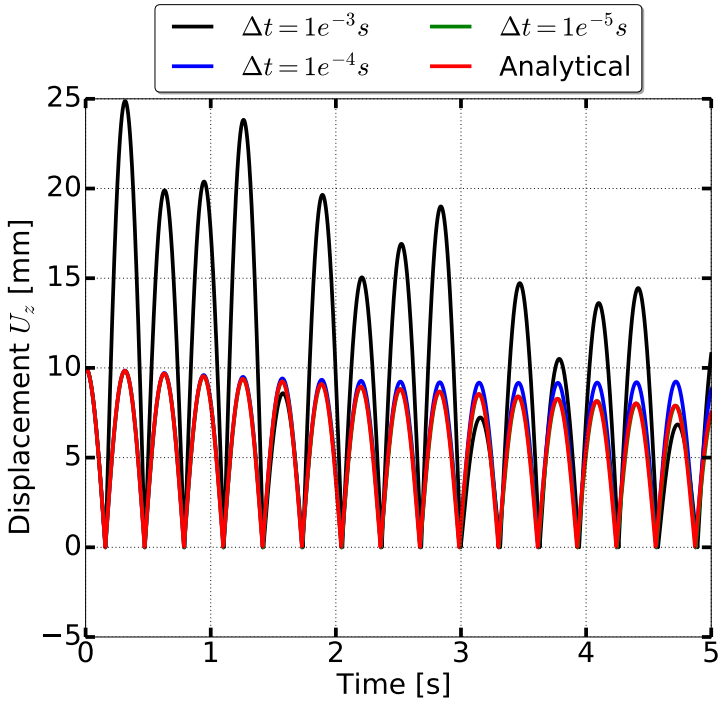

(b) $c_n = 0.1Ns/m$

Figure 4.41: Comparison of response of node 2 for contact normal stiffness of $k_n = 100MPa$ for different time steps Δt for viscous damping of $c_n = 1Ns/m$ and $c_n = 10Ns/m$ with no numerical damping.

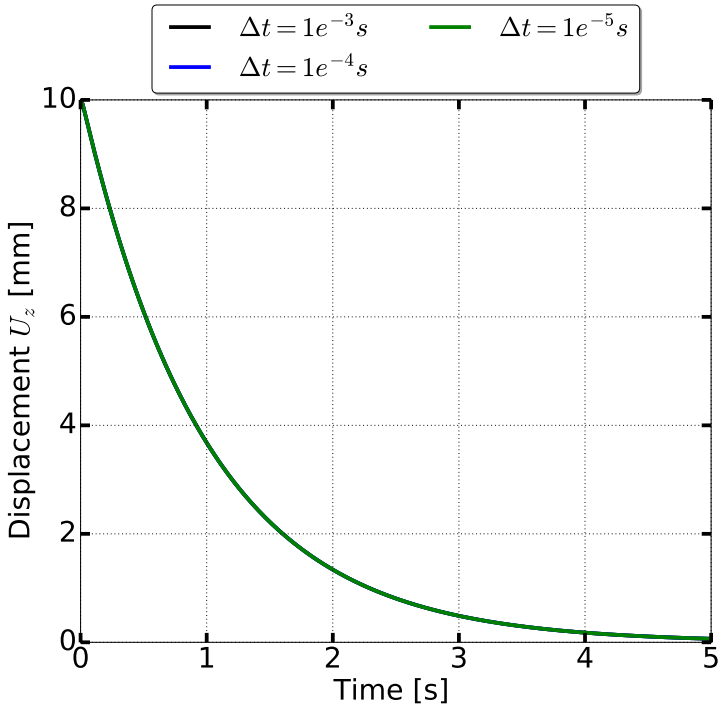

(a) $c_n = 1e^2 Ns/m$

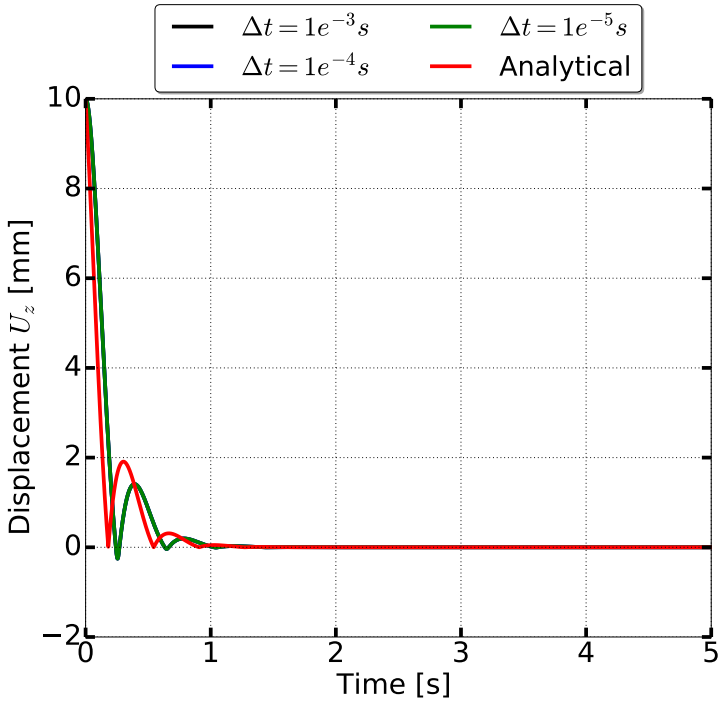

(b) $c_n = 1e^1 Ns/m$

Figure 4.42: Comparison of response of node 2 for initial normal stiffness of $k_i = 1kPa$, stiffening rate of $S_r = 1000$ and maximum normal stiffness of $k_n^{max} = 1GPa$ for different time steps Δt and viscous damping of $c_n = 100Ns/m$, $c_n = 10Ns/m$ with no numerical damping.

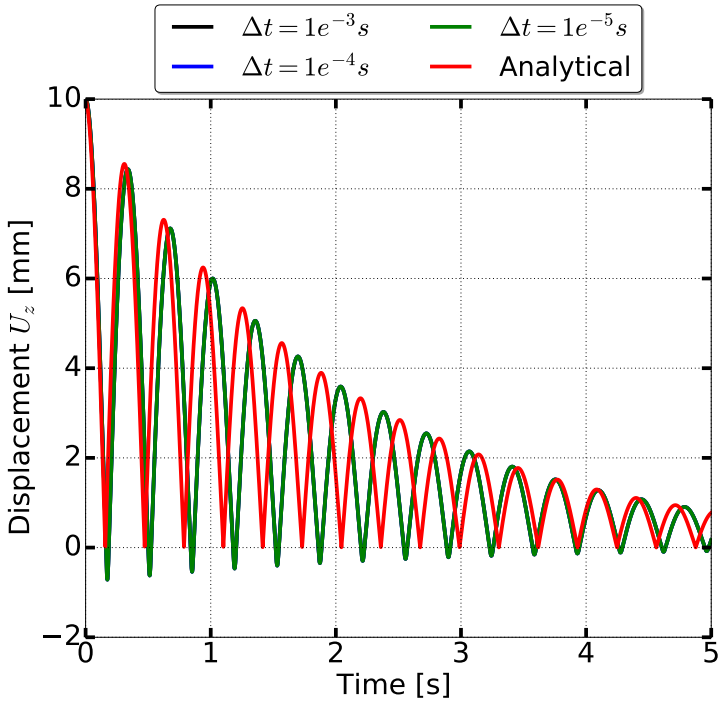

(a) $c_n = 1e^{0} Ns/m$

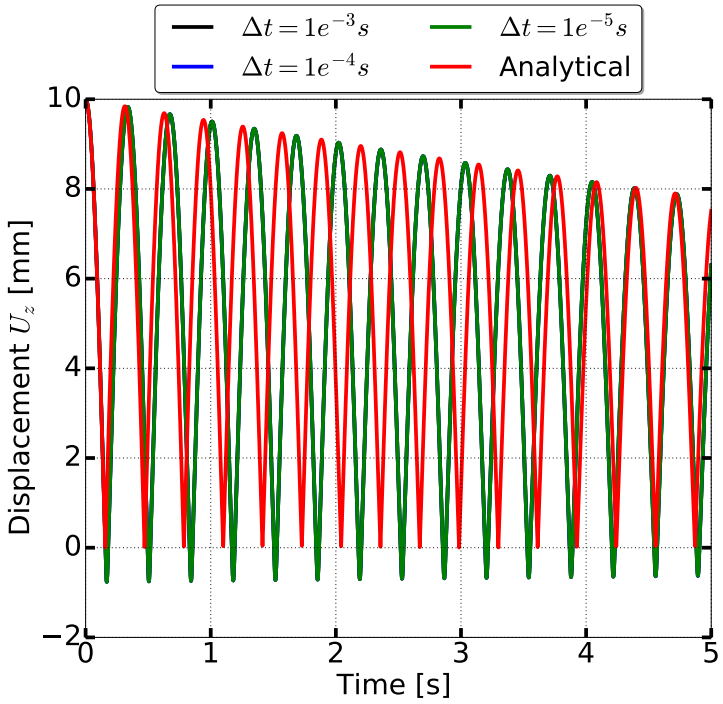

(b) $c_n = 1e^{-1} Ns/m$

Figure 4.43: Comparison of response of node 2 for initial normal stiffness of $k_i = 1kPa$, stiffening rate of $S_r = 1000$ and maximum normal stiffness of $k_n^{max} = 1GPa$ for different time steps Δt and viscous damping of $c_n = 1Ns/m$, $c_n = 0.1Ns/m$ with no numerical damping.

results. This could be seen from the response of all dynamic cases presented in Figures 4.31 to 4.41 where the converged solution becomes closer to the analytical as Δt is reduced.

4.5 Dynamic Tangential Slip Verification

This section verifies the contact element for dynamic case. Below is considered a single friction degree of freedom example which basically represents a normal interaction between the structure and the foundation.

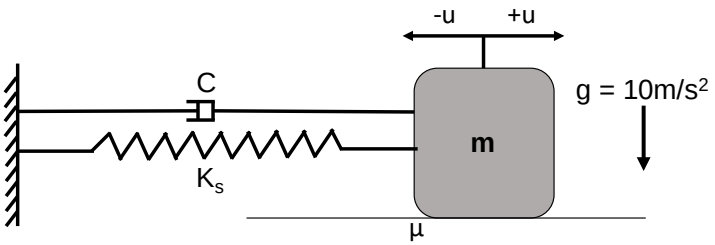

Figure 4.44: Illustration of a frictional single degree of freedom problem.

Figure 4.44 shows a frictional single degree of freedom problem under gravity field g, mass m, friction coefficient μ_r, spring stiffness K_s and damping C. The spring cross-sectional and contact area is taken as $1m^2$. Here both stress based or stress based contact could be used. To have the same response for the stress and force based contact, the shear zone length is taken as $SZ_h = 1m$ so that the magnitude of the shear strain γ is equal to the shear displacement Δ_t. The dynamic behavior of the mass m can be described by the two differential equations shown below:

$$m\ddot{u} + C\dot{u} + K_s\dot{u} = -\mu_r mg \quad for \quad \dot{u} > 0 \tag{4.18}$$

$$m\ddot{u} + C\dot{u} + K_s\dot{u} = \mu_r mg \quad for \quad \dot{u} < 0 \tag{4.19}$$

The analytical solution to this problem for initial displacement u_i and initial velocity $\dot{u_i} = 0$ can be solved using integration methods such as Newmark, Wilson θ, Houbolt and Hilber-Hughes-Taylor method. Here, Newmark method with no numerical damping $\gamma = 0.5$ and very small time step of $\Delta t = 1e^{-}5s$ was used to get the analytical solution for damping C, spring stiffness K_s and frictional coefficient μ_r.

The same problem as described in Figure 4.44 is modeled in FEM as shown in Figure 4.45. Here, the dynamics of that problem is modeled under an application of slow

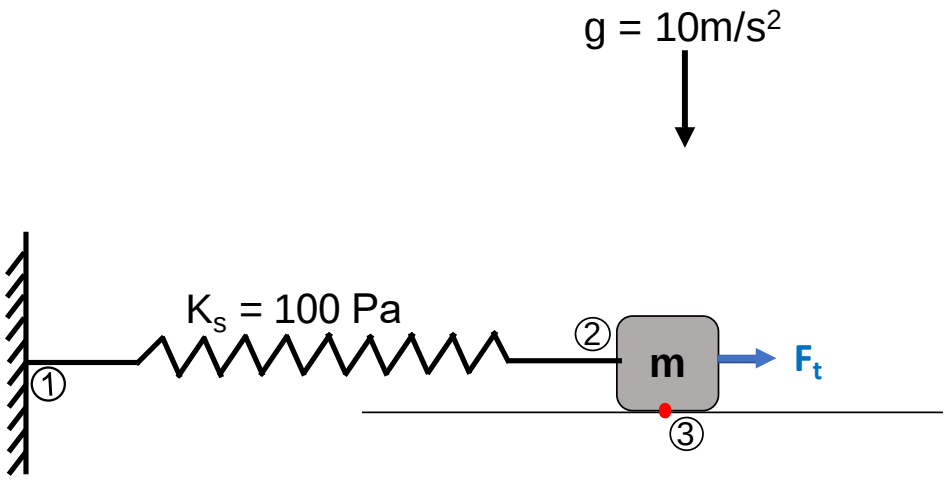

Figure 4.45: Illustration of frictional single degree of freedom problem in FEM.

load of F_t to create an initial displacement u_i with zero initial velocity. Once the initial displacement is achieved, the force F_t is removed. Self-weight is applied under the gravity field g.

In this example, the spring stiffness K_s is taken as $K_s = 100Pa$. The tangential shear stiffness k_t is varied from $k_t = 1kPa$ to $k_t = 100MPa$. The friction coefficient μ_r is taken as $\mu_r = 1$. Thus, the total maximum frictional force $N = \mu_r mg$ for large shear displacements Δ_t. An large initial displacement of $u_i = 0.7m$ is applied. For all the runs, Newmark method was used with no numerical damping. Relative Convergence criteria of $1e^{-3}$ on the unbalanced force was used.

4.5.1 Response Under No Damping

In this case, no tangential viscous damping between contact node pairs was applied. Simulations are run for different shear stiffness k_t and different time steps Δt.

From Figures 4.46 and 4.47, it can be noticed that as the shear stiffness k_t increases the solution becomes much more accurate. As was seen for the normal contact, as the shear stiffness increases, a smaller time step is required to get to the solution close to analytical. It must be noted that for $k_t > 1MPa$, the analysis failed to converge for

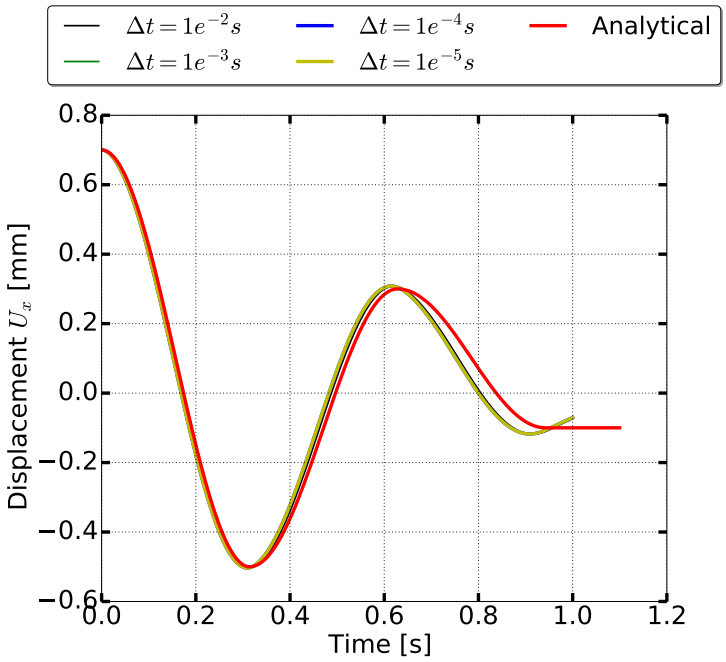

(a) $k_t = 1kPa$

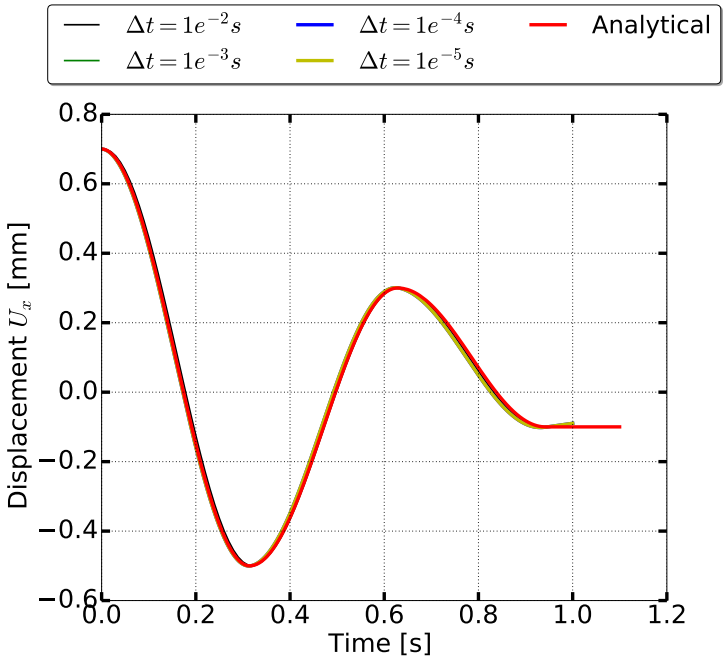

(b) $k_t = 10kPa$

Figure 4.46: Comparison of response of node 3 for shear stiffness $k_t = 1kPa$ and $k_t = 10kPa$ for different time steps Δt with no numerical or viscous damping.

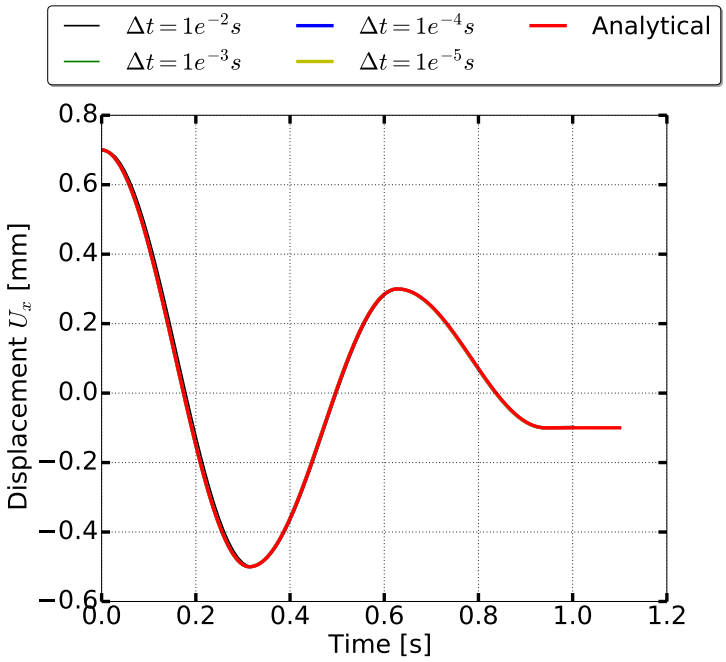

(a) $k_t = 1MPa$

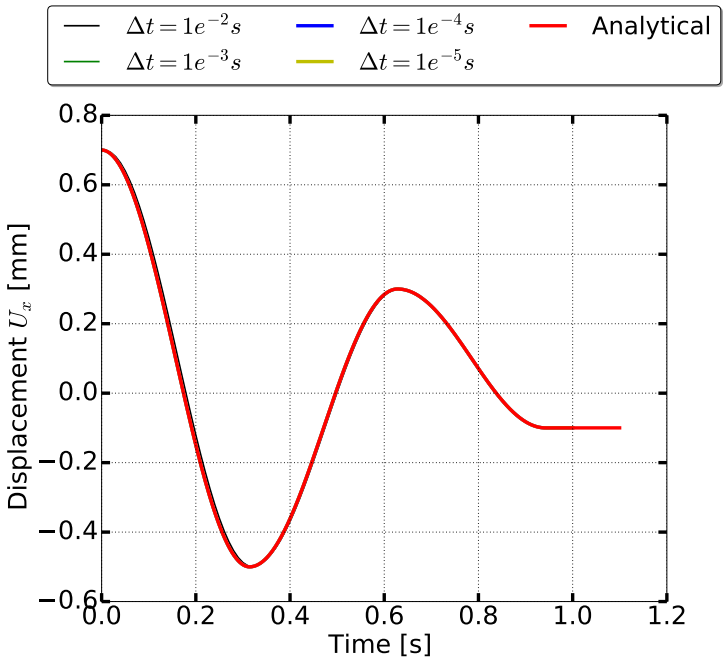

(b) $k_t = 100MPa$

Figure 4.47: Comparison of response of node 3 for shear stiffness $k_t = 1MPa$ and $k_t = 100MPa$ for different time steps Δt with no numerical or viscous damping.

$\Delta t = 1e^{-3}s$ at time $t = 0.62s$. At time $t = 0.62s$, the displacement attains its peak and starts to decrease. At this state, if the incremental time step Δt is large enough, the resulting shear force can lead to convergence oscillations between the extreme ends of the yield surface. For normal contact, this could too happen as described in Section 4.12.2. In such situations, lowering the time step Δt would resolve the convergence problem.

4.5.2 Response Under Tangential Viscous Damping c_t

In this case, a tangential viscous damping c_t between contact node pairs is considered. The shear stiffness was fixed to $k_t = 1MPa$. Simulations were run for different tangential damping c_t and different time steps Δt.

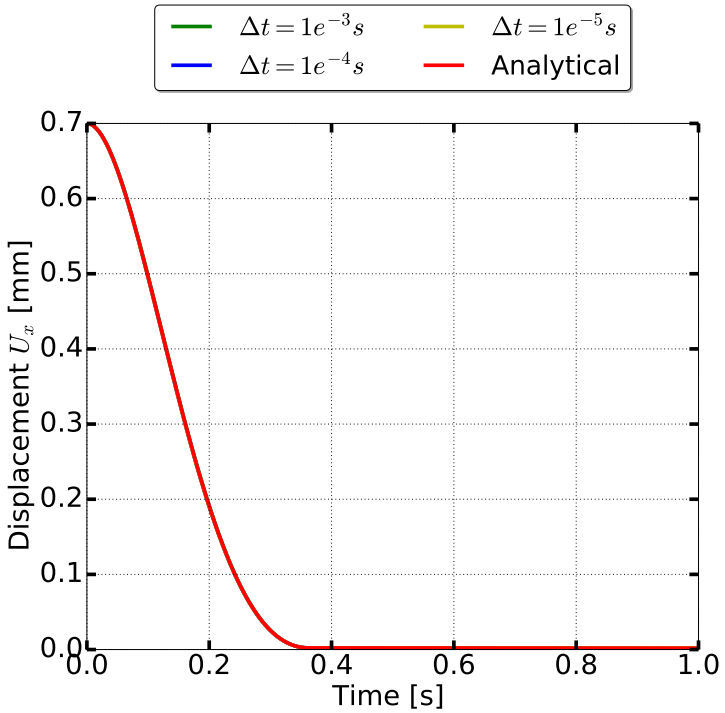

(a) $c_t = 10Ns/m$

Figure 4.48: Comparison of response of node 3 for penalty stiffness $k_t = 1MPa$ and viscous damping $c_t = 10Ns/m$ for different time steps Δt with no numerical damping

In the above plots shown in Figure 4.49 and 4.48 the solution obtained from the FEM simulation matches the analytical solution. This verifies the tangential damping implementation in the contact element.

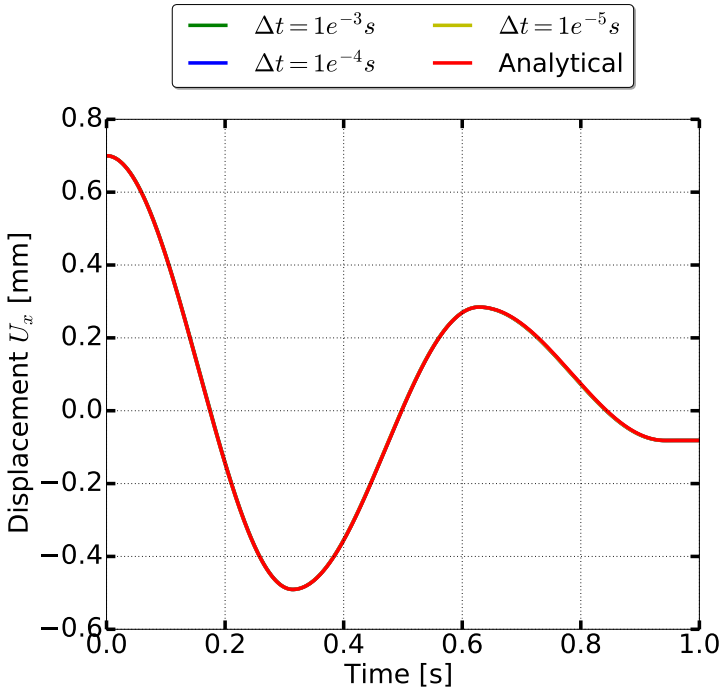

(a) $c_t = 0.1Ns/m$

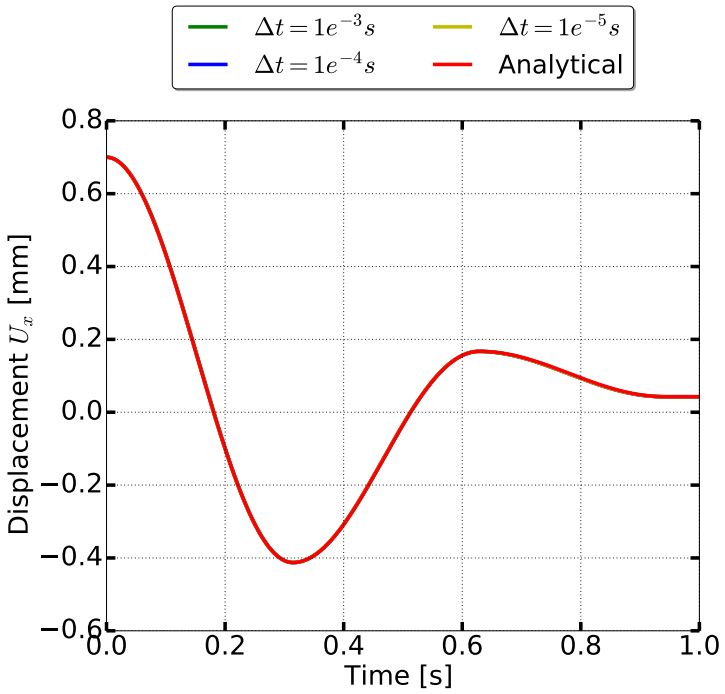

(b) $c_t = 1Ns/m$

Figure 4.49: Comparison of response of node 3 for penalty stiffness $k_t = 1MPa$ and viscous damping $c_t = 0.1Ns/m$ and $c_t = 1Ns/m$ for different time steps Δt with no numerical damping

It must be noted that the frictional shear damping shown in Figure 4.46 and 4.47 is linear, whereas normal viscous damping shown in Figure 4.49 and 4.48 is exponential.

4.6 Energy Dissipation Verification

Contact simulation under seismic loading dissipates a lot of energy at the interface due to continuous frictional force between the sliding bodies. The energy is dissipated as heat and needs to be correctly calculated to evaluate the loss of energy at contact. For soil-structure interaction problems, it is preferred to dissipate energy anywhere except the structure itself. Obviously, the energy dissipated should not possess any stability issues. In such conditions, the energy dissipated at contact interfaces could prove to be quite useful in damping out higher mode vibrations in structure. Also, in more complicated simulations involving non-linear materials, numerical damping, viscous damping, etc. a method must be developed and verified to calculate the energy dissipation at contact. Section 4.1.3 shows the plot of energy dissipation of the interface shear models. Since the normal interface models are modeled as non-linear elastic, there is no dissipation for normal loading and unloading. Section 3.3 describes, about how to calculate the incremental energy for contact element. The incremental energy can be integrated to evaluate total energy dissipation at contact.

For energy verification, the following must hold

- The incremental energy dissipation E_{dis}^{incr} should be always positive

$$\Delta E_{dis}^{incr}(t) \geq 0 \tag{4.20}$$

- Total energy is conserved

$$E_{total}(t) = E_{dis}(t) + E_{kinetic}(t) + E_{potential}(t) = F_{ext}\Delta u \tag{4.21}$$

  where E_{dis} is the dissipated energy, $E_{kinetic}$ is the kinetic energy , $E_{potential}$ is the potential energy and $F_{ext}\Delta u$ is the external applied work.

Here, for verification, the example presented in Figure 4.44 is used with no viscous and numerical damping. The mass is taken as $m = 1kg$, spring stiffness as $K_s = 100Pa$,

friction coefficient as $\mu_r = 1$ and initial displacement as $u_i = 0.7m$. The contact shear stiffness k_t was taken as $k_t = 1MPa$. With these parameters, the total energy initially stored in the system only comprise of strain energy in the spring. Thus, the total energy $E_{total} = 0.5K_s{u_i}^2$ is equal to $E_{total} = 24.5J$.

In the considered example the only source of dissipation is by friction at the interface.

$$E_{disp} = E_{disp}^{con} \tag{4.22}$$

where, E_{disp}^{con} is the energy dissipated at interface due to friction. The incremental frictional dissipation ΔE_{disp}^{con} is calculated from the expression shown in Section 3.3. The kinetic energy of the system is given as $E_{kinetic}(t) = 0.5m\dot{u}(t)^2$. In this example, the potential energy exists due to the spring stiffness K_s and gravity $\boldsymbol{g}$. Since, the potential energy due to gravity g is always conserved and never dissipated, it would not be considered further in dissipation or total energy calculations. Thus, the potential energy at any time t can be calculated as $E_{potential}(t) = 0.5K_s u(t)^2$. The total energy E_{total} can then be written as

$$E_{total}(t) = E_{dis}^{con}(t) + 0.5m\dot{u}(t)^2 + 0.5K_s u(t)^2 = 24.5J \tag{4.23}$$

Figures 4.50 to 4.52 plots the total energy and incremental dissipation with time for different time steps Δt. It also shows the individual components of total energy with time t. The sum of all the energy components in the plots for all time t should be equal to the total energy $E_{total} = 24.5J$.

From the plots, it can be observed that the individual energy components sum up to $E_{total} = 24.5J$. For bigger time step $\Delta t = 0.01s$, the total energy E_{total} is almost close to $E_{input} = 24.5J$ with oscillations around it by $\pm 1J$. However, for finer time step $\Delta t = 1e^{-4}s$, the total energy is a constant line for all time t.

The incremental dissipation $E_{dis}^{incr} \geq 0$ is always positive and thus the total dissipation E_{dis} is always increasing. It must also be noted that as the time step Δt is refined, the incremental dissipation also gets refined too. As a result ,the incremental energy dissipation E_{dis}^{incr} reduces by the same order as Δt is refined.

The plots verify the Equation 4.20 and 3.38. Both Incremental energy dissipation

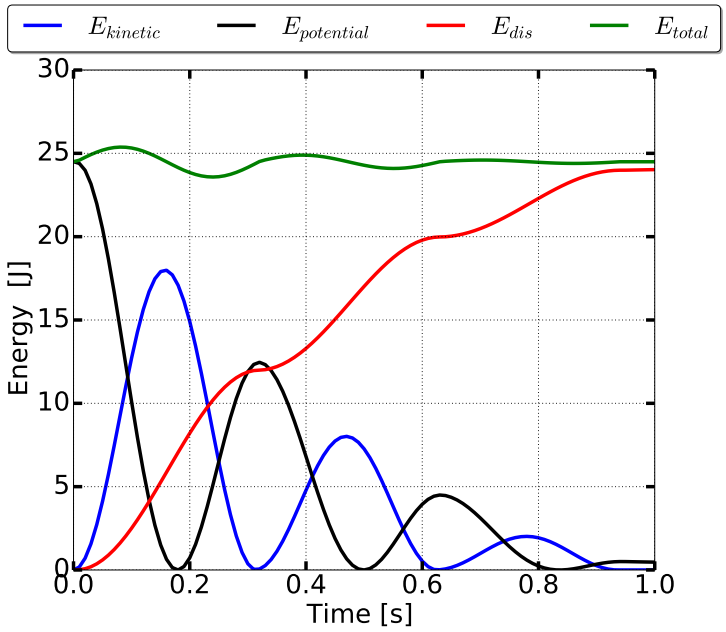

(a) Total Energy

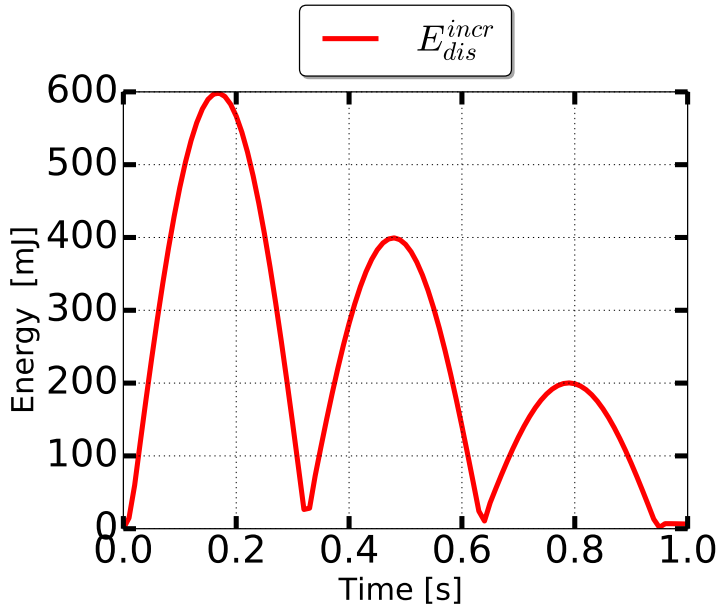

(b) Incremental Dissipated Energy

Figure 4.50: Total energy and incremental dissipation plot for frictional single degree of freedom example for shear stiffness of $k_t = 1MPa$ and time step of $\Delta t = 1e^{-2}s$.

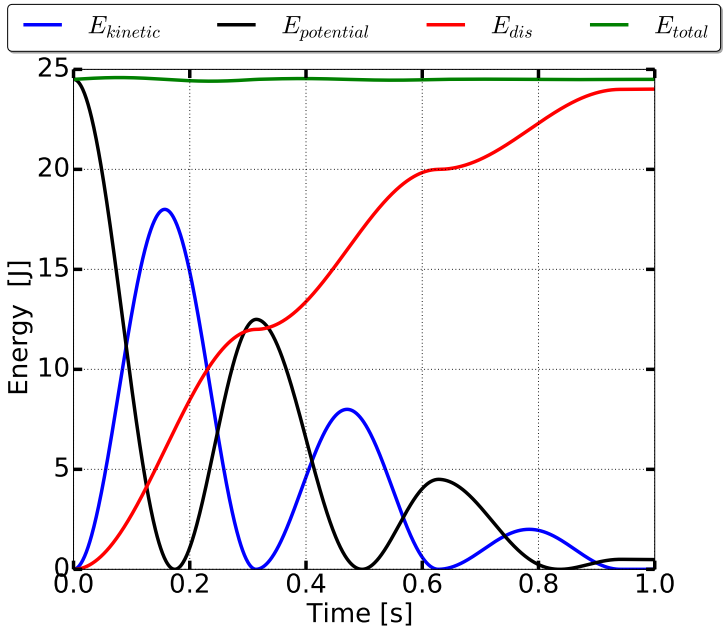

(a) Total Energy

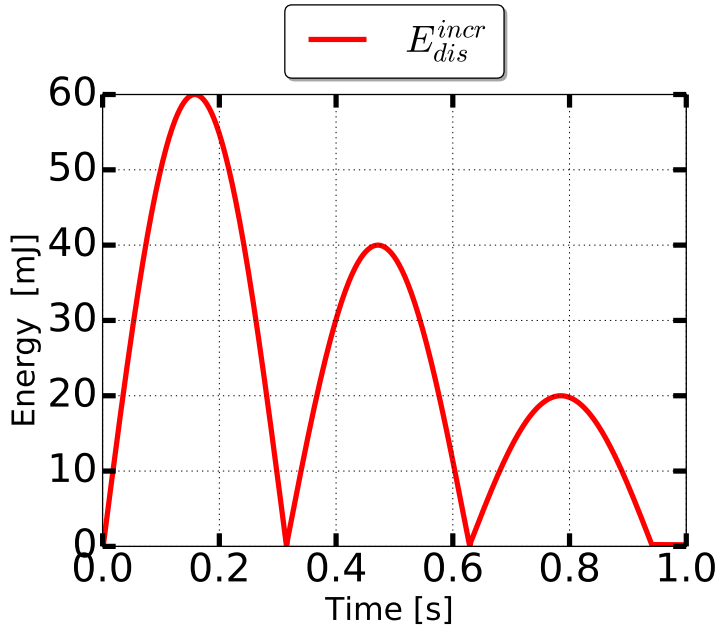

(b) Incremental Dissipated Energy

Figure 4.51: Total energy and incremental dissipation plot for frictional single degree of freedom example for shear stiffness of $k_t = 1MPa$ and time step of $\Delta t = 1e^{-3}s$.

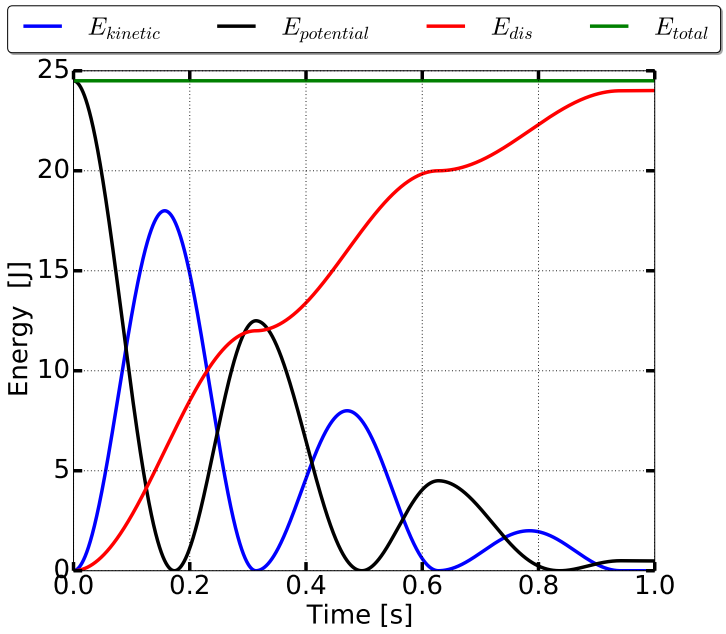

(a) Total Energy

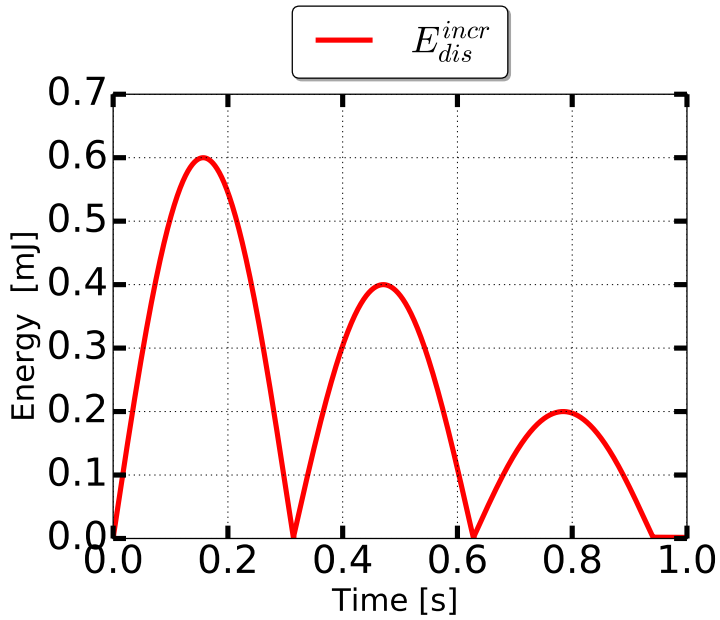

(b) Incremental Dissipated Energy

Figure 4.52: Total energy and incremental dissipation plot for frictional single degree of freedom example for shear stiffness of $k_t = 1MPa$ and time step of $\Delta t = 1e^{-4}s$.

$E_{dis}^{incr} \geq 0$ and total energy conservation $E_{total} = 24.5J$ verifies the implementation and correctness of contact algorithm.

4.7 Interface Behavior Verification for Change in Surface Area, Normal Stress and Shear Zone Thickness for Stress Based Contact

The above sections verified the normal and shear behavior of the force and stress based contacts through different examples. Here the response of the stress based contact subject to different surface area A, normal load and shear zone thickness SZ_h is considered. Being stress based contact, the response would be invariant to the shear zone thickness SZ_h and the contact surface area. Also, for EPPS and NLHS models, the normalized shear response would be independent of normal shear σ_n. However, for NLHSS shear model where the peak normalized shear stress μ_p depends upon confinement σ_n, the normalized shear response is different for different normal stress σ_n.

The surface are of the interface is varied over the range of $10^{-4}m^2$ to $100m^2$. The normal stress is varied over the range of $\sigma_n = 1Pa$ to $\sigma_n = 1GPa$. The shear zone thickness is varied over the range of $SZ_h = 10^{-3}mm$ to $10m$. For each type of normal and shear contact models, the response is verified by changing the above parameters over a wide range.

4.7.1 Normal Contact Models

Figure 4.53 shows the response of Hard contact for change in surface area, normal load and shear zone thickness. Unless varied the normal stiffness was taken as $k_n = 400MPa$, shear zone thickness of $SZ_h = 5mm$ and normal load of $100N$ and surface area of $A = 1m^2$. It can be observed from the plots that the stress based hard contact show the same response to all range of values for surface area, normal load and shear zone thickness. It must be however noted that for larger surface area $A > 100m^2$ or very small shear zone thickness $SZ_h < 1e^{-6}m$, the normal stiffness $K_n = k_nA/SZ_h$ becomes a very large value making the global stiffness matrix ill-conditioned. Figure 4.53 shows that stiffness remains constant with normal strain ϵ and the response exactly matches for different range of normal load, surface area and shear zone thickness.

Figure 4.54 shows the response of Soft contact for change in surface area, normal

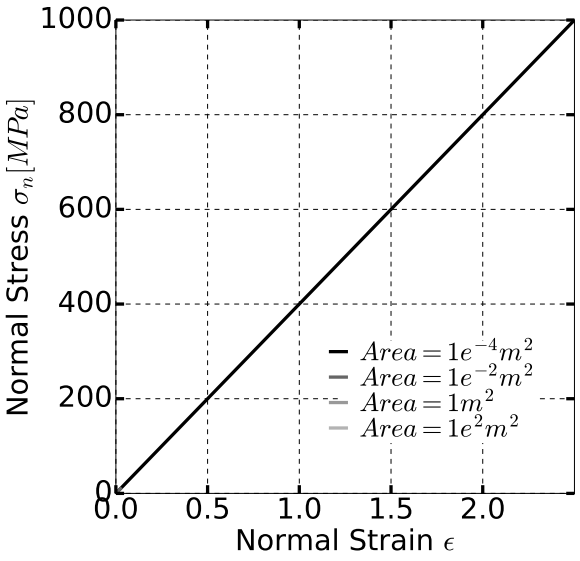

(a) Varying Surface Area

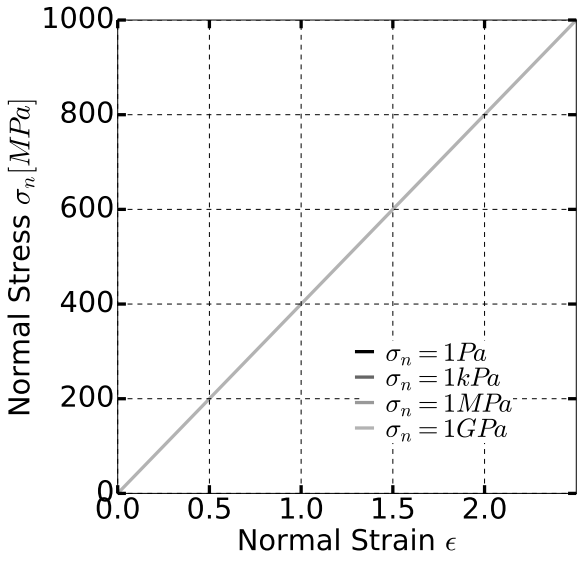

(b) Varying Normal Load

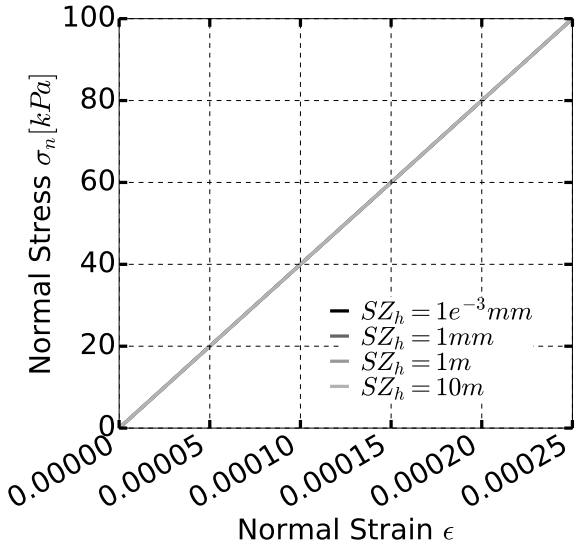

(c) Varying Shear Zone Thickness

Figure 4.53: Hard Contact response with varying surface area, normal load and shear zone thickness SZ_h.

load and shear zone thickness. Unless varied the initial normal stiffness was taken as $k_i = 1MPa$, stiffening rate of $S_r = 100$, maximum normal stiffness $k_n^{max} = 1GPa$, shear zone thickness of $SZ_h = 5mm$, normal load of $100N$ and surface area of $A = 1m^2$. It can be observed from the plots that the stress based soft contact show the same response to all range of values for surface area, normal load and shear zone thickness. As the surface area is increased, the normal stress decreases for the applied load of $100N$. Thus in the plot shown in Figure 4.54(a), the response reaches the maximum normal stiffness $k_n^{max} = 1GPa$ for surface area of $A = 1e^{-4}m^2$ i.e. for a normal stress of $\sigma_n = 100GPa$. Similarly, as the normal load is increased to $\sigma_n = 100GPa$, the stiffness k_n reaches the maximum stiffness of $k_n^{max} = 1GPa$. The normal strain also reaches to 1% for small surface are or large normal load. This again result in stiffening of the contact to its maximum stiffness $k_n^{max} = 1GPa$. Thus in Figure 4.54, the linear response for large normal strain corresponds to the soft contact stiffness reaching the maximum normal stiffness k_n^{max}. For low normal strain $\epsilon < 0.05$, the response is non-linear. This could be seen from Figure 4.54(c), where the shear zone thickness SZ_h is varied keeping the normal stress $\sigma_n = 100kPa$. The response exactly overlaps for different shear zone thickness SZ_h.

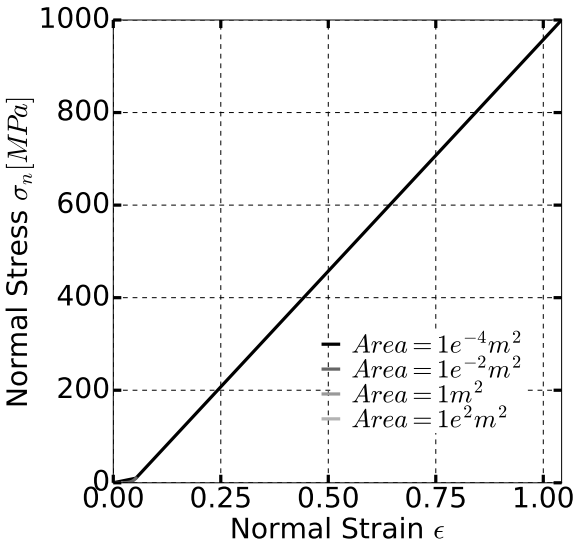

(a) Varying Surface Area

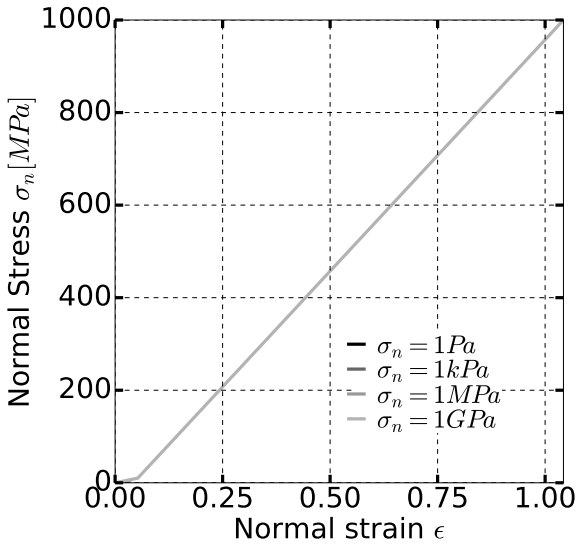

(b) Varying Normal Load

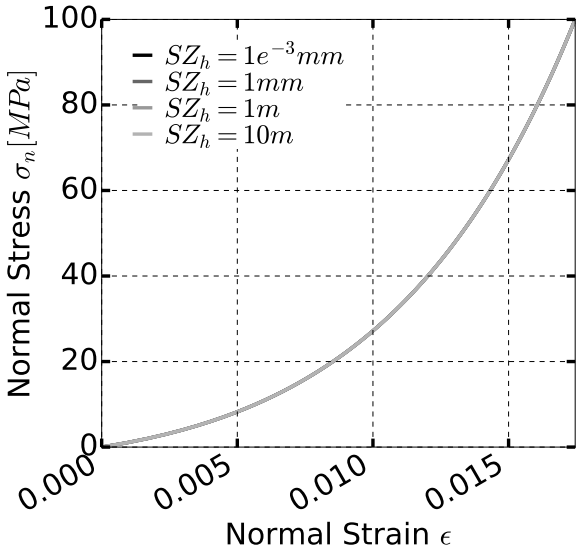

(c) Varying Shear Zone Thickness

Figure 4.54: Soft Contact response with varying surface area, normal load and shear zone thickness SZ_h.

4.7.2 Shear Contact Models

Figure 4.55 shows the response of elastic-perfectly plastic shear model for change in surface area, normal stress and shear zone thickness. Unless the parameters are varied, the shear stiffness was taken as $k_t = 400kPa$, surface area of $A = 1m^2$, residual normalized shear stress $\mu_r = 0.68$ and shear zone thickness of $SZ_h = 5mm$. It can be observed from the plots that the EPPS model shows the same response to all range of values for surface area, normal stress and shear zone thickness.

Figure 4.56 shows the response of non-linear hardening shear model for change in surface area, normal stress and shear zone thickness. Unless the parameters are varied, the shear stiffness was taken as $k_t = 800kPa$, surface area of $A = 1m^2$, residual normalized shear stress $\mu_r = 0.68$ and shear zone thickness of $SZ_h = 5mm$. It can be observed from the plots that the NLHS model show the same response to all range of values for surface area, normal stress and shear zone thickness. However, as observed in Figure 4.56(b) for a very low normal stress of $\sigma_n = 1Pa$, the normalized shear stress response has a small error. For normal stress of $\sigma_n > 1kPa$, the normalized shear response matches and thus overlaps with each other.

Figure 4.57 shows the response of non-linear hardening-softening shear model for change in surface area, normal stress and shear zone thickness. Unless the parameters are varied, the shear stiffness was taken as $k_t = 800kPa$, surface area of $A = 1m^2$, rate of softening $b = 40$, peak plateau size $n = 8$, peak normalized shear stress limit $\mu_{P0} = 0.9$, rate of decrease $k = 0.1$, residual normalized shear stress $\mu_r = 0.68$ and shear zone thickness of $SZ_h = 5mm$. Unlike EPPS and NLHS model, the NLHSS model normalized response depends upon the normal stress σ_n. Thus, with the change in surface area and normal stress, the shear response changes. This could be seen for the plots in Figure 4.57(a) and 4.57(b). For low surface area or normal stress σ_n, a hardening and softening behavior is observed. However, for very small surface area leading to high normal stress σ_n, the normalized stress response is only hardening to the residual normalized shear stress of $\mu_r = 0.68$. In Figure 4.57(a) and Figure 4.57(b) for surface area $A < 0.1m^2$ and normal stress $\sigma_n > 1MPa$, the normalized response only shows hardening response and exactly

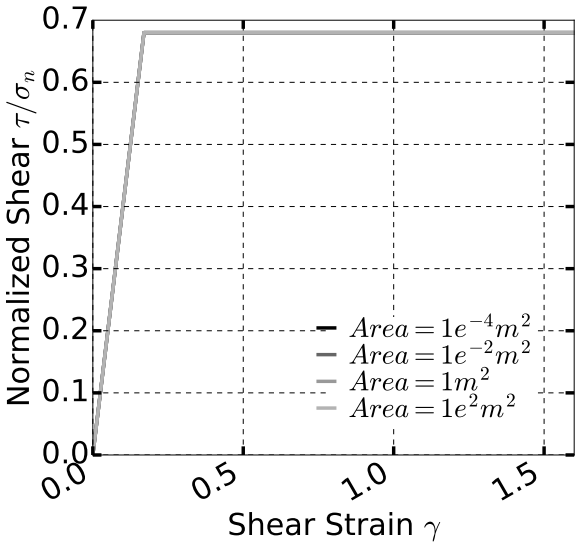

(a) Varying Surface Area

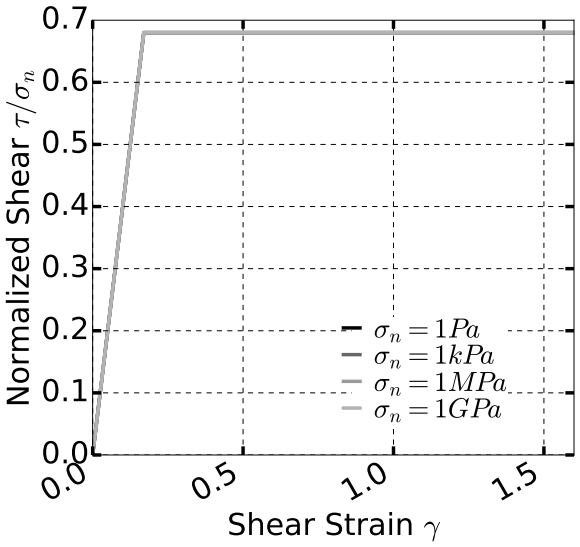

(b) Varying Normal Stress

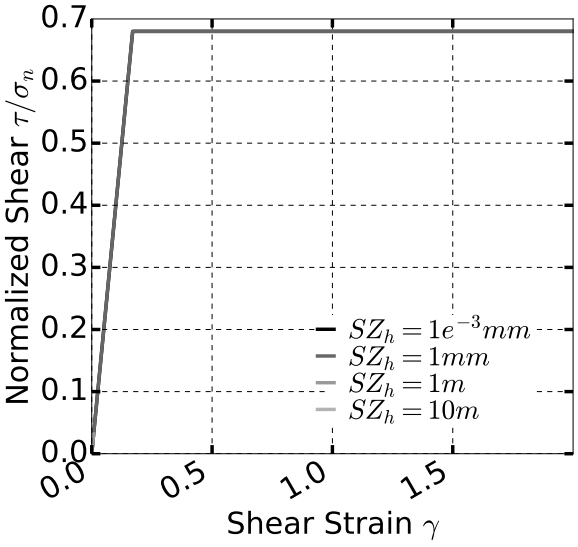

(c) Varying Shear Zone Thickness

Figure 4.55: EPPS Model response with varying surface area, normal load and shear zone thickness SZ_h.

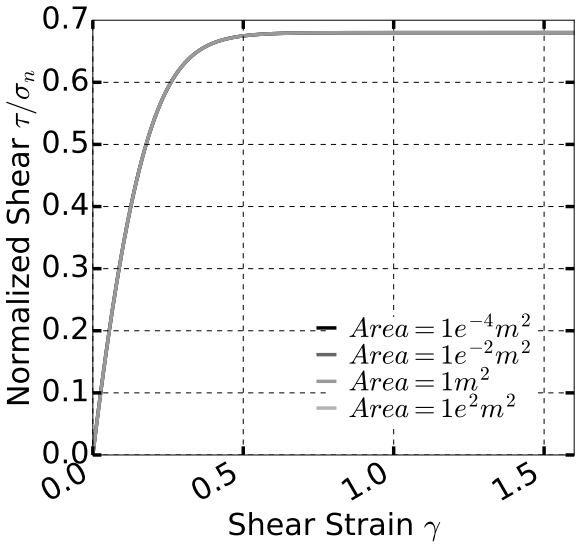

(a) Varying Surface Area

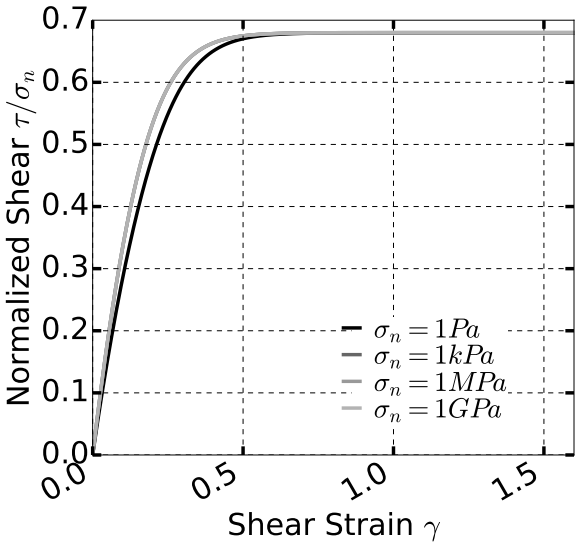

(b) Varying Normal Stress

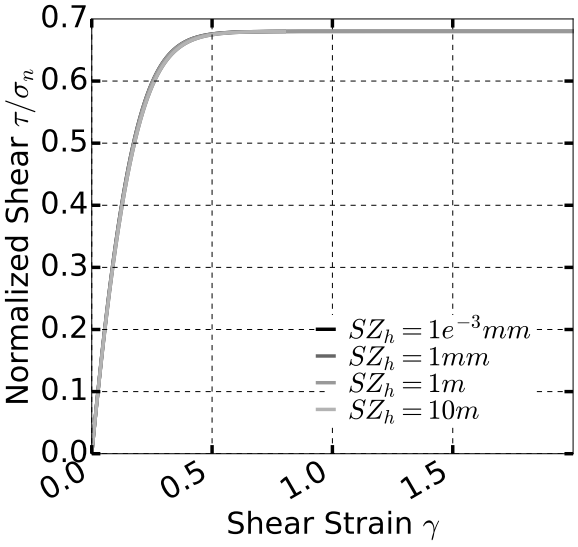

(c) Varying Shear Zone Thickness

Figure 4.56: NLHS Model response with varying surface area, normal load and shear zone thickness SZ_h.

overlaps. Whereas for normal stress $\sigma_n < 1MPa$ and surface area $A > 0.1m^2$ (normal load of 100kN), the response varies with different hardening and softening stages.

However, for change in shear zone thickens SZ_h, the normal stress $\sigma_n = 100kPa$ remains the same. Thus, the shear response exactly matches and overlaps with each other for all the range of shear zone thickness $SZ_h = 10^{-3}mm$ to $SZ_h = 10m$.

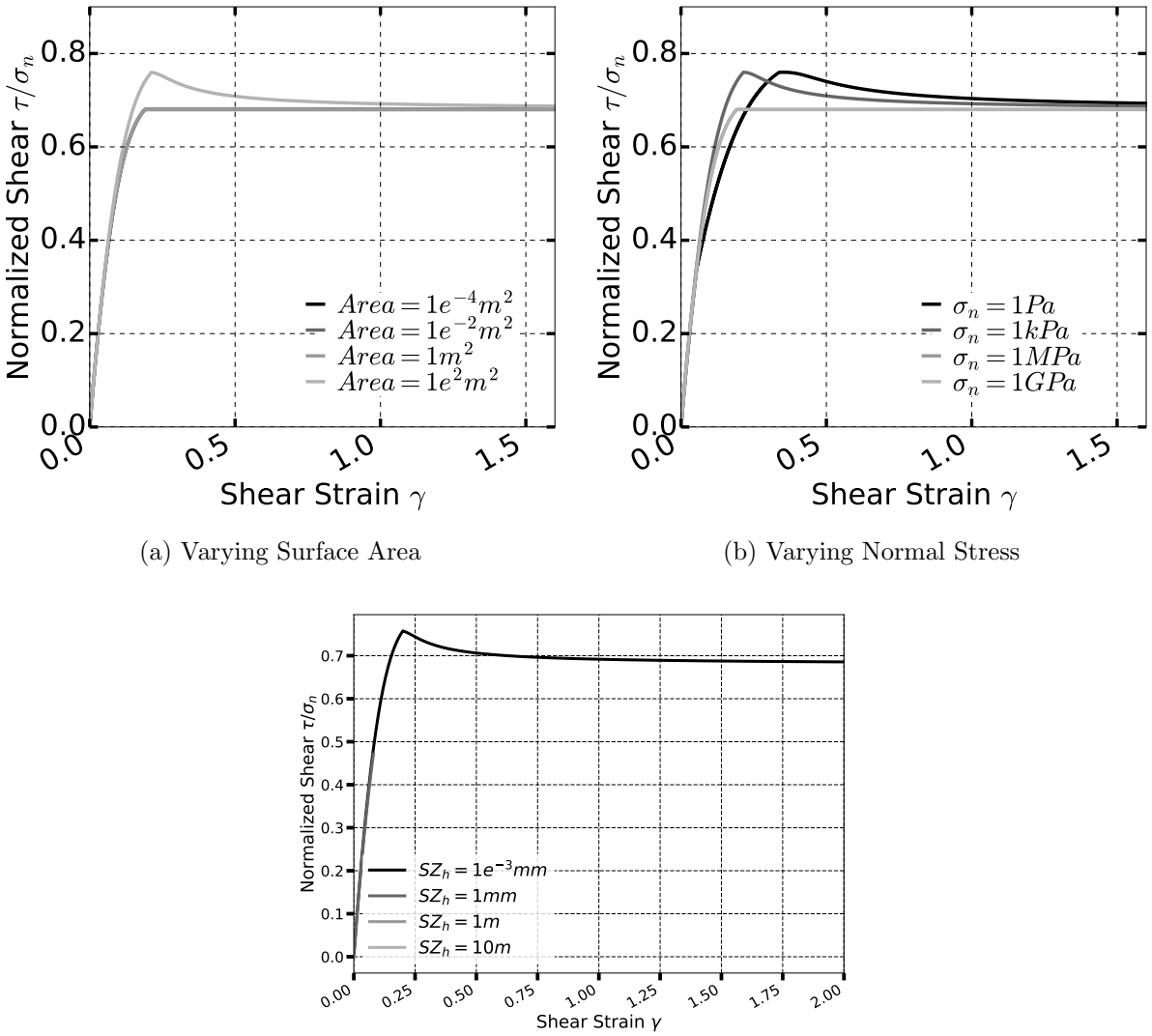

(a) Varying Surface Area

(b) Varying Normal Stress

(c) Varying Shear Zone Thickness

Figure 4.57: NLHSS Model response with varying surface area, normal load and shear zone thickness SZ_h.

4.8 Arbitrary Mesh Verification

The mesh at the interface may not be always regular. It can have different mesh and configurations as shown in Figure 4.58 and Figure 4.61.

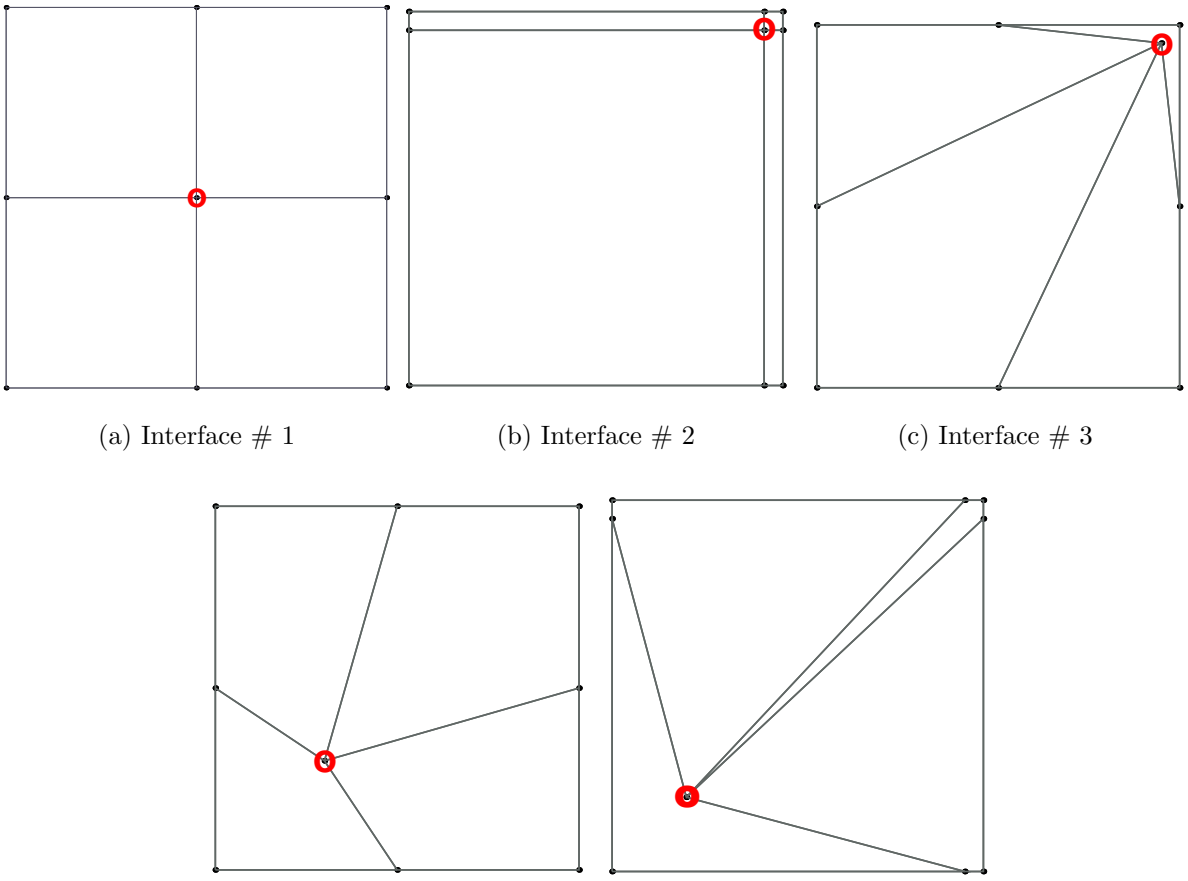

(a) Interface # 1 (b) Interface # 2 (c) Interface # 3

(d) Interface # 4 (e) Interface # 5

Figure 4.58: Interface Types

Section 3.1.1 describes the method to calculate the equivalent surface area when multiple elements are shared by the contact node pair. Figure 4.58 shows a $2m \times 2m$ interface surface geometry with four elements.

To verify the working for correct surface area calculation, the Sresponse of a contact element at the middle node (in red circle) shown in Figure 4.58 is considered. The surface area shared by that node for all the interface types analytically equals to $1m^2$. Thus the response of the contact element should be theoretically same for all the different interface

types. However, we know that the mesh distortion often affects the results in finite element method. Figure 4.59 plots the NLHSS model normal and shear interface for all different interface types. The normal stress σ_n for interface types 1 2 and 4 is equal to the applied stress of $100kPa$. Whereas, for interface type 3 and 4 because of mesh distortion, the normal stress response is little bit smaller by 4%. Similarly, Figure 4.59b shows the shear response for different interface types. It can be observed that interface type 1 shows the correct response whereas others because of mesh distortion have overall some variation in response. It must be noted that these effects are primarily because of distortion in elements or mesh.

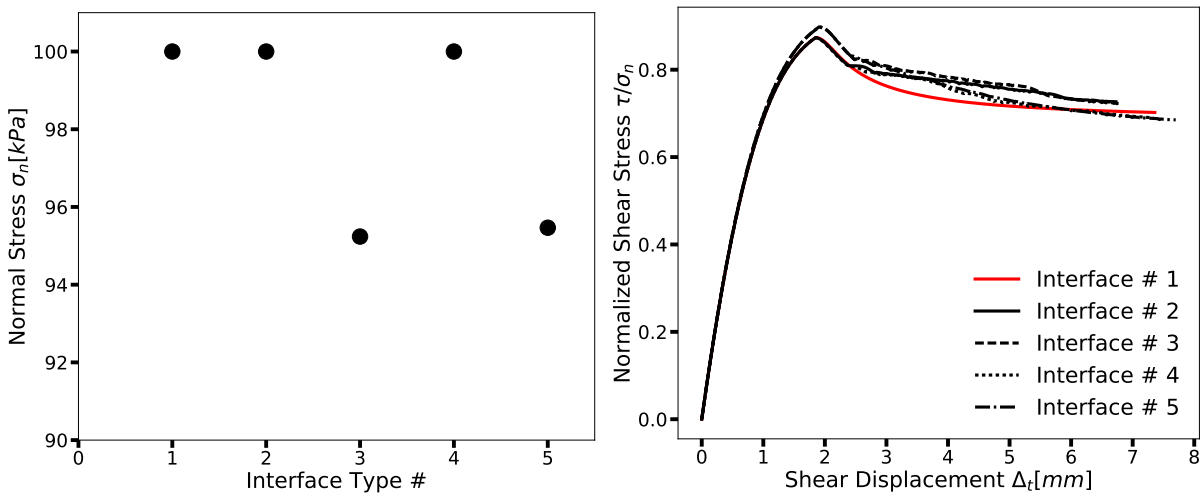

(a) Normal Stress

(b) NLHSS Model Response

Figure 4.59: NLHSS Interface model ($k_t = 1500kPa$, $b = 40$, $n = 8$, $\mu_{P0} = 0.9$, $k = 0.1$, $\mu_r = 0.68$ and $SZ_h = 5mm$) response for a single contact at the middle for different interface types.

For the verification, the next step is to test the response of all the contact elements at the interface for different interface mesh. Figure 4.61 show the mesh for the interface geometry considered in Figure 4.58. The model consists of an upper plate of thickness $0.1m$ and a surface area of $2mm = 4m^2$ with an application of a normal load of $N = 100kPa$ in stage one and then a shear load of $S = 50kN$ in stage two. Figure 4.60 illustrates the problem with normal load N and shear load S. LEPPS model was used to

model the shear behavior. Thus, analytically the linear shear stress distribution generated would result in shear stress of $\tau = 20 - 25kPa$ at the middle of the interface. It must be noted that the bottom plate was fixed while the top plate was only laterally fixed. Since the system is not fully constrained, the whole analysis was simulated as a slow transient analysis with initial normal loading applied in $100s$ and shear loading in $1e^6s$.

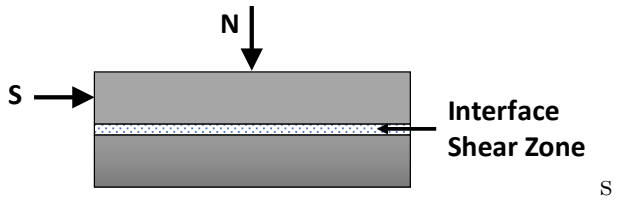

Figure 4.60: Illustration of shear load applied for contact normal stress for different interface mesh.

For all the different interface mesh types shown in Figure 4.61, the normal stress at the interface was $\sigma_n = 95kPa$. The average shear stress and displacement at the middle of interface after application of a tangential load of $80kPa$ is shown in Figure 4.62. It could be seen from the plots that because of mesh distortion, there is a lot of variation in shear response of interface. As the mesh is refined, the shear response scatter diminishes. However, the mesh effect still persists in the response. A more regular mesh results in solution closer to the analytical even for coarse mesh. Figure 4.63 shows the shear response for coarse and fine mesh.

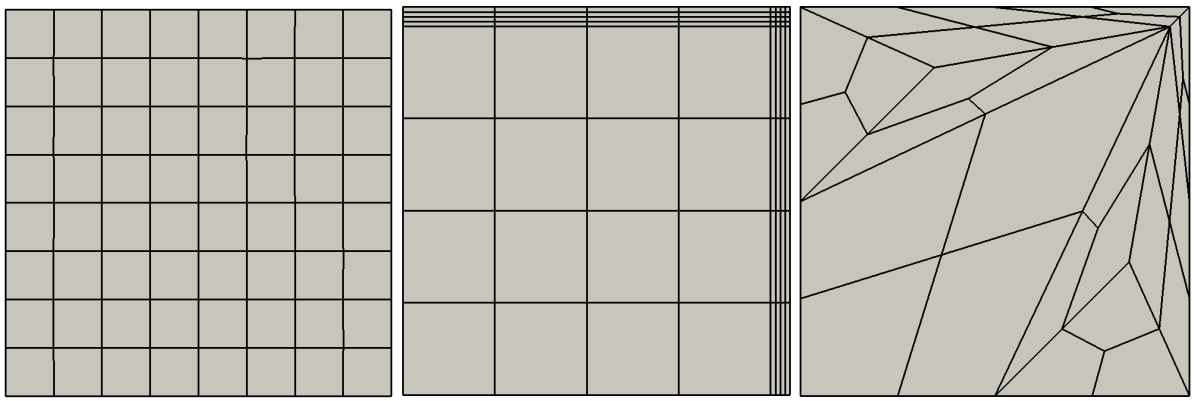

(a) Interface Mesh # 1 (b) Interface Mesh # 2 (c) Interface Mesh # 3

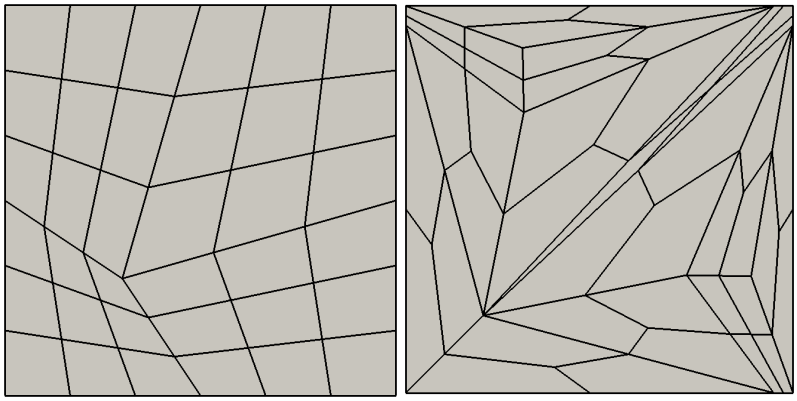

(d) Interface Mesh # 4 (e) Interface Mesh # 5

Figure 4.61: Interface Mesh Types

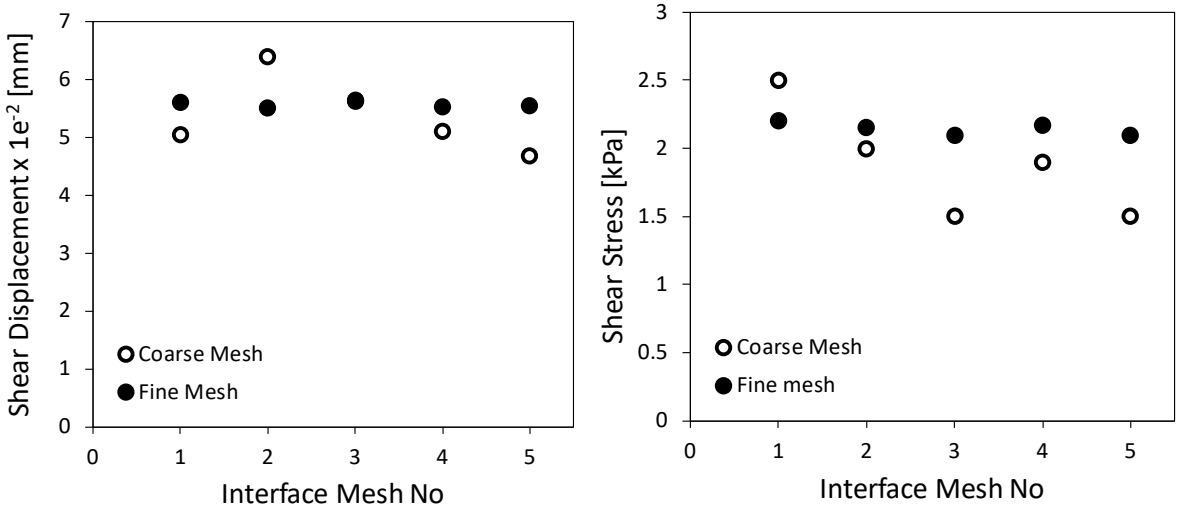

(a) Shear Displacement

(b) Shear Stress

Figure 4.62: Shear displacement and shear stress response for different interface mesh types.

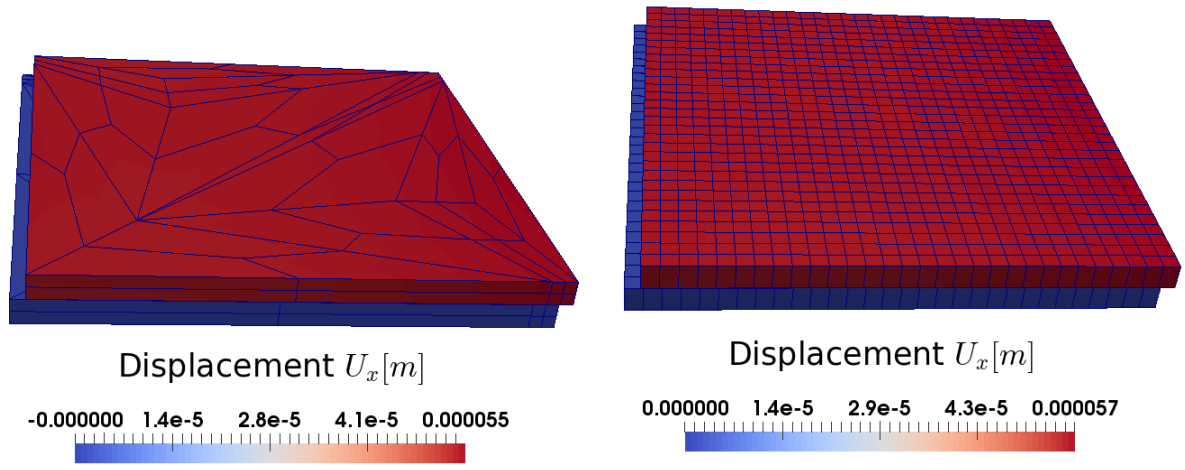

(a) Coarse Mesh : Interface Type #5

(b) Fine Mesh : Interface Type #1

Figure 4.63: Displacement field (amplified 2000 times) for (a) coarse mesh (b) fine mesh.

4.9 Auto Normal Detection Verification

It was realized in Section 3.6 that there is a need to have an auto-normal detection for contact node pairs when they are attached to more than one surfaces. This becomes more important in 3-D when the connected surfaces are curved and have their normals quite different than each other. For nodes attached to a plane surface, contact with only one normal using the surface area calculation (described in Section 3.1.1) would work. But in general, the surface shared by contact node pairs may not lie on one plane. As a result, multiple contact normals acting between the same node-pairs must be detected and applied.

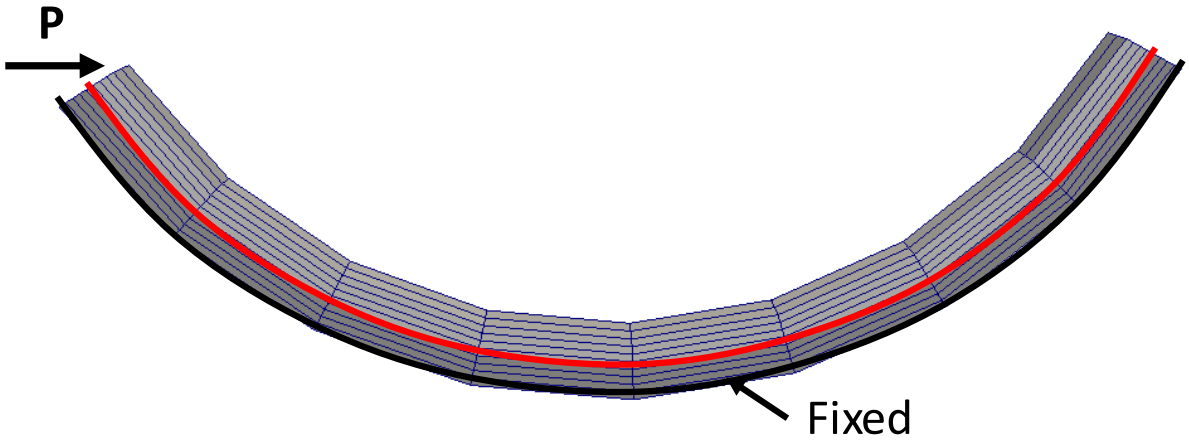

Figure 4.64: Illustration of curved soil-foundation interface.

Here, verification is done using a curved geometry as shown in Figure 4.64. It represents a curved soil-foundation interface. The bottom base is fixed and two loading stages are applied on the upper solid curve. In the first stage self-weight is applied and then in the second stage, a force in the x-direction is applied as shown in Figure 4.64.

Figure 4.65 and Figure 4.66 show the deformed mesh for the two different types of simulations considered. In the first simulation shown Figure 4.65(a) and Figure 4.66(a) multiple auto-normals for each of the contact surface shared by the contact node pair was defined. In the second simulation shown in Figure 4.65(b) and Figure 4.66(b) only one normal perpendicular to the curve was defined.

In the self-weight loading stage shown in Figure 4.65, multiple auto-normal contact

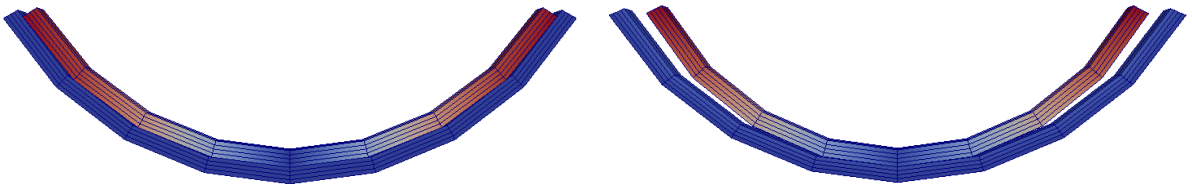

(a) Multiple Auto-Normal (b) Single Contact Normal

Figure 4.65: Deformed mesh configuration (magnified 1000 times) at the end of self-weight for simulations done using (a) Auto-Normal (b) Only one normal contact elements.

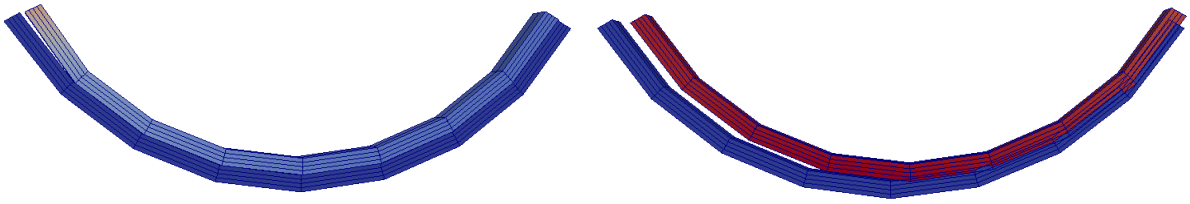

(a) Multiple Auto-Normal (b) Single Contact Normal

Figure 4.66: Deformed mesh configuration (magnified 1000 times) at the end of shear load stage for simulations done using (a) Auto-Normal (b) Only one normal contact elements.

works perfectly fine and all the interface remains in contact. The upper curve block slides down the lower one under self-weight. Whereas, when only one contact normal is specified the upper curve looses contact at the edges. The sliding of the upper block results in loss of contact as it reaches the no contact region as shown in Figure 3.9. This leads to non-realistic behavior. The effect is more pronounced when a shear load is added to the upper block as shown in Figure 4.66. The multiple auto-normal contact results is loss of contact at only the side edge where the load is applied. Whereas when only one-contact normal is specified, the whole upper block loses contact and slides as a rigid block, again because of the same effect as shown in Figure 3.9. The examples thus demonstrate and verify the working of the auto-normal contact for general 3-D simulations.

Figure 4.67 shows a closer look through a simple 3-D problem with corner mesh having less number of elements. The same loading conditions stages are applied. However in this example, the right end is fixed and the two blocks are not allowed to move vertically

resulting in separation of contact as soon as a small shear force is applied. Figure 4.67(a) shows the response to tangential load for the simulation done with multiple auto normals. Relative tolerance of 0.01% was used as the criteria for finding multiple normals. Figure 4.67(b) shows the results where only one normal is defined for each contact node pair. It can be seen from the figures that the one with multiple normals defined automatically does not allow the upper curved block to penetrate the lower block. Whereas for the case with only single normal defined, as soon as the tangential load is applied, there is a loose of contact at the middle node and thus the upper curve block penetrates in the lower one. This is the similar effect that is well explained in Section 3.6 using Figure 4.64.

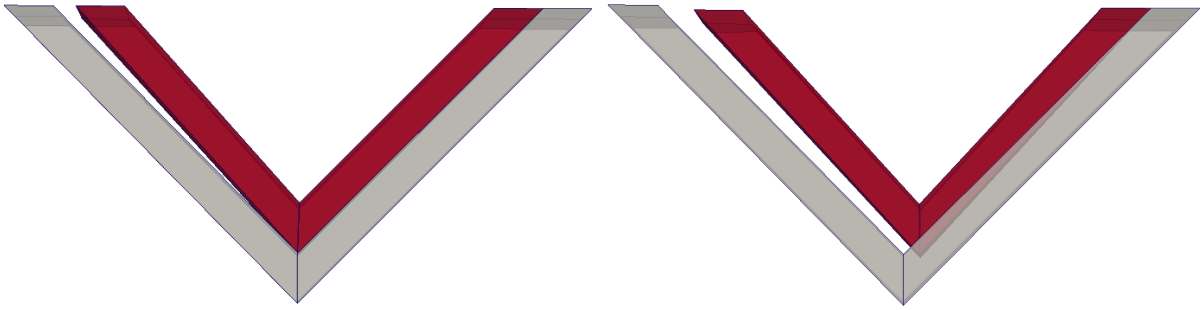

(a) Multiple Auto-Normal (b) Single Contact Normal

Figure 4.67: Deformed mesh configuration (magnified 20000 times) at the end of shear load stage for simulations done using (a) Auto-Normal (b) Only one normal contact elements for corner angle of 90^o.

Figure 4.68 to 4.73 shows the response of single normal with multiple auto normals with corner angle varying from 2^o to 180^o respectively. For all the cases with very sharp to shallow angles, multiple auto normal contact is able to correctly identify the multiple surfaces and enforce the impenetrability conditions as compared to the single normal contact. It must be noted that in the simulations involving planar contact surface, both approaches would work and give the same result.Figure 4.73 shows the case where both the type of contacts with single and multiple normals yield the same result. It must also be noted that as the corner angle increases and it becomes close to a flat interface, the no contact region shown in Figure 3.9 diminishes. Thus, even for almost very flat corner

(a) Multiple Auto-Normal (b) Single Contact Normal

Figure 4.68: Deformed mesh configuration (magnified 20000 times) at the end of shear load stage for simulations done using (a) Auto-Normal (b) Only one normal contact elements for corner angle of 2^o.

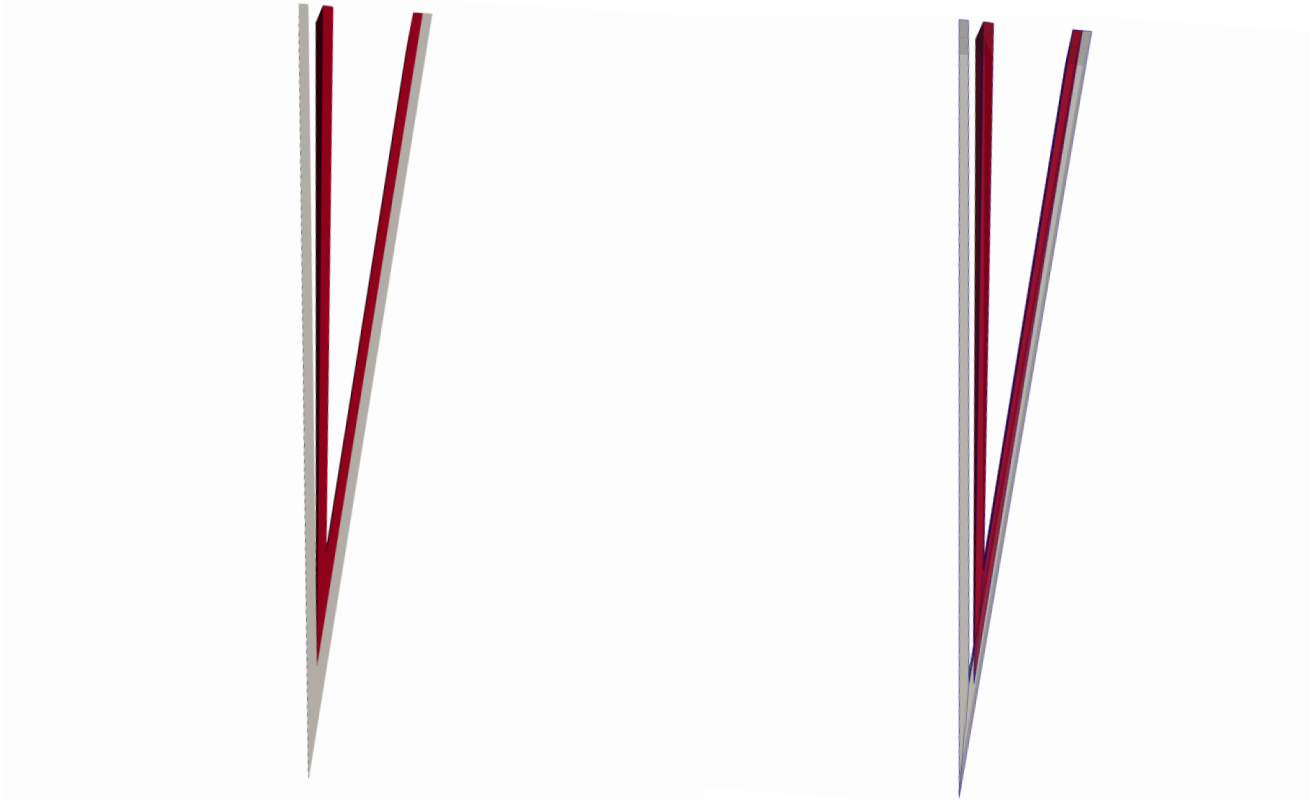

(a) Multiple Auto-Normal (b) Single Contact Normal

Figure 4.69: Deformed mesh configuration (magnified 20000 times) at the end of shear load stage for simulations done using (a) Auto-Normal (b) Only one normal contact elements for corner angle of 10^o.

mesh as shown in Figure 4.72, single normal contact would lead to have a no-contact region and thus would result in erroneous result. However, for completely flat interface, the no-contact region as shown in Figure 3.9 will completely vanish resulting in same deformation for both type of contacts.

(a) Multiple Auto-Normal (b) Single Contact Normal

Figure 4.70: Deformed mesh configuration (magnified 20000 times) at the end of shear load stage for simulations done using (a) Auto-Normal (b) Only one normal contact elements for corner angle of 60^o.

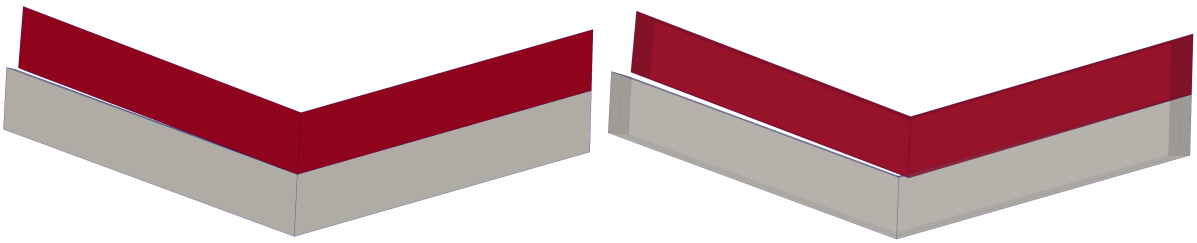

(a) Multiple Auto-Normal (b) Single Contact Normal

Figure 4.71: Deformed mesh configuration (magnified 20000 times) at the end of shear load stage for simulations done using (a) Auto-Normal (b) Only one normal contact elements for corner angle of 150^o.

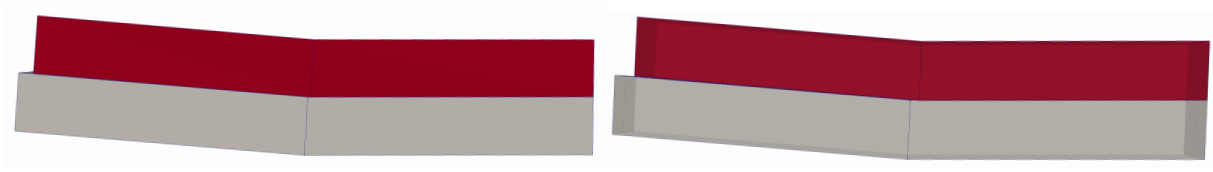

(a) Multiple Auto-Normal (b) Single Contact Normal

Figure 4.72: Deformed mesh configuration (magnified 20000 times) at the end of shear load stage for simulations done using (a) Auto-Normal (b) Only one normal contact elements for corner angle of 176^o.

(a) Multiple Auto-Normal (b) Single Contact Normal

Figure 4.73: Deformed mesh configuration (magnified 20000 times) at the end of shear load stage for simulations done using (a) Auto-Normal (b) Only one normal contact elements for corner angle of 180^o.

4.10 Coupled Contact Verification

As described in Section 1.3 and 3.5, coupled contact follows the same formulation as that of a dry contact with additional constraints as summarized below.

- Effective stress principle govern at the interface

$$\sigma'_{ij} = \sigma_{ij} - p \tag{4.24}$$

- Undrained condition in contact normal direction

$$U_n(soil) = u_n(foundation) \tag{4.25}$$

  where U_n is the fluid, and u_n is the solid displacements for soil and foundation in contact normal direction.

Section 4.1 - 4.6 describes the verification procedure for all the components of a dry contact. Since the coupled contact is derived from the dry contact with additional constraints, Equation 4.24 and 4.25 needs to be verified.

Before proceeding towards the verification, it's important to look at the equilibrium equations governing the upU element. The equilibrium equation for upU element with decoupled solid u and fluid U displacements was presented by [Zienkiewicz et al., 1999] as

$$\sigma'_{ij,j} - (\alpha - n)p_{,i} + (1-n)\rho_s b_i - (1-n)\rho_s \ddot{u}_i + nR_i = 0 \tag{4.26}$$

where σ'_{ij} is the effective stress, p is the fluid pore pressure, α is the material pore-pressure parameter and is equal to $\alpha = 1$ for soil, ρ_s is the solid density, ρ_f is the fluid density, b is the body force per unit mass, R is the seepage force per unit volume and $u(t)$ is the displacement field.

For very slow loading conditions or steady state, the above Equation 4.26 can be simplified as

$$\sigma'_{ij,j} - (1-n)p_{,i} = 0 \tag{4.27}$$

where n is the porosity of the mixture. For soil, the material pore pressure parameter α is taken as $\alpha = 1$. Thus, Equation 4.26 and 4.27 represents the equilibrium equations for dynamic and steady state conditions.

4.10.1 Soil-Foundation Interface

For verification, a soil-foundation system is considered as illustrated in Figure 4.74. The problem consists of a foundation placed on the top of a fully saturated soil. A uniform surface load $\boldsymbol{P}$ is applied to the foundation. For compressive load, both the solid and fluid parts of the soil move together with the foundation as shown in Figure 4.74a Whereas for tensile loading condition, the fluid could be sucked up, thus creating a negative pore-pressure and effective-stress as shown in Figure 4.74b because of the drag force R.

In the above problem, since a normal surface load P is added to the foundation, the effective stress principle at the interface can be written as

$$\sigma'_{ij} = \sigma_{ij} - p \tag{4.28}$$

$$\sigma^{upU}_{zz} = \sigma^{u}_{zz} - p \tag{4.29}$$

$$\sigma^{upU}_{zz} = \boldsymbol{P} - p \tag{4.30}$$

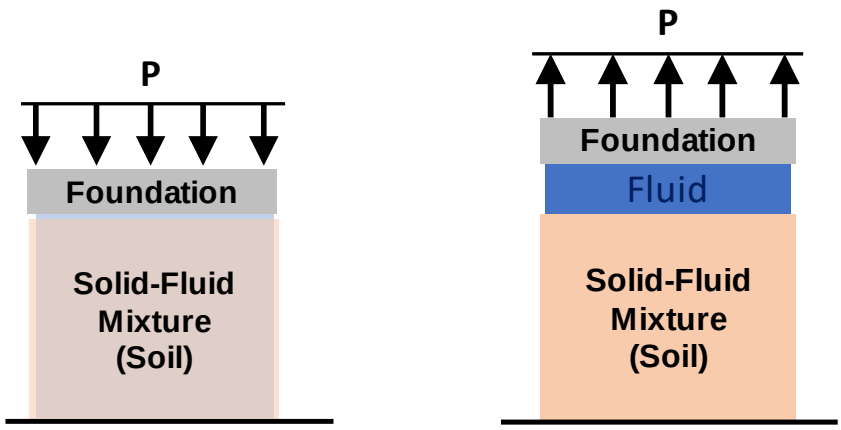

(a) Compression (b) Tension

Figure 4.74: Illustration of soil-foundation system under compressive and tensile loading conditions.

where σ_{zz}^{upU} refers to the traction at the interface in z-direction and p is the pore-fluid pressure. For compression $\boldsymbol{P} < 0$ and for tension $\boldsymbol{P} > 0$. The effective stress principle shown in Equation 4.30 is valid for both compression and tension loading cases. For tensile loading, the pore-pressure in the fluid would depend on porosity n and can be written as

$$p = \frac{\boldsymbol{P}}{n} \tag{4.31}$$

The above Equation 4.31 can be obtained by the force equilibrium in contact normal direction. Equation 4.30 and 4.31 can be used to verify the effective stress principle and undrained conditions at the interface boundary using a single element model as shown in Figure 4.75.

The model consists of an 8-node brick element to represent the foundation and an 8-node brick upU elements to represent the soil below it. Coupled soft contact elements are applied to each node pairs at the soil-foundation interface. The bottom nodes of upU element are fixed for all solid u and fluid U in translational (x,y,z) degrees of freedom. Similarly, the side nodes are fixed in x and y translational degrees of freedom. The contact normal direction is taken as positive $+z$ direction. Similar to Section 4.4, to have the same response of stress based and force based contact, the shear zone thickness is

taken as $SZ_h = 1m$ so that the magnitude of normal strain ϵ is equal to penetration Δ_n. If the shear zone thickness SZ_h is decreased, the corresponding normal strain ϵ would increase for a given penetration Δ_n. Thus, in order to have same stiffness k_n and normal force F_n as before, the stiffening rate S_r should be adjusted by lowering it by the same magnitude such that $S_r \times \epsilon$ is constant. The size of the soil and foundation brick elements are $1m \times 1m \times 1m$ and a uniform surface load of $\boldsymbol{P} = 400Pa$ is applied to the foundation. For this problem, the foundation can be assumed to be very stiff or rigid, thus transferring all the stresses to the contact element and then to the soil. Table 4.1 summarizes the properties of soil (solid-fluid mixture) used in the simulation. The density of fluid (water) is taken as $\rho_f = 1000kg/m^3$ with bulk modulus of $K_{fluid} = 2.16e^5kPa$. The solid particles of soil are quartz with specific gravity of $G_s = 2.6$ and bulk modulus of $K_{solid} = 50e^6kPa$. The porosity of the soil was $n = 30\%$ and Biot's coefficient $\alpha = 1$ was used.

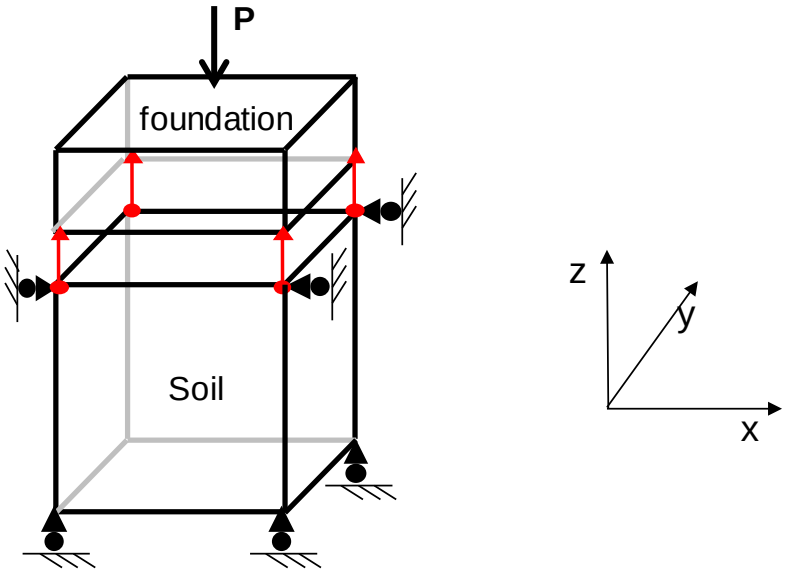

Figure 4.75: Illustration of soil-foundation system under compressive and tensile loading conditions.

The initial normal stiffness k_i is taken as $k_i = 100MPa$ with stiffening rate of $S_r = 1000$ and maximum normal stiffness of $k_n^{max} = 10GPa$. The shear stiffness is taken as $k_t = 10MPa$. For enforcing the undrained condition, the penalty stiffness k_p is taken

Table 4.1: Soil-Mixture parameters

Fluid (Water)		Solid (Quartz)				
Density	Bulk Modulus	Density	Bulk Modulus	Permeability	Porosity	Biot Coefficient
$\rho_f[kg/m^3]$	$K_{fluid}[MPa]$	$\rho_s[kg/m^3]$	$K_{solid}[MPa]$	$k[m/s]$	$n[\%]$	α
1000	216	2650	$5e^4$	$1e^{-4}$ to $1e^{-8}$	50	1

as $k_p = 10GPa$, equal to the maximum normal stiffness k_n^{max}. In the simulations, no numerical or viscous damping is applied. Time step Δt for the simulation is taken small enough as described in Section 4.4.

For the coupled soft contact variation, the initial penalty stiffness k_i and the stiffening rate S_r is varied in simulations. It must be noted that the normal penalty stiffness k_p is set to be high value of $k_p = 10GPa$, to ensure that no drainage is allowed between the *upU_U* and *u_u* dof. A smaller value of k_p would result in some relative displacement in fluid resulting in partial drainage.

4.10.2 Steady State Verification

To verify the steady stage behavior, the surface load $\boldsymbol{P} = 400Pa$ is applied very slowly in total time of $t = 1000s$. The response of contact element are then verified for different porosities, n, of soil. The porosities, n considered here are $n = 0.3$ and $n = 1$.

4.10.2.1 Compressive Loading

When a compressive load is applied to the foundation, all the load transferred to the soil is taken by the fluid. The solid, fluid and the foundation undergo the same vertical displacement. Figure 4.76 and 4.83 shows the response at the interface for porosities of $n = 0.3$ and $n = 1$. Porosity $n = 1$ represents fluid. Soft contact was used with the initial normal stiffness k_i varied from $k_i = 100MPa$ to $k_i = 10GPa$ keeping the stiffening rate S_r constant to $S_r = 1000$. Similarly, in another case stiffening S_r is varied from $S_r = 1e^3$ to $S_r = 1e^9$ keeping initial normal stiffness k_i as $100MPa$. The penalty stiffness k_p is chosen big enough $k_p = 10GPa$ to enforce the undrained condition. The maximum normal stiffness k_n^{max} was also kept constant as $k_n^{max} = 10GPa$.

From the plots shown in Figure 4.76 to Figure 4.83, it could be observed that under no drainage conditions, the response at the interface is the same for the considered different porosities of soil. This is because of the fact that all the load is taken by the fluid which is almost incompressible because of very high bulk modulus K_{fluid}. The plots demonstrate that the effective stress and undrained condition are clearly satisfied. It must be noted that in FEM, the effective stress σ'_{ij} is only calculated at Gauss points. Thus, there will always be a small difference between the real traction at the interface to that inside, however smaller is the element size.

Figure 4.76 to 4.79 shows the response of soft contact for varying initial normal stiffness k_i for porosity $n = 0.3$ and $n = 1.0$ respectively. The total stress, effective stress and pore-pressure in the figures are plotted as positive for compression and negative for compression. From the plots, it can be observed that the effective stress σ' is close to $\sigma' = 0$ for all the cases. Also, the normal penalty stiffness $k_p = 10GPa$ ensures that there is no drainage allowed between upU_U and u_u dofs.

It is interesting to observe that in Figure 4.77 as the initial normal stiffness k_i is increased, the upU_u i.e. the solid displacement becomes closer to the fluid displacement. Since it is a compressive load, a high initial normal stiffness k_i ensures almost no penetration. Whereas a low initial normal stiffness results in some penetration, leading to separation in displacement response of upU_u and u_u. This can be clearly observed in Figure 4.77. As the initial penalty stiffness k_i is increased, the penetration δ_n and relative separation between upU_u and u_u dof becomes smaller and smaller. The similar trend could also be seen in Figure 4.79. However, since the porosity n is very close to 1, the trend is not so prominent as compared to the case with $n = 0.3$. It must be noted that the case of initial normal stiffness $k_i = 10GPa$ also represents a hard contact as the stiffness is equal to maximum normal stiffness k_n^{max} and thus does not change.

Now, the same example is run for different stiffening rate S_r, keeping the initial normal stiffness $k_i = 100MPa$. The response at the interface is shown in Figures 4.80 to 4.83.

From the plots, it could be observed that as the stiffening rate is increased, the contact becomes more of hard type resulting in very small relative penetration between upU_u and

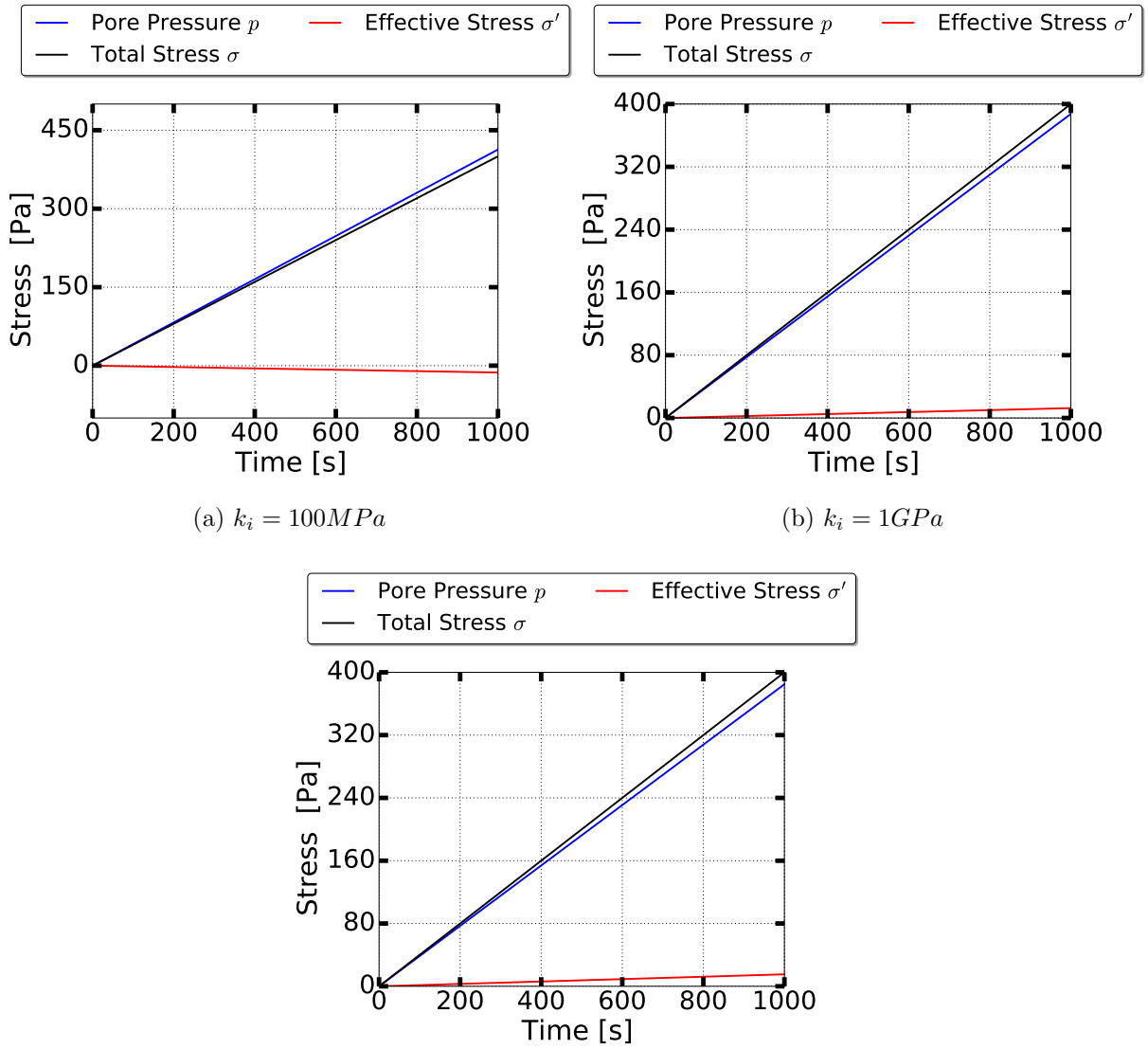

(a) $k_i = 100MPa$

(b) $k_i = 1GPa$

(c) $k_i = 10GPa$

Figure 4.76: Effective stress principle at interface for compressive loading for porosity $n = 0.3$ and stiffening rate $S_r = 1e^3$ with different initial normal stiffness k_i.

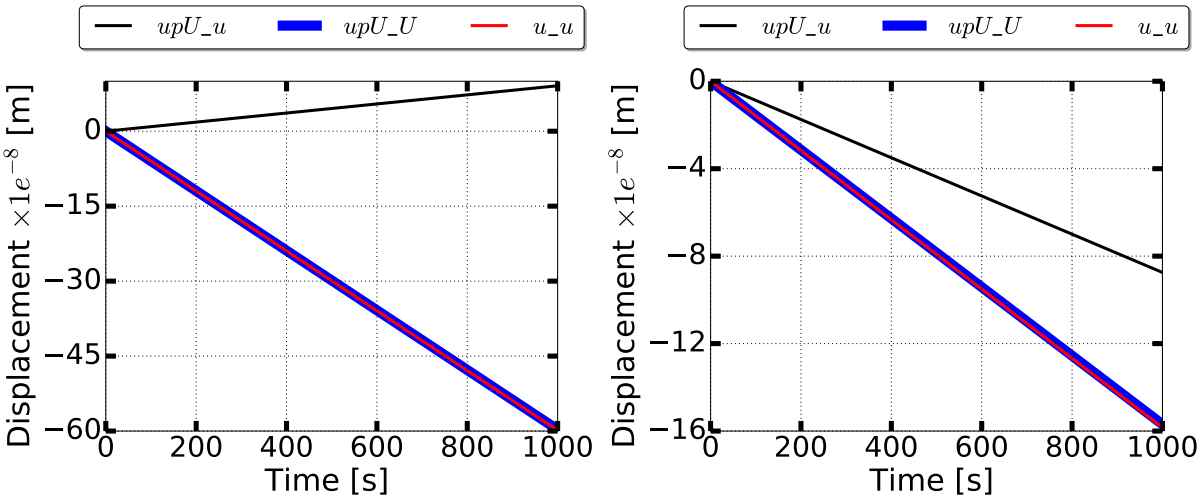

(a) $k_i = 100MPa$

(b) $k_i = 1GPa$

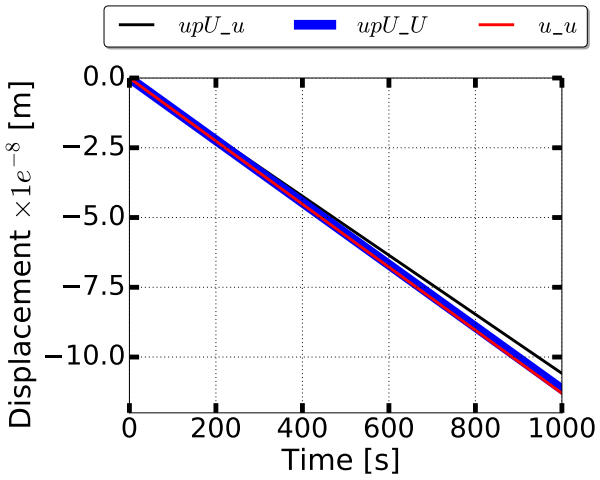

(c) $k_i = 10GPa$

Figure 4.77: Undrained behavior between upU_U and u_u for compressive loading for porosity $n = 0.3$ and stiffening rate $S_r = 1e^3$ with different initial normal stiffness k_i.

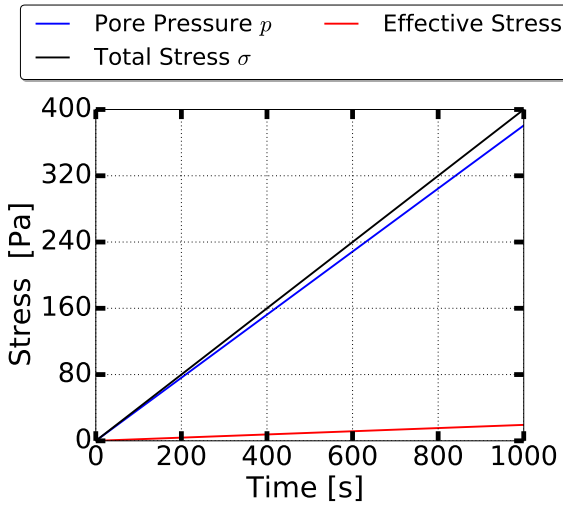

(a) $k_i = 100MPa$

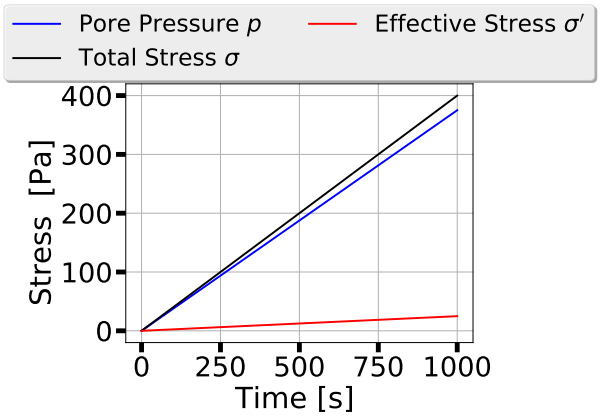

(b) $k_i = 1GPa$

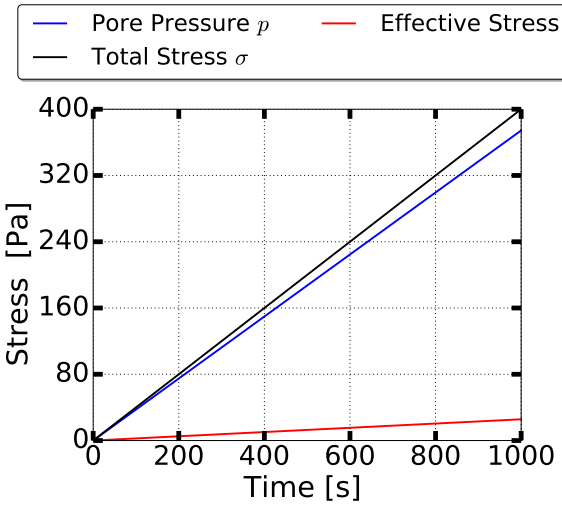

(c) $k_i = 10GPa$

Figure 4.78: Effective stress principle at interface for compressive loading for porosity $n = 1.0$ and stiffening rate $S_r = 1e^3$ with different initial normal stiffness k_i.

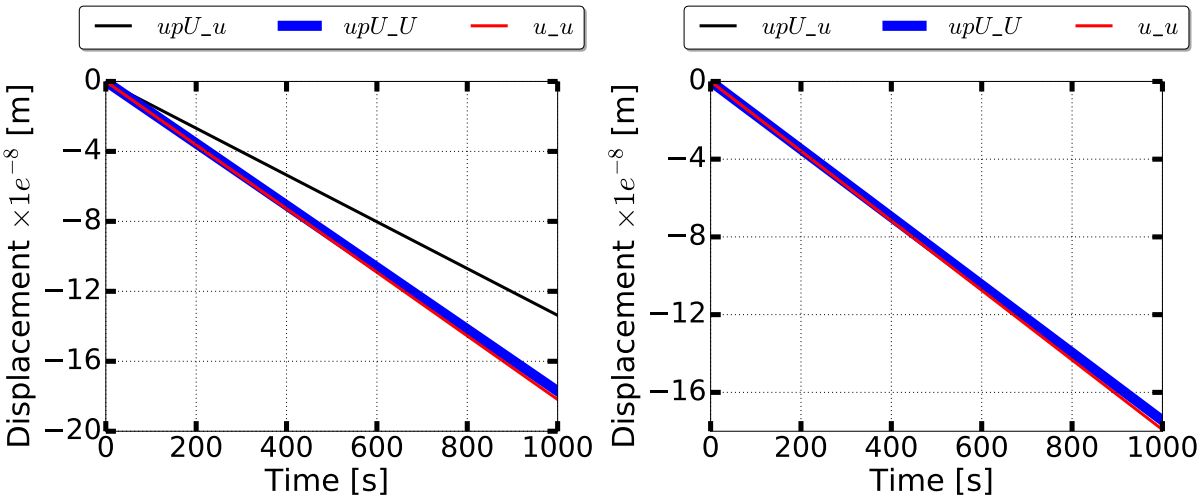

(a) $k_i = 100MPa$

(b) $k_i = 1GPa$

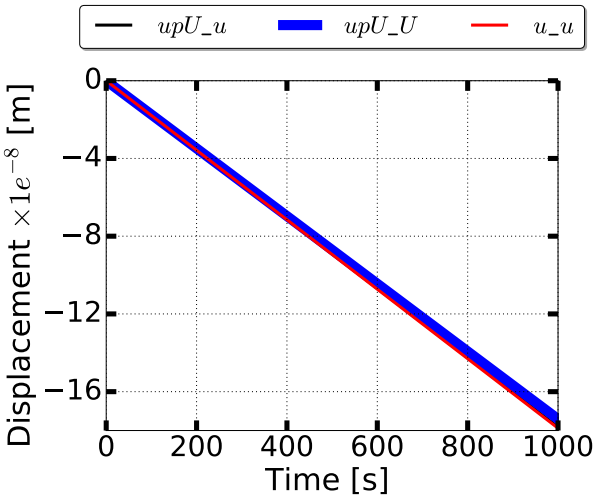

(c) $k_i = 10GPa$

Figure 4.79: Undrained behavior between upU_U and u_u for compressive loading for porosity $n = 1.0$ and stiffening rate $S_r = 1e^3$ with different initial normal stiffness k_i.

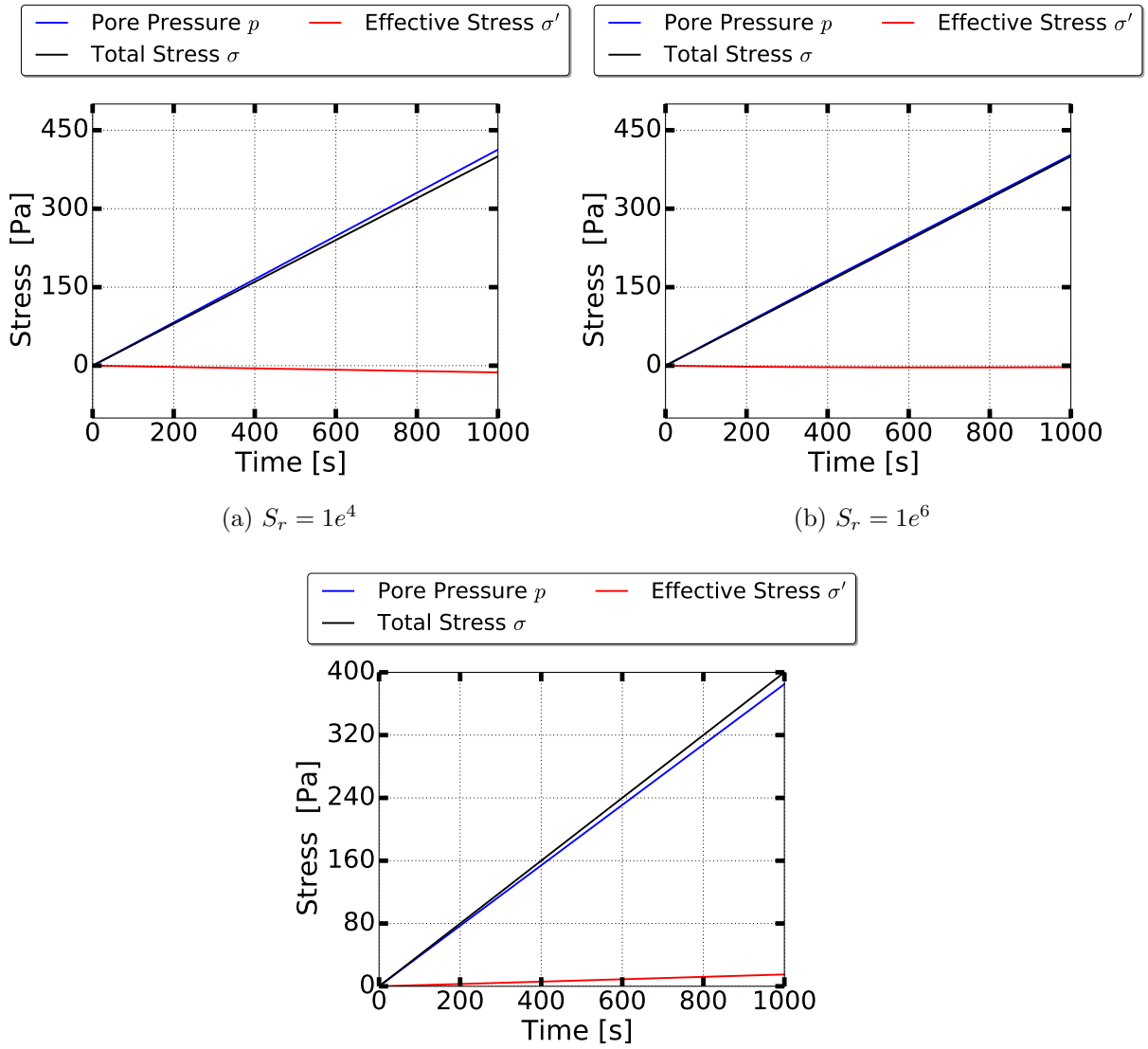

(a) $S_r = 1e^4$

(b) $S_r = 1e^6$

(c) $S_r = 1e^9$

Figure 4.80: Effective stress principle at interface for porosity $n = 0.3$ and initial normal stiffness $k_i = 100MPa$

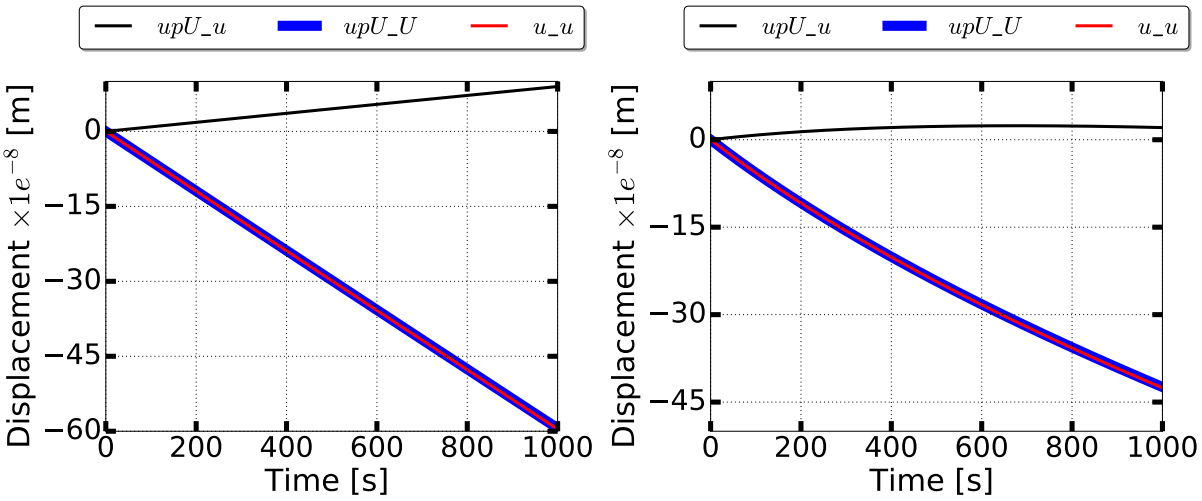

(a) $S_r = 1e^4$

(b) $S_r = 1e^6$

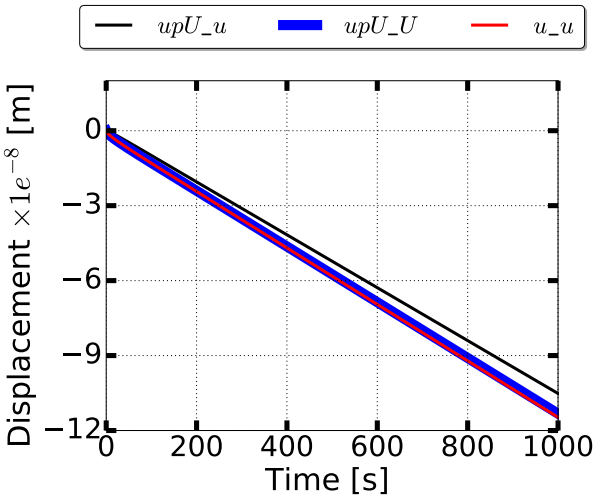

(c) $S_r = 1e^9$

Figure 4.81: Undrained behavior between upU_U and u_u for porosity $n = 0.3$ and initial normal stiffness $k_i = 100MPa$

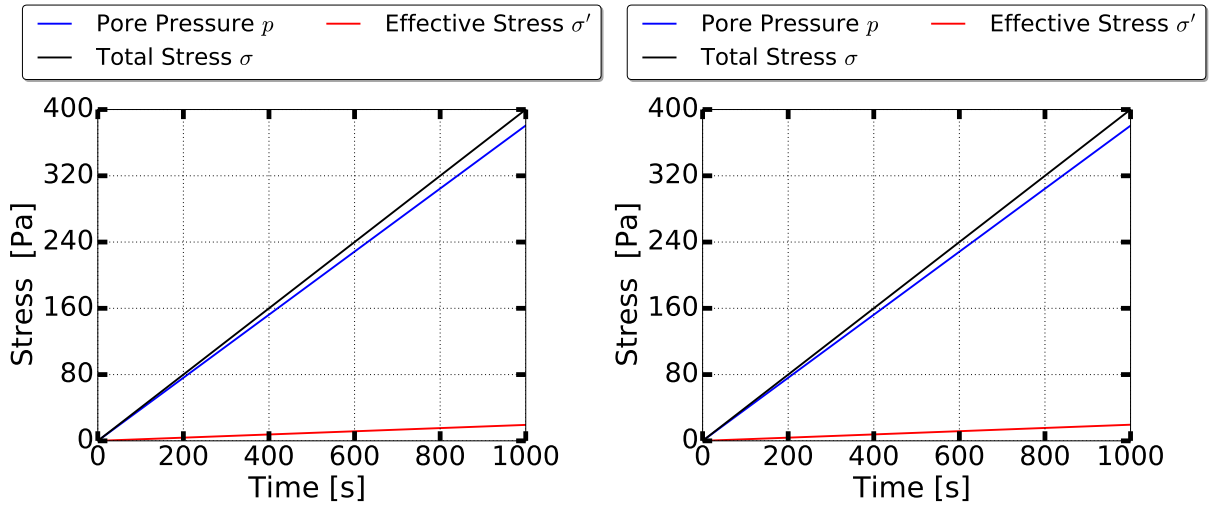

(a) $S_r = 1e^4$ (b) $S_r = 1e^6$

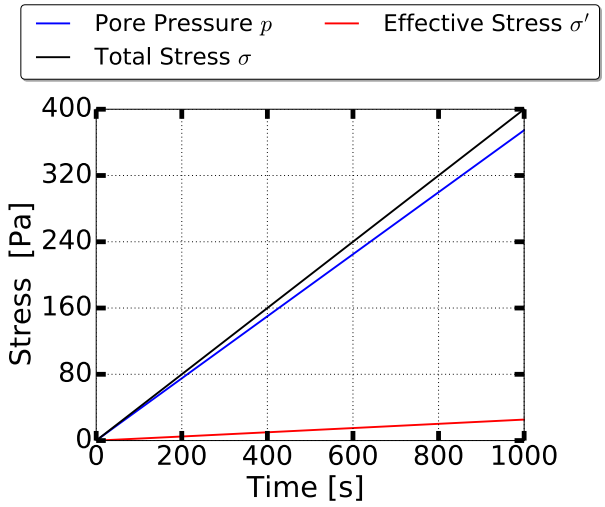

(c) $S_r = 1e^9$

Figure 4.82: Effective stress principle at interface for tensile loading condition for porosity $n = 1.0$ and initial normal stiffness $k_i = 100MPa$with different normal penalty stiffness k_p.

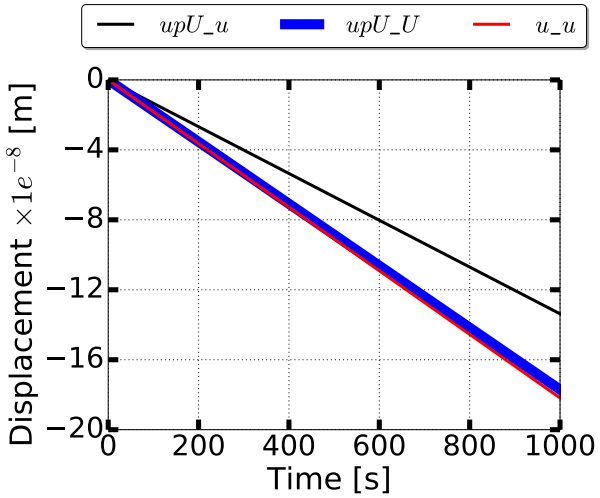

(a) $S_r = 1e^4$

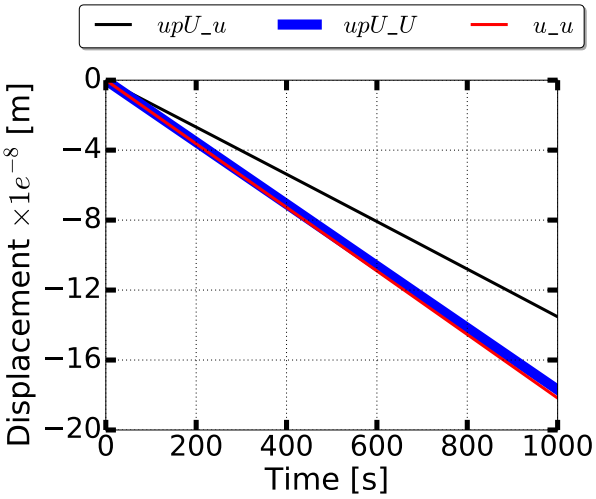

(b) $S_r = 1e^6$

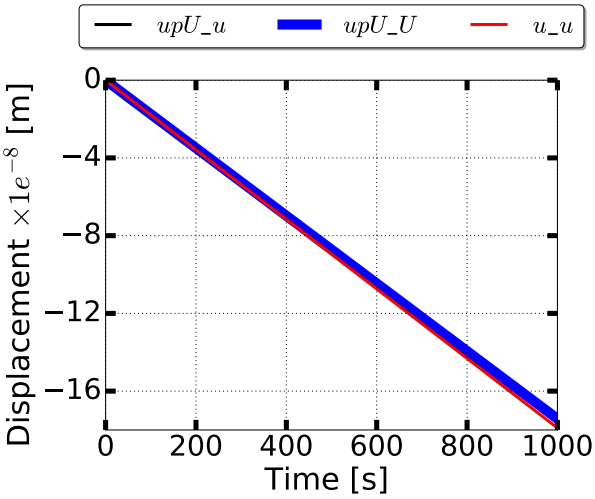

(c) $S_r = 1e^9$

Figure 4.83: Undrained behavior between upU_U and u_u for tensile loading condition for porosity $n = 1.0$ and initial normal stiffness $k_i = 100MPa$ with different normal penalty stiffness k_p.

u_u degrees of freedom (dof). The effective stress principle is always satisfied. However, for low stiffening rate S_r, there is small relative displacement (penetration) between the upU_u and u_u dof. As described earlier, the effects are comparatively minimized as the porosity n in soil is increased.

It must be realized that for undrained simulations, since most of the load is taken by the fluid (water), a small penetration of order of $1e^{-6}m$ is observed in upU_u and upU_U as shown in Figures 4.81 and 4.83. Thus, to increase the normal contact stiffness k_n, a small value of S_r would not produce any significant effect. In such cases, either initial stiffening rate k_i or S_r should be correspondingly increased as per Equation 2.7, to get the correct stiffness for allowable penetration Δ_n.

4.10.2.2 Tensile Loading

In Section 4.10.2.1, it was showed that how initial normal stiffness k_i and stiffening rate S_r effects the response at the interface. Sufficiently high normal penalty stiffness k_p would ensure the correct effective stress development and undrained conditions at interface. Section 4.12.1 describes how to pick the correct penalty stiffness. Here, only initial normal stiffness k_i is varied keeping $S_r = 1e^3/m$. The normal penalty stiffness k_p is taken as $k_p = 10GPa$. For tensile loading conditions, the fluid would be sucked up creating tension in both fluid and solid. As a result the pore-pressure in the fluid and effective stress would be negative. Also, because of the drag force the solid u would settle having its displacement opposite to the fluid displacement U. Because of the tensile loading, the total stress σ becomes negative $\sigma = -400Pa$.

As shown in Equation 4.31, the pore-pressure can be calculated as $\boldsymbol{P}/n$. Thus, for porosity of $n = 0.3$, the pore-pressure in the fluid would be $p = \frac{-400Pa}{0.3} = -1333Pa$. And similarly, for porosity $n = 1$ the pore pressure p is $p = -400Pa$. This is verified from Figures 4.84 and 4.88.

Since the coupled contact element enforces no drainage condition in contact normal direction upU_U and u_u displacements are always equal for both the values of porosities $n = 0.3$ and $n = 1$. For porosity $n = 1$ (fully fluid), there is no solid displacement. The effective stress principle is also verified as could be seen in Figures 4.86 and 4.88.

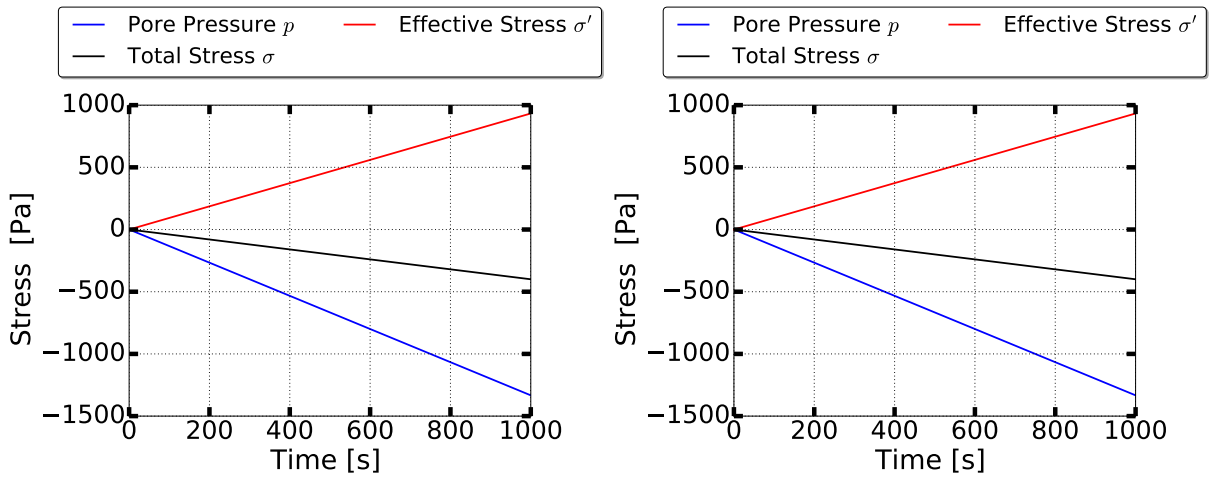

(a) $k_i = 100MPa$

(b) $k_i = 1GPa$

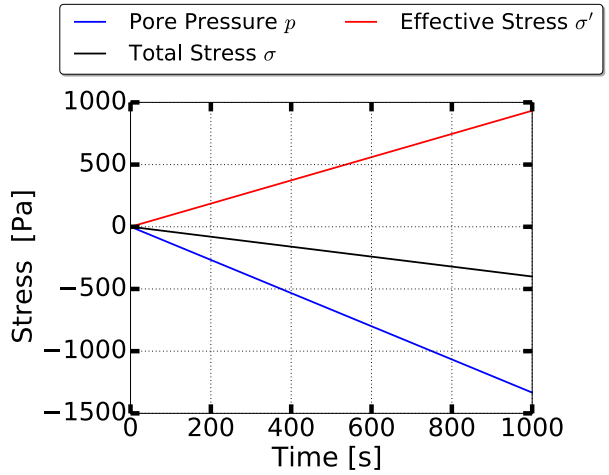

(c) $k_i = 10GPa$

Figure 4.84: Effective stress principle at interface for tensile loading condition for porosity $n = 0.3$, max normal stiffness $k_n^{max} = 10GPa$, stiffening rate $S_r = 1e^3$ and penalty stiffness $k_p = 10GPa$ for different initial normal stiffness k_i.

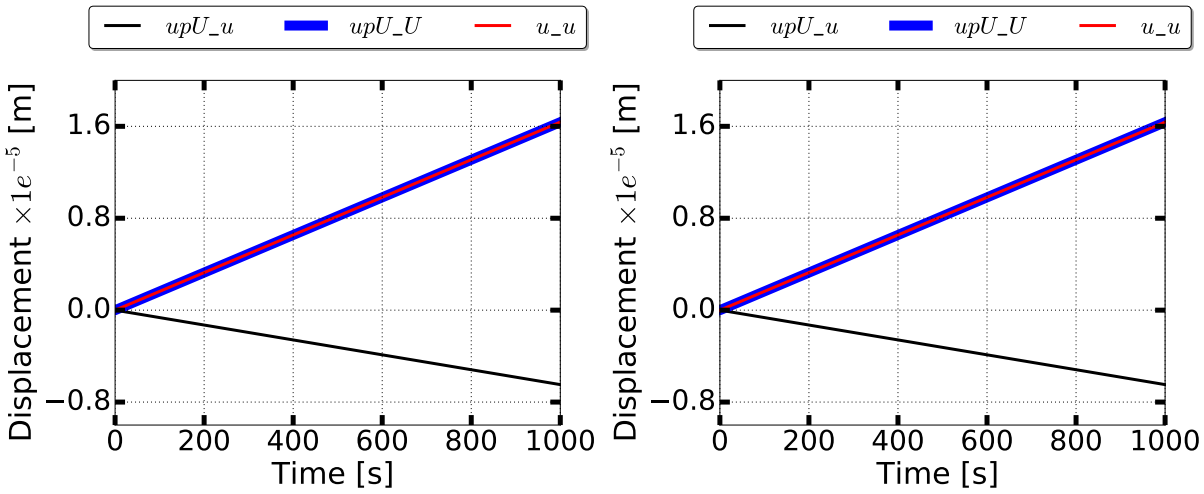

(a) $k_i = 100MPa$

(b) $k_i = 1GPa$

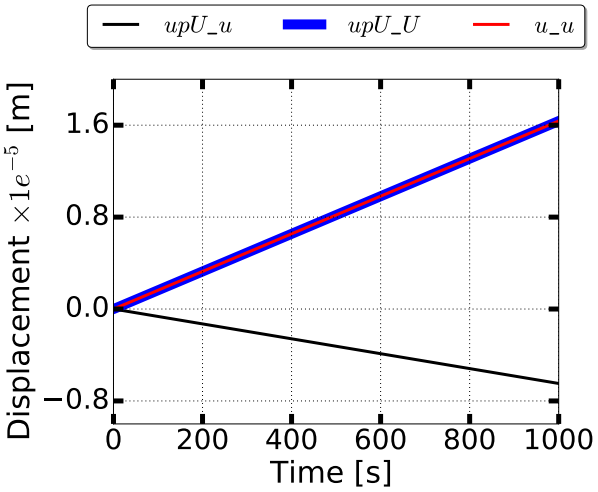

(c) $k_i = 10GPa$

Figure 4.85: Undrained behavior between upU_U and u_u for tensile loading condition for porosity $n = 0.3$, max normal stiffness $k_n^{max} = 10GPa$, stiffening rate $S_r = 1e^3$ and penalty stiffness $k_p = 10GPa$ for different initial normal stiffness k_i.

Figures 4.84 and 4.85 show that there is no effect of initial normal stiffness k_i on interface response. This is because of the no-contact condition during tensile loading. In this case, the normal contact stiffness becomes zero.

However, in the coupled contact formulation the fluid is allowed to be pulled up during uplift. Thus, the penalty stiffness k_p comes into effect. Figure 4.86 to 4.89 shows the response of coupled soft contact for varying normal penalty stiffness k_p for porosity $n = 0.3$ and $n = 0.99$. It can be observed from the plots that the effective stress principle always holds. However, for low penalty stiffness $k_p = 100MPa$, there is a small relative displacement between upU_U and u_u dofs.

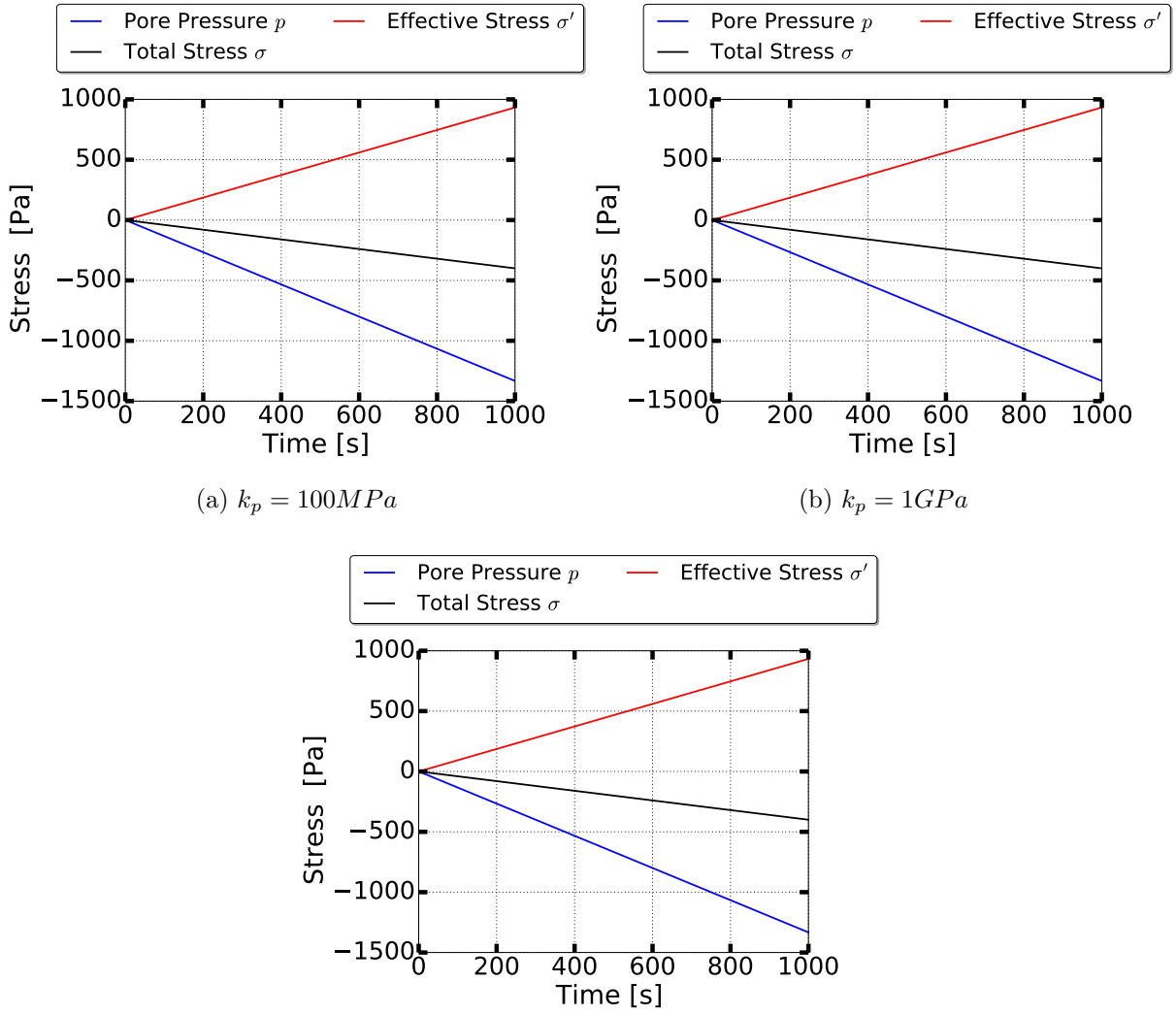

(a) $k_p = 100MPa$

(b) $k_p = 1GPa$

(c) $k_p = 10GPa$

Figure 4.86: Effective stress principle at interface for tensile loading for porosity $n = 0.3$ with different normal penalty stiffness k_p.

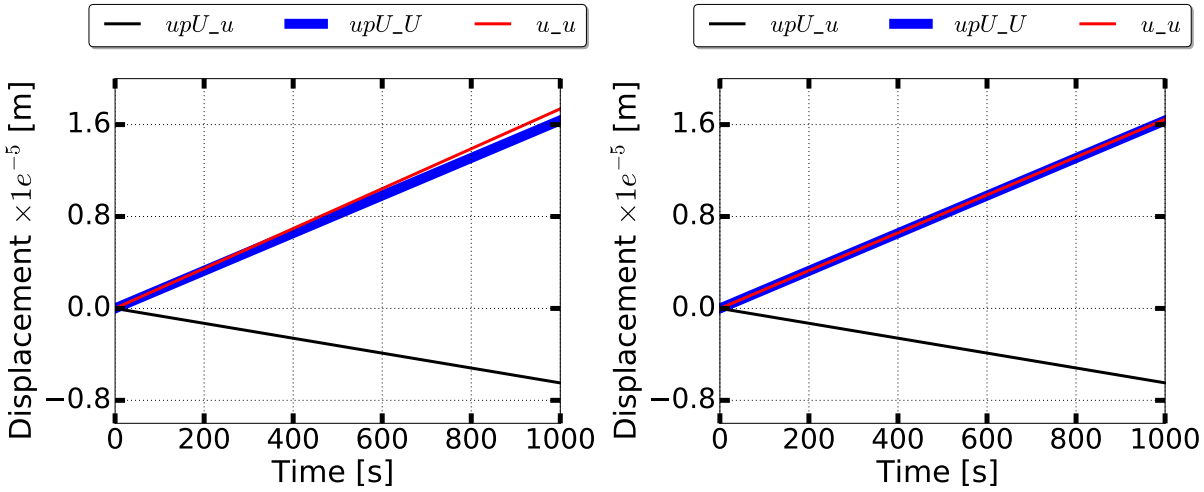

(a) $k_p = 100MPa$

(b) $k_p = 1GPa$

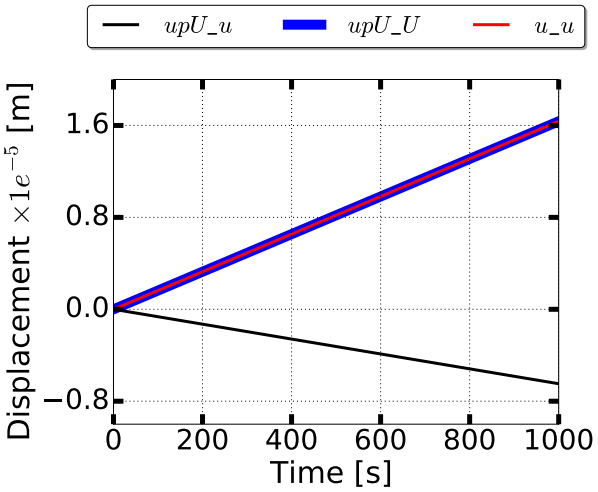

(c) $k_p = 10GPa$

Figure 4.87: Undrained behavior between upU_U and u_u for tensile loading for porosity $n = 0.3$ with different normal penalty stiffness k_p.

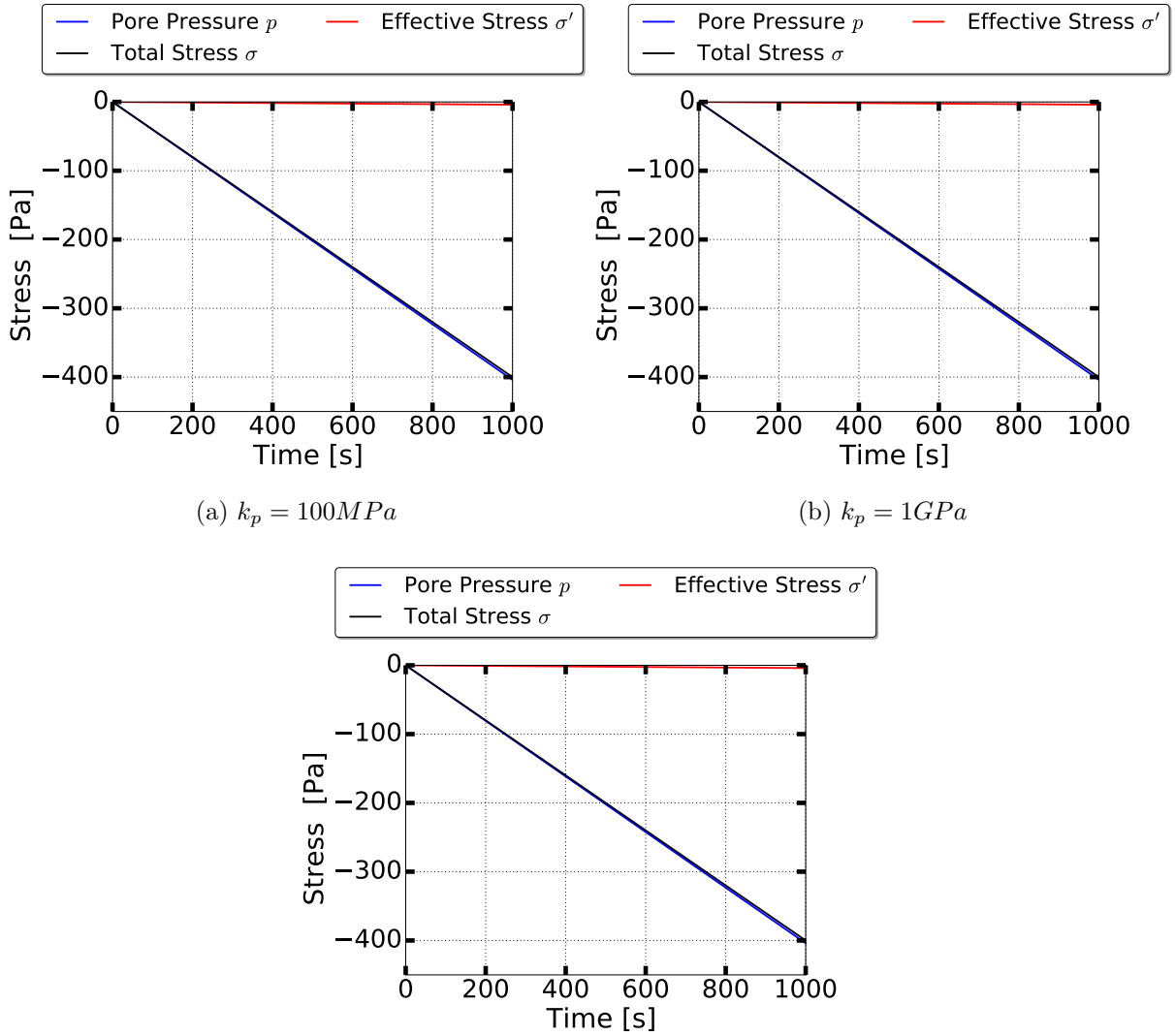

(a) $k_p = 100MPa$

(b) $k_p = 1GPa$

(c) $k_p = 10GPa$

Figure 4.88: Effective stress principle at interface for tensile loading for porosity $n = 0.99$ with different normal penalty stiffness k_p.

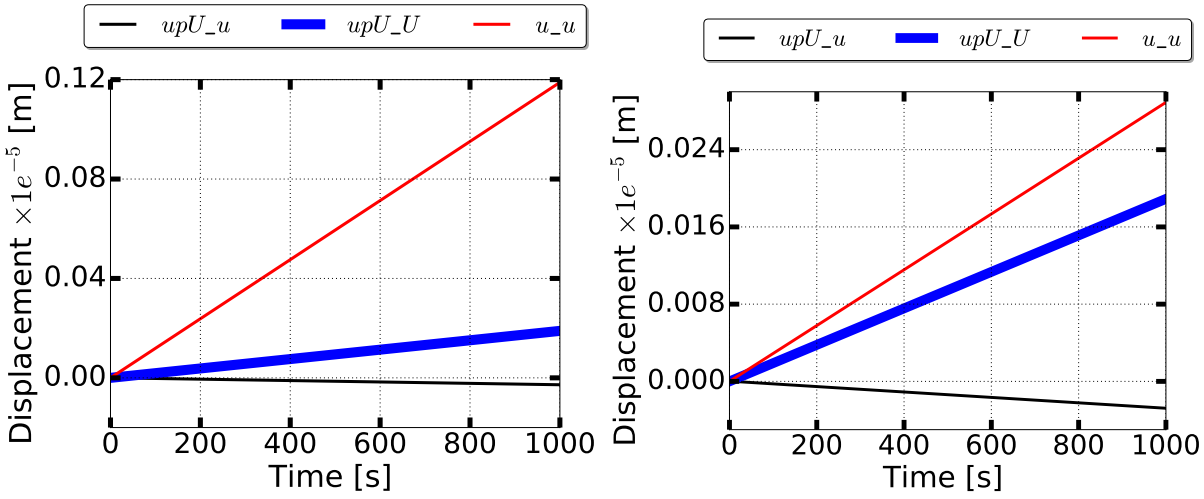

(a) $k_p = 100MPa$

(b) $k_p = 1GPa$

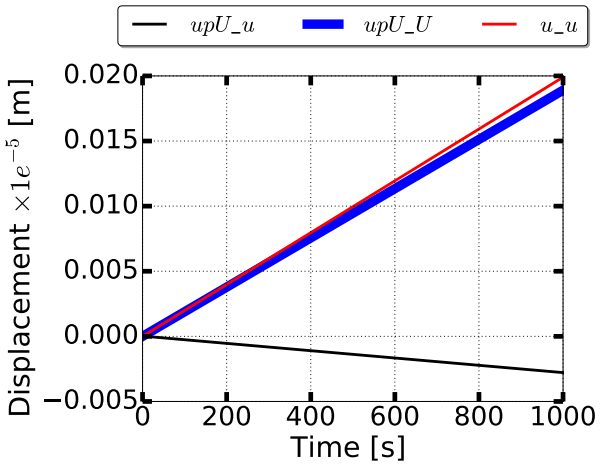

(c) $k_p = 10GPa$

Figure 4.89: Undrained behavior between upU_U and u_u for tensile loading for porosity $n = 0.99$ with different normal penalty stiffness k_p.

4.10.3 Dynamic Simulation Verification

Section 4.10.2 considered the steady state verification with no involvement of acceleration. Here, the dynamic response with two loading stages, one with the application of surface load $\boldsymbol{P}$, and the other with consolidation stage is used to verify the coupled contact. In addition to this, comparisons are made with the dry contact element where undrained condition in contact normal direction is not enforced.

Coupled soft contact was used with initial normal stiffness $k_i = 100MPa$ and stiffening rate $S_r = 1e^3$. The penalty k_p and maximum normal stiffness k_n^{max} was taken as $k_n^{max} = 10GPa$ and $k_p = 10GPa$ respectively.

Here, the same loading of $\boldsymbol{P} = 400Pa$ is applied to the foundation. Scenarios with different permeabilities are chosen to verify the behavior of coupled contact element. The porosity n of the soil is fixed to $n = 0.5$. Three cases of permeabilities, $k = 1e^{-4}m/s$, $k = 1e^{-6}m/s$ and $k = 1e^{-8}m/s$ are considered as shown in Figure 4.91, Figure 4.92 and Figure 4.93 respectively. The permeabilities represent a wide range of soil type from gravel to clay.

The analysis consists of two loading stages. In the first stage, the surface load is applied within 1 second. In the second stage, the system is left to consolidate with time. Since for the coupled contact, no drainage is allowed in contact normal direction, no consolidation takes place. The pore-pressure p remains close to $p = 400Pa$ with very small effective stress $\sigma' \approx 0$. Whereas on the other hand, for the dry contact, because of no enforcement of undrained conditions, excess pore pressure generated in the first loading stage is dissipated leading to settlement and gain of effective stress σ' up-to $\sigma' = 400Pa$.

Figure 4.90 plots the effective stress σ', pore fluid pressure p, fluid displacement U and settlement u in the soil for both coupled and dry contacts for permeability $k = 1e^{-4}m/s$. From the plot, it could be observed that the excess pore pressure increases in the first loading stage for both the type of contacts. However, since the permeability $k = 1e^{-4}m/s$ is too high, the dry contact dissipated some of the excess pore pressure during the first stage itself. Whereas, the coupled contact does not dissipate any pore-pressure. Figure 4.91 to 4.93 plots and compares the excess pore pressure, solid displacement and

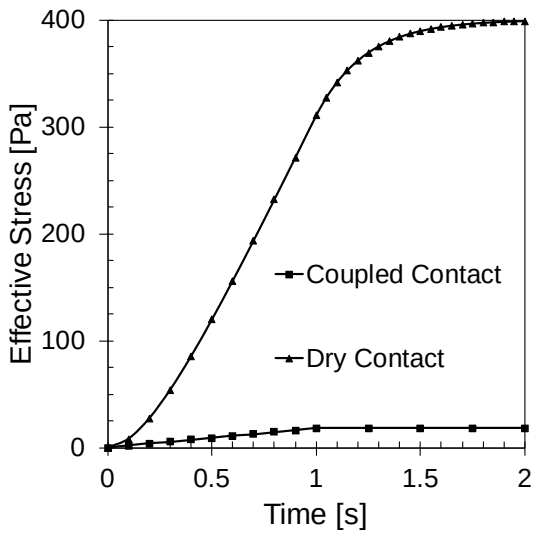

(a) Effective Stress σ'

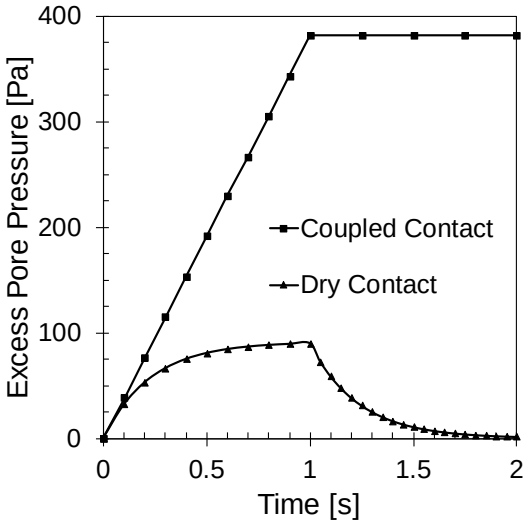

(b) Pore Pressure p

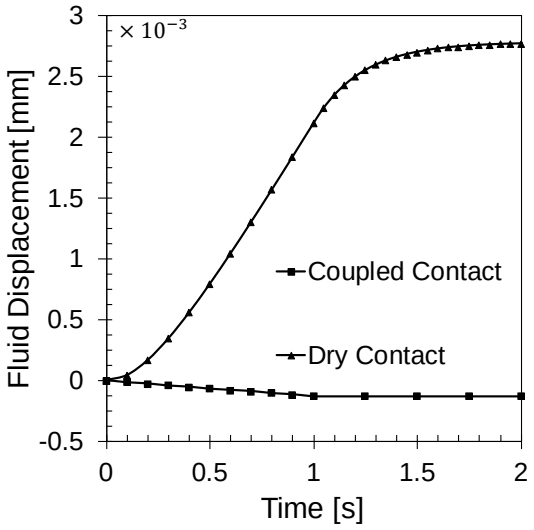

(c) Fluid Displacement

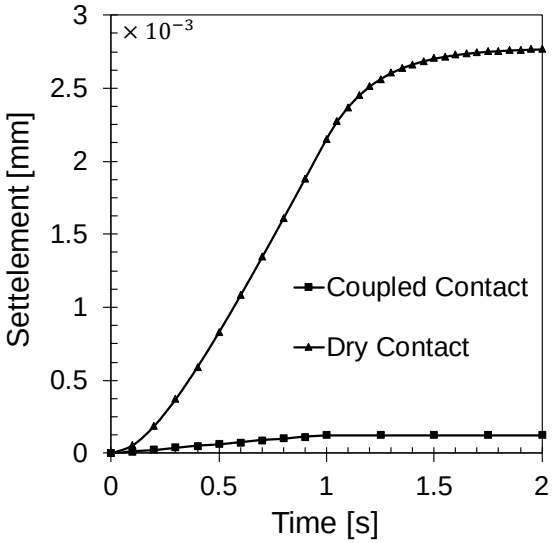

(d) Solid Settlement

Figure 4.90: Response at soil-foundation interface for permeability $k = 1e^{-4}m/s$.

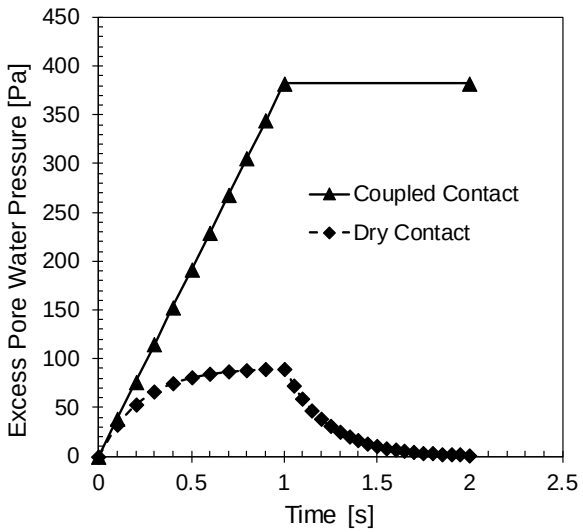

(a) Excess Pore Pressure

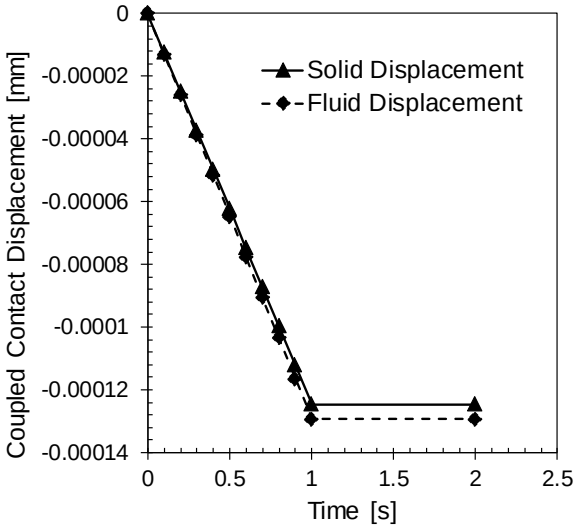

(b) Coupled Contact Displacement

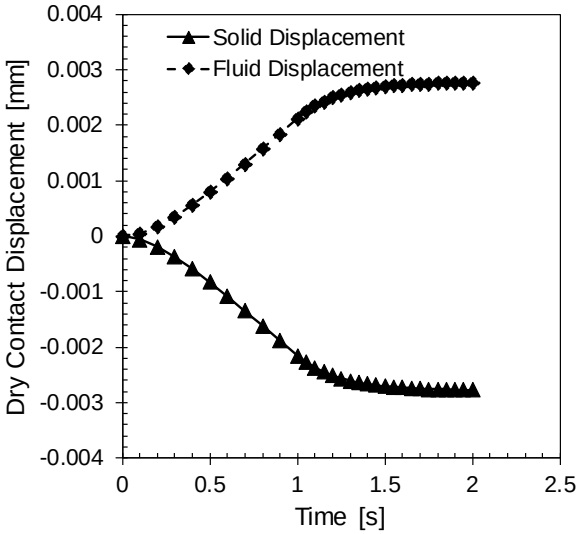

(c) Dry Contact Displacement

Figure 4.91: Response at saturated soil-foundation interface for permeability of $k = 1e^{-4}m/s$.

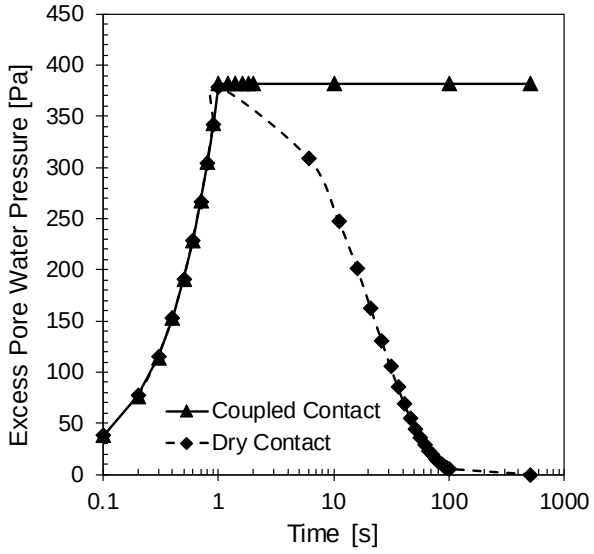

(a) Excess Pore Pressure

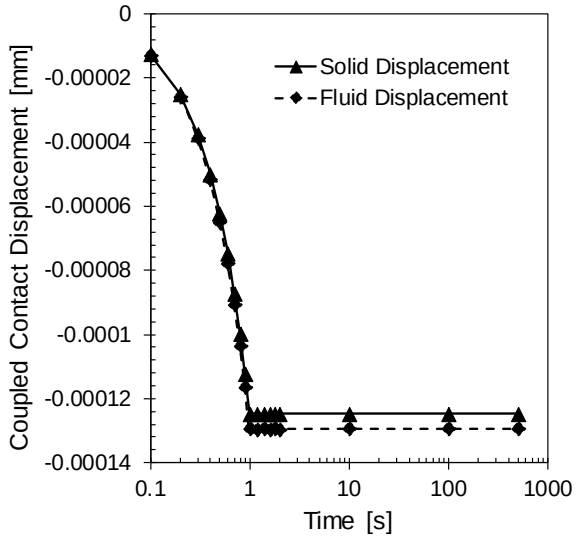

(b) Coupled Contact Displacement

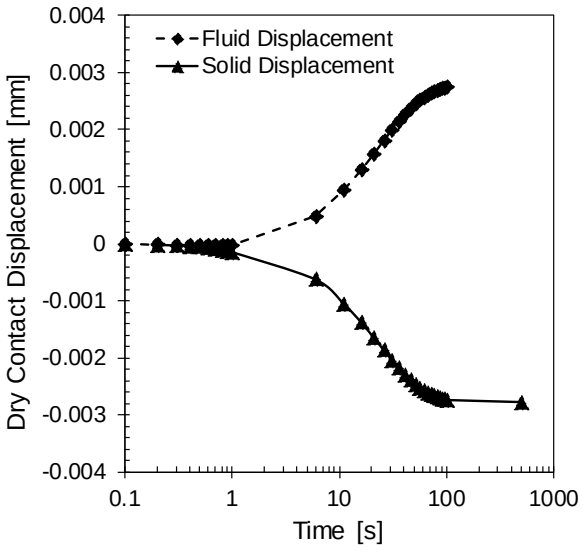

(c) Dry Contact Displacement

Figure 4.92: Response at saturated soil-foundation interface for permeability of $k = 1e^{-6}m/s$.

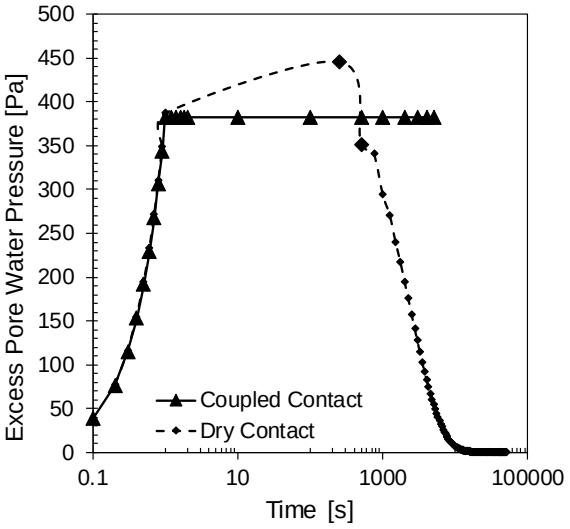

(a) Excess Pore Pressure

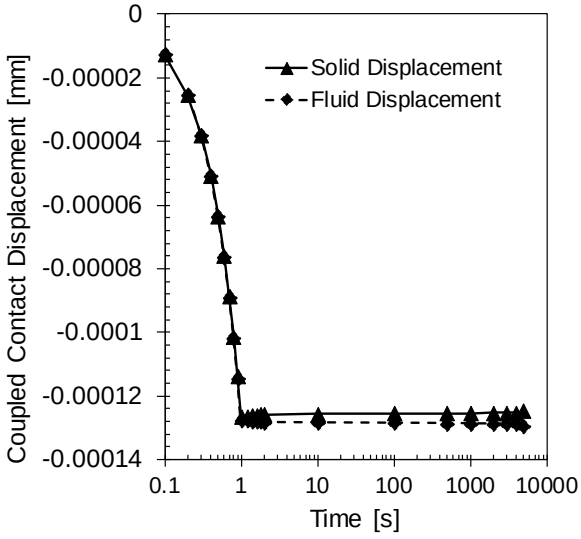

(b) Coupled Contact Displacement

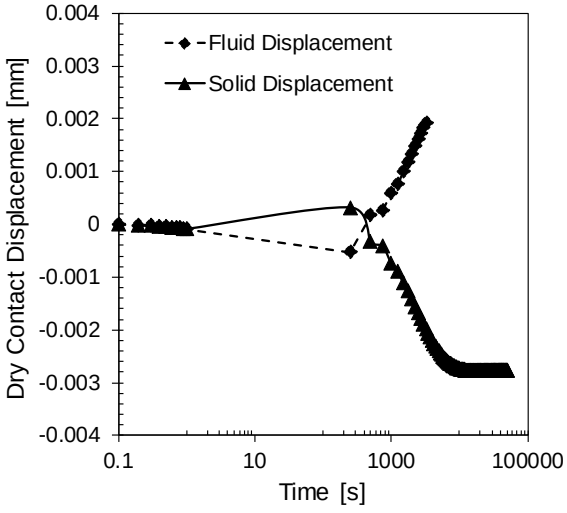

(c) Dry Contact Displacement

Figure 4.93: Response at saturated soil-foundation interface for permeability of $k = 1e^{-8}m/s$.

fluid displacement for both the type of dry and coupled contact for different permeabilities of soil. For low permeability soil $k = 1e^{-6}m/s$ and $k = 1e^{-8}m/s$, there is no dissipation of excess pore-pressure for both coupled and hard contact in the initial loading stage. However, in the second stage, the dry contact dissipated the excess pore-pressure by allowing the fluid to move up below the foundation. The coupled contact maintains the excess pore-pressure generated as there is no path for fluid to move. In both the cases, the effective stress principle σ' is satisfied.

From the plots, it could be observed that for the coupled contact, both solid and fluid displacements are equal and the effective stress is very close to zero thus verifying both the constraints presented in Equation 4.30 and 4.25. The excess pore-pressure remains constant in the second loading stage as it cannot dissipate below the foundation because of the applied no-drainage constraint. Whereas for dry contact, from the initial stage only, the effective stress starts to build up because of drainage (movement) of water in contact vertical direction. The same effect is also seen for different permeability cases considered. This verifies the coupled contact dynamic behavior.

It must also be remarked that the coupled contact can also be used to model the partially saturated soil as demonstrated in [Behbehani, 2017].

4.11 Validation of the Proposed Interface Shear Model

Section 2.4 introduced the three contact models with increasing level of sophistication and modeling parameters. The NLHS and NLHSS models are proposed to capture the shear behavior at the soil-structure interface. The models were developed based on the experimental evidence as described in section 1.4.1. This section validates the proposed model for monotonic and cyclic shear behavior by comparison with the experimental tests from Uesugi et al. [1989]; Fakharian and Evgin [1996]; Shahrour and Rezaie [1997].

Table 4.2 lists the interface model parameters considered for various validation plots. The interface shear zone thickness was taken as $SZ_h = 5mm$. Figure 4.94 and 4.95 shows the test results as well as the model response for loose $D_r = 25\%$ and dense

soil $D_r = 80\%$ at a rough sand-steel interface. Non-linear hardening-softening shear (NLHSS) model was used to model the interface shear response. The plot shows that the model is able to capture the peak normalized shear strength and the softening behavior. Being a simplistic model with comparatively fewer parameters than the advanced models presented in Section 2.4, the model performs quite well. It can be seen that for cyclic loading condition as shown in Figure 4.95(b), the model predicts comparatively higher stiffness. This is because the model doesn't have any internal variables that could model cyclic degradation. However, the model could be extended to capture cyclic degradation by introducing more internal variables and making it dependent on number of cycles or amount of energy dissipated.

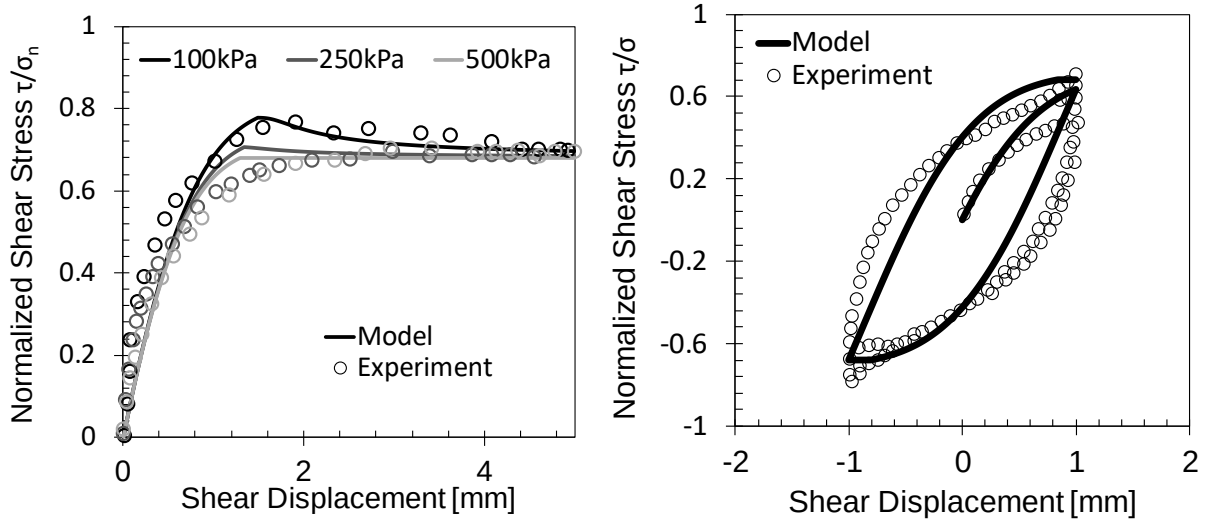

(a) Monotonic (b) Cyclic

Figure 4.94: (a) Monotonic and (b) Cyclic ($\sigma_n = 500kPa$) interface shear response for loose sand $D_r = 25\%$ with rough sand-steel interface (Fakharian and Evgin [1996]).

Figure 4.96 and 4.97 shows the test results as well as model response for loose $D_r = 25\%$ for smooth and rough sand-steel interface respectively. For loose rough sand-steel interface, the non-linear hardening (NLHS) model was used. For rough sand-steel surface, non-linear hardening -softening shear model was used as it shows a peak and softening branch. From Figure 4.96, it could be seen that NLHS model is able to capture the

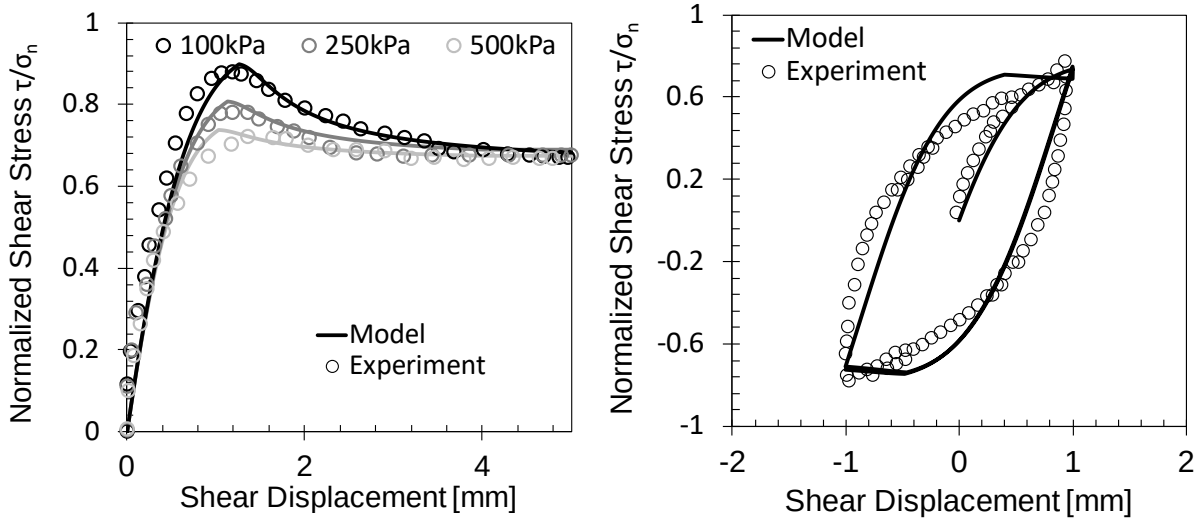

(a) Monotonic

(b) Cyclic

Figure 4.95: (a) Monotonic and (b) Cyclic ($\sigma_n = 500kPa$) interface shear response for dense sand $D_r = 80\%$ with rough sand-steel interface (Fakharian and Evgin [1996]).

Table 4.2: Parameters Considered for Validation of Interface Shear Behavior

Experiment	$k_t[kPa]$	n	b	μ_{p0}	k	μ_r	Model	Figure
Loose Sand-Steel Interface[1]	1100	8	40	0.78	0.08	0.68	NLHSS	Figure 4.94
Dense Sand-Steel Interface[1]	1500	8	40	0.90	0.10	0.66	NLHSS	Figure 4.95
Smooth Sand-Steel Interface[1]	3000	-	-	-	-	0.50	NLHS	Figure 4.96
Rough Sand-Steel Interface[2]	1500	12	40	0.88	0.08	0.66	NLHSS	Figure 4.97
Uesugi et al. [1989]	800	8	80	0.80	0.10	0.54	NLHSS	Figure 4.98

[1] Fakharian and Evgin [1996]

[2] Shahrour and Rezaie [1997]

shear stiffness k_t, peak plateau size parameter n, rate of softening b, peak normalized shear stress parameter μ_{p0}, peak normalized shear stress rate of decrease k and residual normalized shear stress μ_r.

interface monotonic and cyclic shear response. It must be also noted that the smooth sand-steel interface experimental results are stiffer initially than the NLHS model response because of the initial slippage at the interface. From Figure 4.97, it could be observed that the non-linear hardening-softening shear model is able to model quite well both the monotonic and cyclic shear response of rough sand-steel interface. It must be noted that NLHSS models shear strength decreases to the residual strength in each cycle if it reaches the softening branch.

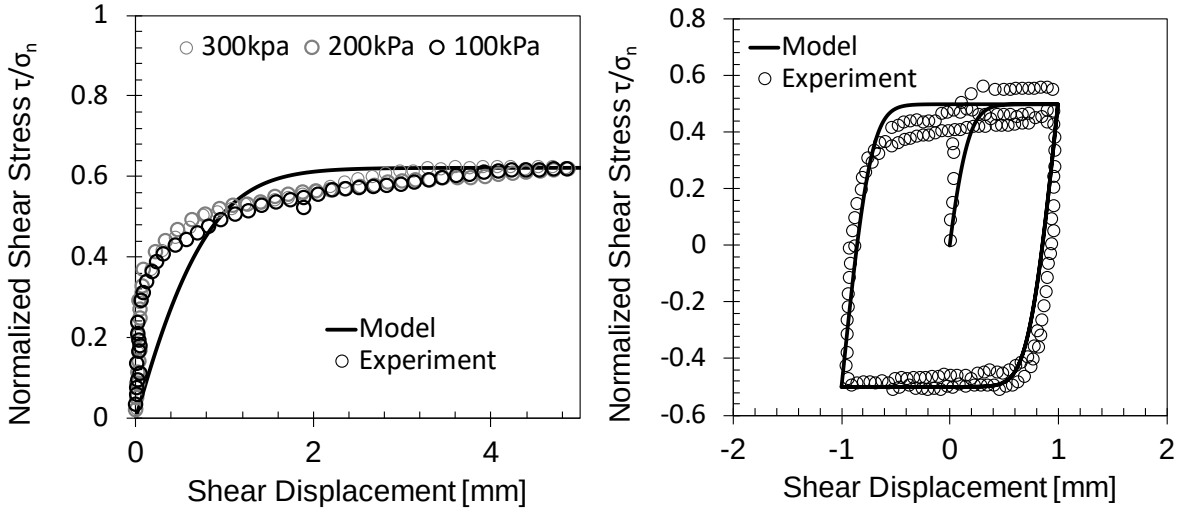

(a) Monotonic (b) Cyclic

Figure 4.96: (a) Monotonic and (b) Cyclic ($\sigma_n = 100kPa$) interface shear response for smooth Hostun sand-steel interface $D_r = 25\%$ (Shahrour and Rezaie [1997]).

Figure 4.98 shows the cyclic shear response for dense sand $D_r = 90\%$ and steel interface with normal stress $\sigma_n = 98kPa$. In the first cycle itself, the interface reaches its normalized peak shear strength $\tau_p/\sigma_n = 0.8$ and softens to the residual shear strength $\tau_r/\sigma_n = 0.54$. Once it reaches the residual strength, the interface does not harden anymore.

It must be noted that the proposed NLHS and NLHSS models have comparatively less parameters than the more sophisticated discussed in Section 2.4. As a result, the cyclic degradation because of particle crushing and instantaneous densification of loose soil cannot be modeled with the limited parameters it has. Although, the model can be extended to incorporate the effects of cyclic degradation and densification by introducing

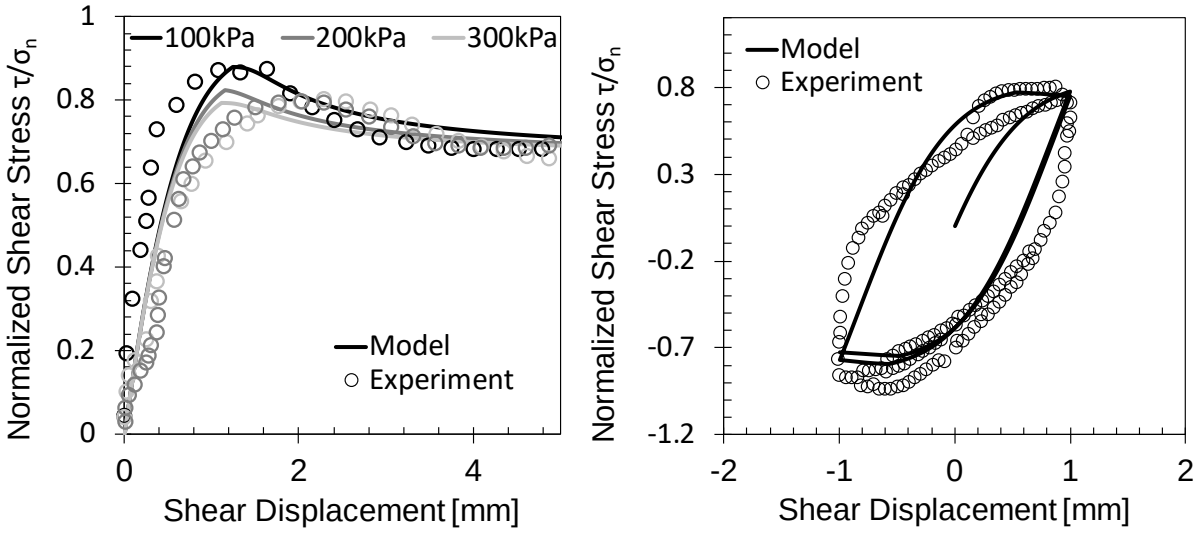

(a) Monotonic

(b) Cyclic

Figure 4.97: (a) Monotonic and (b) Cyclic ($\sigma_n = 100kPa$) interface shear response for rough Hostun sand-steel interface $D_r = 25\%$ (Shahrour and Rezaie [1997]).

more state variables.

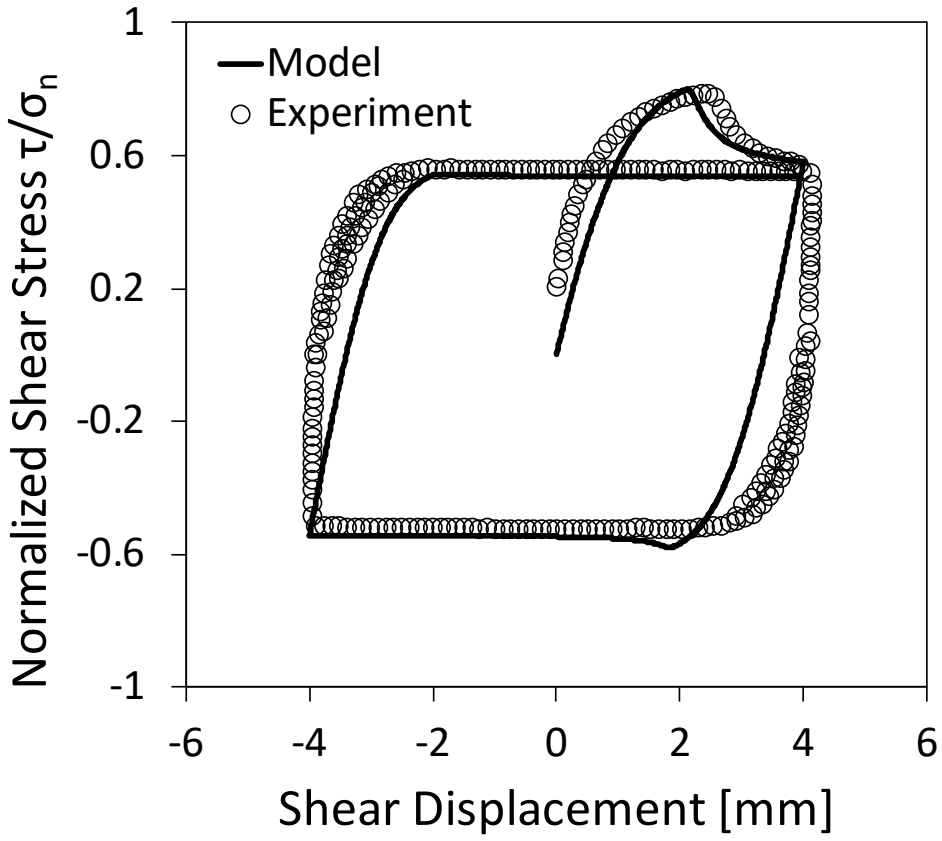

(a) Cyclic

Figure 4.98: Cyclic shear response of Toyora sand ($D_r = 90\%$. $\sigma_n = 98kPa$, $R_n = 0.15$) with steel interface (Uesugi et al. [1989].)

4.12 Numerical Issues

Contact is considered as one of the most important and difficult mechanics problem to solve. As was seen in Section 1.2, contact formulation are non-linear problems involving geometric constraints.

It leads to impenetrability condition i.e. body 1 cannot penetrate in body 2 as shown in Figure 4.99. The impenetrability condition leads to inequality constraints. The unknown contact boundary, contact stresses and abrupt change in contact force makes the global Newton convergence difficult. This section talks about some numerical issues with contact problems and how to tackle them.

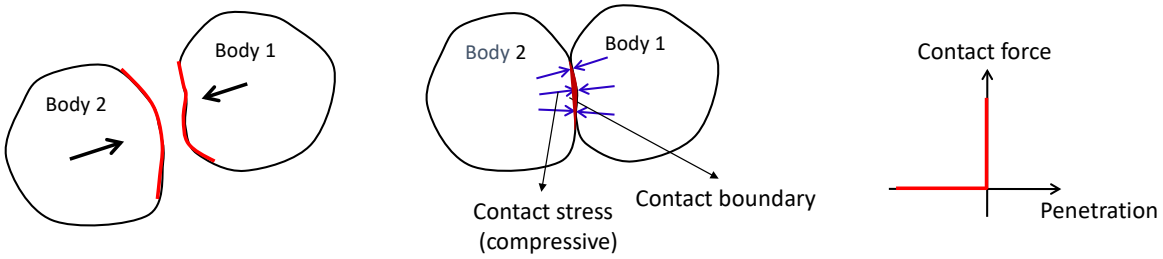

Figure 4.99: Illustration of unknown contact boundary, stress and abrupt change of forces for contact problems.

4.12.1 Choosing Normal Penalty Stiffness

Theoretically for rigid contact, the normal penalty stiffness k_n of contact element should be infinite. However, for numerical reasons, it cannot be infinite. Very high penalty stiffness increases the condition number which makes the problem $KU = F$ difficult to solve. It also results in a larger relative error in solution. The question then comes as to how to pick the penalty stiffness of contact. It should be big enough to constrain the impenetrability condition but at the same time should also be numerically stable. For force based node-to-node contact (Section 3), the penalty stiffness k_n is defined in units of N/m resulting in mesh and material dependence of the contacting bodies. For the surface to surface stress based contact, the normal stiffness k_n is defined in units of Pa and thus has only material dependence of the contacting bodies. For soil-structure interface, the normal penalty stiffness k_n is not rigid but is governed by the experimental tests of interface normal response.

Figure 4.100: Illustration of meshed contact problem between two bodies

Figure 4.100 shows a meshed contact problem between two bodies. The springs between the contact node pairs represent the contact node-to-node elements. Since during contact, the bodies get compressed against each other, the contact force generated should be big enough to cause any possible volumetric compression. The bulk modulus K_b can be thought as the material parameter for deciding contact stiffness k_n. In Figure 4.100 the bulk modulus of the bodies in contact is K_{b1} and K_{b2}. Let's assume that the mesh size of the elements for the two contacting bodies are M_{s1} and M_{s2} respectively.

For force based contact, the total contact force for both the connecting bodies can then be defined as $K_b \times M_s^2$. Allowing a maximum penetration of Δ_n^{max} in the contact bodies, the normal penalty stiffness k_n for the contact element can be chosen as

$$k_n \geq \frac{min(K_{b1}M_{s1}^2, K_{b2}M_{s2}^2, ..)}{\Delta_n^{max}} \tag{4.32}$$

where K_{bi} and M_{s2} are the bulk modulus and mesh size of the connecting elements to the contact node pairs. For stress based contact, the normal stress should be large enough from the connected elements to enforce the impenetrability condition. Similar to Equation 4.32, the normal stiffness for stiff contact could be taken as

$$k_n \geq min(K_{b1}, K_{b2}, ..) \tag{4.33}$$

It must be noted that for allowing very small penetration Δ_n, the normal stiffness k_n should correspondingly be made higher.

With this chosen normal penalty stiffness k_n, the minimum time step requirement Δt can also be picked as discussed in Section 4.4. The shear stiffness k_t for rigid contact should be also high enough. For soil-structure interface, it is governed by the experimental test results. A large shear stiffness k_t leads to oscillating convergence issues as discussed in Section 4.12.2. Thus, unless the time step Δt is very small, it would be recommended to have shear stiffness k_t to be $2-4$ magnitudes lower than the normal stiffness k_n.

For soft contact, the above discussion could be used to set the maximum normal stiffness k_n^{max}. The initial stiffness k_i can be taken as equal to the maximum of stiffness of contacting bodies. The stiffness rate S_r then can be found out by solving Equation 2.8 for Δ_n^{max}.

For coupled contact, in order to enforce the no-drainage condition, the penalty stiffness k_p can be taken as equal or even few magnitude $O(1) - O(2)$ higher than the normal stiffness k_n. It must be noted that if the penalty stiffness for contact problems are large, the time step Δt should also be correspondingly made smaller.

4.12.2 Oscillating Convergence

Contact problems often lead to oscillating convergence problems because of an abrupt change of contact stiffness and force. It can be caused by oscillations in the contact normal or slip states as shown in Figures 4.101 and 4.102 respectively. It happens because of very high stiffness k_n, k_t with larger time steps Δt. In Figure 4.101, for iteration n a small

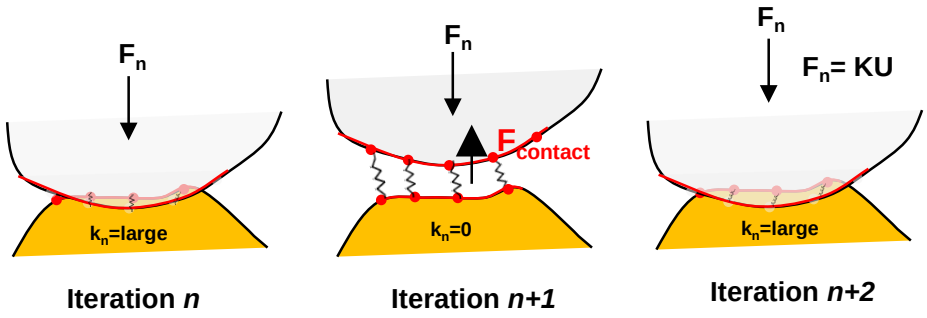

Figure 4.101: Illustration of oscillating convergence problem during normal contact.

penetration Δ_n is introduced. Because of large normal stiffness k_n, a large contact force is developed which pushes the body out of contact in iteration $n+1$. At this point, since there is no contact, the contact normal penalty stiffness k_n becomes zero which results in a net application of force F_n making the two bodies again come in contact (iteration $n+2$). This process continues, again and again, leading to oscillating convergence.

Figure 4.102, demonstrates oscillating convergence problems during sliding of contact bodies. For iteration n, a net force f_t^{net} causes one body to slide over the other. Because of slippage (sliding), a large deformation is created in the adjacent body, which creates a large rebound force f_t^{net} in opposite direction for iteration $n+1$. The force f_t^{net}, if is large enough can make the body slide in opposite direction. At the material level, the contact state thus moves back-and-forth on the yield surface. leading to oscillating convergence

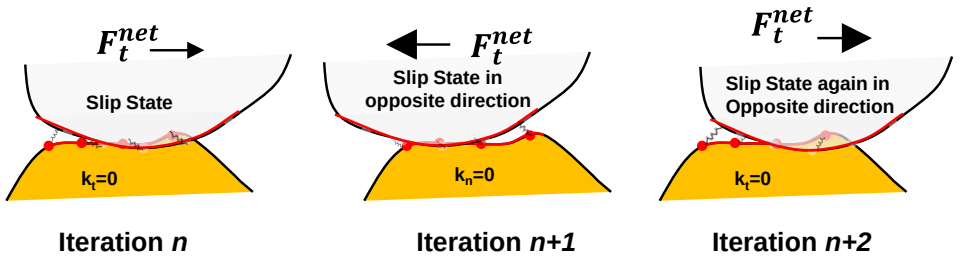

Figure 4.102: Illustration of oscillating convergence problem during slip.

issues.

The oscillating problem as discussed above is caused by high stiffness with large time steps. Thus to solve this issue, either the stiffness k_n, k_t should be reduced or time step Δt should be made smaller.

4.12.3 Contact Stabilization Using Viscous Damping

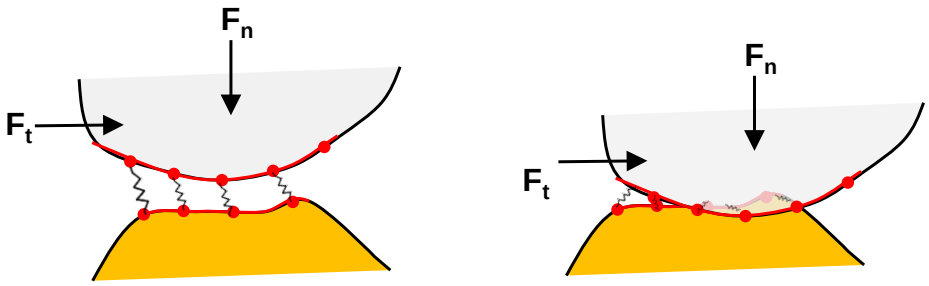

Figure 4.103: Illustration of contact with normal and tangential loading.

In contact problems, to satisfy the impenetrability condition, a large contact force is applied to the contacting bodies. Often these forces can be larger in relation to the external forces, which can lead to spurious accelerations. Thus, it is advised to add a small amount of viscous damping c_n and c_t in contact normal and tangential direction respectively. The viscous damping stabilizes the contact simulation. See Section 3.4 for more details.

4.12.4 Sub-Stepping

As described in Section 4.12.2, the problem of oscillating convergence or any other convergence problems can be solved by reducing the simulation time steps Δt. Auto sub-

stepping can be used to automatically subdivide a big step by a factor of 2 and so forth until convergence is achieved.

Newton line search coupled with sub-stepping could prove to be even more fruitful for convergence. Alternatively, for improving convergence, the mesh size can also be reduced or the element order can be increased.

Among all, auto sub-stepping is highly recommended for contact problems. In Real ESSI Simulator [Jeremić et al., 2017] the sub-stepping option was implemented to tackle the non-convergence issue.

4.12.5 Rigid Body Motion In Contact

Convergence issues can also be caused by possible rigid body motion during static analysis. This can occur at the beginning of the static analysis due to non-establishment of initial contact conditions.

Before running a static analysis, it must be checked whether contacting bodies are initially in contact. Since for node to node contact, the contact nodes should have same coordinates. Equality of the coordinates of the contact element mesh must be checked and verified. In Real ESSI Simulator [Jeremić et al., 2017], the rigid body check was implemented that could be used as an initial dry run to check the model.

Chapter 5

Applications

5.1 Soil-Structure Interaction at Interface in Nuclear Power Plants (NPP) on Shallow Foundation

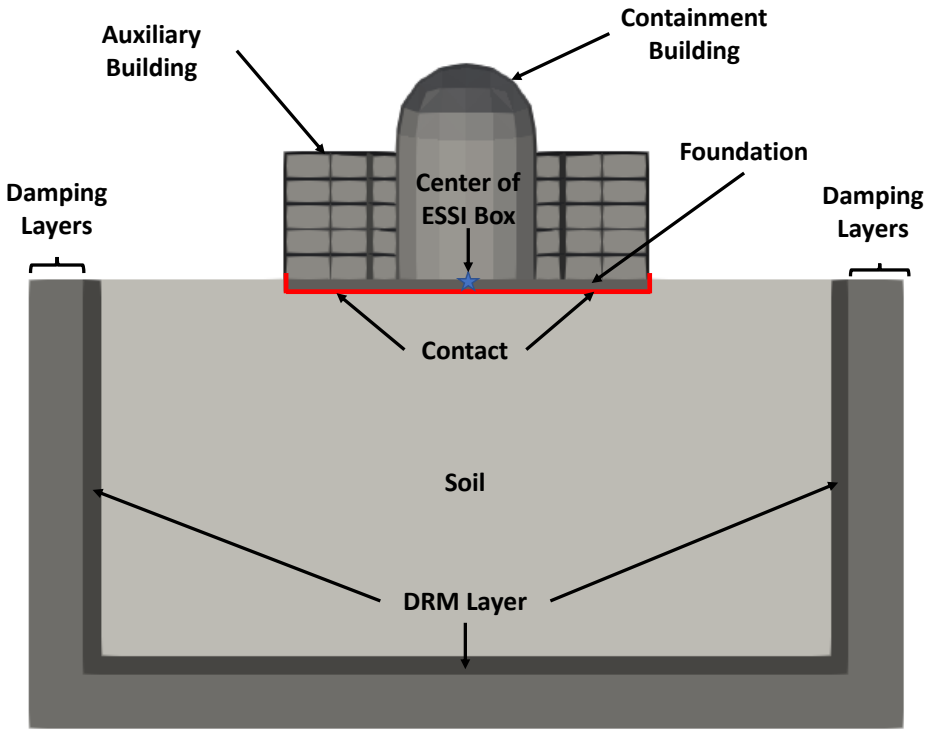

Figure 5.1: Nuclear Power Plant model with shallow foundation

The Nuclear Power Plant (NPP) modeled here is a symmetric structure on a shallow

foundation of thickness of $3.5m$ and length of $100m$. Figure 5.1 shows a slice view of the model in normal y-direction (perpendicular to plane of the paper). Solid brick elements were used to model the soil and foundation, and shell elements for the structure. The shear wave velocity V_s for the soil was taken as $V_s = 500m/s$ with unit-weight of $\gamma = 21.4kN/m^3$. The Poisson's ratio ν of the soil was taken as $\nu = 0.25$. The foundation and the NPP structure is made of concrete of Young's modulus $20GPa$, Poisson's ratio of $\nu = 0.21$ and density of $\rho = 2400kg/m^3$. The interface was modeled with soft dry contact elements with EPPS model with coefficient of friction as $\mu_r = 0.35$. Soil with a lateral extent of $50m$, and depth of $120m$, from the NPP structure was modeled. The Domain reduction method (DRM) was used to apply 3-D motions all around the model. 3-D motions were developed by [Rodgers, 2017] using SW4 [Petersson and Sjögreen, 2017]. The motions and its Fourier spectra at the center of the model are shown in Figure 5.2 and Figure 5.3 respectively.

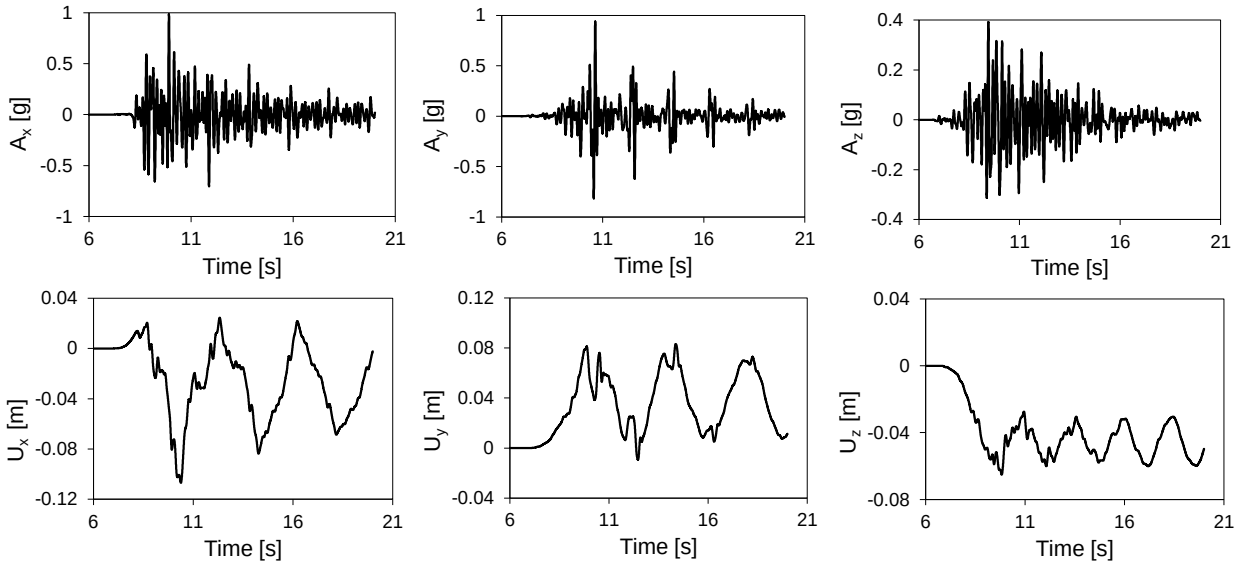

Figure 5.2: Acceleration and Displacement Time Series of Motion

Analysis were performed for cases of elastic and elastic-plastic soil. For elastic-plastic soil, Von-Mises with non-linear kinematic hardening of Armstrong Frederick type with yield strength achieved at 1% shear strain and initial kinematic hardening rate $H_a = 3e^5kPa$ was considered.

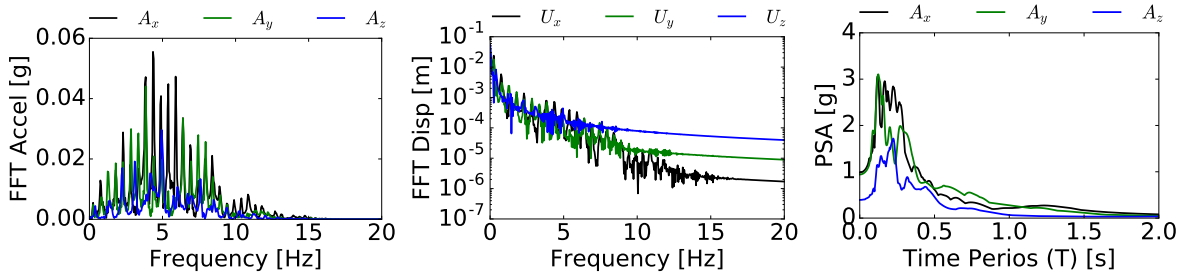

Figure 5.3: Strong Motion Fourier Transform and Response Spectrum

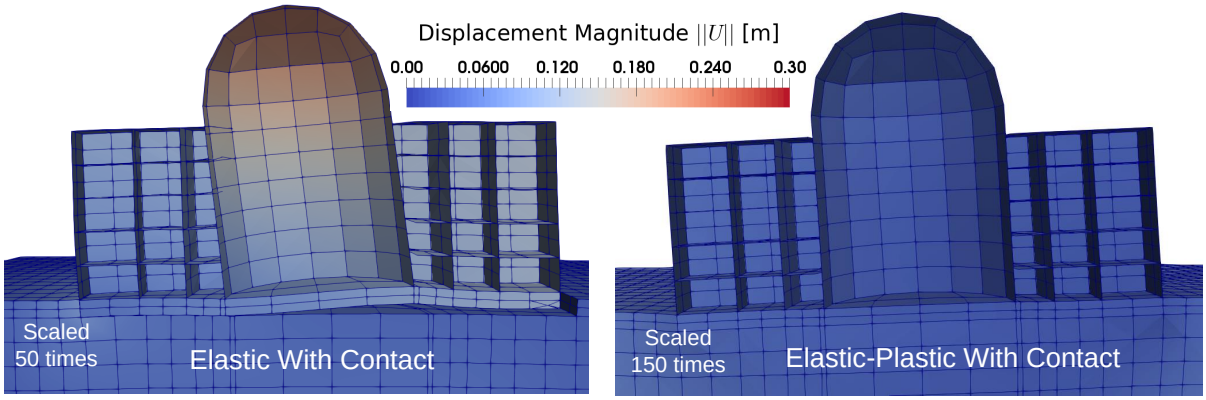

Figure 5.4: Deformation of the NPP structure at 11 seconds

Figure 5.4 shows the response for elastic vs elastic-plastic soil with contact at $11sec$. The introduction of contact in elastic case results in significant opening and closing of gaps at the soil-foundation. On the other hand, The elastic-plastic case with contact does not see any uplift i.e. loss of contact to foundation with soil. In fact, most part of the foundation remains almost always in contact with the inelastic soil. The elastic-plastic soil dissipates most of the seismic energy leading to very small or no uplift at soil-foundation interface as compared to the elastic case.

Figure 5.5a shows the accumulated plastic dissipation density field of the NPP model at the end of seismic event for another considered earthquake Sinha, Feng, Yang, Wang, Orbović, McCallen and Jeremić [2017]. The super-structure does not dissipate energy since it is modeled as a linear elastic material. Significant amount of seismic energy is dissipated in the contact zone between the structure and underlying soil, especially at regions around the corners and edges of the foundation. An arch-shaped elastic region

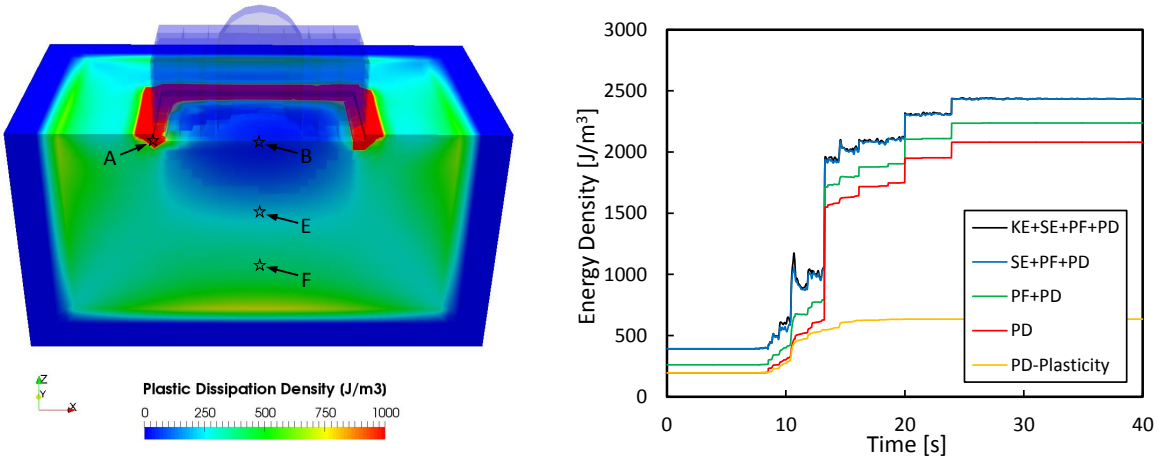

(a) Plastic dissipation density field

(b) Evolution of energy components at location A

Figure 5.5: Energy dissipation in NPP model for inelastic (elastic-plastic soil with contact)

is formed under the structure, where the soil moves together with the foundation and dissipates little energy. Such observation is consistent with classic bearing capacity analysis, which also indicates the formation of a relatively undeformed "passive zone" beneath foundation.

As can be observed in Figure 5.5a, the plastic dissipation density at location (A) is the highest. From Figure 5.5b, it can be observed that more than 80% of the total input work is dissipated due to material plasticity or contact slipping. About 70% of the energy dissipation happens due to contact slipping, which indicates that the property and behavior of the interface between foundation and soil is crucial in SSI system. It is worth pointing out that there is about 10% of the input work transformed into plastic free energy, which falls in the typical range reported by Taylor and Quinney [1934].

5.2 3-D Modeling of Shallow Soil-Foundation System (SFS) in Saturated soil conditions

An example similar to the one presented in Section 4.10, is now modeled as a 3-D shallow soil-foundation system, to study the effects of the coupled with the dry contact element Sinha, Behbehani and Jeremić [2017]. In this example for the first loading stage (A), foundation's self-weight is applied within 1 sec. In the second loading stage (B), the system is left to respond for another 300 seconds. A concrete structure of height $2m$ rests on the foundation of length $3m$ and width $2m$ perpendicular to the plane of the paper as shown in Figure 5.6. The properties of the model are the same that used for the simple 1-D model as summarized in Table 4.1. Coupled soft contact with initial normal stiffness of $k_i = 500MPa$, stiffening rate of $S_r = 1e5$, maximum normal stiffness of $k_n^{max} = 10GPa$ and penalty stiffness $k_p = 10GPa$ was used. The mesh size Δ_h of the model was $\Delta_h = 250cm$. Thus, the total pressure σ_{zz} acting at the base of the foundation at the end of stage A, was equal to $\sigma_{zz} = 25kPa$.

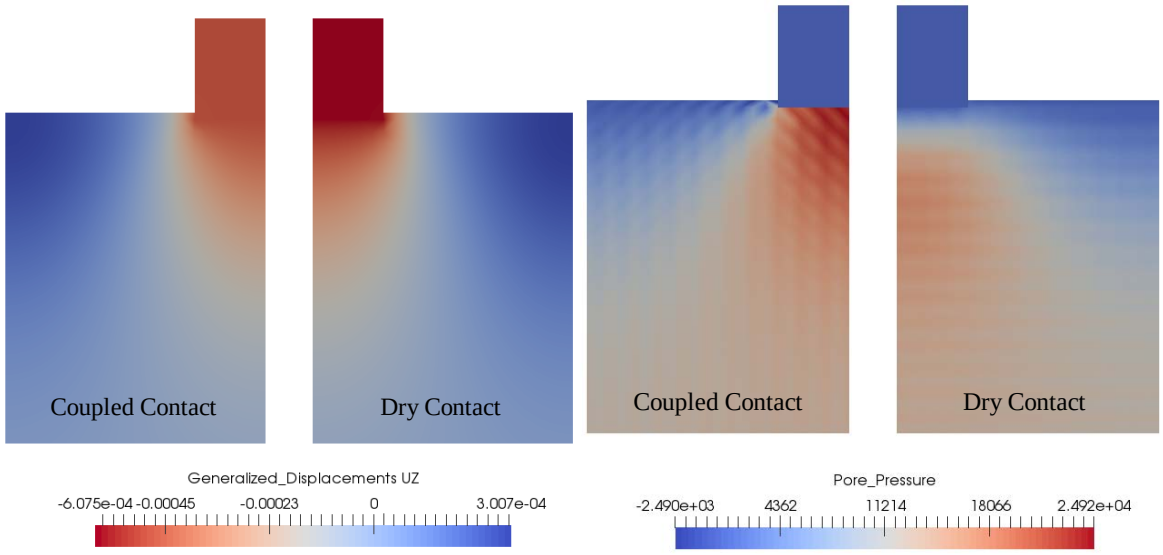

(a) Solid Displacement in z-direction

(b) Excess Pore Pressure generation

Figure 5.6: Displacement in z direction and excess pore pressure generated in soil-foundation system after application of foundation's self-weight stage (A).

Figure 5.6 shows the excess pore pressure and z-displacement of the soil. It can be observed that in the initial loading stage, the coupled contact has comparatively lower displacement than the dry contact. Since the dry contact does not restrict drainage below the foundation, the soil settles more as the pore-pressure gets dissipated. This effect is evident from Figure 5.6 (b), where the excess pore-pressure is plotted over the entire volume of soil. It can be observed that for the coupled contact, the excess pore pressure p generated below the foundation is almost equal to $p = 25kPa$ of the applied load. On the other hand, almost no excess pore pressure is apparent at the foundation-soil interface as the dry contact interface acts as a free drainage surface.

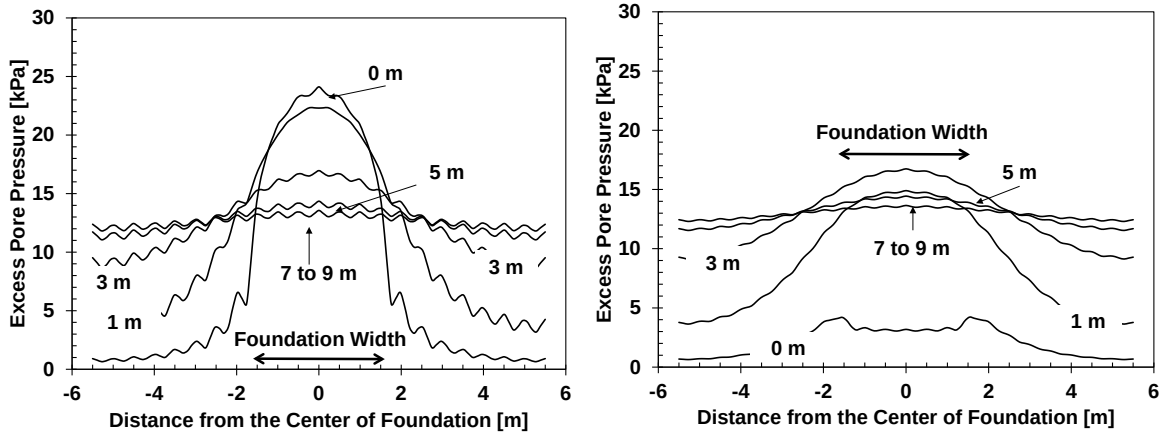

(a) Coupled Contact

(b) Dry Contact

Figure 5.7: Excess pore-pressure profile generated in soil at the end of stage (A) located at any $+ve$ z distance below the base of foundation.

The plot of excess pore-fluid pressure profile at any distance $+ve$ z distance below the base of the foundation is shown in Figure 5.7. It can be seen from the plots that for the coupled contact case, the excess pore-fluid pressure generated below the foundation $(0m)$, closely matches with the analytical solution of $p = 25kPa$. The soil just below the foundation experiences highest pore-fluid pressures whereas deeper soil experiences comparatively less excess pore pressure generation. Also, the excess pressure gets more widely and uniformly distributed for soils located at deeper depth $(7 - 9m)$.

For dry contact, the excess pore-fluid pressure profile shown in Figure 5.8 (b) appears

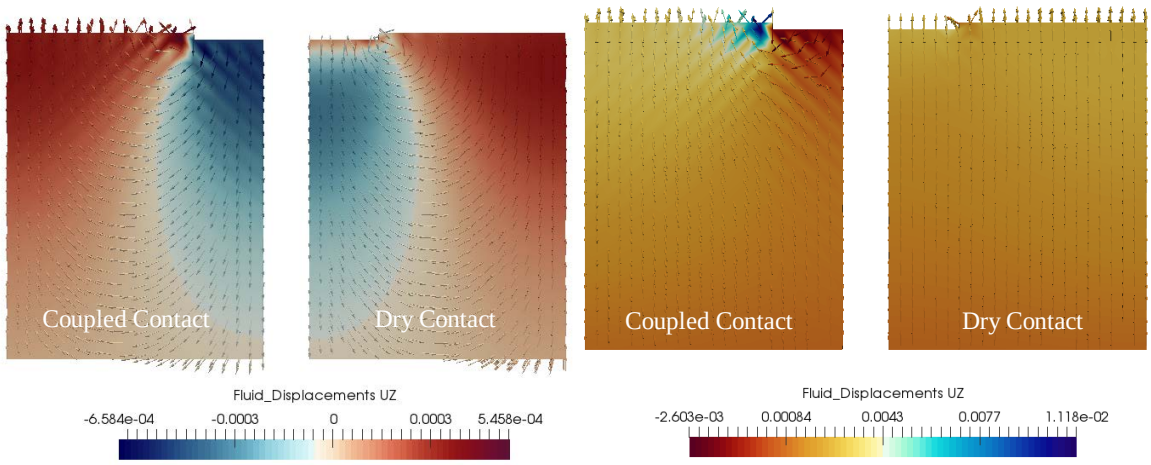

(a) Initial (b) Final

Figure 5.8: Fluid displacement in z-direction

to be entirely contrasting to the coupled contact. The excess pore-fluid pressure below the foundation ($0m$) is very small and increases for the soil at deeper depths ($1 - 3$m) and then starts to again decrease for even higher depths ($7 - 9m$). This defect of dry contact is because of its inability to enforce the effective stresses and drainage conditions below the base of the foundation. As a result, fluid from the bottom and sides of the foundation rushes toward the bottom and results in comparatively higher settlement and lower void ratio (e). This effect can be seen in the initial stage (A) as shown in Figure 5.8 (a), where excess pore fluid pressure generates $+ve$ z fluid displacement (red color) on the soil surface as well as below the foundation. The same can be seen in the final stage (B), where for the dry contact, the fluid has almost same final $+ve$ z displacement everywhere. The non-realistic $+ve$ fluid displacement at the base of the foundation, illustrates the inability of the dry contact to model soil-foundation interface correctly in saturated soil conditions.

For the coupled contact, as shown in Figure 5.8, excess pore fluid pressure is only dissipated in the soil few meters deeper and away from the foundation. Figure 5.8, shows that high pore-fluid pressure rushes to the edge of the foundation for quick drainage. This results in larger fluid-displacements close to the foundation. Pore fluid below the

foundation moves sideways and then upwards to release the excess pore-pressure. The flow lines could be seen as vectors in Figure 5.8 (b). The soil below the foundation has *ve* fluid displacements, illustrating the fact that since drainage is not allowed in contact normal direction, the only way to dissipate excess pore pressure is to flow sideways.

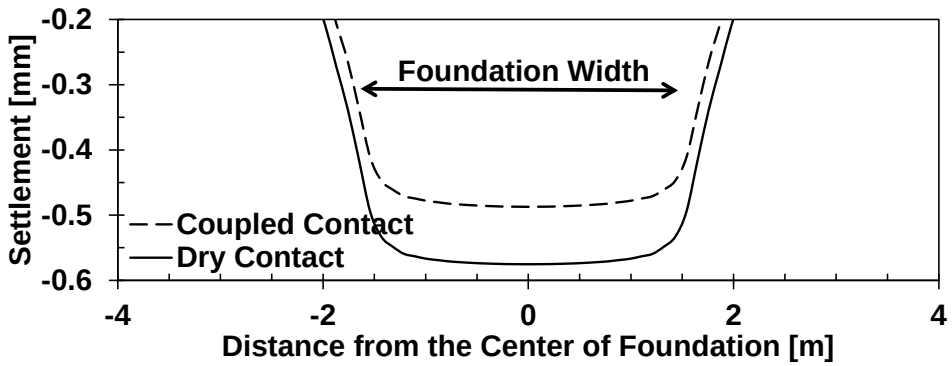

Figure 5.9: Final Settlement profile of the soil below foundation

Figure 5.9 shows the final settlement in soil below the foundation. The dry contact results in comparatively higher settlement prediction than the coupled contact. Since, the mechanical strength of the soil is inversely proportional to the void ratio (e), large settlement would result in over-prediction of shear strength.

Chapter 6

Conclusion

Presented here, was a high fidelity simulation methodology to model soil-foundation interface for dry as well as partially and fully saturated soil conditions. A new soft contact model with non-linear normal (axial) interface behavior was developed. Two new elasto-plastic interface shear models, Nonlinear Hardening Shear (NLHS) and Nonlinear Hardening Softening Shear (NLHSS), with fewer material parameters were developed to model the nonlinear hardening and softening shear response at soil-structure interfaces. The shear interface models were validated against the known experimental data for monotonic as well as cyclic response at soil-structure interface.

With the developed interface models, surface to surface dry contact with node-to-node type was developed and implemented in Real ESSI Simulator System. A new coupled contact element was also developed to correctly model the dynamic pore-fluid pressure changes at the soil-foundation interface for submerged conditions. It was shown that the new element was able to correctly enforce the effective stress principle and undrained condition at soil-foundation interface. Effect of dry and coupled contact in modeling of submerged interface was also discussed.

Extensive verification was carried out for the developed contact elements and interface models. Numerical challenges with contact and ways to prevent them has also been discussed in detail. Finally, application to two realistic soil-structure interaction (SSI) problems, one on Nuclear Power Plant (NPP) and other with submerged shallow soil-foundation system has been demonstrated.

Appendix A

Domain Specific Language (DSL) for the Implemented Contact Elements in Real ESSI Simulator System

A.1 Force Based Contact Elements

The force based contacts are used for contact between two nodes which does not belong to any surface. It could be used to model contact between structural elements. It must be noted that in this element, the contact normal vector n needs to be explicitly defined in global coordinate system.

1. **Hard Contact**:

```
add element # <.> type ForceBasedHardContact with nodes
   (<.>,<.>)
        normal_stiffness = <N/m>
        tangential_stiffness = <N/m>
        axial_viscous_damping = <Ns/m>
        shear_viscous_damping = <Ns/m>
        friction_ratio = <.>
        contact_plane_vector = (<.>,<.>, <.>);
```

2. **Soft Contact**:

```
add element # <.>  type ForceBasedSoftContact with nodes
   (<.>,<.>)
        initial_axial_stiffness = <N/m>
        stiffning_rate = <1/m>
        max_axial_stiffness = <1/m>
        tangential_stiffness = <N/m>
        axial_viscous_damping = <Ns/m>
        shear_viscous_damping = <Ns/m>
        friction_ratio = <.>
        contact_plane_vector = (<.>,<.>, <.>);
```

3. **Coupled Hard Contact**:

```
add element # <.> type ForceBasedCoupledHardContact with
   nodes (<.>,<.>)
         normal_stiffness = <N/m>
         normal_penalty_stiffness = <N/m>
         tangential_stiffness = <N/m>
         axial_viscous_damping = <Ns/m>
         shear_viscous_damping = <Ns/m>
         friction_ratio = <.>
         contact_plane_vector = (<.>,<.>, <.>);
```

4. **Coupled Soft Contact**:

```
add element # <.>  type ForceBasedCoupledSoftContact with
   nodes (<.>,<.>)
         initial_axial_stiffness = <N/m>
         stiffning_rate = <1/m>
         max_axial_stiffness = <1/m>
         normal_penalty_stiffness = <N/m>
         tangential_stiffness = <N/m>
         axial_viscous_damping = <Ns/m>
         shear_viscous_damping = <Ns/m>
         friction_ratio = <.>
         contact_plane_vector = (<.>,<.>, <.>);
```

The terms associated with the DSL's are enlisted here

- **axial_stiffness** k_n : refers to the penalty stiffness in contact normal direction. See Equation 2.5

- **initial_axial_stiffness** k_i : refers to the initial penalty stiffness in contact normal direction for soft contact. See Equation 2.6

- **max_axial_stiffness** k_n^{max} : refers to the maximum achievable stiffness in contact normal direction for soft contact element. See Equation 2.8

- **axial_penalty_stiffness** k_p : refers to the penalty stiffness to enforce U-u DOF in coupled contact in contact normal direction. See Equation 3.44

- **stiffening_rate** S_r : It defines the exponential rate at which the stiffness of soft contact increases. See Equation 2.6

- **shear_stiffness** k_t : It refers to the penalty stiffness in tangential direction. See Section 2.3.1

- **axial_viscous_damping** c_n : It defines the visco-elastic stiffness in contact normal direction. See Section 3.4

- **shear_viscous_damping** c_t : It defines the visco-elastic stiffness in contact tangential direction. See Section 3.4

- **friction_ratio** μ : refers to friction coefficient between the two interface layers. See Section 2.6

- **contact_plane_vector** $\overrightarrow{n}$: refers to contact plane vector in global coordinate direction. See Section 3

  Note : It must be noted that the contact_plane_vector $\overrightarrow{n}$ is defined in the direction from node i to node j as shown in Figure 3.8

A.2 Stress Based Contact Elements

If the contact is applied between two surfaces or one node and a surface, a stress based contact can be used, It must be noted that in this element, the contact normal vector n needs to be explicitly defined in global coordinate system.

1. **Hard Contact**:

```
add element #<.>  type StressBasedHardContact_ElPPlShear
   with nodes (<.>,<.>)
        normal_stiffness = <Pa>
        initial_shear_stiffness =  <Pa>
        axial_viscous_damping =  <Pa*s>
        shear_viscous_damping =   <Pa*s>
        residual_friction_coefficient =  <.>
        shear_zone_thickness = <m>
        contact_plane_vector = (<.>,<.>, <.>);
```

```
add element #<.>  type
   StressBasedHardContact_NonLinHardShear with nodes
   (<.>,<.>)
        normal_stiffness = <Pa>
        initial_shear_stiffness =  <Pa>
        axial_viscous_damping =  <Pa*s>
        shear_viscous_damping =   <Pa*s>
        residual_friction_coefficient =  <.>
        shear_zone_thickness = <m>
        contact_plane_vector = (<.>,<.>, <.>);
```

```
add element #<.>  type
   StressBasedHardContact_NonLinHardSoftShear with nodes
   (<.>,<.>)
         normal_stiffness = <Pa>
         initial_shear_stiffness = <Pa>
         rate_of_softening = <.>
         size_of_peak_plateau = <.>
         axial_viscous_damping =  <Pa*s>
         shear_viscous_damping =  <Pa*s>
         peak_friction_coefficient_limit = <.>
         peak_friction_coefficient_rate_of_decrease     = <.>
         residual_friction_coefficient =  <.>
         shear_zone_thickness = <m>
         contact_plane_vector = (<.>,<.>, <.>);
```

2. **Soft Contact**:

```
add element #<.>  type StressBasedSoftContact_ElPPlShear
   with nodes (<.>,<.>)
         initial_axial_stiffness =  <Pa>
         stiffning_rate =  <.>
         max_axial_stiffness = <Pa>
         initial_shear_stiffness =  <Pa>
         axial_viscous_damping =  <Pa*s>
         shear_viscous_damping =   <Pa*s>
         residual_friction_coefficient =  <.>
         shear_zone_thickness = <m>
         contact_plane_vector = (<.>,<.>, <.>);
```

```
add element #<.>  type
   StressBasedSoftContact_NonLinHardShear with nodes
   (<.>,<.>)
        initial_axial_stiffness =  <Pa>
        stiffning_rate =  <.>
        max_axial_stiffness = <Pa>
        initial_shear_stiffness =  <Pa>
        axial_viscous_damping =  <Pa*s>
        shear_viscous_damping =   <Pa*s>
        residual_friction_coefficient =  <.>
        shear_zone_thickness = <m>
        contact_plane_vector = (<.>,<.>, <.>);
```

```
add element #<.>  type
   StressBasedSoftContact_NonLinHardSoftShear with nodes
   (<.>,<.>)
        initial_axial_stiffness =  <Pa>
        stiffning_rate =  <.>
        max_axial_stiffness = <Pa>
        initial_shear_stiffness = <Pa>
        rate_of_softening = <.>
        size_of_peak_plateau = <.>
        axial_viscous_damping =  <Pa*s>
        shear_viscous_damping =  <Pa*s>
        peak_friction_coefficient_limit = <.>
        peak_friction_coefficient_rate_of_decrease    = <.>
        residual_friction_coefficient =  <.>
        shear_zone_thickness = <m>
```

```
        contact_plane_vector = (<.>,<.>, <.>);
```

3. **Coupled Hard Contact**:

```
add element #<.>  type
   StressBasedCoupledHardContact_ElPPlShear with nodes
   (<.>,<.>)
        normal_stiffness = <Pa>
        normal_penalty_stiffness = <Pa>
        initial_shear_stiffness =  <Pa>
        axial_viscous_damping =  <Pa*s>
        shear_viscous_damping =   <Pa*s>
        residual_friction_coefficient =  <.>
        shear_zone_thickness = <m>
        contact_plane_vector = (<.>,<.>, <.>);
```

```
add element #<.>  type
   StressBasedCoupledHardContact_NonLinHardShear with nodes
   (<.>,<.>)
        normal_stiffness = <Pa>
        normal_penalty_stiffness = <Pa>
        initial_shear_stiffness =  <Pa>
        axial_viscous_damping =  <Pa*s>
        shear_viscous_damping =   <Pa*s>
        residual_friction_coefficient =  <.>
        shear_zone_thickness = <m>
        contact_plane_vector = (<.>,<.>, <.>);
```

```
add element #<.>  type
   StressBasedCoupledHardContact_NonLinHardSoftShear with
   nodes (<.>,<.>)
         normal_stiffness = <Pa>
         normal_penalty_stiffness = <Pa>
         initial_shear_stiffness = <Pa>
         rate_of_softening = <.>
         size_of_peak_plateau = <.>
         axial_viscous_damping =  <Pa*s>
         shear_viscous_damping =  <Pa*s>
         peak_friction_coefficient_limit = <.>
         peak_friction_coefficient_rate_of_decrease     = <.>
         residual_friction_coefficient =  <.>
         shear_zone_thickness = <m>
         contact_plane_vector = (<.>,<.>, <.>);
```

4. **Coupled Soft Contact**:

```
add element #<.>  type StressBasedSoftContact_ElPPlShear
   with nodes (<.>,<.>)
         initial_axial_stiffness =  <Pa>
         stiffning_rate =  <.>
         max_axial_stiffness = <Pa>
         normal_penalty_stiffness = <Pa>
         initial_shear_stiffness =  <Pa>
         axial_viscous_damping =  <Pa*s>
         shear_viscous_damping =   <Pa*s>
         residual_friction_coefficient =  <.>
```

```
        shear_zone_thickness = <m>
        contact_plane_vector = (<.>,<.>, <.>);
```

```
add element #<.>  type SoftContact_NonLinHardShear with
   nodes (<.>,<.>)
        initial_axial_stiffness =  <Pa>
        stiffning_rate =  <.>
        max_axial_stiffness = <Pa>
        normal_penalty_stiffness = <Pa>
        initial_shear_stiffness =  <Pa>
        axial_viscous_damping =  <Pa*s>
        shear_viscous_damping =   <Pa*s>
        residual_friction_coefficient =  <.>
        shear_zone_thickness = <m>
        contact_plane_vector = (<.>,<.>, <.>);
```

```
add element #<.>  type
   StressBasedSoftContact_NonLinHardSoftShear with nodes
   (<.>,<.>)
        initial_axial_stiffness =  <Pa>
        stiffning_rate =  <.>
        max_axial_stiffness = <Pa>
        normal_penalty_stiffness = <Pa>
        initial_shear_stiffness = <Pa>
        rate_of_softening = <.>
        size_of_peak_plateau = <.>
        axial_viscous_damping =  <Pa*s>
```

```
shear_viscous_damping = <Pa*s>
peak_friction_coefficient_limit = <.>
peak_friction_coefficient_rate_of_decrease = <.>
residual_friction_coefficient = <.>
shear_zone_thickness = <m>
contact_plane_vector = (<.>,<.>, <.>);
```

The terms associated with the DSL's are enlisted here

- **axial_stiffness** k_n : refers to the penalty stiffness in contact normal direction. The units are in Pa. See Equation 2.5

- **initial_axial_stiffness** k_i : refers to the initial penalty stiffness in contact normal direction for soft contact. The units are in Pa. See Equation A.1

$$\sigma_n = k_i exp(-S_r \epsilon)\epsilon \tag{A.1}$$

- **max_axial_stiffness** k_n^{max} : It refers to the maximum achievable stiffness in contact normal direction for soft contact element. The units are in Pa. It provides an cap to the maximum normal stiffness to prevent from numerical issues. See Equation 2.8 which shows the form the force based contact. For the stress based contact replace penetration Δ_n with normal strain ϵ.

- **axial_penalty_stiffness** k_p : It refers to the penalty stiffness to enforce U-u DOF in coupled contact in contact normal direction. The units are in Pa. See Section 3.44

- **stiffening_rate** S_r : It defines the exponential rate at which the stiffness of soft contact increases. For stress based contact the stiffness increases exponentially as a function of normal strain $\epsilon = \Delta_n / SZ_h$. Thus it is unit-less for the stress based contact and is shown in Equation A.1.

- **initial_shear_stiffness** k_t : It refers to the penalty stiffness in tangential direction for confinement of $P_0 = 100kPa$. See Section 2.4

- **rate_of_softening** : It is unit-less quantity which refers to the rate of softening of the interface once the peak friction coefficient μ_p is attained. See Section 2.4.3

- **size_of_peak_plateau** : It is unit-less quantity which refers to size of plateau when the peak friction coefficient μ_p is attained. See Section 2.4.3

- **axial_viscous_damping** c_n : It defines the visco-elastic stiffness in contact normal direction. See Section 3.4

- **shear_viscous_damping** c_t : It defines the visco-elastic stiffness in contact tangential direction. See Section 3.4

- **peak_friction_coefficient_limit** μ_{p0} : It refers to the upper limit of peak friction coefficient μ_p for low confinement. See Section 2.4.3

- **peak_friction_coefficient_rate_of_decrease** k : It refers to the rate of decrease of peak friction coefficient μ_p with logarithmic increase of normalized normal stress $\frac{\sigma}{P_0=100kPa}$. See Section 2.4.3

$$\mu_p(\sigma) = max(\mu_{p0}, \mu_{p0} - klog(\frac{\sigma}{P_0 = 100kPa})) \tag{A.2}$$

- **residual_friction_coefficient** μ_r : It refers to friction coefficient between the two interface layers. See Section 2.4

- **shear_zone_thickness** SZ_h : It refers to the thickness of shear zone in soil at soil-foundation interface. See Section 2.2

- **contact_plane_vector** $\overrightarrow{n}$: It refers to contact plane vector in global coordinate direction. See Section 3

  Note : It must be noted that the contact_plane_vector $\overrightarrow{n}$ is defined in the direction from node i to node j as shown in Figure 3.8

In the above contact DSL's there are basically three type of shear interface models EPPS, NLHS and NLHSS as described in Section 2.4.

A.3 Auto Surface to Surface Contact Elements

If the contact is applied between two conformal surfaces, the auto-detection of contact elements between the given node pairs can be used. It must be noted that the following DSL's are applicable only for conforming surface to surface mesh. Since, the contact normal vector n are auto detected, in these DSL's the normal vector n does not need to be defined.

1. **Hard Contact**:

```
add element #<.>  type StressBasedHardContact_ElPPlShear
   with nodes (<.>,<.>)
        normal_stiffness = <Pa>
        initial_shear_stiffness =  <Pa>
        axial_viscous_damping =  <Pa*s>
        shear_viscous_damping =   <Pa*s>
        residual_friction_coefficient =  <.>
        shear_zone_thickness = <m>;
        surface_vector_relative_tolerance = <>;
```

```
add element #<.>  type
   StressBasedHardContact_NonLinHardShear with nodes
   (<.>,<.>)
        normal_stiffness = <Pa>
        initial_shear_stiffness =  <Pa>
        axial_viscous_damping =  <Pa*s>
        shear_viscous_damping =   <Pa*s>
        residual_friction_coefficient =  <.>
        shear_zone_thickness = <m>;
```

```
        surface_vector_relative_tolerance = <>;
```

```
add element #<.>  type
   StressBasedHardContact_NonLinHardSoftShear with nodes
   (<.>,<.>)
        normal_stiffness = <Pa>
        initial_shear_stiffness = <Pa>
        rate_of_softening = <.>
        size_of_peak_plateau = <.>
        axial_viscous_damping =  <Pa*s>
        shear_viscous_damping =  <Pa*s>
        peak_friction_coefficient_limit = <.>
        peak_friction_coefficient_rate_of_decrease     = <.>
        residual_friction_coefficient =  <.>
        shear_zone_thickness = <m>;
        surface_vector_relative_tolerance = <>;
```

2. **Soft Contact**:

```
add element #<.>  type StressBasedSoftContact_ElPPlShear
   with nodes (<.>,<.>)
        initial_axial_stiffness =  <Pa>
        stiffning_rate =  <.>
        max_axial_stiffness = <Pa>
        initial_shear_stiffness =  <Pa>
        axial_viscous_damping =  <Pa*s>
        shear_viscous_damping =   <Pa*s>
        residual_friction_coefficient =  <.>
```

```
        shear_zone_thickness = <m>;
        surface_vector_relative_tolerance = <>;
```

```
add element #<.>  type
   StressBasedSoftContact_NonLinHardShear with nodes
   (<.>,<.>)
        initial_axial_stiffness =  <Pa>
        stiffning_rate =  <.>
        max_axial_stiffness = <Pa>
        initial_shear_stiffness =  <Pa>
        axial_viscous_damping =  <Pa*s>
        shear_viscous_damping =   <Pa*s>
        residual_friction_coefficient =  <.>
        shear_zone_thickness = <m>;
        surface_vector_relative_tolerance = <>;
```

```
add element #<.>  type
   StressBasedSoftContact_NonLinHardSoftShear with nodes
   (<.>,<.>)
        initial_axial_stiffness =  <Pa>
        stiffning_rate =  <.>
        max_axial_stiffness = <Pa>
        initial_shear_stiffness = <Pa>
        rate_of_softening = <.>
        size_of_peak_plateau = <.>
        axial_viscous_damping =  <Pa*s>
        shear_viscous_damping =  <Pa*s>
```

```
        peak_friction_coefficient_limit = <.>
        peak_friction_coefficient_rate_of_decrease     = <.>
        residual_friction_coefficient =  <.>
        shear_zone_thickness = <m>;
        surface_vector_relative_tolerance = <>;
```

3. **Coupled Hard Contact**:

```
add element #<.>  type
   StressBasedCoupledHardContact_ElPPlShear with nodes
   (<.>,<.>)
        normal_stiffness = <Pa>
        normal_penalty_stiffness = <Pa>
        initial_shear_stiffness =  <Pa>
        axial_viscous_damping =  <Pa*s>
        shear_viscous_damping =   <Pa*s>
        residual_friction_coefficient =  <.>
        shear_zone_thickness = <m>;
        surface_vector_relative_tolerance = <>;
```

```
add element #<.>  type
   StressBasedCoupledHardContact_NonLinHardShear with nodes
   (<.>,<.>)
        normal_stiffness = <Pa>
        normal_penalty_stiffness = <Pa>
        initial_shear_stiffness =  <Pa>
        axial_viscous_damping =  <Pa*s>
        shear_viscous_damping =   <Pa*s>
```

```
        residual_friction_coefficient =  <.>
        shear_zone_thickness = <m>;
        surface_vector_relative_tolerance = <>;
```

```
add element #<.>  type
   StressBasedCoupledHardContact_NonLinHardSoftShear with
   nodes (<.>,<.>)
        normal_stiffness = <Pa>
        normal_penalty_stiffness = <Pa>
        initial_shear_stiffness = <Pa>
        rate_of_softening = <.>
        size_of_peak_plateau = <.>
        axial_viscous_damping =  <Pa*s>
        shear_viscous_damping =  <Pa*s>
        peak_friction_coefficient_limit = <.>
        peak_friction_coefficient_rate_of_decrease     = <.>
        residual_friction_coefficient =  <.>
        shear_zone_thickness = <m>;
        surface_vector_relative_tolerance = <>;
```

4. **Coupled Soft Contact**:

```
add element #<.>  type StressBasedSoftContact_ElPPlShear
   with nodes (<.>,<.>)
        initial_axial_stiffness =  <Pa>
        stiffning_rate =  <.>
        max_axial_stiffness = <Pa>
        normal_penalty_stiffness = <Pa>
```

```
        initial_shear_stiffness = <Pa>
        axial_viscous_damping = <Pa*s>
        shear_viscous_damping = <Pa*s>
        residual_friction_coefficient = <.>
        shear_zone_thickness = <m>;
        surface_vector_relative_tolerance = <>;
```

```
add element #<.> type SoftContact_NonLinHardShear with
   nodes (<.>,<.>)
        initial_axial_stiffness = <Pa>
        stiffning_rate = <.>
        max_axial_stiffness = <Pa>
        normal_penalty_stiffness = <Pa>
        initial_shear_stiffness = <Pa>
        axial_viscous_damping = <Pa*s>
        shear_viscous_damping = <Pa*s>
        residual_friction_coefficient = <.>
        shear_zone_thickness = <m>;
        surface_vector_relative_tolerance = <>;
```

```
add element #<.> type
   StressBasedSoftContact_NonLinHardSoftShear with nodes
   (<.>,<.>)
        initial_axial_stiffness = <Pa>
        stiffning_rate = <.>
        max_axial_stiffness = <Pa>
        normal_penalty_stiffness = <Pa>
```

```
initial_shear_stiffness = <Pa>
rate_of_softening = <.>
size_of_peak_plateau = <.>
axial_viscous_damping =  <Pa*s>
shear_viscous_damping =  <Pa*s>
peak_friction_coefficient_limit = <.>
peak_friction_coefficient_rate_of_decrease     = <.>
residual_friction_coefficient =  <.>
shear_zone_thickness = <m>;
surface_vector_relative_tolerance = <>;
```

The terms associated with the DSL's are enlisted here

- **axial_stiffness** k_n : refers to the penalty stiffness in contact normal direction. The units are in Pa. See Equation 2.5

- **initial_axial_stiffness** k_i : refers to the initial penalty stiffness in contact normal direction for soft contact. The units are in Pa. See Equation A.3

$$\sigma_n = k_i exp(-S_r \epsilon)\epsilon \tag{A.3}$$

- **max_axial_stiffness** k_n^{max} : It refers to the maximum achievable stiffness in contact normal direction for soft contact element. The units are in Pa. It provides an cap to the maximum normal stiffness to prevent from numerical issues. See Equation 2.8 which shows the form the force based contact. For the stress based contact replace penetration Δ_n with normal strain ϵ.

- **axial_penalty_stiffness** k_p : It refers to the penalty stiffness to enforce U-u DOF in coupled contact in contact normal direction. The units are in Pa. See Section 3.44

- **stiffening_rate** S_r : It defines the exponential rate at which the stiffness of soft contact increases. For stress based contact the stiffness increases exponentially as

a function of normal strain $\epsilon = \Delta_n / SZ_h$. Thus it is unit-less for the stress based contact and is shown in Equation A.3.

- **initial_shear_stiffness** k_t : It refers to the penalty stiffness in tangential direction for confinement of $P_0 = 100kPa$. See Section 2.4

- **rate_of_softening** : It is unit-less quantity which refers to the rate of softening of the interface once the peak friction coefficient μ_p is attained. See Section 2.4.3

- **size_of_peak_plateau** : It is unit-less quantity which refers to size of plateau when the peak friction coefficient μ_p is attained. See Section 2.4.3

- **axial_viscous_damping** c_n : It defines the visco-elastic stiffness in contact normal direction. See Section 3.4

- **shear_viscous_damping** c_t : It defines the visco-elastic stiffness in contact tangential direction. See Section 3.4

- **peak_friction_coefficient_limit** μ_{p0} : It refers to the upper limit of peak friction coefficient μ_p for low confinement. See Section 2.4.3

- **peak_friction_coefficient_rate_of_decrease** k : It refers to the rate of decrease of peak friction coefficient μ_p with logarithmic increase of normalized normal stress $\frac{\sigma}{P_0 = 100kPa}$. See Section 2.4.3

$$\mu_p(\sigma) = max(\mu_{p0}, \mu_{p0} - klog(\frac{\sigma}{P_0 = 100kPa})) \tag{A.4}$$

- **residual_friction_coefficient** μ_r : It refers to friction coefficient between the two interface layers. See Section 2.4

- **shear_zone_thickness** SZ_h : It refers to the thickness of shear zone in soil at soil-foundation interface. See Section 2.2

- **surface_vector_relative_tolerance** : It defines the relative tolerance criteria used to find out the auto-surface normals for conforming surface-to-surface mesh.

In the above contact DSL's there are basically three type of shear interface models EPPS, NLHS and NLHSS as described in Section 2.4.

References

Arnold, M. and Herle, I. [2006], 'Hypoplastic description of the frictional behaviour of contacts', *Numerical methods in geotechnical engineering* pp. 101–6.

Aubry, D., Hujeux, J., Lassoudiere, F. and Meimon, Y. [1982], A double memory model with multiple mechanisms for cyclic soil behaviour, *in* 'Proceedings of the Int. Symp. Num. Mod. Geomech', pp. 3–13.

Aubry, D., Modaressi, A. and Modaressi, H. [1990], 'A constitutive model for cyclic behaviour of interfaces with variable dilatancy', *Computers and Geotechnics* **9**(1-2), 47–58.

Bandis, S., Lumsden, A. and Barton", N. [1983], 'Fundamentals of rock joint deformation', *International Journal of Rock Mechanics and Mining Sciences & Geomechanics Abstracts* **20**(6), 249 – 268.

Batista, D., Royis, P. and Doanh, T. [2003], 'Time-integration of a hypoplastic constitutive equation in finite element modelling', *Mathematical and computer modelling* **37**(5), 615–621.

Behbehani, F. [2017], Theoretical and numerical modeling of unsaturated soil using coupled elements, Master's thesis, University of California Davis.

Bishop, A. W. [1959], 'The principle of effective stress', *Teknisk ukeblad* **39**, 859–863.

Bishop, A. W. and Blight, G. [1963], 'Some aspects of effective stress in saturated and partly saturated soils', *Geotechnique* **13**(3), 177–197.

Bolton, M. [1986], 'The strength and dilatancy of sands', *Geotechnique* **36**(1), 65–78.

Boulon, M. [1989], 'Basic features of soil structure interface behaviour', *Computers and Geotechnics* **7**(1-2), 115–131.

Boulon, M., Ghionna, V. N. and Mortara, G. [2003], 'A strain-hardening elastoplastic model for sand-structure interface under monotonic and cyclic loading', *Mathematical and computer modelling* **37**(5-6), 623–630.

Boulon, M. and Nova, R. [1990], 'Modelling of soil-structure interface behaviour a comparison between elastoplastic and rate type laws', *Computers and Geotechnics* **9**(1-2), 21–46.

Breysse, D., Niandou, H., Elachachi, S. and Houy, L. [2005], 'A generic approach to soil–structure interaction considering the effects of soil heterogeneity', *Geotechnique* **55**(2), 143–150.

Brumund, W. and Leonards, G. [1973], 'Experimental study of static and dynamic friction between sand and typical constuction materials', *Journal of Testing and Evaluation* **1**(2), 162–165.

Crisfield, M. A. [1981], 'A fast incremental / iterative solution procedure that handles snap - through', *Computers & Structures* **13**, 55–62.

Crisfield, M. A. [1987], 'Consistent schemes for plasticity computation with the Newton Raphson method', *Computational Plasticity Models, Software, and Applications* **1**, 136–160.

Crisfield, M. A. [1991], *Non–Linear Finite Element Analysis of Solids and Structures Volume 1: Essentials*, John Wiley and Sons, Inc. New York, 605 Third Avenue, New York, NY 10158–0012, USA.

Crisfield, M. A. [1997], *Non–Linear Finite Element Analysis of Solids and Structures Volume 2: Advanced Topics*, John Wiley and Sons, Inc. New York, 605 Third Avenue, New York, NY 10158–0012, USA.

Dafalias, Y. F. [1985], A missing link in the macroscopic constitutive formulation of large plastic deformations, *in* A. Sawczuk and G. Bianchi, eds, 'Plasticity Today: Modelling, Methods and Applications', Elsevier Applied Sciences Publishers, pp. 135–151.

Dafalias, Y. F. [1986], 'Bounding surface plasticity. I: Mathematical foundations and hypoplasticity', *ASCE Journal of Engineering Mechanics* **112**(9), 966–987.

Day, R. and Potts, D. [1994], 'Zero thickness interface elementsnumerical stability and application', *International Journal for numerical and analytical methods in geomechanics* **18**(10), 689–708.

de Borst, R. [1987], 'Smeared cracking, plasticity, creep, and thermal loading - a unified approach', *Computer Methods in Applied Mechanics and Engineering* **62**, 89–110.

de Borst, R. and Feenstra, P. H. [1990], 'Studies in anysotropic plasticity with reference to the hill criterion', *International Journal for Numerical Methods in Engineering* **29**, 315–336.

De Gennaro, V. and Frank, R. [2002], 'Elasto-plastic analysis of the interface behaviour between granular media and structure', *Computers and Geotechnics* **29**(7), 547–572.

DeJong, J. T. and Westgate, Z. J. [2009], 'Role of initial state, material properties, and confinement condition on local and global soil-structure interface behavior', *ASCE Journal of Geotechnical and Geoenvironmental Engineering* **135**(11), 1646–1660.

Dejong, J. T., White, D. J. and Randolph, M. F. [2006], 'Microscale observation and modeling of soil-structure interface behavior using particle image velocimetry', *Soils and Foundations* **46**(1), 15–28.

Desai, C. [1981], 'Behavior of interfaces between structural and geologic media'.

Desai, C. and Nagaraj, B. [1988], 'Modeling for cyclic normal and shear behavior of interfaces', *Journal of engineering mechanics* **114**(7), 1198–1217.

Desai, C. S. and Siriwardane, H. J. [1984], *Constitutive Laws for Engineering Materials With Emphasis on Geologic Materials*, Prentice–Hall, Inc. Englewood Cliffs, NJ 07632.

Desai, C., Zaman, M., Lightner, J. and Siriwardane, H. [1984], 'Thin-layer element for interfaces and joints', *International Journal for Numerical and Analytical Methods in Geomechanics* **8**(1), 19–43.

Dodds, J. and Robert, H. [1987], 'Numerical techniques for plasticity computations in finite element analysis', *Computers & Structures* **26**(5), 767–779.

DAguiar, S. C., Modaressi-Farahmand-Razavi, A., Dos Santos, J. A. and Lopez-Caballero, F. [2011], 'Elastoplastic constitutive modelling of soil–structure interfaces under monotonic and cyclic loading', *Computers and Geotechnics* **38**(4), 430–447.

Evgin, E. and Fakharian, K. [1997], 'Effect of stress paths on the behaviour of sand steel interfaces', *Canadian geotechnical journal* **33**(6), 853–865.

Fakharian, K. [1996], *Three-dimensional monotonic and cyclic behaviour of sand-steel interfaces: Testing and modelling.*, University of Ottawa (Canada).

Fakharian, K. and Evgin, E. [1995], Simple shear versus direct shear tests on interfaces during cyclic loading, *in* 'Proceedings of International Conference on Recent Advances in geotechnical Earthquake Engineering and Soil Dynamics', Vol. 1, University of Missouri–Rolla.

Fakharian, K. and Evgin, E. [1996], 'An automated apparatus for three-dimensional monotonic and cyclic testing of interfaces', *Geotechnical Testing Journal* **19**(1), 22–31.

Fakharian, K. and Evgin, E. [1997], 'Cyclic simple-shear behavior of sand-steel interfaces under constant normal stiffness condition', *Journal of Geotechnical and Geoenvironmental Engineering* **123**(12), 1096–1105.

Fakharian, K. and Evgin, E. [2000], 'Elasto-plastic modelling of stress-path-dependent behaviour of interfaces', *International Journal for Numerical and Analytical Methods in Geomechanics* **24**(2), 183–199.

Fakharian, K., Evgin, E. et al. [2002], A comprehensive experimental study of sand-steel interfaces subjected to various monotonic and cyclic stress paths, *in* 'The Twelfth International Offshore and Polar Engineering Conference', International Society of Offshore and Polar Engineers.

Francavilla, A. and Zienkiewicz, O. [1975], 'A note on numerical computation of elastic contact problems', *International Journal for Numerical Methods in Engineering* **9**(4), 913–924.

Frank, R., Guenot, A. and Humbert, P. [1982], Numerical analysis of contacts in geomechanics, *in* '4th Int. Conf. Num. in Geomechs', Vol. 1, pp. 37–45.

Gajan, S. and L.Kutter, B. [2009], 'Contact interface model for shallow foundations subjected to combined cyclic loading', *ASCE Journal of Geotechnical and Geoenvironmental Engineering* **135**(3), 407–419.

Gens, A., Carol, I. and Alonso, E. [1990], 'A constitutive model for rock joints formulation and numerical implementation', *Computers and Geotechnics* **9**(1-2), 3–20.

Ghaboussi, J., Wilson, E. L. and Isenberg, J. [1973], 'Finite element for rock joints and interfaces', *Journal of Soil Mechanics & Foundations Div* **99**(Proc Paper 10095).

Goodman, R. E., Taylor, R. L. and Brekke, T. L. [1968], 'A model for the mechanics of jointed rocks', *Journal of Soil Mechanics & Foundations Div* .

Haraldsson, A. and Wriggers, P. [2000], 'A strategy for numerical testing of frictional laws with application to contact between soil and concrete', *Computer Methods in Applied Mechanics and Engineering* **190**, 963–977.

Herrmann, L. R. [1978], 'Finite element analysis of contact problems', *Journal of the Engineering Mechanics Division* **104**(5), 1043–1057.

Hill, R. [1950], *The Mathematical Theory of Plasticity*, The Oxford Engineering Science Series, 1st. edn, Oxford at the Clarendon Press.

Hu, L. and Pu, J. [2004], 'Testing and modeling of soil-structure interface', *Journal of Geotechnical and Geoenvironmental Engineering* **130**(8), 851–860.

Jardine, R. J., Potts, D., Fourie, A. and Burland, J. [1986], 'Studies of the influence of non-linear stress–strain characteristics in soil–structure interaction', *Geotechnique* **36**(3), 377–396.

Jeremić, B. [1994], Implicit integration rules in plasticity: Theory and implementation, Master's thesis, University of Colorado at Boulder.

Jeremić, B., Jie, G., Cheng, Z., Tafazzoli, N., Tasiopoulou, P., Abell, F. P. J. A., Watanabe, K., Feng, Y., Sinha, S. K., Behbehani, F., Yang, H. and Wang, H. [2017], *The Real ESSI Simulator System*, University of California, Davis and Lawrence Berkeley National Laboratory. `http://real-essi.info/`.

Jeremić, B., Jie, G., Preisig, M. and Tafazzoli, N. [2009], 'Time domain simulation of soil–foundation–structure interaction in non–uniform soils.', *Earthquake Engineering and Structural Dynamics* **38**(5), 699–718.

Jetteur, P. [1986], 'Implicit integration algorithm for elastoplasticity in plane stress analysis', *Engineering Computations* **3**, 251–253.

Kishida, H. and Uesugi, M. [1987], 'Tests of the interface between sand and steel in the simple shear apparatus', *Geotechnique* **37**(1), 45–52.

Klisinski, M., Mroz, Z. and Runesson, K. [1992], 'Structure of constitutive equations in plasticity for different choices of state variables', *International Journal of Plasticity* **8**, 221–243.

Kojić, M. and Bathe, K.-J. [1987], 'The "effective stress function" algorithm for thermo elasto plasticity and, creep', *International Journal for Numerical Methods in Engineering* **24**, 1509–1532.

Kolymbas, D. [1977], 'A rate-dependent constitutive equation for soils', *Mechanics Research Communications* **4**(6), 367–372.

Kolymbas, D. [1985], A generalized hypoplastic constitutive law, *in* 'Proceedings of the Eleventh International Conference on Soil Mechanics and Foundation Engineering', San Francisco, USA, p. 2626.

Kolymbas, D. [1991], 'An outline of hypoplasticity', *Archive of Applied Mechanics* **61**(3), 143–151.

Kolymbas, D., Herle, I. and Von Wolffersdorff, P. [1995], 'Hypoplastic constitutive equation with internal variables', *International Journal for Numerical and Analytical Methods in Geomechanics* **19**(6), 415–436.

Kolymbas, D. and Wu, W. [1993], 'Introduction of hypoplasticity', *Modern approaches to plasticity* pp. 213–223.

Konter, A. W. A. [2005], Advanced finite element contact benchmarks, Technical report, Netherlands Institute for Metals Research.

Littleton, I. [1976], 'An experimental study of the adhesion between clay and steel', *Journal of terramechanics* **13**(3), 141–152.

Liu, H. and Ling, H. I. [2008], 'Constitutive description of interface behavior including cyclic loading and particle breakage within the framework of critical state soil mechanics', *International journal for numerical and analytical methods in geomechanics* **32**(12), 1495–1514.

Liu, H., Song, E. and Ling, H. I. [2006], 'Constitutive modeling of soil-structure interface through the concept of critical state soil mechanics', *Mechanics Research Communications* **33**(4), 515–531.

Liu, J., Zou, D. and Kong, X. [2014], 'A three-dimensional state-dependent model of soil–structure interface for monotonic and cyclic loadings', *Computers and Geotechnics* **61**, 166–177.

Lubliner, J. [1990], *Plasticity Theory*, Macmillan Publishing Company, New York.

Martinez, A., Frost, J. D. and Hebeler, G. L. [2015], 'Experimental study of shear zones formed at sand/steel interfaces in axial and torsional axisymmetric tests', *Geotechnical Testing Journal* **38**(4), 409–426.

Mašín, D. [2005], 'A hypoplastic constitutive model for clays', *International Journal for Numerical and Analytical Methods in Geomechanics* **29**(4), 311–336.

Mortara, G., Boulon, M. and Ghionna, V. N. [2002], 'A 2-d constitutive model for cyclic interface behaviour', *International journal for numerical and analytical methods in geomechanics* **26**(11), 1071–1096.

Mortara, G., Mangiola, A. and Ghionna, V. N. [2007], 'Cyclic shear stress degradation and post-cyclic behaviour from sand–steel interface direct shear tests', *Canadian Geotechnical Journal* **44**(7), 739–752.

Navayogarajah, N., Desai, C. and Kiousis, P. [1992], 'Hierarchical single-surface model for static and cyclic behavior of interfaces', *Journal of engineering mechanics* **118**(5), 990–1011.

Nguyen, Q. S. [1977], 'On the elastic plastic initial - boundary value problem and it numerical integration', *International Journal for Numerical Methods in Engineering* **11**, 817–832.

Nogami, T., Otani, J., Konagai, K. and Chen, H.-L. [1992], 'Nonlinear soil-pile interaction model for dynamic lateral motion', *Journal of Geotechnical Engineering* **118**(1), 89–106.

Oberkampf, W. L. and Trucano, T. G. [2002], 'Verification and validation in computational fluid dynamics', *Progress in Aerospace Sciences* **38**(3), 209–272.
URL: *http://www.sciencedirect.com/science/article/pii/S0376042102000052*

Ortiz, M. and Simo, J. C. [1986], 'An analysis of a new class of integration algorithms for elastoplastic, constitutive relations', *International Journal for Numerical Methods in Engineering* **23**, 353–366.

Pastor, M., Zienkiewicz, O. and Chan, A. [1990], 'Generalized plasticity and the modelling of soil behaviour', *International Journal for Numerical and Analytical Methods in Geomechanics* **14**(3), 151–190.

Petersson, N. A. and Sjögreen, B. [2017], 'High order accurate finite difference modeling of seismo-acoustic wave propagation in a moving atmosphere and a heterogeneous earth model coupled across a realistic topography', *Journal of Scientific Computing* pp. 1–34.

Potyondy, J. G. [1961], 'Skin friction between various soils and construction materials', *Geotechnique* **11**(4), 339–353.

Rodgers, A. [2017], Private communications. SW4 – Real ESSI connection.

Runesson, K., Samuelsson, A. and Bernspång, L. [1986], 'Numerical technique in plasticity including solution advancement control', *International Journal for Numerical Methods in Engineering* **22**, 769–788.

Runesson, K. and Sture, S. [1989], 'Stability of frictional materials', *Journal of Engineering Mechanics* **115**(8), 1828–1833.

Sachdeva, T. and Ramakrishnan, C. [1981], 'A finite element solution for the two-dimensional elastic contact problems with friction', *International Journal for Numerical Methods in Engineering* **17**(8), 1257–1271.

Segura, J. and Carol, I. [2008], 'Coupled HM analysis using zero-thickness interface elements with double nodes. part i: Theoretical model', *International Journal for Numerical and Analytical Methods in Geomechanics* **32**, 2083–2101.

Segura, J. M. and Carol, I. [2004], 'On zero-thickness interface elements for diffusion problems', *International Journal for Numerical and Analytical Methods in Geomechanics* **28**(9), 947–962.

Shahrour, I. and Rezaie, F. [1997], 'An elastoplastic constitutive relation for the soil-structure interface under cyclic loading', *Computers and Geotechnics* **21**(1), 21–39.

Sheng, D., Wriggers, P. and Sloan, S. W. [2007], 'Application of frictional contact in geotechnical engineering', *ASCE International Journal of Geomechanics* **7**(3), 176–185.

Simo, J. C., Kennedy, J. G. and Govindjee, S. [1988], 'Non - smooth multisurface plasticity and viscoplasticity. loading / unloading, conditions and numerical algorithms', *International Journal for Numerical Methods in Engineering* **26**, 2161–2185.

Simo, J. C. and Taylor, R. L. [1985], 'Consistent tangent operators for rate-independent elastoplasticity', *Computer Methods in Applied Mechanics and Engineering* **48**, 101–118.

Simo, J. C. and Taylor, R. L. [1986], 'A returning mapping algorithm for plane stress elastoplasticity', *International Journal for Numerical Methods in Engineering* **22**, 649–670.

Sinha, S. K., Behbehani, F. and Jeremić, B. [2017], Modelling of buoyant forces in earthquake soil-structure interaction, *in* 'Proceedings of the 15th International Conference of the International Association for Computer Methods and Advances in Geomechanics (IACMAG 15)', Wuhan, China.

Sinha, S. K., Feng, Y., Yang, H., Wang, H., Orbović, N., McCallen, D. B. and Jeremić, B. [2017], 3-d non-linear modeling and its effects in earthquake soil-structure interaction, *in* 'Proceedings of the 24th International Conference on Structural Mechanics in Reactor Technology (SMiRT 24)', Busan, South Korea.

Stewart, J. P., Fenves, G. L. and Seed, R. B. [1999], 'Seismic soil-structure interaction in buildings. i: Analytical methods', *Journal of Geotechnical and Geoenvironmental Engineering* **125**(1), 26–37.

Stutz, H. H. [2016], Hypoplastic Models for Soil-Structure Interfaces-Modelling and Implementation, PhD thesis, Christian-Albrechts Universität Kiel.

Stutz, H., Mašín, D., Sattari, A. and Wuttke, F. [2017], 'A general approach to model interfaces using existing soil constitutive models application to hypoplasticity', *Computers and Geotechnics* **87**, 115–127.

Stutz, H., Mašín, D. and Wuttke, F. [2016], 'Enhancement of a hypoplastic model for granular soil–structure interface behaviour', *Acta Geotechnica* **11**(6), 1249–1261.

Tamagnini, C., Viggiani, G., Chambon, R. and Desrues, J. [2000], 'Evaluation of different

strategies for the integration of hypoplastic constitutive equations: Application to the cloe model', *Mechanics of Cohesive-frictional Materials* **5**(4), 263–289.

Tang, H., Tang, Y., Stepp, J., Wall, I., Lin, E., Cheng, S. and Lee, S. [1989], 'A large-scale soil-structure interaction experiment: Design and construction', *Nuclear Engineering and Design* **111**(3), 371 – 379.
URL: *http://www.sciencedirect.com/science/article/pii/0029549389902483*

Taylor, G. I. and Quinney, H. [1934], 'The latent energy remaining in a metal after cold working', *Proceedings of the Royal Society of London. Series A, Containing Papers of a Mathematical and Physical Character* **143**(849), 307–326.

Tejchman, J. and Wu, W. [1995], 'Experimental and numerical study of sand–steel interfaces', *International journal for numerical and analytical methods in geomechanics* **19**(8), 513–536.

Temam, R. [1985], *Mathematical Problems in Plasticity*, Gauthier–Villars.

Truesdell, C. [1955], 'Hypo-elasticity', *Journal of Rational Mechanics and Analysis* **4**, 83–1020.

Truesdell, C. [1963], 'Remarks on hypo-elasticity', *Journal of Research of the National Bureau of Standards-B. Mathematics and Mathematical Physica* **67**(3), 141–143.

Uesugi, M. and Kishida, H. [1986*a*], 'Frictional resistance at yield between dry sand and mild steel', *Soils and foundations* **26**(4), 139–149.

Uesugi, M. and Kishida, H. [1986*b*], 'Influential factors of friction between steel and dry sands', *Soils and foundations* **26**(2), 33–46.

Uesugi, M., Kishida, H. and Tsubakihara, Y. [1989], 'Friction between sand and steel under repeated loading', *Soils and foundations* **29**(3), 127–137.

Uesugi, M., Kishida, H. and Uchikawa, Y. [1990], 'Friction between dry sand and concrete under monotonic and repeated loading', *Soils and Foundations* **30**(1), 115–128.

von Wolffersdorff, P.-A. [1996], 'A hypoplastic relation for granular materials with a predefined limit state surface', *Mechanics of Cohesive-frictional Materials* **1**(3), 251–271.

Wang, S., Kutter, B. L., Chacko, M. J., Wilson, D. W., Boulanger, R. W. and Abghari, A. [1998], 'Nonlinear seismic soil-pile structure interaction', *Earthquake spectra* **14**(2), 377–396.

Wolf, J. and Hall, W. [1989], 'Soil-structure-interaction analysis in time domain', *Nuclear Engineering and Design* **111**(3), 381 – 393.

Wolf, J. P. [1989], 'Soil-structure-interaction analysis in time domain', *Nuclear Engineering and Design* **111**(3), 381 – 393.
URL: *http://www.sciencedirect.com/science/article/pii/0029549389902495*

Wriggers, P. [2002], *Computational Contact Mechanics*, John Wiley & Sons.

Wu Tai, T. [1966], 'The effect of inclusion shape on the elastic moduli of a two - phase material', *International Journal of Solids and Structures* **2**, 1–8.

Yang, H., Sinha, S. K., Feng, Y., McCallen, D. B. and Jeremić, B. [2017], 'Energy dissipation analysis of elastic-plastic materials [in print]', *Computer Methods in Applied Mechanics and Engineering* .

Yoshimi, Y. and Kishida, T. [1981], 'A ring torsion apparatus for evaluating friction between soil and metal surfaces', *Geotechnical Testing Journal* **4**(4), 145–152.

Zienkiewicz, O. [1970], *Analysis of Non Linear Problems in Rock Mechanics with Particular Reference to Jointed Rock Systems*, publisher not identified.
URL: *https://books.google.com/books?id=qjTtSAAACAAJ*

Zienkiewicz, O. C., Chan, A. H. C., Pastor, M., Schrefler, B. A. and Shiomi, T. [1999], *Computational Geomechanics with Special Reference to Earthquake Engineering*, John Wiley and Sons. ISBN 0-471-98285-7.

Zienkiewicz, O. C. and Taylor, R. L. [1991], *The Finite Element Method*, Vol. 2, Fourth edn, McGraw - Hill Book Company.